Laboratoire de Constructions Hydrauliques
Ecole Polytechnique Fédérale de Lausanne

Communication 24

Efficiency of brushwood fences in shore protection against wind-wave induced erosion

Selim Sayah

Editeur : Prof. Dr A. Schleiss

Lausanne, 2006

Communications du Laboratoire de constructions hydrauliques ISSN 1661-1179
Ecole Polytechnique Fédérale de Lausanne
Editeur: Prof. Dr A. Schleiss

Preface

Shore protection in Swiss Lakes is a topic of great interest because several sandy beaches suffer severe erosion. Soft protection measures have been widely used since the late 20th century and designed on only empirical bases. They consist of detached porous wooden structures such as brushwood fences and palisades. The experience showed that their efficiency was not always satisfactory. In his research work, Dr. Selim Sayah evaluated systematically the behavior and efficiency of the widely used brushwood fences by the means of physical and numerical modelling. The results were compared with field measurements carried out at Lake Biel. The purpose of his research was to provide reliable technical criteria and recommendations for an enhanced design of such soft shore protection measures.

The behavior of brushwood fences built over a fixed bed was extensively investigated on a downscaled model. The key finding of this first series of experimental tests was a new empirical relationship to calculate the efficiency of the brushwood fences expressed by the transmission coefficient of waves as a function of the relative freeboard of the structure, its porosity, and the incoming wave steepness.

Dr. Selim Sayah examined for the first time the interaction of a movable bed with the brushwood fences and their efficiency in favoring sand deposition. Based on a new theoretical approach to downscale the movable bed characteristics, the effect of a porous brushwood fence on the shoreline and bottom evolution was studied. The influence of the movable bed on the transmission coefficient of the protection structure was analyzed and empirical relationships were developed for the salient formation and sand deposition behind the protection

He also studied the effects of single and double gaps in a porous linear structure using a carefully calibrated numerical model. The wave field between the structure and the shoreline was modelled and diffraction diagrams of the transmitted waves were established. His outlined methodology in numerical modelling was successfully applied to a case study, where detached porous structures were used to protect the shoreline against erosion. He demonstrated that such approach could be easily applied on practical cases where a protection is needed to mitigate shore erosion.

We would like to thank Dr. Andreas Matheja and Dr. Stephan Mai from the University of Hannover, Germany for their contributions in the field of numerical modelling as academic guests at LCH-EPFL. Furthermore we thank Christoph Iseli from the Association for the Protection of Lake Biel, Dr. Andreas Huber and Prof. William Kamphuis from Queen's University, Kingston, Canada for their significant support and guidance. We also thank gratefully the Swiss Innovation Promotion Agency KTI/CTI for their financial support under grant KTI 7670.1 as well as the financial project partners: Swiss Federal Office for Water and Geology, Canton Berne, Association for the Protection of Lake Biel, Swiss Foundation for Landscape Protection and Association for Biotechnical Engineering.

Prof. Dr. Anton J. Schleiss

to my beloved mother
Martha and father Mikhael
who taught me how to learn

Abstract

"Efficiency of brushwood fences in coastal protection against wind-wave induced erosion"

Shore protection in confined water bodies is of major importance in Switzerland where many lakes suffer severe shore erosion. It occurs mainly in shallow zones due to several reasons such as: the fluctuations of the water level , the wind-wave impact during major wind events, and the increasing effect of incident waves due to solid reenforcement by non-adapted protection measures. In order mitigate this increased erosion and enhance the shore stability by sustainable coastal structures, pioneer and soft measures have been built during the past decades. Although such solutions proved their efficiency, they raised a new challenge for engineers: how to build soft and porous media that take into consideration the hydraulic and hydrodynamic conditions of the project site, and enhance its efficiency in sand trapping and shoreline accretion.

By means of experimental and numerical modelling, the performance of a typical soft measure, called brushwood fence, was investigated in hydrodynamic conditions similar to those found in reality. A downscaled model of 1 : 10 was built on a fixed bed, and then tested in a wave tank of 10 m length and 6 m width under incoming perpendicular and regular waves. The response of the structure regarding the transmission coefficient has been analyzed for five dimensionless variables: 1) the relative freeboard of the structure R_c/H_i, 2) its relative height h/H_i, 3) the relative wave number kd, 4) the wave steepness H_i/gT^2, and 5) the porosity of the structure p. The analysis of their effect on the performance of the protection structure allowed the establishment of an empirical relationship for the transmission coefficient. It takes into account the geometrical characteristics of the structure as well as the local hydrodynamic conditions. The response of the structure has to be treated separately in relation to its immersion condition. When the structure is submerged, every dimensionless variable has a differentiated effect on the transmission coefficient in comparison to the condition when the structure is emerging. The relative freeboard, wave steepness and the porosity are the three key variables in the response of the structure regarding wave damping.

The efficiency of detached brushwood fences built on a movable bed was tested under the action of waves with fixed characteristics. The bed material was made of a granular, fine sand with a diameter $d_{50} = 0.18\ mm$. The evolution of the shoreline and the transmission coefficient of the structure were determined using a first series of tests. It was demonstrated that time has negative impact on wave damping, at least during the period where the bed in the vicinity of the structure evolves to its equilibrium state. A second series of tests established the effect of the distance S of the detached structure (length B) from the shoreline on its evolution and on the deposited and eroded sand volumes at the leeside of the structure. It was proven that the wave motion through the porous media hinders the formation of significant salients and prevents the formation of tombolos when the structure was very close to the shoreline. Thus, for high ratio $B/S = 1.48$ no tombolo was formed in line with non porous breakwaters. The deposited and eroded volumes were also evaluated in a third series of tests with the presence of a single gap in the brushwood fences. The effect of the width of the gap on these volumes was analyzed. The results proved that the main deposition area is located between the gap and the shoreline where sediments are transported by the diffracted waves at the edges of the brushwood fences. The highest deposition rate at this location corresponds to the ratio $B/S = 0.25$.

Using the solver of the elliptic mild slope equation developed under Mike 21, the wave field in an enclosed area surrounded by a porous structure was numerically investigated. The calibration of some major variables in the numerical model such as wave breaking and bottom friction parameters, based on the experimental results, proved the adequacy of the selected numerical scheme. The effect of a single and double gap in a linear infinite porous media was afterwards evaluated and diffraction diagrams were built for the enclosed wave field. A rule was proposed to use a relative gap width $G/Wmax$ less then 0.12. The wave field for two gaps is different and significantly influenced by the spacing between the gaps. For low spacing values ($Es/G = 2$), waves in the middle of the protected area are high along the structure and very low close to the shore. For high spacing values ($Es/G = 5$), the wave field is also significantly deformed. However, values of Es/G comprised between 3 and 4 seem to be most appropriate since the corresponding wave field is less deformed. The two gaps configuration does not significantly increase the residual total energy behind the structure. It is relatively constant with spacing variations between two gaps and increased slowly with the increase of a single gap width.

The experimental observations and the numerical results were successfully applied in Mörigen bordering Lake Biel. The wave fields were calculated numerically behind a series of segmented brushwood fences. Several wind-wave regimes and varying water levels were analyzed to optimize the performance of the porous protection structures.

Résumé

"Protection contre l'érosion des rives lacustres par des barrages à claire-voie"

La protection des rives lacustres contre l'érosion représente une problématique de grande importance pour la majorité des lacs suisses. Cette érosion accrue se manifeste particulièrement dans les zones peu profondes. Elle est souvent due a plusieurs facteurs en interaction, comme la fluctuation du plan d'eau, l'impact des vagues générées par les vents extrêmes ou les constructions inadaptées aux rives des lacs. Ces dernières souvent trop rigides, amplifient de ce fait l'impact des vagues incidentes et réfléchis. Pour lutter contre cette érosion et augmenter la stabilité des rives en utilisant des structures côtières plus appropriées et durables, des mesures douces et poreuses sont proposées et construites pendant les trois dernières décennies. Bien qu'elles aient prouvé leur efficacité, elles soulèvent une nouvelle question pour les ingénieurs : comment construire efficacement de telles structures en se basant sur une approche scientifique qui considère les conditions limnimétriques et hydrodynamiques du site?

Sur la base d'une approche expérimental et numérique, la performance d'une mesure typique, appelée barrage à claire voie, est étudiée dans des conditions semblables à la réalité. Un modèle réduit (échelle 1 : 10) est construit sur un lit fixe, et testé dans un bassin à houle d'une longueur de 10 m et d'une largeur de 6 m, soumis à des vagues incidente perpendiculaires et régulières. La réponse du barrage à claire voie est mesurée par son coefficient de transmission. Les variables de cette étude sont la porosité et la hauteur de la structure ainsi que la profondeur d'eau et la période de vague incidente. L'analyse de plusieurs variables adimensionnelles a permis l'établissement d'une relation empirique pour le calcul du coefficient de transmission. Elle considère les caractéristiques géométriques de la structure ainsi que les conditions hydrodynamiques locales. L'effet du barrage à claire voie construit sur un lit mobile est également examiné. Ce dernier est constitué d'un sable fin granulaire de diamètre $d_{50} = 0.18\ mm$. L'évolution de la ligne de rive et du coefficient de transmission de la structure sont déterminées sur la base d'une première série d'essais. Une seconde série d'essais a permis d'établir, d'une part, l'effet de la distance de la structure sur l'évolution de

la ligne de rive et, d'une autre part, les volumes de sable déposés et érodés dans la partie protégée par la structure. Ces volumes sont également évalués pendant une troisième série d'essais avec la présence d'une simple ouverture dans les barrages à claire voie. L'effet de la largeur de l'ouverture sur ces volumes est examiné de même.

Avec le logiciel Mike 21 (solveur *elliptic mild slope equation*), le champ de vague dans une zone limitée par la structure poreuse est étudié numériquement. Basé sur les résultats expérimentaux, le calibrage des principales variables du modèle numérique tels que les paramètres liés aux déferlements des vagues et à la rugosité du fond, a prouvé la pertinence du choix du modèle numérique. L'effet de l'ouverture (simple ou double) dans des structures poreuses infinies et linéaires est évalué, permettant ainsi l'établissement des diagrammes de diffraction. Les effets de la période de vague et la perte de leur énergie incidente due à la présence des ouvertures est également évalués. Des recommandations liées à la construction sont élaborées et concernent la largeur d'une simple ouverture et l'espacement entre deux ouvertures consécutives. Finalement, la modélisation numérique a donnée l'approche adéquate pour le traitement de cas similaires.

Les observations expérimentales et les résultats numériques sont employés dans une dernière étape pour calculer numériquement le champ de vague derrière les barrages à claire voie à Mörigen dans le lac de Bienne. Cette étude de cas, basée sur des mesures in situ de vents et de vagues, a démontré l'importance de l'utilisation de la modélisation numérique pour des cas réels où plusieurs régimes de vagues de vent ainsi qu'un niveau d'eau variable pourraient modifier de manière importante l'efficacité des structures de protection.

Zusammenfassung

"Schutz gegen Seeufererosion mit Lahnungen"

Der Schutz von natürlichen Seeufern ist an den Schweizer Mittelandseen von grosser Bedeutung, weil grosse Abschnitte durch Erosionen infolge des Wellenschlages gefährdet sind. Neben Windwellen können auch Wasserspiegelschwankungen und Bootsverkehr Ufererosionen verursachen. Auch fest verbaute Uferabschnitte können Wellen ungünstig auf ungeschützte Bereiche ablenken und ufernahe Erosionen verursachen.

Um diesen erhöhten Erosionen zu begegnen und die Uferstabilität durch nachhaltige Uferstrukturen zu stabilisieren, sind in den vergangenen Dekaden weiche Uferschutzmassnahmen entwickelt worden. Obwohl diese Massnahmen Ihre Effektivität in der Praxis gezeigt haben, sind sie auch Ausgangspunkt eines neuen Aufgabengebiets für den Ingenieur: Wie sind solche weichen Uferschutzmassnahmen auf wissenschaftlicher Grundlage unter Berücksichtigung der hydraulischen und hydrodynamischen Randbedingungen in der Natur auszubilden?

Im physikalischen und numerischen Modell wurde die Wirksamkeit von Lahnungen als Beispiel einer typischen Uferschutzmassnahme für naturähnliche hydrodynamische Bedingungen untersucht. Dazu wurde die Wirksamkeit von Lahnungen zunächst in einem 6 m breiten und 10 m langen Wellenbecken im Masstab 1:10 bei fester Sohle für senkrecht anlaufende, regelmässige Wellen ermittelt. Eine Quantifizierung der Wirksamkeit erfolgte im wesentlichen durch den Transmissionskoeffizienten, welcher für verschiedene Porositäten und Lahnungshöhen bei verschiedenen Wassertiefen und sechs Hauptwellenperioden gemessen wurde. Die Analyse des Einflusses verschiedener dimensionsloser Variablen auf die Wirksamkeit der Uferschutzmassnahme erlaubte die Einführung einer empirischen Beziehung für den Transmissionskoeffizienten. Diese berücksichtigt sowohl die Geometrie der Schutzmassnahme als auch die zu erwartenden hydrodynamischen Bedingungen.

Daneben wurde der Einfluss von vorgelagerten Lahnungen für Einzelwellen im Modell mit beweglicher Sohle untersucht. Das Sohlmaterial bestand aus feinstkörnigem Sand mit einem Durchmesser von $d50 = 0.18\ mm$. In einer ersten Versuchsreihe wurde der Transmissionskoeffiziernt und die

Entwicklung der Uferlinie gemessen. In einer zweiten Versuchsreihe wurde der Einfluss des Abstands der Lahnungen von der Uferlinie einerseits auf deren Entwicklung und andererseits auf die Erosions- bzw. Sedimentationsmenge bestimmt. Schliesslich wurde in einer dritten Versuchsreihe die Bedeutung von Einzelöffnungen im Lahnungsbauwerk auf die Sedimentation und Erosion untersucht.

Um die Ergebnisse aus dem physikalischen Modell auf beliebige Situtationen in der Natur übertagen zu können, wurden numerische Simulationen durchgeführt. Zur numerischen Modellierung wurde ein unter MIKE 21 entwickelter Gleichungslöser für die "Elliptic Mild Slope"-Gleichung eingesetzt. Die Kalibrierung der wesentlichen Modellparameter, wie der Parameter des Wellenbrechens und der Bodenreibung, erwies die Anwendbarkeit des gewählten numerischen Lösungsverfahrens. Mit Hilfe des numerischen Modells wurde der Einfluss von Einzel- und Doppelöffnungen in geradlinigen porösen Bauwerken untersucht und die Ergebnisse in Diffraktionsdiagrammen für den wellenberuhigten Bereich zusammengefasst. Zudem wurden Bemessungsregeln hinsichtlich der Breite von Einzelöffnungen und hinsichtlich des Abstandes aufeinanderfolgender Öffnungen in den Lahnungen gegeben.

Die Ergebnisse der physikalischen und numerischen Modellierung wurden abschliessend verwendet, um das Wellenfeld hinter einer Lahnung bei Möringen im Bieler See zu berechnen. Dieses auf in-situ Wind und Wellenmessungen basierende Anwendungsbeispiel zeigte die Bedeutung der numerischen Simulation in der Praxis, wo verschiedene Windregime und variierende Wasserstände die Wirksamkeit von Uferschutzmassnahmen signifikant beeinflussen.

Table of Contents

Notations

The following symbols are used in this document:

Roman Symbols

Δh_l	in preliminary head-loss tests: linear head-loss
Δh_s	in preliminary head-loss tests: minor head loss of the structure
Δh_t	in preliminary head-loss tests: measured total head-loss
Δt	general definition for time duration
ΔZ	in experimental tests with movable bed: height indicating sand deposition when positive and sand erosion when negative
$\hat{A}_\delta$	peak value of the wave orbital excursion
$_m$	subscript used for model scale
$_p$	subscript used for prototype scale
A	sediment scale parameter
B	length of a detached coastal structure
b	distance between adjacent wave rays after transformation
b	width of the coastal detached structure (breakwaters, brushwood fences)
B_*	dimensionless length of a detached coastal structure $B_* = \frac{B}{X}$
b_0	distance between initial adjacent wave rays
c	phase velocity of waves
c_g	group velocity of waves
D	grain diameter
d	water depth
D_*	dimensionless grain diameter
D_m	downscaled grain size
D_p	prototype grain size

d_{50}	median grain size
$Dmax$	maximum distance of the structure from the shoreline
dx	in experimental tests with movable bed: grid width
dy	in experimental tests with movable bed: grid length
E	energy for monochromatic waves
e_b	energy dissipation due to wave breaking
e_f	energy dissipation due to bed friction
E_{RD}	average rate of energy dissipation due to the presence of the structure
Es	gap spacing
F	Froude number
f	damping coefficient of a breakwater
f_p	linear friction factor due to energy loss in porous media
f_s	linear friction factor due to energy loss in sponge layers
f_w	wave energy loss factor
G	gap width between two detached structures
g	acceleration due to gravity
H	wave height
h	in preliminary head-loss tests: angle of the triangular weir
H_0	wave height in deep water
h_b	water depth at the breakwater
H_i	incident wave height measured before the coastal structure
H_R	reflected wave height
H_s	significant wave height
H_T	transmitted wave height
H_{max}	maximum allowable wave height
H_{rms}	root mean square wave height
$J_f(p)$	Jacobian of the non-linear system of equations f
k	wave number
K_D	dissipation coefficient
k_n	Nikuradse roughness parameter
k_p	permeability coefficient

K_R	reflection coefficient
K_s	shoaling coefficient
K_T	transmission coefficient
KE	kinetic energy of incoming waves
L	wave length
L_0	wave length in deep water
L_i	wave length at intermediate depth
L_{sw}	wave length in shallow water
P	wave generated flow in X direction
p	porosity of the experimental model of the brushwood fences defined as the open space per unit surface
PE	potential energy of incoming waves
Q	in preliminary head-loss tests: water flow across the weir
Q	wave generated flow in Y direction
Q_b	fraction of the breaking waves
$Q_{s,i}$	intermediate sediment transport rate (or sediment flow)
$Q_{s,t}$	total sediment transport rate (or sediment flow)
R_*	Reynolds number of grain $R_* = \frac{u_* D}{\nu}$
R_c	freeboard of a coastal structure $R_c = h - h_b$ or $R_c = h - d$
R_w	wave related Reynolds number
S	in experimental tests with movable bed: distance of a detached coastal structure from the shoreline
S	inertial coefficient
s	ratio of densities of grain and water
S_0	deep water wave steepness
T	wave period
t	time
T_r	return period
u_*	bed shear velocity
U_L	wind speed over land
U_W	wind speed over water
U_w	orbital velocity just above sea bed
U_w	wave orbital velocity just above bed

U_{wcr}	threshold orbital velocity
v	in preliminary head-loss tests: flow velocity
V_d	deposited sand at the leeside of a detached coastal structure
V_e	eroded sand at the leeside of a detached coastal structure
V_s	deposited sand at the leeside of a detached coastal structure
$V_{d,*}$	dimensionless deposited sand volume at the leeside of a detached coastal structure $V_{d,*} = \frac{V_d}{V_s}$
$V_{e,*}$	dimensionless deposited sand volume at the leeside of a detached coastal structure $V_{e,*} = \frac{V_e}{V_s}$
w	constant of the empirical equation of K_T
$Wmax$	maximum width of the protected area
X	X coordinate of the zone where the depsition/erosion volumes are being calculated
X	distance of the detached coastal structure from to the head of the salient
x_l	distance of the leeside surface upper limit to the structure
Y	Y coordinate of the zone where the depsition/erosion volumes are being calculated
Y	salient width
Y_*	dimensionless salient width $Y_* = Y/S$
z	depth of a specific point
z_i	instantaneous distance of the wave gauge to the water level
z_{it}	distance of the wave gauge to the water level corresponding to iteration number it of wave measurements

Greek Symbols

α	beach or coastal structure face slope
α	in experimental tests with movable bed: deposition factor behind a breakwater
α	in preliminary head-loss tests: water level above the weir
α	phase shift
α	wave angle with the shoreline after transformation
α_0	initial wave angle with the shoreline
β_i	factors of the empirical equation of K_T

ε	porosity of a breakwater
γ_1	first wave breaking parameter
γ_2	second wave breaking parameter
λ_D	scale ratio for grain size
λ_L	scale ratio for distances
λ_T	scale ratio for time
λ_τ	scale ratio for shear-stress
λ_{F_*}	scale ratio for the densimetric Froude number
λ_{R_*}	scale ratio for the grain size Reynolds number
λ_{u_*}	scale ratio for bed shear velocity
μ	bottom friction
∇	horizontal gradient operator
ν	kinematic viscosity
Ψ	wave mobility number
ρ_s	grain density
ρ	water density
σ	angular frequency of wave
σ_{it}	standard deviation of the iteration number it of wave measurements
τ_{cr}	threshold bed shear-stress
τ	bed shear-stress
τ_w	wave related bed shear-stress
θ_{cr}	threshold Shields parameter
θ	peak mobility parameter
ξ	local Iribarren parameter
ζ	in preliminary head-loss tests: minor head-loss coefficient
ζ	water surface elevation
ζ_{R_*}	in preliminary head-loss tests: Reynolds minor head-loss coefficient

1. Introduction

1.1. Shore erosion and soft protection in confined water surfaces: a renewed old issue

Shore erosion and effective shore protection measures are well researched for seas and oceans. Regarding lakes, there remain many research opportunities, because the approaches used for seas and oceans are not always applicable to shallow areas in lakes, where soft protection measures are generally more adapted (see Fig. 1.1). The current design of shore protection measures overestimates sometimes the dimension of the structures, which could be detrimental to the natural coastal aspects. Also, the impact of wind generated waves on soft (and porous) shore protection measures has been often been underestimated in the past.

Figure 1.1.: Combined shore protection measures in Lake Biel, using breakwaters and palisades (wooden piles) to protect natural reed, grown on the beach

The above mentioned issues can be verified along the shores of Lake Biel in Switzerland (see Fig. A.1 in Appendix A). The diversion of the Aar river into the lake modified its natural equilibrium and lead to the development of vegetation and reeds along its shores. Constructions related to human activity brought some additional harmful impact on the shore stability. Thus, since the late thirties of the past century, an increase in erosive forces clearly appears in the 60% remaining natural shore of the lake (Ostendorp et al., 1995).

a) b)

Figure 1.2.: (a) Tree eroded roots due to wave action at the southern shore of Lake Biel; (b) Submerged brushwood fences used as protection agent against wave induces erosion at the Grande Cariçaie of Lake Neuchâtel

In order to mitigate landscape degradation (see Fig. 1.2a), pioneer soft designs were constructed at several localities (see Fig. A.1). Since 1985, the "Association for the Protection of Lake Biel" (VBS) has been developing soft techniques for the protection of reed beds to mitigate bank erosion. Backed by cantonal and federal services, the association initiated soft bio-technical measures, including brushwood fences (see Fig. 1.2b and 1.3), wooden piles, called palisades, both used as groins or breakwaters, armour layer of gravel, and reed plantations used as shore consolidation agent (Iseli, 1992). Although these kinds of shore protection are in place (see Table A.1), there has not been comprehensive scientific research to optimize their design for lakes. In the North Sea, soft measures (essentially brushwood fences) are widely used to protect the foundation of shore protection dikes against erosion, by providing an efficient porous wave damping screen (Mai, Lieberman and Zimmermann, 1999).

The European Commission edited a guide for coastal erosion and management (Eurovision, 2004). This guide aims to provide coastal managers with stat-of-the-art of coastal erosion management solutions in Europe. An interesting approach for the variation of the coastal erosion intensity on temporal scales due to natural factors was presented (see Fig. 1.4). Although

Figure 1.3.: Brushwood fences used in Lake Biel for the protection of reeds against high incident waves

this approach is developed for open sea coasts, shores in confined water surfaces suffer in many cases the same erosion problems due to similar phenomena. Eurovision (2004) concluded on coastal erosion with the following observation:

"Coastal erosion results from a combination of various factors - both natural and human-induced - which has different time and space patterns and have different nature (continuous or incidental, reversible or non-reversible). In addition, uncertainties still remain about the interactions of the forcing agents, as well as on the significance of non-local causes of erosion."

This underlines the importance to understand the key agents behind erosion. In this study, a quasi-detailed analysis of the wind regimes over Lake Biel is provided (see Section 1.2). This analysis is applicable for all the confined water surfaces where wind-waves are the prevailing eroding action.

Another relevant observation raised by the same report was the importance of a human induced coastal erosion. This is also applicable to confined water surfaces and more specifically, lakes in Switzerland, where human interventions resulted in many cases in shore erosion instead of helping shoreline accretion.

"Past measures to manage coastal erosion have generally been designed from a local perspective: they have ignored the influence of non-local forcing agents and have disregarded the sediment transport processes within the larger coastal system. As a consequence, they have locally aggravated coastal erosion problems, and have triggered new erosion problems in other places. They still

influence the design of present measures." (Eurovision, 2004)

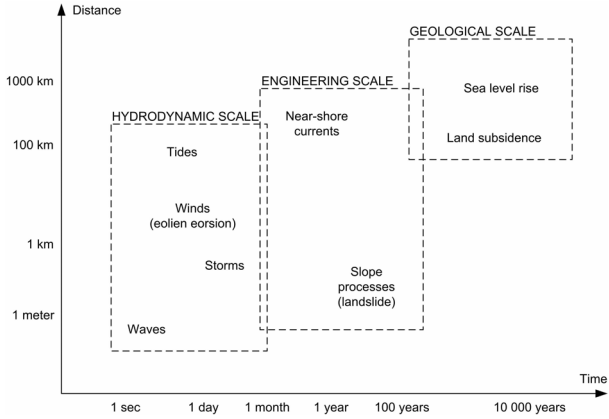

Figure 1.4.: Time and space patterns of natural factors of coastal erosion after Eurovision (2004)

1.2. Wind driven waves: example on Lake Biel in Switzerland

In addition to anthropogenic impacts, the natural location of a confined water surface and the prevailing wind regimes constitute a serious contribution favoring instability of sandy shores. Lake Biel, for instance, lies in the axis parallel to the Plateau Central of Switzerland. This Plateau Central is characterized by two surrounding mountain chains. The Jura mountain chain along the northern border of the Plateau, and the Central Alps chain, along its southern border. This topographic configuration results in canalizing the wind over the Plateau Central favoring two main wind regimes. This was confirmed by Bruschin and Falvey (1980).

Over Lake Biel, the wind blows therefore in two main regimes (see Figs. 1.5). The first one, called "Le Vent", is a South-Western wind, prevailing on average 45% of the time. The second main regime called "La Bise", is a North-Eastern long lasting wind, prevailing on average 27% of the time. The IDF curves (Intensity-Duration-Frequency) of both regimes are presented in Fig. 1.5. A comprehensive statistical analysis of the prevailing wind regimes is presented in the on-going research by Sayah et al. (2006) based on Gumbel distribution for extreme wind events.

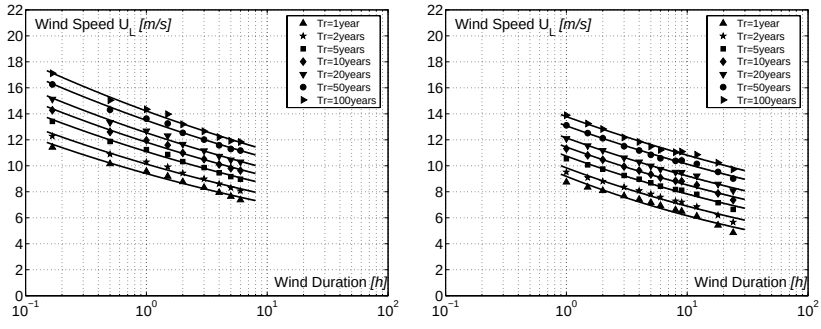

Figure 1.5.: Wind regimes at Lake Biel: (a) Le Vent [210 °-240 °]; La Bise [30 °-60 °] after Sayah et al. (2006)

The IDF curves are based on statistical analysis of 26 years of over land wind measurements at Payerne (30 km south of Lake Biel). For defined wind duration and selected return period (T_r), the curves provide a corresponding wind speed. In reality, by providing wind speed, such curves are relevant for the calculation of wind-waves in confined water surface (known fetch) for a defined return period. The relation between wind speed and wind duration is non-linear.

In situ wind measurements over Lake Biel (Müller et al., 2005) during 8 wind events showed that wind speed tends to increase after a transition from a land surface. However, due to the behavior of water roughness as a function of wind speed, the ratio of over water wind speed at a fixed level to over land wind speeds (U_W/U_L) is not constant, but varies nonlinearly as a function of wind speed. Yet, the exact magnitude and characteristics of the transition depend on the roughness properties of the terrain and vegetation on one hand, and on the stability of the air flow on the other hand. Resio and Vincent (1982) presented a simple approximation of this wind speed variation based on a logarithmic fitting curve to the asymptotic over land and over water wind speed values.

Furthermore, for the case of Lake Biel, Sayah, Mai, Boillat and Schleiss (2005) demonstrated that wind speeds over water follows a power-law curve. The ratio U_W/U_L tends to infinity when U_L tends to zero and to 1 when U_L is higher then 20 m/s. The latter fitting depends mostly over the location of on water measurement station and on the wind regime. For "mean" wind speeds (vary between 6 and 8 m/s in Switzerland), corresponding to recurrent wind events, such fitting provides a rough ratio of U_W/U_L equal to 1.25. Thus, wind over water is 25% stronger than wind over land for average wind events.

It is possible to transform wind statistics into wave statistics using

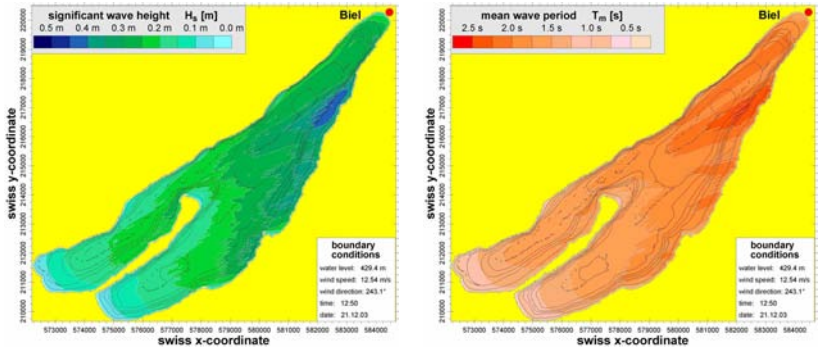

a) b)

Figure 1.6.: Wave field in Lake Biel during an event of "Le Vent" (Dec. 20-21.2203): (a) Significant wave heights and (b) mean wave periods after Sayah, Mai, Boillat and Schleiss (2005)

numerical simulations. For that purpose the numerical model Swan (Booij et al., 1996) was applied using a numerical model of Lake Biel with a square grid of 5 m. Using sound calibration approach developed by Mai, Ohle and Zimmerman (1999), it was possible to understand on a macroscopic scale the impact of the wind on the entire confined water surface. Using a single wind event measured over the surface of the Lake during 20^{th} and 21^{st} December 2003, it was possible to realize the importance of wind-generated waves in this type of small and confined water surface. The average wind speed during this South-Western wind event was 7.5 m/s.

During the "Le Vent" wind regime, the maximum wave heights and periods in Lake Biel amount to 0.5 m and 2.5 s, respectively . They have to be expected near Mörigen (see Fig. A.1). The non-stationary numerical simulations reveal that wind triggers the wave conditions in Lake Biel with a relatively short response time of a few hours. The research of Bruschin and Schneiter (1978) confirmed this observations.

These statistical analysis and numerical modelling (for which results can easily corroborated by in-situ observations during a major wind event) confirms two main points:

- In some defined topographic configuration, the wind develops constant directional regimes during several hours or even days.
- Small confined water surfaces can present significant hydrodynamic actions on the shores due to wind driven waves

The importance of identifying and understanding the key forces that trigger waves are the basis to understand their effect on the shores. The evaluation of these effect leads to more adapted solutions to protect the

local shore ecosystem against disturbance brought by the combined effect of wave action and human interventions. In Table A.1, a short overview of some selected soft *measures* (instead of *structures* since it has a hard and concrete-made connotation) are described. They are mainly adapted to shallow areas for average to small lakes wind-wave-actions.

1.3. Scientific and technical objectives of the present research

The present research is part of the EROSEE project. Its objective is to study the interactions of selected soft protection techniques with incident waves and to evaluate their effect on the sediment transport, using physical and numerical modelling as well as field investigations. The *Berne University of Applied Sciences* was charged to carry out field investigation at Lake Biel (wind, wave, and bathymetric measurements). The *Laboratory of Hydraulic Constructions* was charged to carry out experimental and numerical modelling of the brushwood fences. This research aims at a better understanding of the behavior of these structures and as a results, help to establish their scientific design basis. The findings are applicable to any shallow regions present in confined water surfaces.

Lacking adequate scientific basis for the design of soft shore protection techniques can have negative consequences. Often, protections do not provide the targeted solution, for example stopping the shoreline from moving backward, or substantially damping waves during big wind events or high water levels. Other issues are related to the energy of strong waves, reducing the structural stability of the protections.

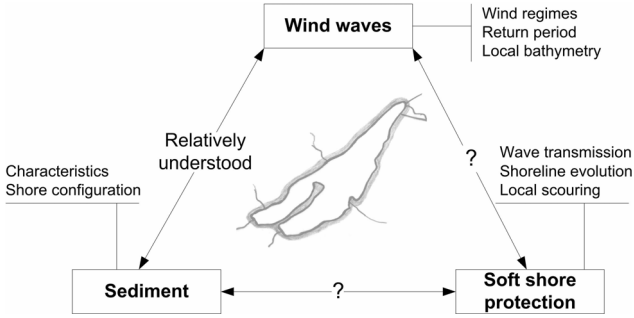

Figure 1.7.: Further research is needed in order to better understand the interaction of the soft shore protection techniques with waves and sediment transport after Sayah et al. (2004)

Fig. 1.7 illustrates the need for research in order to understand and quantify the interaction between the soft shore protection measures, the hydrodynamics of a specific site, and the sediment transport related mostly to bank erosion. This can be presented following a three axes relationship (iron triangle):

- The ***influence*** of a soft protection structure on the incident waves and the wave field in the protected area. This influence is described by the efficiency of a soft porous structure (i.e. brushwood fences) in damping waves (described by the transmission coefficient)
- The ***impact*** of the geometry and site configuration of a soft protection structure on the sediment transport in its vicinity and the evolution of a sandy shoreline
- The ***interaction*** of incident waves with the sea-bed related to sediment transport and bed morphology

While the wave-sediment interaction axis has been investigated for many decades (see article collection of Bagnold (1963)), the two other axes are little researched. Recently, Sumer et al. (2001) published a comprehensive review of past and current research related to scour around coastal structures, mainly breakwaters. Referring to several studies, the authors presented a relevant and straight-to-the-point approach in describing the flow and scour pattern at detached breakwaters, submerged breakwaters, and the sediment behavior close to the structure. However, concerning soft and porous structures, there is little research and insight available. This is probably due to the fact that their design is less costly and mostly used in mild hydrodynamic conditions.

The interaction of waves with porous media has been investigated by several researchers. While a comprehensive and interesting approach was presented by Sollitt and Cross (1976) that analyzed wave reflection and transmission at permeable breakwaters, more recent approaches based of physical and numerical analysis were amongst others published by Scarlatos and Singh (1987), Losada et al. (1995), Ting et al. (2004). Research on porous structures such as brushwood fence, on hydrodynamic climate and geometrical characteristics are not abundant.

In a report published by von Lieberman et al. (1997) at *Franzius-Institut für Wasserbau und Küsteningenieurwesen* of the *University of Hannover* in Germany, authors presented a study on a prototype model of brushwood fences. They investigated the efficiency of multiple configurations of the measure under different wave conditions. This study is acknowledged as a first serious and systematic effort to test the structure's response to wave attack. Further research opportunities remain, notably, 1) establishing clear relationships between the waves and the structure's geometrical characteristics (height, width, porosity, etc.), 2) the response of a movable bed to wave attack in the vicinity of the brushwood fences, and 3) systematic numerical modelling

corresponding to simple configurations of the wave field in the protected area.

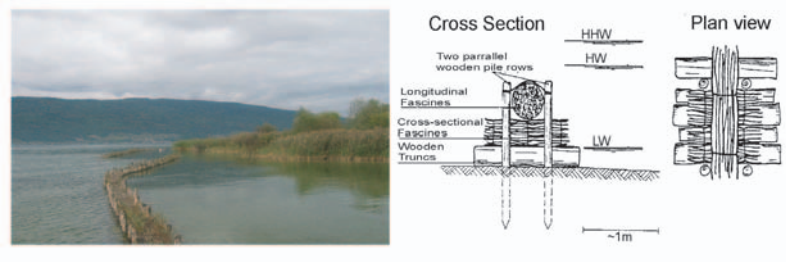

Figure 1.8.: Brushwood fences (made of willow trees) is the selected soft shore protection structure for the present research

Based on above, the objectives of the present research are:

- Developing design recommendations for a selected soft shore protection measure, the brushwood fences (see Fig. 1.8 for the description of the different components and Table A.1 for the exact definition). This will be based on experimental analysis carried out in a wave tank. The efficiency of the structure will be tested on a fixed bed regarding the transmission coefficient. Its influence on the shoreline evolution and its efficacy in sand trapping will also be evaluated by tests on a movable bed.
- To model numerically porous structures with identical characteristics to the brushwood fences in terms of porosity and transmission. This will provide a detailed description of the protected wave field between the structure and the shoreline. The effect of a single and double gap will be studied to develop a recommendation regarding the dimensioning principles.
- To apply the results of physical and numerical modelling on a real life case where brushwood fences are used as a protection agent against wind-wave impact on a sandy shore. Field measurements will be used for defining boundary conditions for the numerical model.

1.4. Scope and methodology

As mentioned above, the objective of this research is to study the interaction of the selected soft shore measure, i.e. the brushwood fences, with incident waves and evaluate its effect on sediment transport, using physical and numerical modelling. This research aims at establishing pragmatic technical recommendations for its design basis.

The same approach allows to evaluate other protection methods. A similar approach was for example applied on palisade (refer to Table A.1

for the exact definition) by Sayah, Metral, Boillat and Schleiss (2005) using experimental investigation. However, additional efforts are needed in order to investigate further geometrical configurations and to establish a sound basis for their design. Other porous media like tree groins or gabion vertical breakwaters (applied as well in many cases where wave climate, hydrodynamics and bathymetric configurations permit) could be examined using the same approach.

In India for example, soft protection measures have been applied along large rivers to prevent bank erosion. They were built perpendicularly to the shore and functioned therefore as groins. In Japan, similar brushwood fences were used along the Shingashi River as bank consolidation agent (Aso, 1998). The geometrical disposition was parallel (and almost integrated) to the bank. In the United Kingdom, brushwood fences were used to prevent the erosion of tidal saltmarsh (Trimley marshes at Orwell estuary, Essex), and to enhance natural sedimentation by slowing erosive currents (Colenutt, 2001).

The methodology of the present research (see Fig. 1.9) will be focused on the use of brushwood fences as wave damping agents similarly to breakwaters. However, while the latter are usually dimensioned as a non porous structures, the former are porous and their variable porosity with time and the construction procedure play a major role in their efficiency.

The proposed structure of this reports is as following:

- Chapter 1 provides a comprehensive description of the problematic of shore erosion in confined water bodies and set-up the main research goals.
- Chapter 2 gives a detailed description of theoretical background and literature review. It defines the main theory used in this research related to the wave transformation and propagation, and the interaction between sediment and waves. The literature review encompass the theory and researches related to the interaction of waves with porous structures. Moreover, it provides a thorough description of the effect of coastal structures on shoreline changes and scour.
- Chapters 3, 4 and 5 refer to phase 1 of the current research (see Fig. 1.9). They deal with the experimental set-up and physical modelling. A downscaled 1 : 10 physical model of the brushwood fences was constructed and tested in a wave tank where a typical bathymetry found at shallow region in Swiss lakes was applied. The boundary conditions concerning wave characteristics were established according to realistic waves characteristics. Experimental tests are divided into two main series, tests with fixed bed, where the efficiency of the brushwood fences is measured regarding transmitted waves, and tests with movable bed, where the geometrical disposition of a detached single and double structure was investigated according to sediment transport and shoreline evolution. This method of testing was applied by many researcher such as Suh and Dalrymple

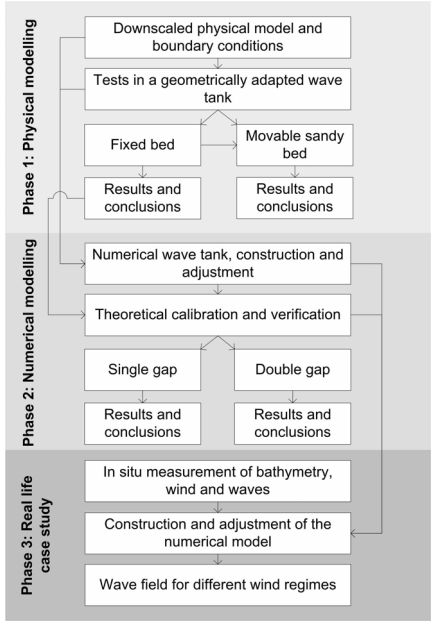

Figure 1.9.: Methodology of the present research

(1986),Yu (1995), Ming and Chiew (2000), Debaillon et al. (2001), Ting et al. (2004), etc.

- In Chapter 6, the results of the physical tests with fixed bed will be used in the first stage to adjust a numerical model similar to the wave tank (phase 2 in Fig. 1.9). This adjustment is based on adequate bathymetric gridding and sponge values installation in line with the configuration of the wave tank. This is followed by a theoretical calibration of the numerical model of the wave tank based on wave breaking parameters and bottom roughness provided by the numerical scheme developed by Madsen and Larsen (1987).
- Chapter 7 provides a validation of the adjustment based on the results of wave heights measurements during experimental tests as suggested by (Thompson et al., 1996). The authors used the mild slope equation that allows the introduction of porous media by adding dissipative friction values over the bottom. This equation is used under the Mike 21 EMS solver developed by Warren and Bach (1992) (among other partners) at the Danish Hydraulic Institute.
- The objective of Chapter 7 is to provide a detailed description of a simple wave field in an enclosed area surrounded by brushwood fences. It includes the effect of single and double gaps in a linear structure. This will help

to establish geometrical recommendations concerning gap widths and gap spacings. The mild slope equation is very adequate for modelling porous structures. It has been used in several studies by researchers such as Thompson et al. (1996), Zyserman et al. (2000), Beltrami et al. (2001), Zanuttigh et al. (2003), and Lee (2005).

- The numerical model, following the same calibration principles defined in Chapter 6, will be used in Chapter 8 to calculate the wave field in a real life case study (phase 3 in Fig. 1.9). In-situ measurements, of waves, winds and bathymetry, carried out by the *Berne University of Applied Sciences* are introduced in the model (BFH, 2002). Based on statistical analysis, three wind regimes are used to generate the boundary conditions of wave characteristics provided by Swan. The wave field is analyzed around segmented brushwood fences in a shallow area of the shores along lake Biel in Mörigen.

2. Theoretical background and literature review

2.1. General definition of coastal terms

In order to ensure better communication, the main coastal terms are defined in the following. Fig. 2.1 provides a detailed description of the terminology used for shore regions. They are inspired from the *Glossary of Coastal Terminology* introduced in the year 1998 by Brian Voigt:

- Beach face: The section of the beach normally exposed to the action of wave and water level variations
- Breaker zone: It starts at the line of breaker, i.e. when incident wave start breaking.
- Coast: A strip of land of indefinite length and width that extends from the coastline to the first major change in terrain features
- Coastal area: The wider zone that starts where waves affect significantly the cross shore profile of the sea bed and ends with the coast
- MHWL=mean high water level; MWL=mean water level; MLWL= mean low water level
- Nearshore zone: Contrary to the offshore zone, nearshore zone is the zone where usually the sea bed starts to be influenced by the wave action
- Offshore zone: The zone beyond the nearshore zone where sediment motion induced by waves alone effectively ceases and where the influence of the sea bed on wave action is small
- Shoreface/Littoral zone: The narrow zone seaward from the low water level shoreline permanently covered by water, over which the beach sands and gravels actively oscillate with changing wave conditions
- Shore/Beach: That strip of ground bordering any body of water which is alternately exposed, or covered by tides and/or waves. A shore of unconsolidated material is usually called a beach
- Shoreline: The intersection of a specified plane of water with the shore
- Regular/irregular waves: while regular waves propagates with constant period, irregular waves propagates with random wave periods (and in practice, also heights), which are typical for natural wind-induced waves
- Long/short waves: Long waves (sometimes are swell waves) have a period above about $30s$ and can be generated by wave groups breaking in the surf zone. Short waves are waves with inferior period

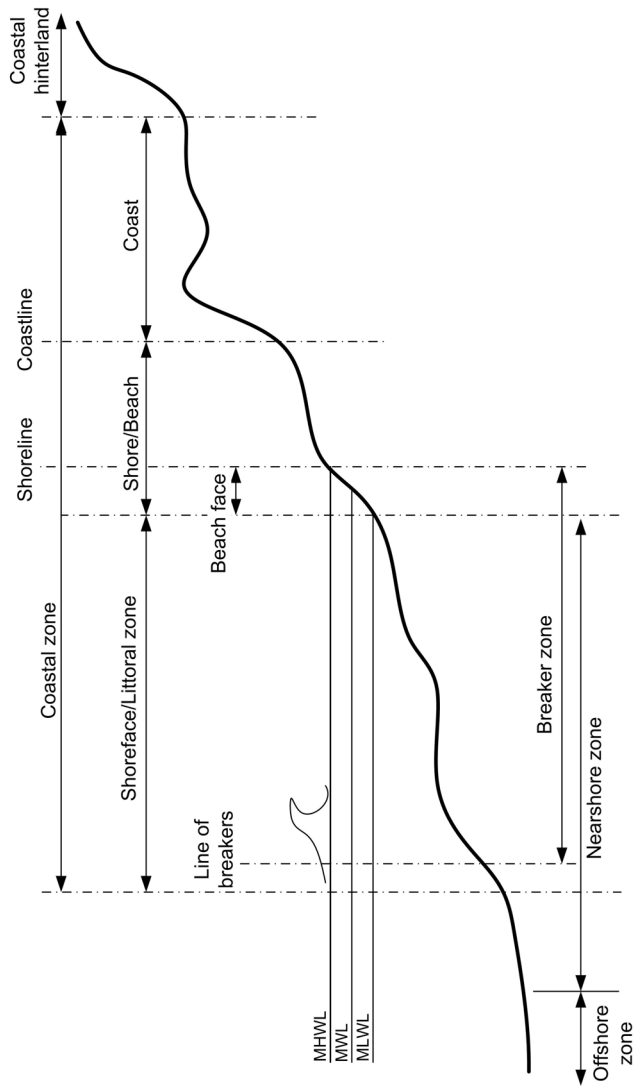

Figure 2.1.: Definition of coastal terms, adapted from USACE (2001)

2.2. Propagation and transformation of waves

Wind waves (usually irregular waves) are generated as a result of the action of wind on the surface of water. The wave height (H), wave period (T), propagation direction and duration of the wave field at a certain location depend on:

- The wind field (speed, direction and duration).
- The fetch of the wind field (meteorological fetch) or of the water area (geographical fetch).
- The water depth over the wave generation area.

When waves leave the area of their generation, they are transformed due to phenomena occurring in the natural environment. When they approach the coastal area, they are affected by the bathymetry of the bottom. Several processes occur including refraction, shoaling, bed friction and wave-breaking. The latter, however, sometimes occurs at deep water when the waves gets too steep. If the incident waves meet major structures or abrupt changes in the coastline, they will be transformed by diffraction. These phenomena are explained hereafter.

2.2.1. Definition of the different water regions

Fig. 2.2 describes the influence of the bottom on the orbital velocities generated by short-waves. Hence, the values of the horizontal and vertical components increase with depth decrease to the point that waves induced currents are the same on the surface as well as on the bed. Hence, waves propagate from the area of their generation, which is usually an area of Deep Water (see Fig. 2.2a) through an Intermediate Depth water area (see Fig. 2.2b), to reach the nearshore region, which is usually a Shallow Water area (see Fig. 2.2c).

The limits of these areas depend on the wave length L and water depth d. They are defined as follows (Ippen, 1966):

- *Deep Water:* $d/L > 1/2$
- *Intermediate Depth:* $1/20 < d/L < 1/2$
- *Shallow Water:* $d/L < 1/20$

Wave length calculation is related to the water depth according to the following:

In Deep Water:

$$L_0 = \frac{gT^2}{2\pi} \tag{2.1}$$

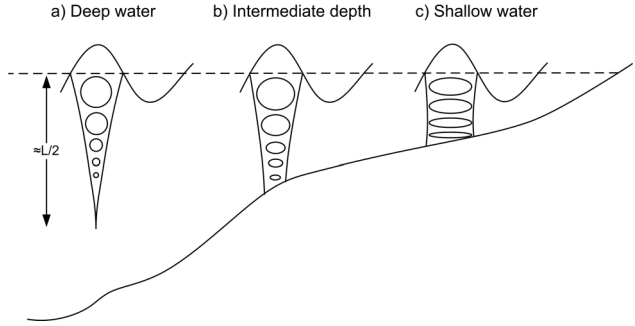

Figure 2.2.: Definition of water areas during waves propagation and influence of the bottom on the water particle trajectories adapted from Ippen (1966)

In Intermediate Depth:

$$L_i = L_0 \tanh(\frac{2\pi d}{L_i}) \tag{2.2}$$

In Shallow Water:

$$L_{sw} = T_0\sqrt{gd} \tag{2.3}$$

where L_0, L_i and L_{sw} are respectively the wave lengths in Deep Water, Intermediate Depth and Shallow water, T the wave period and g the acceleration due to gravity.

2.2.2. Shoaling and refraction of waves

Shoaling is the deformation of the waves, which starts when the water depth becomes less than half of the water length, i.e. when waves propagate in Intermediate Depth area (see Section 2.2.1). The shoaling causes the reduction in the wave propagation velocity as well as shortening and steepening of the waves.

The *shoaling coefficient* K_s is given by the following equation:

$$K_s = \frac{H}{H_0} = \sqrt{\frac{1}{2}\frac{1}{n}\frac{1}{\tanh(kd)}} \tag{2.4}$$

where H is the wave height related to the water depth d, H_0 is the wave height in the deep water, and k is the wave number given by

$$k = \frac{2\pi}{L} \tag{2.5}$$

and

$$n = \frac{1}{2}(1 + \frac{2kd}{\sinh(2kd)}) \tag{2.6}$$

It is to be noted that K_s is equal to 1 in deep water, decreases with the water depth to 0.91 and then increases to infinity as the water depth approaches zero (see Fig. 2.3)

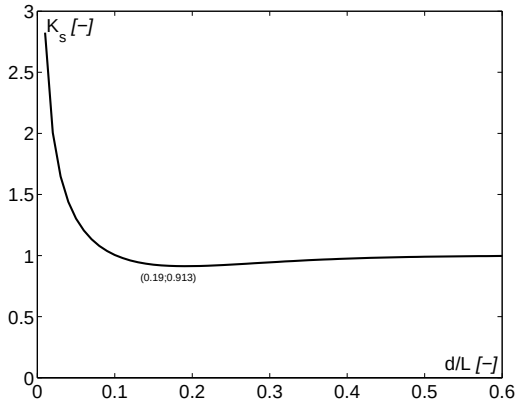

Figure 2.3.: Shoaling coefficient K_s

Wave refraction is the change of direction of wave propagation when the wave fronts travel at an angle with the depth contours in shallow water. The refraction is caused by the fact that the waves propagate more slowly in shallow water than in deep water. Hence, two different water particles on the same wave front will have two different velocities. As a consequence, the wave front turns and tends to become aligned with the depth contours.

The *refraction coefficient* K_r is given by the following equation:

$$K_r = \sqrt{\frac{b_0}{b}} = \sqrt{\frac{\cos\alpha_0}{\cos\alpha}} \tag{2.7}$$

where b_0 is the distance between initial adjacent wave rays (see Fig. 2.4), b is the distance between adjacent wave rays after transformation, α_0 the initial wave angle with the shoreline and α the wave angle with the shoreline after transformation.

2.2.3. Diffraction and breaking of waves

Diffraction can be observed when there are sheltering structures such as breakwaters. It is the process by which the waves propagate into the lee zone

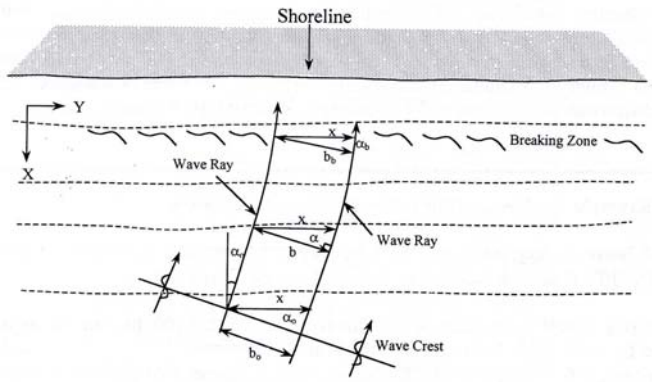

Figure 2.4.: Wave Refraction after Kamphuis (2000)

behind the structures by energy transmittance laterally along the wave crests. This process tends to move energy away from higher waves to the area of lower waves. Initial wave energy is thus reduced as diffracted waves are produced. The calculation of wave diffraction is quite complicated and often made using numerical models.

Wave shoaling causes wave height to increase to infinity in very shallow water (see Fig. 2.3). However there is a physical limit to the steepness of the waves, H/L. When this limit is exceeded, the wave breaks and dissipates its energy. Limits of wave breaking are defined as follows:

- For Deep Water, waves break when $H_0/L_0 > 0.142$ (Michell, 1893)
- For Intermediate Depth, waves break when $H_0/L_i > \tanh(2\pi\ d/L_i)$ (Miche, 1944)
- For Shallow Water, waves break when $H_0/d > 0.78$ (Munk, 1949)

Breaking waves are generally divided into three main types, depending on the steepness of the waves and the slope of the shoreface. *Spilling* when steep waves break over a flat shoreface, *Plunging* when the upper part of the waves breaks on the lower part, dissipating most of the energy, *Surging* when the lower part of the wave surges up on the shoreface, and *Collapsing* when the upper part of the wave collapse on the shoreface. Fig. 2.5 shows the different wave breaking types.

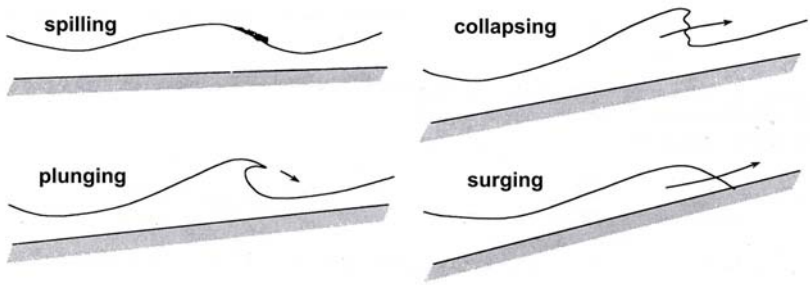

Figure 2.5.: Types of breaking wave related to wave steepness and beach gradient (Wood and Fleming, 1969)

2.3. Interaction between waves and sediment

Waves play a major role in generating bed load sediment transport due to shear stresses applied on the seabed. They may imply the establishment of several sediment transport regimes characterized by ripples or dunes formation, depending on the shear stresses values.

Concerning the impact of waves on the shore, they may form longshore currents, parallel to the shoreline, or shore-normal currents. In both cases, sediment transport is generated and can result in erosion or accretion of the beach (removal and addition of volumes of sand). Erosion normally results in shoreline recession (movement of the shoreline inland); accretion causes the shoreline to move seaward.

In the following sections, a detailed description of the interaction of waves with a granular non-cohesive sea-bed is presented. The goal is to provide the basic equations and criteria involved in wave-sediment interaction phenomenon. Additional descriptions of the wave generated bed load and total load sediment transport, in addition to beach equilibrium profile design will be provided in later chapters.

2.3.1. Wave generated currents near the bottom

The simplest type of water wave considered in this section is the *monochromatic* wave with single wave height and period. If the wave has a very small height compared to its wavelength, it approximates well to a sinusoidal variation in surface elevation and orbital velocity (see Fig. 2.2). The related properties are given by the linear wave theory.

USACE (2001) describes the orbital velocity due to waves propagation for each three water region (see Section 2.2.1) by using its horizontal and vertical components, respectively u and v, of the generated orbital velocity.

The two components of the orbital velocity are given for a z depth as follows:

For *Deep Water*

$$u = \frac{\pi H}{T} e^{\frac{2\pi z}{L}} \cos\theta \tag{2.8a}$$

$$v = \frac{\pi H}{T} e^{\frac{2\pi z}{L}} \sin\theta \tag{2.8b}$$

For *Intermediate Depth*:

$$u = \frac{H}{2}\frac{gT}{L}\frac{\cosh[2\pi(z+d)/L]}{\cosh(2\pi d/L)} \cos\theta \tag{2.9a}$$

$$v = \frac{H}{2}\frac{gT}{L}\frac{\sinh[2\pi(z+d)/L]}{\cosh(2\pi d/L)} \sin\theta \tag{2.9b}$$

For *Shallow Water*:

$$u = \frac{H}{2}\sqrt{\frac{g}{d}} \cos\theta \tag{2.10a}$$

$$v = \frac{H\pi}{T}(1+\frac{z}{d}) \sin\theta \tag{2.10b}$$

where θ is the angle of the orbital velocity vector with the horizontal and d the water depth.

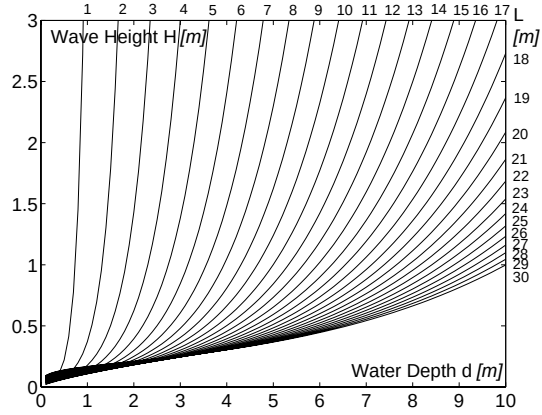

Figure 2.6.: Wave threshold for sediment grain $d_{50} = 0.18\ mm$

Soulsby (1997) gives the expression of the wave orbital velocity just above sea-bed U_w due to a monochromatic wave:

$$U_w = \frac{\pi H}{T \sinh(kd)} \tag{2.11}$$

where k is the wave number.

Bonnefille (1992) gives the expression of the wave generated shear velocity applied on the bottom, which is quite similar to Eq. 2.11. The main difference is that it adds the effect of the kinematic viscosity ν of the liquid to the value of the orbital velocity:

$$u_* = 2.2(\frac{\nu H^2}{T^3 \sinh(kd)})^{\frac{1}{4}} \tag{2.12}$$

The wave generated orbital velocities are mainly used to determine whether incident waves implies sediment transport. Since every sand particle diameter is characterized by its threshold motion, orbital velocities will be the agent that provoke the particle motion whenever the shear stress applied on the bed exceeds the critical one. Example of the wave threshold is provide in Fig. 2.6 that is capable of initiating granular sand with a diameter $d_{50} = 0.18\ mm$.

2.3.2. Wave defined threshold of motion

The threshold (or initiation) of motion of sediments on the seabed is reached when the wave generated current velocity (see Section 2.3.1) slowly increases to reach a certain value at which few grains begin to move.

The threshold of motion related to waves could be associated to applications related to river hydraulics. Therefore, Shields (1936) gives a precise definition of the threshold of motion in terms of the ratio of the force exerted by the bed shear-stress that acts to move a grain on the bed, to the submerged weight of the grain counteracting this. The threshold Shields parameter θ_{cr} (see Fig. 2.7), is defined as:

$$\theta_{cr} = \frac{\tau_{cr}}{g(\rho_s - \rho)D} \tag{2.13}$$

where ρ_s is the grain density, ρ the water density, D the grain diameter and τ_{cr} the threshold bed shear-stress defined by:

$$\tau_{cr} = \rho u_*^2 \tag{2.14}$$

where the shear velocity u_* can be calculated using Eq. 2.12.

Soulsby and Whitehouse (1997) provided an algebraic expression that fits closely Shield's curve with respect to wave and current data. It reads as following:

$$\theta_{cr} = \frac{0.30}{1 + 1.2D_*} + 0.55[1 - e^{-0.020D_*}] \tag{2.15}$$

where the dimensionless grain diameter D_* is given as following:

$$D_* = [\frac{g(\rho_s/\rho - 1)}{\nu^2}]^{\frac{1}{3}} D \tag{2.16}$$

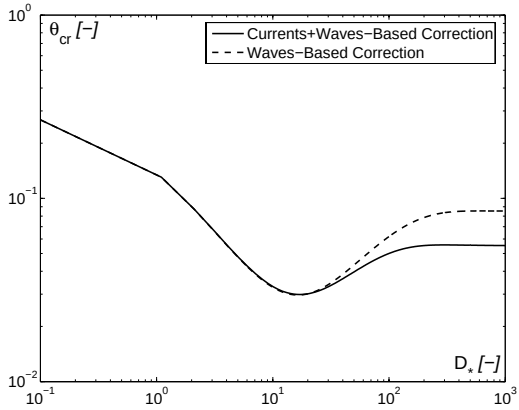

Figure 2.7.: Threshold of motion of sediment beneath waves and/or currents (Soulsby and Whitehouse, 1997)

Fig. 2.7 gives Shield curve based on the above mentioned correction. An additional curve is plotted that provide an approximation of the same Shield curves with the respect to the wave data exclusively. The curve define the threshold values of θ_{cr} above which sediment particles are transported by the increasing bottom shear stresses. Under such values no movement could be initiated.

Bonnefille (1992) defined the threshold of motion using the Reynolds number of grain R_* and the dimensionless grain diameter D_* (see Fig. 2.8).

The Reynolds number R_* of grain with a diameter D is equal to:

$$R_* = \frac{u_* D}{\nu} \tag{2.17}$$

The author divided the Reynolds values into three main regions, every one with a specific threshold condition as follows:

$$for\ R_* < 12 \qquad \Rightarrow D_* = 2.5R_*^{\frac{4}{5}} \tag{2.18a}$$

$$for\ 12 < R_* < 1000 \ \Rightarrow D_* = 3.8R_*^{\frac{5}{8}} \tag{2.18b}$$

$$for\ 1000 < R_* \qquad \Rightarrow D_* = 2.7R_*^{\frac{2}{3}} \tag{2.18c}$$

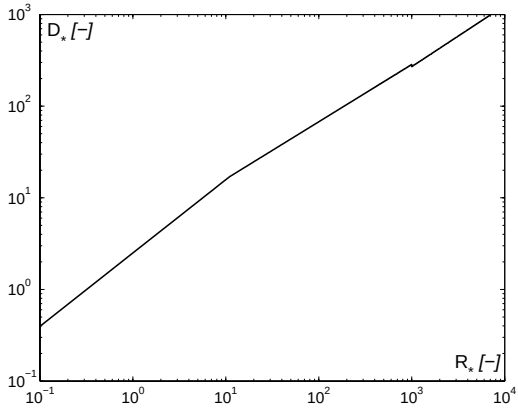

Figure 2.8.: Threshold of motion of sediment beneath waves following Bonnefille (1992).

Komar and Miller (1975) determined two conditions for the threshold orbital velocity U_{wcr} given by:

$$U_{wcr} = [0.118g(s-1)]^{\frac{2}{3}} D^{\frac{1}{3}} T^{\frac{1}{3}} \quad for\ D < 0.5mm \tag{2.19a}$$

$$U_{wcr} = [1.09g(s-1)]^{\frac{4}{7}} D^{\frac{3}{7}} T^{\frac{1}{3}} \quad for\ D > 0.5mm \tag{2.19b}$$

where s is the ratio of densities of grain and water ρ_s/ρ. Even if these equations are widely used, the disadvantage is that they have a large discontinuity at $D = 0.5\ mm$.

2.4. Interaction of waves and porous structures

This section mainly treats the theory regarding the interaction of incident waves with shore protection structures. However, since the related theory is very broad, it is proposed to focus the research on the transmission of incident

waves through vertical porous media (i.e. permeable structures). In fact, the soft measures described in Chapter 1 for shore protection, are porous, and mainly used to *damp* incident waves parallel to the shoreline, but not to create a fully *reflective* media. Hence, they could be considered as permeable structures.

The first approach is to investigate the influence of vertical and permeable breakwaters on reflected and transmitted waves as shown in Fig. 2.9. This investigation will thereafter be followed by an analogy with brushwood fences.

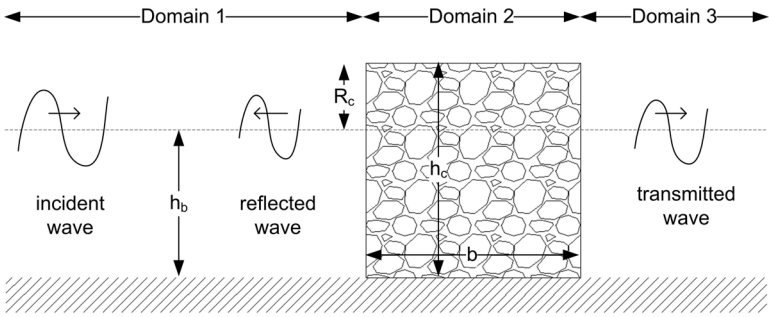

Figure 2.9.: Schematic draw of the theoretical model of a permeable breakwater modified after Losada et al. (1998)

Fig. 2.9 shows the existence of three main domains that concern wave propagation and energy loss:

- Domain 1 and 3: incident, reflected and transmitted waves outside the structure.
- Domain 2: the flow generated by wave propagation inside the structure is subjected to resistance forces due to the added mass of discrete grains within the porous medium.

2.4.1. Wave transmission through porous/permeable media

Wave dissipation is characterized by the ability of the structure to damp wave action and is thus directly related to wave transmission, reflection, and the structure characteristics. Wave overtopping and breaking depend on water depth and wave height. The well-known expression for energy dissipation is given by Eq. 2.20 and proposed by Thornton and Calhoun (1972):

$$K_D^2 + K_R^2 + K_T^2 = 1 \tag{2.20}$$

where K_D is the dissipation coefficient of a porous structure, K_R the reflection coefficient and K_T the transmission coefficient.

The reflection and transmission coefficients are determined as follows:

$$K_R = \frac{H_R}{H} \tag{2.21a}$$

$$K_T = \frac{H_T}{H} \tag{2.21b}$$

where H_R, H_T, and H are the reflected, transmitted, and incident wave height, respectively.

The wave heights described above are usually determined experimentally. Then the dissipation coefficient is calculated using Eqs. 2.20 and 2.21.

Many researchers analyzed the effect of permeable breakwaters on incident waves. They are usually constructed with well-defined granular materials that allow the transmission of waves through the interstices. The oldest and comprehensive study that treats this subject goes back to the year 1976, when Sollitt and Cross (1976) evaluated analytically and based on experimental tests the influence of permeable breakwaters on the reflection and transmission of waves. Authors analyzed mainly the long wave solutions (when wave length exceeds the water depth by a factor of 20) for both, the transmission coefficient, K_T, and the reflection coefficient, K_R. The proposed solutions follows Eqs. 2.22a and 2.22b:

$$K_T = \left(\frac{(S-\varepsilon^2)^2 - f}{(S+\varepsilon^2) + (f + 2\varepsilon\sqrt{gh_b}/(\sigma b)}\right)^{\frac{1}{2}} \tag{2.22a}$$

$$K_R = \left(\left(1 + \frac{\sigma b f}{2\varepsilon\sqrt{gh_b}}\right)^2 + \left(\frac{\sigma b(S+\varepsilon^2)}{2\varepsilon\sqrt{gh_b}}\right)^2\right)^{-\frac{1}{2}} \tag{2.22b}$$

where S the inertial coefficient, ε the porosity, f the damping coefficient, h_b the water depth at the breakwater, b the width of the breakwater, and σ the angular frequency of waves.

In order to calculate σ, it is necessary to rewrite the dispersion equation for long wave solution as follows:

$$k^2 h_b^2 = \frac{\sigma^2 h_b}{g} \tag{2.23}$$

where k reads for the wave number and kh_b the dimensionless wave number.

In order to better understand the influence of the different variables used in Eqs. 2.22a and 2.22b, Fig. 2.10 shows the influence of the two main variables,

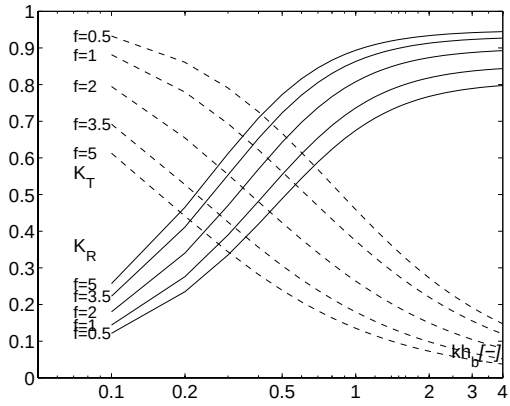

a)

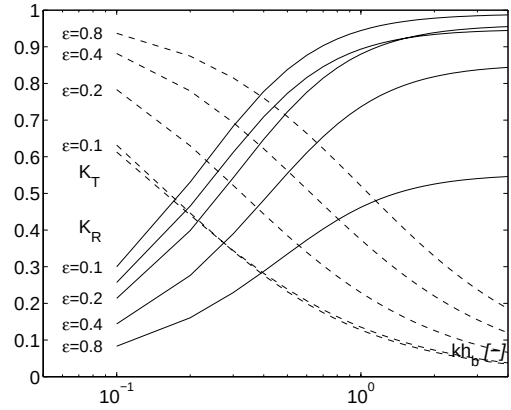

b)

Figure 2.10.: (a) Influence of the damping coefficient on the reflection and transmission coefficient for $h_b/b = S = 1$, $\epsilon = 0.4$, according to dimensionless wave number; (b) Influence of the porosity on the reflection and transmission coefficient for $h_b/b = S = f = 1$, according to dimensionless wave number

the damping coefficient and the porosity of the breakwater, on transmission and reflection, according to the dimensionless wave number kh_b.

Fig. 2.10a shows that an increase in the reflection coefficient accompanies the increased damping. This could result in the conclusion that, the increased damping produced an increased resistance to wave penetration, and an increase in internal wave decay. Furthermore, the reflection coefficient reaches an upper limit near $kh_b = 1.0$, where it attains a relative maximum. However, the transmission coefficient attains its minimum far beyond $kh_b = 1.0$.

The dependance on porosity is shown in Fig. 2.10b. Again, the reflection and transmission coefficients are plotted according to wave number kh_b, and considered for a particular case where the breakwater is square ($h_b/b = 1$) and damping coefficient equal to unity. Most of natural gravel materials have porosities in the range of $0.3 < \varepsilon < 0.5$. The curves shows that decreasing porosity causes an increase in the reflection coefficient and simultaneously a decrease in the transmission coefficient at all wave numbers. The reflection coefficient appears to be most sensitive to changes in porosity and this sensitivity increases with the kh_b.

Long wave transmission trough porous breakwaters were later investigated with an analytical method by Scarlatos and Singh (1987). The authors developed a new model that includes the effect of damping due to bed friction. They calculated the transmission coefficient, K_T, and the reflection coefficient, K_R, according to Eqs. 2.24a and 2.24b, respectively:

$$K_T = \frac{-Q}{1-Q} \tag{2.24a}$$

$$K_R = \frac{1}{1-Q} \tag{2.24b}$$

where Q is a variable calculated in Eq. 2.25:

$$Q = -2k_p \frac{h_b}{b} \frac{\sqrt{k^2+\mu^2}}{\sigma} \frac{1}{cos(\alpha)} \tag{2.25}$$

where μ is the bottom friction, α the phase shift, and k_p the permeability coefficient.

The average rate of energy dissipation due to the presence of the structure, E_{RD}, is given by Eq. 2.26:

$$E_{RD} = 1 - K_T^2 - K_R^2 = \frac{-2Q}{(1-Q)^2} \tag{2.26}$$

Plotting Eq. 2.26 according to Eqs. 2.24a and 2.24b, the structure is reflective or transmissive to whether $0 \leq -Q \leq 1$ or $-Q > 1$ (see Fig. 2.11).

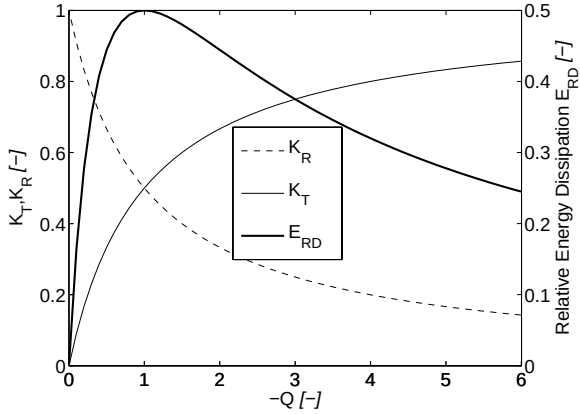

Figure 2.11.: Relative energy dissipation with respect to structure characteristics following Scarlatos and Singh (1987)

The maximum influence of the breakwater on energy dissipation occurs when $Q = -1$. Fig. 2.11 shows how E_{RD} is significantly sensitive to Q in a reflective type of structure in contrast with the same values of E_{RD} in a transmissive structure. Since the main influence of the breakwater is expressed through k_p and b, once the wave characteristics are established, then Fig. 2.11 may be interpreted to yield optimum values of k_p and b in order to attain the desirable transmission and reflection.

Losada et al. (1995) revisited the theory of Sollitt and Cross (1976) and examined on the basis of experimental study the effect of a porous media on wave induced-flow and showed the importance of the transition and transmission regions within the structure (situated in domain 2 in Fig. 2.9). The relative width of the structure, b/h_b, associated with the formation of a standing wave and resonant conditions inside the structure, was found to be an important parameter in establishing the location of the two regions. The transition region is characterized by very irregular records with secondary peaks, little or no dissipation and important higher harmonics in the velocity spectra. Dissipation is the most important factor in the transmission region where the flow tends to become more regular. The porous structure works as a filter, filtering out the higher frequencies as the oscillations propagate towards the leeside of the structure.

The porosity of a vertical permeable structure was later studied by Requejo et al. (2002). While using different gravel granulometry, hence different porosities, the author studied the effectiveness of the structure on wave action. Analytical expressions for functional performance variables (reflection, transmission and dissipation) and for stability (horizontal

and vertical forces, including the corresponding overturning moments) are then obtained. These expressions were numerically exploited to demonstrate the capability of the model for design purposes. The parameters required in the porous flow model are expressed in terms of the porous material characteristics. Although the authors carried out a comprehensive investigation and broadened the theory of Sollitt and Cross (1976) concerning porosity parameters and waves loads, they didn't provide any direct analytical solutions like D'Angremond et al. (1996) (see Section 2.4.2).

Ting et al. (2004) analyzed the effect of porosity of submerged breakwater on wave transmission and fixed relative values for energy loss E_{loss}. Although they didn't provide either any analytical or direct solutions, the authors carried out a comprehensive investigation and showed how the porosity of a submerged breakwater affects the non-breaking wave transformation. The experimental results indicated that increasing breakwater porosity reduces the height of reflected waves and that model widths negligibly influence the K_R and K_T when model heights are fixed. K_R is usually less than 0.1 when $kh_b > 2$ and K_R is maximum near $kh_b = 0.5$. K_T is maximum when kh_b is between 1.3 and 2.0. It is minimum when kh_b is near 0.7. The energy loss is maximum when kh_b is near 0.81 and is minimum for models with higher porosities. The porosity does affect the energy of the primary wave. The effect of porosity becomes significant, as the model gets higher. When harmonic waves are generated, some primary wave energy is transferred to higher-frequency components. The variation in energy loss of the primary wave can be as high as 0.6. When the porosity influence becomes significant, E_{loss} decreases as porosity increases and is above 0.75, while E_{loss} decreases slowly as $kh_b < 1.3$ and remain almost constant at around 0.4 as $kh_b > 1.3$ when the porosity is less than 0.75.

Such qualitative results proved that when it is submerged, the structure has a different response concerning wave transmission and reflection than in an emerging condition, as described by Sollitt and Cross (1976). This could leads to the conclusion that both conditions need to be treated separately.

2.4.2. Wave transmission through brushwood fences

In analogy with breakwaters, the interaction of brushwood fences and waves depends mainly on wave transmission and reflection. Wave attack on permeable structures such as brushwood fences and the response of the latter to hydrodynamic loading are very strongly related to the phenomena of flow through porous media. However, there is no specific formulation covering the effect of porosity on the interaction of brushwood fences and waves.

In fact, compared to permeable breakwaters, when an incident wave hits the brushwood fences, its energy will be partitioned between reflection, dissipation, and transmission. In order to prevent a high impact on the shore,

the transmission should be prevented as much as possible. However, since brushwood fences are always permeable, it is unrealistic to completely prevent wave transmission.
The wave damping at brushwood fences is described, as for breakwater, by three main variables as following (D'Angremond et al., 1996):

$$relative\ freeboard: \ \frac{R_c}{H_s} \tag{2.27a}$$

$$relative\ crest\ width: \ \frac{b}{H_s} \tag{2.27b}$$

$$local\ Iribarren\ parameter: \ \xi = \frac{\tan(\alpha)}{\sqrt{s_{0p}}}\ where\ s_{0p} = \frac{g}{2\pi}\frac{H_s}{T_p^2} \tag{2.27c}$$

where R_c is the freeboard of the structure, H_s the significant wave height, b the structure width, α the beach or structure slope, and T_p the spectral peak wave period.
The transmission coefficient K_T of the permeable structure is defined by the formula:

$$K_T = -\beta_1 \frac{R_c}{H_s} + \beta_2 (\frac{b}{H_s})^{-\beta_3}(1 - e^{-\beta_4 \xi}) \tag{2.28}$$

where β_i's are parameters related to the structure's permeability.
For permeable breakwater, the following values are considered:

$$\beta_1 = 0.4 \ ; \ \beta_2 = 0.64 \ ; \ \beta_3 = 0.31 \ ; \ \beta_4 = 0.5$$

Using a single porosity (equal almost to 0.5), Mai, Lieberman and Zimmermann (1999), examined on the basis of a full scaled prototype model, the transmission of wave through brushwood fences. The authors analyzed the effect of water level variation on the transmission coefficient of a brushwood fence as well as the changes of the transmitted mean wave period. They mainly demonstrated that the wave damping of a brushwood fence decreases significantly when water levels are above its crest height. However, the wave period remains almost constant even after transmission. They consequently rewrote Eq. 2.28 as follows:

$$K_T = -\beta_1 \frac{R_c}{H_s} + w \tag{2.29}$$

where β_1 and w are variables that depend both on the brushwood fences characteristics. They are equal to:

$$\beta_1 = 0.06 \ ; \ w = 0.68$$

The straight line in Fig. 2.12 based on Eq. 2.29 reveals that the damping in brushwood fences is much more efficient where the structure is emerged

compared to submerged conditions. However, it also shows that the efficiency of the structure decreases linearly at the same rate when water levels vary at both, emerged and submerged structure conditions. Compared to Sollitt and Cross (1976) and Ting et al. (2004), this conclusion seems to be different. Since brushwood fences are basically considered as porous structures, they should have similar trends to permeable breakwaters when they submerged or emerged.

2.5. Interaction of coastal protection structures and movable bed

2.5.1. Shoreline changes in the vicinity of detached structures under regular waves

Coastal protection structures are generally associated with shoreline erosion. They are divided into 2 categories (Rijn, 1998):

- Shore parallel structures: seawall, dikes, revetments, artificial island, detached breakwaters, etc.
- Shore-normal structures: groins, jetties, etc.

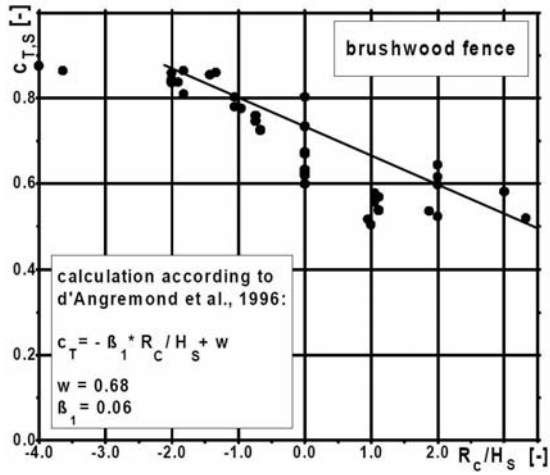

Figure 2.12.: Transmission coefficient of brushwood fences according to Mai, Lieberman and Zimmermann (1999) (on vertical axis $C_T = K_T$)

In this section, a detailed analysis of the effect of a detached breakwater will be provided. It is defined as a shore parallel structure, built inside or outside the surfzone (see Section 2.1 for definition) with two purposes, either to protect a ship wharf from wave action or as coastal protection measure (Mangor, 2001). A detached breakwater could be submerged or emerging, single or multiple (segmented).

In the present section, such a detached structure, in accordance with the current research, will be considered and analyzed as a structure designed for shore protection against wind-wave erosion. The shore protection will therefore be described by its influence on the shoreline evolution. Brushwood fences, as explained in Section 1.1 are often used as a detached structure, hence the importance to evaluate them with respect to the theory of detached breakwaters.

Detached structures have long been analyzed by specialists. The analysis was mainly focused on their effectiveness in favoring an accretion of the protected area in the leeside of the structure. For instance, based on a model study, a research carried out by Shinohara and Tsubaki (1966) concerned the shoreline changes of a sandy beach induced offshore breakwater. This study presented the basic approach to deal with this problematic. Authors evaluated therefore, using laboratory experiments, the evolution of the shoreline with time, in the presence of a breakwater for two wave steepness. Three main conclusions were derived:

- The diffraction of intruding waves are the main causes of the changes of shoreline and sand movement
- The formation of tombolo and salient depend on the ratio B/S (see Fig. 2.13 for definition)
- In case of high wave steepness, the deposition of sand in the sheltered area is reduced and depends less of B/S

Sixteen years later, a project carried out by Nir (1982), analyzed the effect of artificial offshore structures on many beaches of the Israeli coast. The author presented an interesting study on the evolution, during many years, of the deposited sand volumes behind such structures. His work, although only based on field observations, it could be considered as the basis for any future scientific study concerning the formation of salients and tombolos behind breakwaters in real life cases.

Rosen and Vajda (1982) based on physical experiments, presented the sedimentological influences of a detached breakwater. Authors analyzed mainly the equilibrium state reached by sediment movement in the sheltered area of a single breakwater. They based the analysis on many dimensionless ratios that were used later on by many other researchers. The main ratios they used are expressed as following:

- breakwater length/breakwater distance from the shoreline $= B/S$
- Salient width/breakwater distance from the shoreline $= Y/S$
- Eroded sand area/accreted sand area

Based on a case study that concerned the building of an offshore airport at the Sennan Coast in Japan, Mizumura and Shiraishi (1981) used many notion developed before and proposed a model study calibrated with aerial photos of the sandy coast concerned with this project. The authors proposed a combined system of offshore breakwater and groynes that proved to lessen the occurrence of accretion of the shore.

As shown in Fig. 2.13, this accretion could be described by two types: formation of salient or tombolo. Each one depends on the dimensions of the structure as well as its geometrical implantation in the nearshore area. The main criteria seems to be the dimensionless breakwater length B_* as expressed in Eq. 2.30:

$$B_* = \frac{B}{S} \tag{2.30}$$

where B is the breakwater length and S its distance from the initial shoreline.

The criteria for the formation of salient and tombolo are shown in Fig. 2.13 following the value of B_* . They were summarized by Rijn (1998) and Silvester and Hsu (1997).

Based on many experiments and field measurement carried out by several researches, Silvester and Hsu (1997) developed a relationship between the dimensionless value of the breakwater length B_* and the breakwater to salient distance $X_* = \frac{X}{B}$ as follows:

$$\frac{X}{B} = 0.67[\frac{B}{S}]^{-1.21} \tag{2.31}$$

where X is the distance of the breakwater to the head of the salient as shown in Fig. 2.13.

Concerning physical experiments carried out with a movable bed and offshore structures, Suh and Dalrymple (1986) presented a relevant physical study on the effect of single and multiple detached breakwaters on the morphological changes in their vicinity. The authors reported three important dimensionless variables to be analyzed: the surfzone width, the length of the breakwater, and the gap spacing. They used two types of sand with a median size diameter of 0.3 and 0.6 mm. Based on several field studies and on the results of the physical experiments realized with a single wave period of 1.2 s, the authors derive two relationships describing the erosion/accretion phenomenon behind single and multiple breakwaters. The first one is related

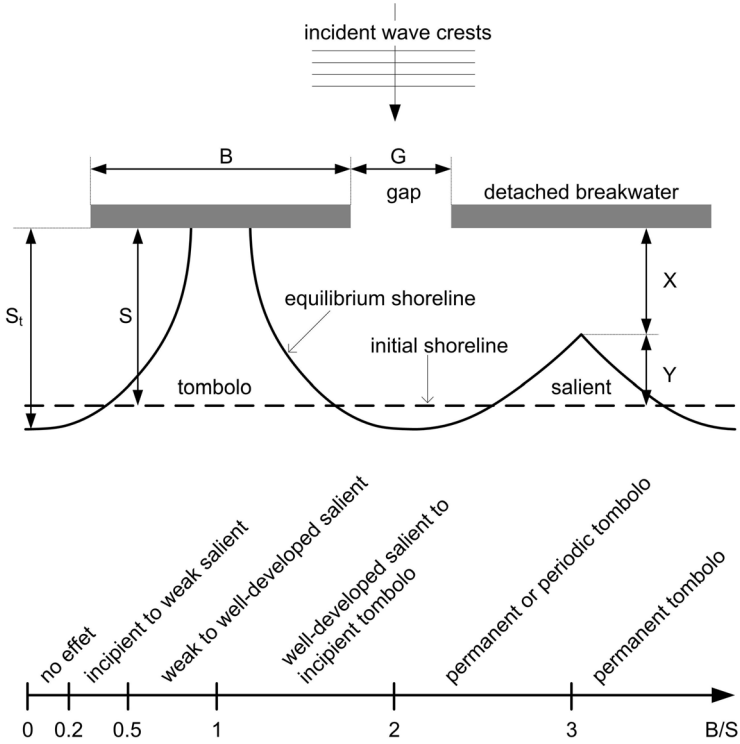

Figure 2.13.: Shoreline evolution behind detached breakwater, formation of tombolo and salient after Rijn (1998) and Silvester and Hsu (1997)

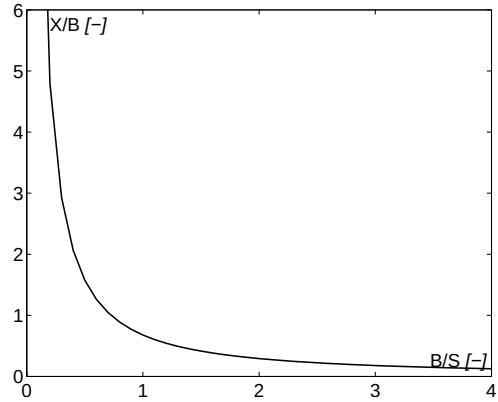

Figure 2.14.: Relationship between X/B versus B/S after Silvester and Hsu (1997)

to the deposited sand volume trapped behind a breakwater and is expressed as follows:

$$V_{d,*} = \frac{\alpha Y_*^2}{2} \tag{2.32}$$

where $V_{d,*}$ is the dimensionless deposited volume behind a single breakwater due to the formation of the salient and given by Eq. 2.33

$$V_{d,*} = \frac{V_d}{V_s} \tag{2.33}$$

where V_s , the total sheltered volume behind the breakwater is given by Eq. 2.34:

$$V_s = \frac{SBh_b}{2} \tag{2.34}$$

where h_b is the water depth at the breakwater and α is a deposition factor that takes into account the deposition of sand in the vicinity of the salient. It could varies between 1 and 8.

Additional relationships related to the geometry of the salient was derived based mainly on the authors field observations and was tested by physical experiments. This concerns the dimensionless value of the the salient width $Y_* = Y/S$ and given by:

$$Y_* = 14.8\frac{G_*}{B_*^2} exp[-283(\frac{G_*}{B_*^2})^2] \tag{2.35}$$

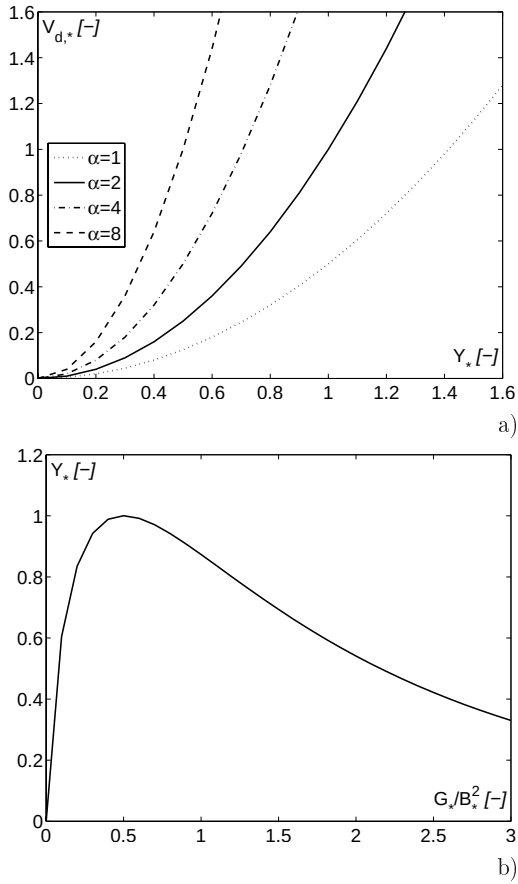

Figure 2.15.: Relation between (a) $V_{d,*}$ and Y_* and (b) Y_* and $\frac{G_*}{B_*^2}$ after Suh and Dalrymple (1986)

Eqs. 2.32 and 2.35 are represented in Fig. 2.15. Suh and Dalrymple (1986) noticed that the results provided in Fig. 2.15b based on physical tests do not fit adequately with the results based on field observation. They concluded that this difference may be caused by the variability of real wave climates and scale and laboratory effects during tests.

The influence of a single gap on the process of sand accretion in the sheltered area of the breakwater was tested physically by Harris and Herbich (1986). The authors used used similar notions as Suh and Dalrymple (1986) and demonstrated that the volume trapped (or accreted) behind

the breakwaters would be dependant of the B/S, H/L, and G/B. They mentioned however that the relative distance B/S is the most important and influenceable factor. The distance is more important than the gap width although the results showed that the volume of the trapped sand increases when the gap width G decreases.

A more recent investigation of a segmented submerged breakwater based on physical experiments was carried out by Biezen et al. (1999). The authors underlined the importance of the $3D$ effect of submerged breakwaters in relation to sediment transport. Using a mobile-bed with an average diameter of $0.09\ mm$, they proved that gaps between breakwater could lead to unexpected scouring. Since the return flow is concentrated in the gaps, this results with local high velocity in the seaward direction favored the erosion of the deposited material in the leeside of the breakwater.

Regarding the shoreline changes behind a detached breakwater, Ming and Chiew (2000), based on series of experiments with movable bed of $0.25\ mm$, analyzed the effect of a single emerging breakwater on shoreline evolution. They evaluated the effect of the length and distance of the breakwater to the shoreline. Furthermore, the criteria for the formation of tombolo and salient as well as the surface values of the salient as a function of the breakwater dimensions was studied. The values proposed for their criterion were situated in the known ranges defined by others researches. This confirmed that their boundary conditions were adequate.

2.5.2. Scour pattern around detached structures

In a marine environment, a detached protection structure favors significant changes in the surrounding morphology of the sea-bed. In fact, a detached structure could change the flow pattern in the immediate neighborhood, influencing the sediment transport regime and the formation of dune and ripples generated by the incident waves. In this section, a thorough description of the past and actual research that concerns such effect will be provided.

It should be mentioned that the scour in the vicinity of coastal structures is of particular concern since it may affect their stability. Hence, the research was usually concerned with developing analytical formulations that took into account hydrodynamic loading as well as the form of the structure and the bed characteristics. For instance, the scour at bridge piles in rivers, theory explored in depth by Breusers and Raudkivi (1991). It appears that the scour problem in the vicinity of structures built in rivers is most extensively studied since it concerns mainly matters of human security (for the cases of bridges piles). However, scour pattern and morphological changes in the vicinity of coastal marine structure (see Fig. 2.16) have not received the same attention (Sumer et al., 2001).

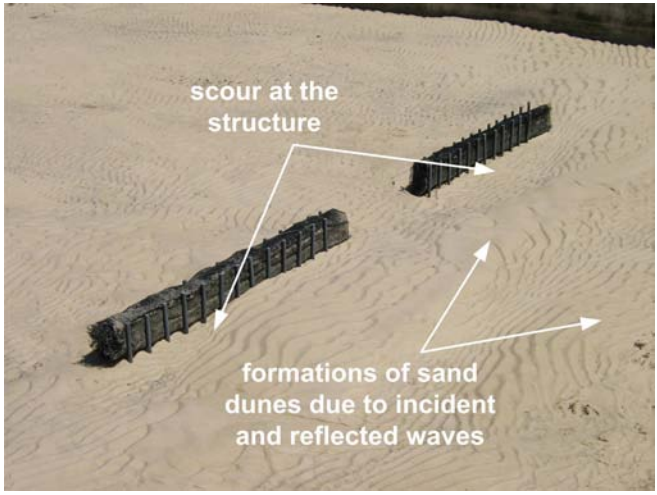

Figure 2.16.: Effect of regular waves on the erosion and movable bed evolution in the vicinity of brushwood fences (see Chapter 5)

Silvester and Hsu (1997) presented a comprehensive description of the main phenomena related to the scour in the vicinity of coastal structures. Based on multiple references, the authors discussed the effect of normal and short crested waves on the sea-bed morphology in the vicinity of breakwaters. This concerns the following points:

- For normal waves conditions, in the presence of a detached vertical full/partial reflective breakwater, the scour occurs at the nodal zones of $L/4$, $3L/4$, and $5L/4$ in the seaward direction. Furthermore, accretion occurs at the antinode of 0, $L/2$, and L. It has to be noted that L is the wave length of the incident normal regular wave.
- Many physical experiments were carried out with angled regular and irregular waves, with a movable bed formed with a very fine sand (approximately 0.1 mm) and with wave periods near to $1s$ and heights of almost 10 cm. Such experiments where able to describe the morphology changes due to the presence of a breakwater with a different form. They showed that, in order to obtain significant results, a typical test run takes more that 10 *hours* to reach its equilibrium state.
- For irregular, shore crested waves, the undulated erosion-accretion bed form is almost non-existent. This is due to the fact that every wave has its own reflection manner, hence, its own node and anti-node emplacement which favors a more uniform sea-bed but less eroded one.

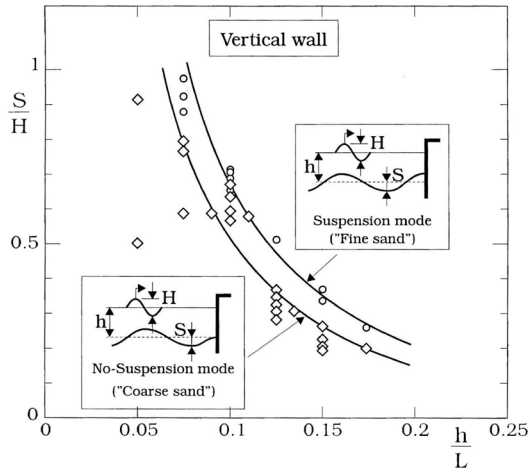

Figure 2.17.: Scour depth at a vertical non-porous breakwater after Sumer and Fredsoe (2000)

In 2D experiments, Sumer and Fredsoe (2000) tested the scour mainly at the toe of vertical and rubble-mound breakwaters. With a mean grain size equal to 0.2 mm, they analyzed the movable bed response to regular and irregular waves. The selected wave heights varied between 6 and 13 cm with periods varying between 1 and 3s. The 2D results are presented in Fig. 2.17. It appeared that the scour depth at the rubble-mound breakwater is smaller than that at the vertical-wall breakwater. Furthermore, it decreases with the decreasing slope of the rubble-mound breakwater. Finally, the regular waves induce higher scour depths than that for irregular waves.

2.6. Conclusions and needs for further research

The theoretical background in Sections 2.2 and 2.3 provided a thorough description of the most important variables and phenomena closely related to the present research. On one hand, they offered a good understanding of the wave propagation and transformation, and on the other, they defined the basics relates to the interaction of waves with a bed formed of granular material. Additional theoretical backgrounds are provided afterwards following the needs. For instance in Chapter 3 where the theory of head-loss in the brushwood fences is given, together with the theory of the downscaled

model (hydraulic and sediments), and in Chapter 6 where the theory of wave friction over a sandy bottom is presented.

Based on theoretical and experimental approaches, Section 2.4 showed how many researchers tried to understand the interaction of porous media with incident waves. This interaction was based mainly on the evaluation of the transmission and reflection coefficients of this porous media which depends mostly on its geometrical characteristics like porosity and heights, and on hydrodynamic conditions like incident wave characteristics and water depth. Although no in-depth investigation was carried out for brushwood fences, it is supposed that any study would have several common aspects related to permeable breakwaters. In fact, the direct evaluation of the hydraulic response of this soft structures appears to be missing. Additionally, when numerical modelling is concerned, no systematic evaluations was carried out, more specifically none of them proposed a detailed description of the wave field in a sheltered area surrounded by porous structures. In Section 7.1.4 a detailed description for the need for further investigation based on numerical modelling is provided. This concerns mainly the influence of the presence of gaps in brushwood fences.

Many researchers investigated the influence of the presence of detached coastal structures on the evolution of the shoreline. Section 2.5 showed also the importance of the scour in their vicinity when coastal structures are built over a granular sandy bottom. However, none of the researches investigated the interaction of porous structures like brushwood fences with a movable bed. Moreover, no 3D investigation was carried out, showing for instance the effect of the distance of the structure from the shoreline, together with the varying gap width on the surrounding eroded sandy bottom and the formation of eroded and accreted cells.

Reportedly, it has to be noted that none of this developments, basically numerical, concerning the hydraulic response of porous media, have been thoroughly utilized to model real life cases. Therefore, there is a strong need to know whether this could be easily used and applied to understand/solve situations where brushwood fences field is constructed to protect an eroding shores. This is achieved in Chapter 8 where, based on in-situ field measurements in Lake Biel, a numerical model is built and used for this purpose.

3. Experimental set-up and testing procedures

The present chapter outlines the experimental step-up of the physical experiments and provides a detailed description of the testing procedure and tests program for fixed and movable bed. For the former, only waves are measured and for the latter, in addition to waves, the bathymetry changes are measured after each test. Furthermore, a detailed description of the downscaling procedure of waves and sediments will be provided. The objectives of this chapter are the following:

- To provide the basis for the selection of an appropriate scale of the physical model of the brushwood fences
- To understand and test the behavior of the selected sand for experimental tests with movable bed
- To give a thorough description of the tests with fixed and movable bed

3.1. Description of the main experimental set-up

3.1.1. Wave tank description and adjustment

Physical tests are conducted in a wave tank at the *Laboratory of Hydraulic Constructions (LCH)* of the *Swiss Federal Institute of Technology (EPFL)*. It is 10 m long, 6 m wide, and 1.3 m deep as shown on Fig. 3.1. A pneumatic wavemaker is used to generate monochromatic unidirectional waves (2 in Fig. 3.1).

In order to reproduce a realistic typical bathymetry of Lake Biel, a concrete horizontal platform was built in the wave tank (5 in Fig. 3.1). Being almost 50 cm high, this platform is used to form the basis of the sediment placed on top (4 in Fig. 3.1). A geotextile membrane is used to confine the sediment in order to prevent material infiltration through the joints in the platform. The configuration of the sediment slopes represent a typical nearshore region. The bathymetric transition configuration is simulated by a 50% slope built with ethernite plaques (7 in Fig. 3.1).

Three packs of two wave gauges (A, B, C in Fig. 3.1), are attached to an aluminium non-deformable beam fixed over the wave tank in the longitudinal

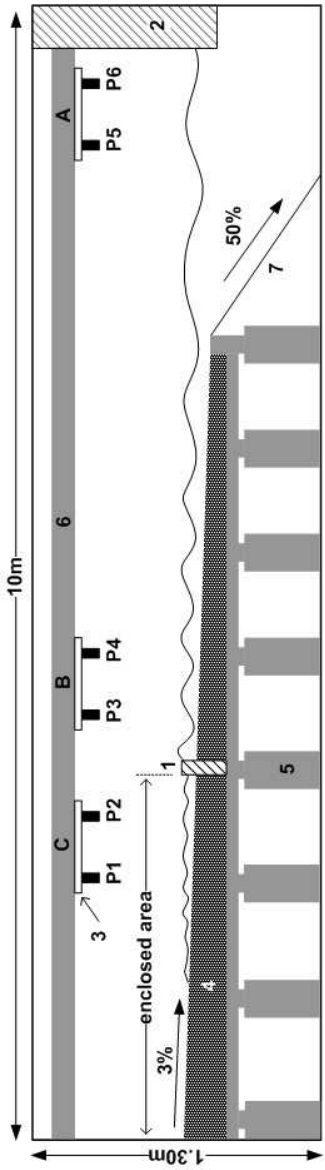

1: Downscaled physical model of the brushwood fences; **2:** Pneumatic wave maker capable of generating monochromatic unidirectional waves; **3:** Ultrasonic wave gauges assembled by a group of two and fixed to a horizontal plastic platform; **4:** Sand with an average 3% running slope used as a fixed or movable bed; **5:** Concrete platform built as a basis for the sand bed; **6:** Aluminum beam used as a support for the the ultrasonic wave gauges; **7:** Transitional slope constructed with ethernite plaques

Figure 3.1.: Schematic drawing of the wave tank at the *Laboratory of Hydraulic Constructions (LCH)*

direction (6 in Fig. 3.1). The instrumentation for data acquisition are located in the cabin B as shown in Fig. 3.2. Above the wave tank, a mobile metallic bridge in used in order to take photos during the experiments. The bridge can be used during tests without influencing the measurements since the aluminium beam is totally disconnected. The brushwood fences model is placed at the middle of the wave tank (1 in Fig. 3.1).

Waves generated in the wave tank are unidirectional and monochromatic. Therefore, the wave crests generated from the system D in Fig. 3.2 are always parallel to the width of the tank unless they are diffracted by the structure. They are generated by periodic air pressure applied uniformly over the surface of water from the triangular black boxes. The level of this system could be changed according to the desired water level in the tank using a small vertical aluminium rail fixed over the wall. The procedure of changing this level is time-consuming. Special attention should be given to the horizontal alignment of the 4 boxes since they are not connected. Thus a very small vertical difference between them could result in unstable and non-uniform generated waves.

The cabin A (see Fig. 3.2) contains the mechanical motor for wave generation (see Fig. 3.3). Waves are generated as mentioned above by cyclic air pressure applied over the surface of water. The periodicity is produced by a metallic arm connected from one side to a rotating disk and from the other side to a wind piston. The arm length could be changed by sliding its end over the rail fixed on the disk. This applies changes on the generated wave heights. Wave frequency is the same frequency of the motor axes rotation. It could be changed easily by rotating the disk G in Fig. 3.3.

3.1.2. Measurement devices

Wave measurements

The characteristics of waves are measured simultaneously by six ultrasonic gauges fixed at almost 40 cm above water level. The first two gauges (see group A in Fig. 3.1), near to the wave maker (see 2 in Fig. 3.1) measure incident waves not yet significantly influenced by reproduced bathymetry in the wave tank. Depending on water level depths and wave periods, the region where they are located could be deep or intermediate water depth.

The second pair of gauges (see group B in Fig. 3.1), measures incident and reflected waves (on the structure) in the intermediate or shallow water where the influence of the bathymetry of the bottom is major. They are situated in the seaward direction according to the structure location. The third pair of gauges (see group C in Fig. 3.1), at the leeside of the structure, measure transmitted waves through the structure.

The concept of using always a pair of ultrasonic gauges enables the measurements of generated wave characteristics without using any formula

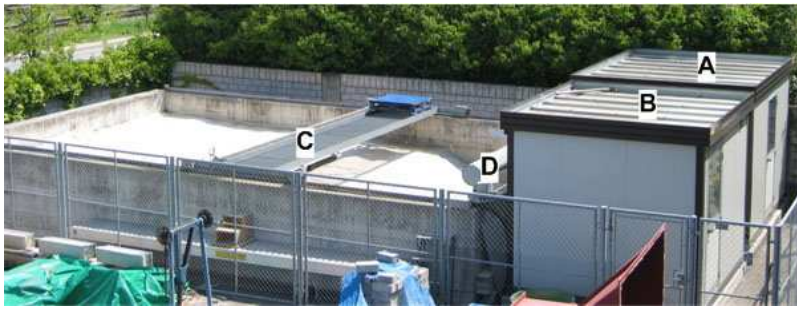

A: First cabin where the motor for wave generation are located; **B:** Second cabin where a PC and data acquisition instrumentations used for wave measurements are located; **C:** Mobile bridge used for taking photos and bathymetry measurements

D: PVC conducts and boxes used for pneumatic generation of waves by applying uniform air pressure over the surface of water

Figure 3.2.: General layout of the wave tank where experimental tests are conducted

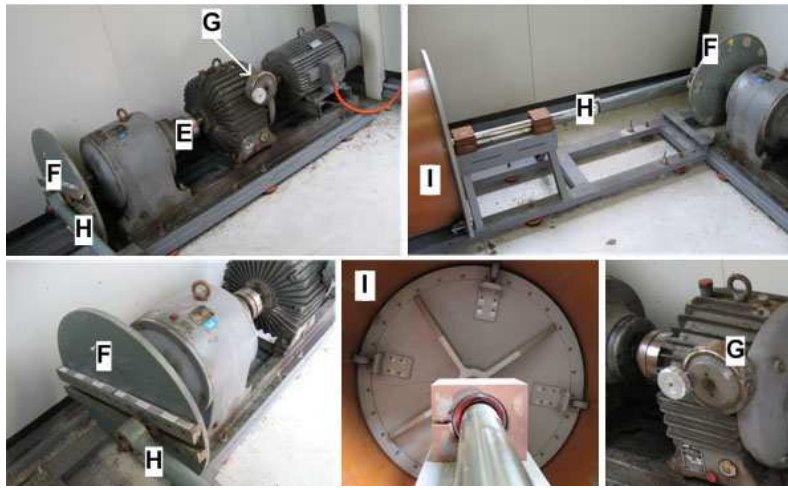

E: Electrical powered rotative motor for wave generation; **F:** Disk with an annotated median rail for arm regulation; **G:** Annotated disk for the control of the rotating frequency of the motor; **H:** Arm for the regulation of the wave height; **I:** Piston used for generating periodic air impulsion

Figure 3.3.: Devices for wave generation

related to wave length since the nature of region may change as a function of the water depth and wave characteristics. It has to be noted that the formulae for calculation of wave length are different for each type of region (Deep, Intermediate or Shallow Water in Section 2.2.1). After calculating wave period from measures given only by one gauges, by combining the second gauge measurements the wave length could be obtained.

As shown in Fig. 3.4, the wave gauge (K) is an ultrasonic analog cylindrical sensor (Baumer Electric, Switzerland). The main characteristics of this sensor are listed as following:

- Sensing range: 100 *to* 700 mm
- Beam angle: 10^o
- Resolution: less than 0.3 mm
- Sonic frequency: 230 kHz
- Geometry: Cylinder with a 30 mm diameter and 70 mm height
- Output signal in volt

The PC located in cabin B receives the six signals of the six wave gauges. Using the LabView signal processing software, the raw data in volts are saved in the computer's memory. Then, the calibration values for each sensor are

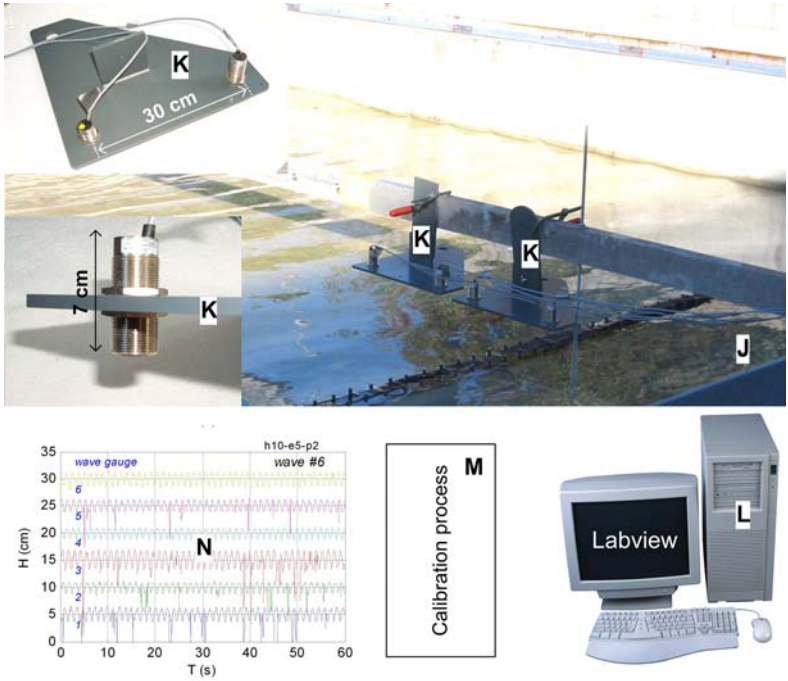

J: Wave measurements during experimental tests before and behind the protection structure ; **K:** Coupled wave probes using ultrasonic signals measuring water level variation; **L:** Mainframe PC receiving and saving raw results in volt of 6 signals of each wave probe via LabView software; **M:** Signal transformation from volts to heights using probes calibration values; **N:** 'semi-raw' results of each wave probes showing heights [cm] versus time [s]

Figure 3.4.: Ultrasonic sensors for the measurements of wave characteristics during experimental tests

applied, transforming by this process the volt signal into distance signal as shown in M and N signal process stages in Fig. 3.4.

Measurements of the bathymetry

The measurements of the bathymetry concerns the topography changes of the bottom of the wave tank when performing tests with the movable sandy bed. For each movable bed test (see Section 3.4.3), the bathymetry is measured before and after. No bathymetric evolution is considered during the test.

The proposed technique used for the measurement of the bathymetry is based on manual measurement using a level gauge fixed on the existent movable bridge and described in Fig. 3.5.

In order to prevent the effect of penetration of the level gauge in the sandy bottom, a cylindrical plastic head was added (see R in Fig. 3.5). It was observed that such a device works efficiently only when the water is drained from the sandy bottom. Otherwise, even with a large head, the level gauge could easily penetrate in the sandy wet bed producing inaccurate results.

A more detailed description of the measurement method and data acquisition and analysis will be provided in Section 3.4.3.

3.2. Selection of waves and sediments for physical modelling

3.2.1. Downscaling of waves

The purpose of this section is to select an appropriate scale of the physical model to be used during experimental tests. In the present case, where tests involve interaction of waves with the protection structure and the movable bed, the selection of the model scale has two constraints:

- Appropriate similarity of waves in the wave tank compared to wind-waves present for instance at Lake Biel
- Appropriate selection of sediment characteristics, able to reproduce for similar loadings, similar transport process as in reality

The approach is based first on the selection of a model scale value that respects the first point. Then, a selection of an appropriate sediment that respects the second point is carried out on the basis of the scale defined by point one. Before comparing waves over Lake Biel with the wave range that could be generated by the wave maker, it is important to define the parameters, related to wave characteristics, used for such comparison.

The similarity rules used of downscaling prototypes at a small model scale should provide the above mentioned parameters. Therefore, specific

O: Mobile platform installed over the bridge allowing easy movements back and forth; **P:** Transversal aluminium beam totally independent of the mobile bridge and used as a basis for the level gauge; **Q:** Level gauge able to slide back and forth over the beam and used of bathymetric measurements; **R:** Head of the level gauge

Figure 3.5.: Manual technique for the measurements of the bathymetry during experimental tests with movable bed

attention has to be given to the selection of the appropriate similarity rules. For practically all free-surface coastal physical modelling problems, the forces associated with surface tension and elastic compression are relatively small, and so can be safely ignored (Warnock, 1950). This would therefore exclude Weber and Cauchy criterion. An appropriate hydrodynamic scaling law will largely concern gravity or viscous forces. Viscous forces at this first stage are irrelevant since they concern only the interaction of water and waves with the rough bottom sandy bed.

Therefore, Froude's similarity rules could be considered. In principle, these rules are mainly used for free surface flows, for which the viscosity forces are less important than the gravity forces. Froude similarity prescribes that the ratio between inertial and gravity forces should be conserved. They are considered as applicable in this case of modelling, where viscosity is negligible. This reads as follows (Hughes, 1993):

$$F = \sqrt{\frac{inertial force}{gravity force}} = \sqrt{\frac{\rho L^2 V^2}{\rho L^3 g}} = \frac{V}{\sqrt{gL}} \tag{3.1}$$

where L could be considered as a characteristic dimension of the wave, V particle water velocity, ρ the water density, and g the acceleration of gravity.

The Froude number should be the same in the model (subscript m) as in the prototype (subscript p), this implicates the following:

$$(\frac{V}{\sqrt{gL}})_p = (\frac{V}{\sqrt{gL}})_m \tag{3.2}$$

Defining the model scale ratio for distances λ_L, time λ_T, and velocities λ_V as follows (Yalin, 1971):

$$\lambda_L = \frac{L_m}{L_p} \tag{3.3a}$$

$$\lambda_T = \frac{T_m}{T_p} \tag{3.3b}$$

$$\lambda_V = \frac{V_m}{V_p} \tag{3.3c}$$

and replacing Eqs. 3.3 in Eq. 3.2, the scale ratio of time and velocities could be expressed as a function of λ_L:

$$\lambda_T = \sqrt{\lambda_L} \tag{3.4a}$$

$$\lambda_V = \sqrt{\lambda_L} \tag{3.4b}$$

At this stage, after defining the similarity rules for distances, time, and velocities, the waves generated by the wave maker in the experimental setup are compared with the waves generated by wind events over Lake Biel. This will provide the approximate model scale for which the downscaled waves are most representative of realistic waves.

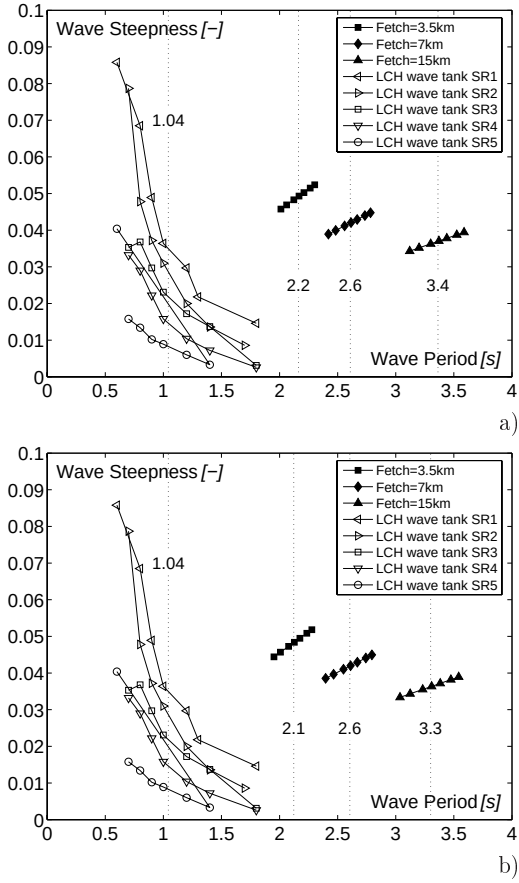

Figure 3.6.: Comparison of wave generated in the wave tank and waves at Lake Biel for different fetchs and the two main wind regimes: (a) *Le Vent* (sector [210°-240°]) (b) *La Bise* (sector [30°-60°])

Based on wind and wave calculation in Lake Biel as described in Section 1.2, the following rules for the selection of the appropriate wind-waves are respected:

- Selected wind-waves must correspond to the most representative wind station beside Lake Biel. The station that provides the highest wind values should be considered
- It is important to take into account the durations of wind-waves following wind event that correspond to a fetch limited condition
- For the duration that corresponds to the maximal values of wind velocities and fetch limited condition, all the return periods should be used
- It is recommended to calculate afterwards wind-waves for different fetch values with respect to distances in the lake

The comparison of waves based on the above-mentioned rules can be seen in Fig. 3.6. The wind station at Neuchâtel is selected for that purpose and wind velocities of the two main regimes, South-Western (see Fig. 3.6a) and North-Eastern (see Fig. 3.6b) are reasonable. The highest, average, and lowest fetchs are selected in the calculation of waves. This reads 15, 7 and 3.5 km, respectively.

Concerning waves generated in the wave maker, five series are considered (SR1 to SR5 in Fig. 3.6) according to the arm length of the wave generator as described in Fig. 3.3. All the possible wave periods are also considered.

Fig. 3.6 provides the steepness of waves according to the wave period for experimental waves and wind-waves over Lake Biel as well as the period averages for each series. The average ratio of the highest mean period of wind-waves over Lake Biel for both wind main regimes and mean period of experimental waves is equal to 3.22. After applying the time scale ratio as described in Eq. 3.4a, a geometric model scale of $\lambda_L = 1 : 10$ seems to be applicable. The lowest mean values of wind-wave periods could also be generated for the selected model scale, since the period range of experimental waves covers a significantly wide interval.

3.2.2. Theoretical approach for grain size selection

As explained at the beginning of Section 3.2.1, the second stage of the model scale definition and verification, is the selection of a grain size to be used during experimental tests with a movable bed. The movable bed model in the present case is composed of granular material that can be transported by hydrodynamic forces imposed by the selected waves and/or wave-generated currents. It has to be noted that (Hughes, 1993):

- The sea-bed is not able to evolve in a fixed-bed model in response to changing hydrodynamic forcing: a serious model limitation in significant changes in the seafloor would be due to waves and currents
- The modified model bathymetry may influence incoming wave characteristics before reaching a quasi-equilibrium condition

Consequently, the sediment characteristics for the physical model should be selected very carefully. Hudson et al. (1979) gave two basic rules for movable bed selection in coastal related experiments:

- Fully understanding of the physical process involved in sediment transportation during physical model experiments
- Ensuring that the relative magnitude of all dominant process are the same in model as in prototype

In a paper concerning the similarity relation between site and laboratory scour phenomenon, Matumoto et al. (1991) modelled scour around structure using granular sand material. They based their downscaling method of prototype grain size using only Froude similarity. They stipulated that only such similarity is applicable when prototype material is very coarse. However, when this material is rather fine, is was recommended to carry out a more detailed analysis. Furthermore, the authors noticed that when applying Froude similarity, the scour around structures is relatively higher (20% to 30%) in the model than in the prototype. Thus, in order to have a more accurate modelling, a detailed theoretical analysis of the sediment modelling is proposed.

The major goal of the mobile bed physical experiments it to identify the effect of the structure on the shoreline erosion and the local scour. Additionally, in the absence of the structure, the hydrodynamic forces should induce cross-sectional behavior in similarity with real life conditions. In his section that concerned the physical modelling of coastal processes, Kamphuis (1996) proposed two approaches to model the mobile bed. The first is related to bed load dominated sediment transport model and the second is related to suspension dominated model. The former is usually defined by the correct reproduction of the initiation of movement and the latter is defined by the sediment suspending mechanism and the grain fall velocity.

Moreover, two major criteria for the sediment threshold of motion where presented in Section 2.3.2. The first one could be described by the Shield-Soulsby criterion and the second one by Bonnefille criterion. Each criterion refers therefore to the bottom shear stresses formulations defined respectively by each one. When selecting the grain diameter in reference to the model scale, a special attention should be given to the fact that a granular prototype sand has to be modelled with a granular model sand as well. If the selected sediment model grain size happens to fall in the cohesive sediment range, this will implies fundamental differences in the sediment transport processes and the model would not be a dynamic representation of the prototype.

For the experimental tests with movable bed, it is proposed to use the finest granular material that could be found. It is a quartz sand with a mean diameter of $d_{50} = D_m = 0.18\ mm$ (see granulometric curve in Fig. 3.7).

In the following, the prototype sand mean diameter (full scale) is calculated, based on the selected model sand. By this approach, it is possible

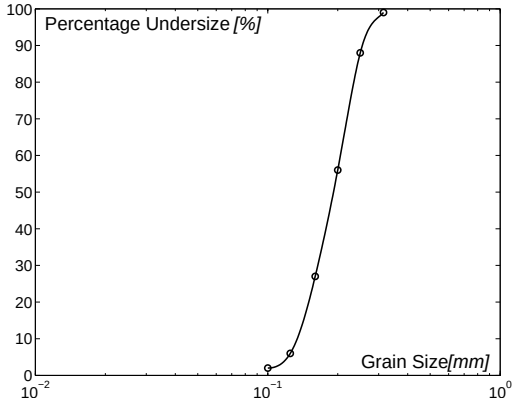

Figure 3.7.: Mobile-bed material used during the experimental tests S26®: density= 2.65; grain size=0.1 to 0.315 mm; d_{50} = 0.18 mm; hardness (Mohs Scale)> 7; chemical propriety: 99.10% of SiO_2

to verify whether the selected sand for experimental tests corresponds to reality.

The ratio of the wave generated shear velocity between prototype and model as expressed in Eq. 2.12, based on Eqs. 3.3 is equal to:

$$\lambda_{u_*} = \frac{u_{*m}}{u_{*p}} \tag{3.5a}$$

$$\lambda_{u_*} = \lambda_L^{\frac{1}{8}} \tag{3.5b}$$

Eq. 2.12 gives the bottom shear stress velocity induced by waves. Bonnefille (1992) included in this expression, the effect of the dynamic viscosity of the liquid ν. Since ν is the same for prototype and model, when applying Eq. 3.5a, ν is removed. This implies that the result of the calculation of λ_{u_*} will not be similar to scale ratio of velocities equal to Eq. 3.4b.

In order to calculate the prototype grain size D_p, it is proposed firstly to replace Eqs. 2.16 and 2.17 in Eqs. 2.18. This will result in an non-linear equation having the following form:

$$aD_p - bD_p^c = 0 \tag{3.6}$$

where

$$a = [\frac{g(\rho_s/\rho - 1)}{\nu^2}]^{\frac{1}{3}} \tag{3.7a}$$

$$for\ R_* < 12 \qquad \Rightarrow b = 2.5[\frac{u_{*p}}{\nu}]^c\ ;\ c = \frac{4}{5} \tag{3.7b}$$

$$for\ 12 < R_* < 1000 \ \Rightarrow b = 3.8[\frac{u_{*p}}{\nu}]^c\ ;\ c = \frac{5}{8} \tag{3.7c}$$

$$for\ 1000 < R_* \qquad \Rightarrow b = 2.7[\frac{u_{*p}}{\nu}]^c\ ;\ c = \frac{2}{3} \tag{3.7d}$$

The solution of Eq. 3.6 is as following:

$$log(D_p) = \frac{log(\frac{a}{b})}{(c-1)} \tag{3.8}$$

Therefore, the procedure to calculate the D_p will be the following:

1. Calculating R_{*m} using Eqs. 2.18 for the three different Reynolds domains and for a sand range of D_{*m}

↓

2. Calculating u_{*m} using Eqs. 2.17 for the three different Reynolds domains

↓

3. Using the ratio defined in Eq. 3.5b, calculating u_{*p} for the three different Reynolds domains

↓

4. Calculating a and b following Eqs. 3.7

↓

5. Calculating D_p for the three different Reynolds domains following Eq. 3.8

The second approach based on the threshold Shields parameter θ_{cr} is more direct and provides similar results. It is assumed that:

$$\theta_{cr,p} = \theta_{cr,m} = cte \Rightarrow \lambda_{\theta_{cr}} = 1 \tag{3.9}$$

Therefore, based on the expression of θ_{cr} as provided in Eq. 2.13, the similarity ratios of D and τ are equal:

$$\lambda_\tau = \lambda_D \tag{3.10}$$

Based on Eqs. 2.14 and 3.5b, the similarity ratio of D is thus equal to:

$$\lambda_\tau = \lambda_{u_*}^2 \tag{3.11a}$$

$$\lambda_D = \lambda_{u_*}^2 \tag{3.11b}$$

$$\lambda_D = \lambda_L^{\frac{1}{16}} \tag{3.11c}$$

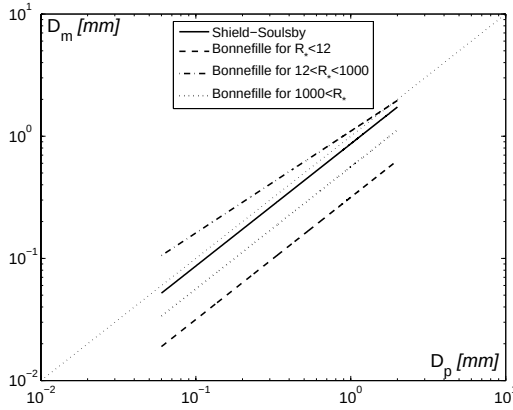

Figure 3.8.: Prototype grain size calculation based on the $1:10$ model scale, where fine sediments are used during experimental tests with movable bed

This leads to the graphic as shown in Fig. 3.8 where the ratio λ_D is represented following the theoretical approaches as described above.

The selection of the prototype grain diameter D_p is based on the results as presented in Fig. 3.8. This selection could be based on different theories as described above. The selected grain size with a mean diameter $d_{50,m} = 0.180\ mm$ corresponds therefore to the following full scale grain sizes:

- Shield+Soulsby: $d_{50,p} = 0.207\ mm$
- Bonnefille average: $d_{50,p} = 0.450\ mm$

Table 3.1 provides a short description of the material found at some representative selected shores on Lake Biel. It shows that natural lake shores have a wide range of granular material varying mainly from silt to gravel. The resulting diameters D_p fall within this wide range of sediment.

3.2.3. Qualitative preliminary tests for wave-sediment interaction

Several preliminary tests were carried out in order to evaluate qualitatively the hydrodynamic response of the mobile-bed due to wave action. Fig. 3.9a shows the response of three different granular materials due to perpendicular monochromatic wave action. They are installed on the platform of the wave tank with a slope of almost 3%. The coarsest sand MBS1 with a grain size diameter of $[1-5\ mm]$ is commonly found on typical shores of the major lakes in Switzerland. It represents a prototype of full scaled material. The second

Emplacement	Clay [%]	Silt [%]	Sand [%]	Gravel [%]	Rock [%]	d_{50} [mm]	Protection type	
Vingelz	0.00	0.00	34.49	65.51	0.00	4.40	embankment	artificial
Ipsach	0.00	0.00	6.55	92.12	1.33	10.70	embankment	artificial
Von Rütte-Gut	0.86	38.27	60.87	0.00	0.00	0.070	brushwood fences	natural
Mörgin	0.00	0.00	72.34	27.66	0.00	0.33	embankment	natural
Hagneck	0.00	0.00	23.00	75.11	1.88	14.00	embankment	natural
Lüscherz	0.00	0.00	24.93	74.90	0.17	11.00	embankment	artificial
St. Petersinsel	0.18	2.91	14.72	82.18	0.00	8.00	embankment	natural
Erlach	0.00	0.00	25.93	74.07	0.00	7.20	embankment	artificial
La Neuveville	0.00	0.00	33.75	65.84	0.410	7.00	embankment	natural

Table 3.1.: Existent material samples at different shore locations on Lake Biel (BFH, 2002)

coarse sand MBS2 has a grain size diameter of $[0.3 - 1\ mm]$. The finest one MBS26, with a grain size diameter of $[0.1 - 0.315\ mm]$ is the material selected on the basis of the theoretical approach of sediment down-scaling as described in Section 3.2.2.

test number	H	T	d	L	Ripples formation		
	[m]	[s]	[m]	[m]	MBS1	MBS26	MBS2
PRE1	0.02	1.00	0.10	0.70	no	small	no
PRE2	0.05	0.80	0.10	0.50	no	big	no
PRE3	0.08	0.60	0.10	0.40	no	big	small

Table 3.2.: Preliminary experimental tests for the comparison of the three mobile-bed material

Wave conditions and qualitative results are provided in Table 3.2. Each test duration was almost 2 *hours*. After each test, the bathymetry was corrected to the initial 3% cross-sectional slope. Generated waves in each test were measured by the ultrasonic gauges. Their characteristics remain almost constant during the duration of each test.

Tests demonstrated that practically only the finest sand presents a clear sediment transport regime. As shown on Fig 3.9, the sand MBS26, with a grain size ranging in the interval $[0.10 - 0.315\ mm]$ exceeds its initial deposition area and initiates ripple formation. For the coarsest sand MBS1 no sediment movement is perceptible. The sand MBS2 starts moving at a very high wave frequency. However, this frequency does not corresponds to an average wave frequency as presented in Fig 3.6. This sand could be also disregarded since its response to hydrodynamic loading is very slow. The finest sand MBS26 therefore appears the most adequate for the experimental tests with a mobile bed. It has to be noted that this sand is the finest quartz granular material that is normally available. This leads to the conclusion that the sand MBS26 is able to show good sediment transport processes under wave action calculated on the basis of similarity rules identical to real wind-wave over Lake Biel.

3.2.4. Laboratory and scale effects

The laboratory effects are defined by the logical ratio between model boundary conditions and real-life boundary conditions (Kamphuis, 2000). If it is equal to one, then experimental set-up adequately reproduces real life conditions. If not, efforts should be given in order to decrease this effect.

Fig. 3.10 tries to clarify this effect based on the actual set-up of the wave tank during the experiments. When no structure is present, the wave reflected on the cross-wall (C) could be considered a laboratory effect. Additionally the

a)

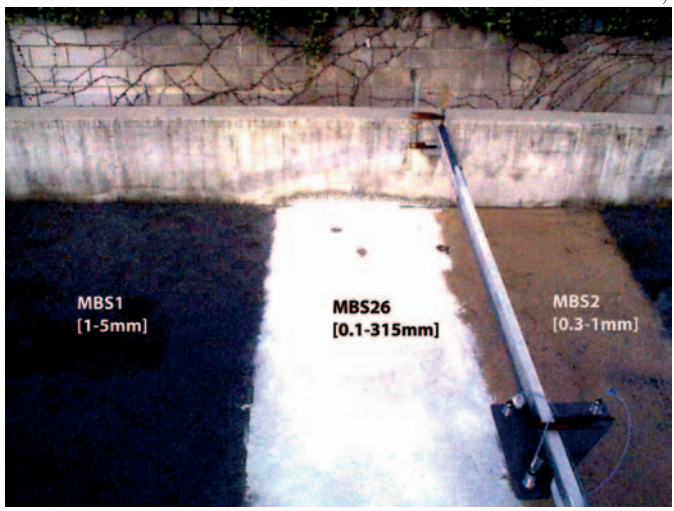

b)

Figure 3.9.: Preliminary tests (a) in the wave tank comparing the very fine sand in the middle with two other coarser ones at left and right(b)

waves reflected on the longitudinal wall (E) during tests with structure are also considered a laboratory effect. In fact, for both cases, open boundary conditions are present in real life. Therefore, when waves are reflected on the beach, they propagate to infinity (almost) and lose their energy due to bottom friction. The same process occurs with the presence of the protective structure. In this case the diffraction process is able to change the propagation direction of the incident wave and the longitudinal wall-faces become reflective surfaces.

The best way to prevent surface reflection would have been the installation of specially designed perforated panels, or rubberized 'horsehair' mats, that absorb up to 95% of the incident waves energy. However since such equipment was not available, effort was made to reduce the laboratory effect:

- Waves A and B are the same as in reality (with respect to model scale). However, waves C do not exist in reality. Therefore the incident waves during experimental tests are measured at wave gauges A and B (see Fig. 3.11) and their characteristics are adapted in accordance with the real wave range.
- It is difficult to fully contain the effect of the reflected waves E. However, the incident perpendicular wave are measured at the longitudinal axe of the wave tank. This limits the influence of waves E. It has to be noted that such waves are very small and can be neglected (experimental observation).

The laboratory effects in such a short wave model are also related to the generated wave spectrum. In real life, the hydrodynamic response of the protection structures is related to the directional wind-wave spectrum. Nevertheless, experimental waves have a unidirectional spectrum. This effect could not be eliminated since the present experimental set-up is not able to generate such spectrum. In lakes, where wind regimes seem to be quasi-stable and well defined, this approximation could accepted.

In addition to this common laboratory effects in fixed-bed models, movable-bed models have also such effect summarized by Hughes (1993). Based on experiments done by Chestnutt, Hughes and Fowler, the importance of the distance of the beach to the wave generator boxes was showed. When the beach reflected regular waves re-reflect on the wave generator boxes, the difference of phase between this waves and the generated initial waves influences the profile development. Moreover, the initial beach cross-sectional slope seem to influence beach erosion rates during experiments. It was decided therefore to begin movable-bed tests with an initial slope reasonably near to the equilibrium beach profile.

The scale effect during experimental tests could be explained in the present case by the difference between the scaling of the gravity driven phenomenon compared to the viscosity related ones. The former is defined by

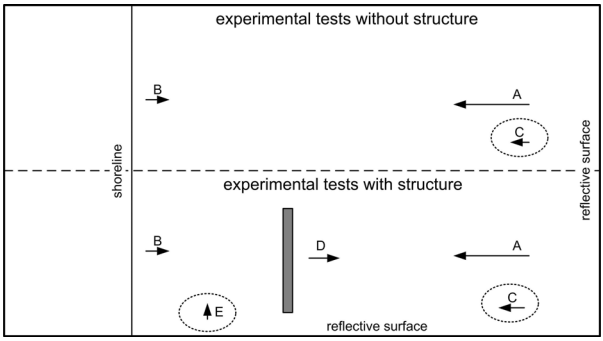

Figure 3.10.: Laboratory effect during the experimental tests related to the physical set-up; A=generated waves; B=beach reflected waves; C=wall-face reflected waves; D=structure reflected waves; E=wall-face reflected waves; Circle=laboratory effect

the proper down-scaling of waves as explained thoroughly in Section 3.2.1. The latter concerns the interaction of wave with the movable-bed. It is very difficult to find a satisfactory agreement between all the requirements needed for the downscaling of the wave-sediment interaction. Usually only some important criteria are respected and modelled as described in Section 3.2.2. The others will therefore be responsible of the so-called scale effect.

In a Sand Model, where the movable bed is formed by real sand instead of lightweight material as the present case, the scale effect could be described by the incipient motion of sediment. It is investigated by determining the prototype-to-mode scale ratio for the densimetric Froude number and grain size Reynolds number. They are given by Eqs. 3.12a and 3.12b, respectively (Kamphuis, 1996).

$$\lambda_{F_*} = [\frac{\lambda_L}{\lambda_D}]^{-\frac{1}{4}} \tag{3.12a}$$

$$\lambda_{R_*} = \lambda_L^{-\frac{1}{8}} \lambda_D^{-\frac{11}{8}} \tag{3.12b}$$

Based on Section 3.2.1 and Eq. 3.11c, the numeric values will be equal to:

$$\lambda_{F_*} = \frac{1}{1.14} \tag{3.13a}$$

$$\lambda_{R_*} = \frac{1}{1.62} \tag{3.13b}$$

Therefore, both numbers are less in downscaled model than in the prototype. This brings out the conclusion that incipient motion of the sediment require relatively higher shear stresses to initiate the movement in the model than in the prototype. This scale effect should be considered when using the movable-bed experimental results for practical engineering problems. However, for the present case, where the physical modelling does not really represent a real case scenario, the difference between model and prototype could be disregarded.

3.3. Design and behavior of the physical model of brushwood fences

3.3.1. Concept of the downscaled model

Section 3.2.1 provided the appropriate scale factor to be used for a downscaled physical model. Subsequently, this section describes the choice of the adequate concept for the construction of the model of the brushwood fences. In real life, the fences are mainly constructed, as described in Chapter 1, with tree branches (called "fascine") inserted between two parallel wooden pile rows. For the physical modelling, this rigid structure of wooden piles is constructed as shows in Fig. 3.11.

The spacing between the wooden piles is fixed to an approximate value of 6 cm. The main two variables of the rigid structure are the height h and the width b of the fascine. The plastic piles, having a 1 cm diameter and 15 cm length, are fixed (but not attached) on a PVC plastic platform. They can be easily changed is order to have different values for b. The height h can be as well easily modified by changing the level of the platform buried under the bottom level (see Fig. 3.11).

For the case of Lake Biel, the fascine are made of the willow trees. In reality, their porosity varies approximately between 0.2 and 0.8 (Iseli, 1992). Considering the permeability, no estimation is made. Hence, in order to choose a similar material for the physical modelling, capable of reproducing a realistic response, it is necessary to respect at least the similarity in porosity. After trying to model real fascine by choosing thin plastic sticks with a diameter similar to the average diameter of a tree branches, it appeared that is almost impossible to build such a model with this method since the sticks are very thin and multiple, and must be placed in a very precise way in order to have well defined porosity. Therefore this concept was abandoned.

The system was replaced, as shown on Fig. 3.12, by a much easier and accurate way. It consists of building the fascine by enrobing a very highly porous media provided by Colbond® (B Fig. 3.12a) by a geotextile (A Fig. 3.12a). It is assumed, in principle, that the overall porosity of the fascine

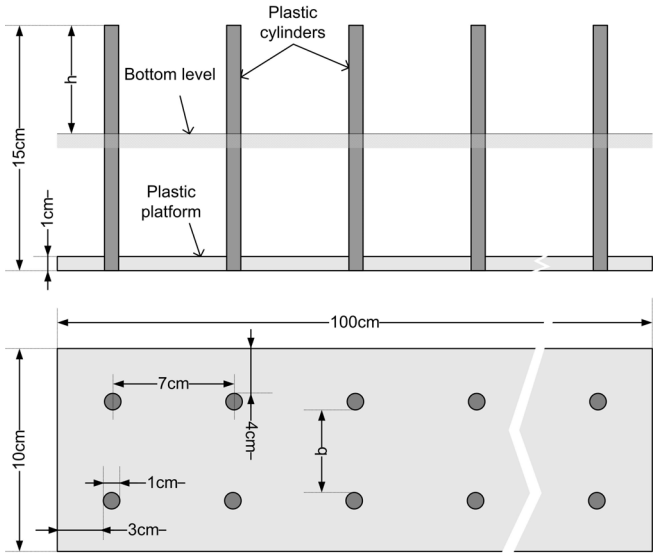

Figure 3.11.: A schematic draw of the 1 : 10 down-scaled rigid structure of the physical model of brushwood fences

is approximately the same as the geometrical porosity of the geotextile. By using this method, changing the porosity of the fascines becomes a very easy task. It is done by replacing the geotextile with another one with different porosity.

However, the porosity of one layer of geotextile, calculated geometrically, does not, by any means, represent the real porosity of the fascine since, in reality, the drag coefficient of the porous geotextile have big influence on the overall response of the model to the incoming waves. Furthermore, additional hydraulic tests were performed in order to determine the real response of the entire fascine (see Section 3.3.2).

Nevertheless, different types of geotextile HaTe® are considered for the physical tests (see Fig. 3.13). It is assumed that this first estimation of their geometrical characteristics is able to give basic relative notion for their dynamic response in water. Afterwards, the additional tests determine the corresponding permeability and response to hydrodynamic loadings.

Table 3.3 shows the geometric characteristics of the three main geotextile types used for the physical model of brushwood fences. This selection provides a good range of porosities for fascine. The porosity calculated in Table 3.3 is defined as the surface of empty space in a geotextile surface unit, divided by the total surface of the same unit. Practically, the porosity values are

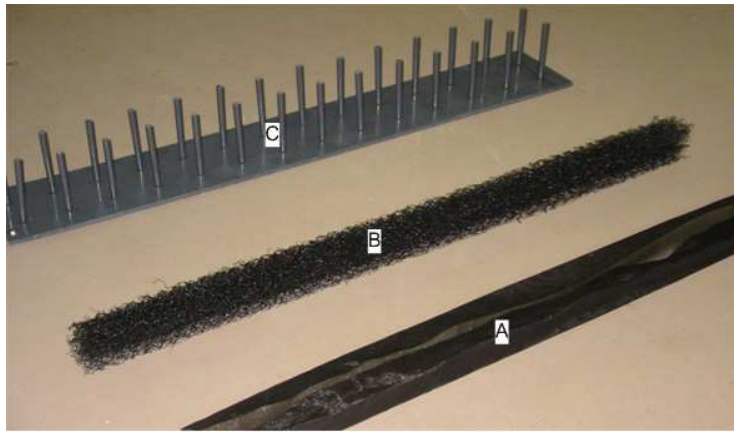

a)

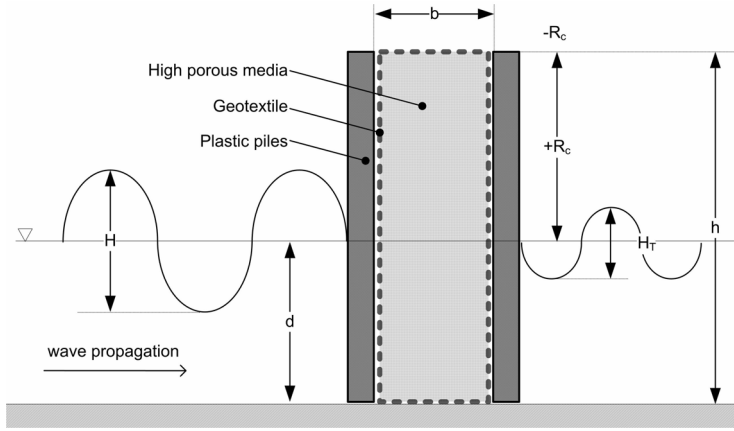

b)

Figure 3.12.: (a) Three main components of the physical model on brushwood fences; (b) The same model placed in the wave tank

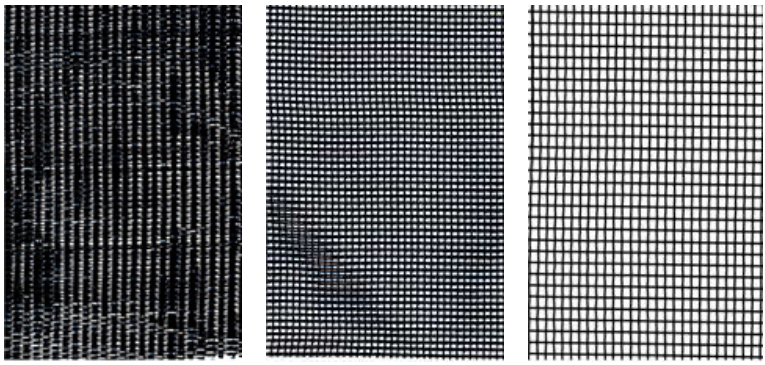

a) b) c)

Figure 3.13.: Three types of HaTe® geotextile used for the physical model of brushwood fences: (a)HaTe D 00.006, P1 (b)HaTe C 00.520, P2 (c)HaTe D 50.145, P3 (scale 1:1)

calculated using a specially designed MatLab© function that calculates the surfaces of white and dark pixels in an image (Oehy, 2003).

Type	Nomenclature	Grid width [mm]	Permeability [m/s]	Porosity [-]	Line width [mm]
P1	HaTe D 00.006	0.4	100.10^{-3}	0.16	1.0
P2	HaTe C 00.520	0.45	250.10^{-3}	0.36	0.6
P3	HaTe D 50.145	1.2	$>> 250.10^{-3}$	0.62	0.4

Table 3.3.: Geometrical characteristics of the three main types of the geotextile

3.3.2. Head-loss of the physical model

The goal of this section is to evaluate and compare the different elements used for the construction of the physical model of brushwood fences. This process is based on the calculation of the minor head-loss coefficient due to the presence of the structure in a straight pipe. For this purpose, a specific installation was built as described in Fig. 3.14. The physical model was mounted in a fixed cylindrical instrument installed within the pipe. For each water flow value, the pressure behind (A in Fig. 3.14) and after (B in Fig. 3.14) the model was measured using a twin tube hydraulic piezometer. The flow in the pipe was measured simultaneously by an electromagnetic flowmeter and an ultrasonic

water level gauge fixed over an elevated water recuperation tank at the end of the pipe where a triangular weir served to calculate the flow.

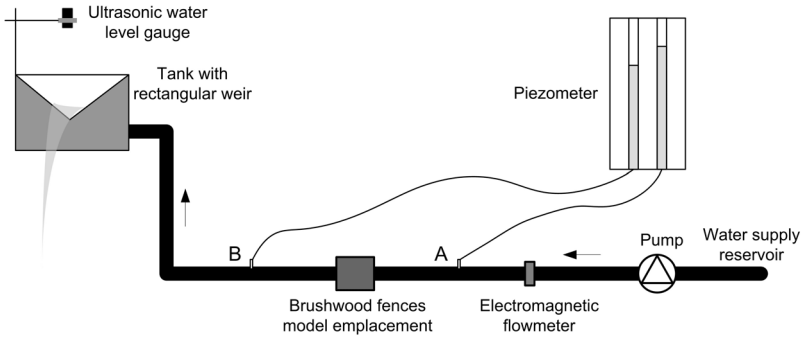

Figure 3.14.: A schematic draw of the experimental set-up for measuring the head-loss of the model of the brushwood fences

The flow values used during tests varied between 4 and 12 l/s. For each configuration, head-losses were measured for four consecutive flow values. The flow measurements were compared using different formulaes (Bazin, Gourley and Thompson) for triangular weir recommended by Lencastre (1984), together with the direct values provided by the electromagnetic flow meter. It was shown that the latter gives higher values when compared to the former more accurate calculations. Therefore, it was decided to use the formula of Gourley et Crimp for a triangular weir as described by the Eq. 3.14:

$$Q = 1.32tan(\frac{\alpha}{2})h^2.47 \tag{3.14}$$

where Q the flow across the weir, α the angle of the triangular weir, and h the water level above the weir.

Series	Structure width b [cm]	Flow Q [l/s]
HL0	-	4 *to* 12
HLP0	$2.5 - 5 - 7.5 - 10$	4 *to* 12
HLP1	$2.5 - 5 - 7.5 - 10$	4 *to* 12
HLP2	$2.5 - 5 - 7.5 - 10$	4 *to* 12
HLP3	$2.5 - 5 - 7.5 - 10$	4 *to* 12

Table 3.4.: Test series for head-loss characteristics of the physical model of brushwood fences

Table 3.4 shows the five tests series carried out for the head-loss evaluation. The first one, HL0, is used to calculate the sum of the linear head-loss between A and B and the minor head-loss due to the section contraction made by the presence of the cylinder used for fixing the physical model in the pipe. The second test series HLP0, measures the head-loss due to the presence of the structure with only the middle high porous element (B Fig. 3.12a). Finally, series HLP1, HLP2, and HLP3 give the head-loss due to the presence of the entire physical model made by the two main elements (A and B in Fig. 3.12a), and thus for the three selected porosities (see Table 3.3).

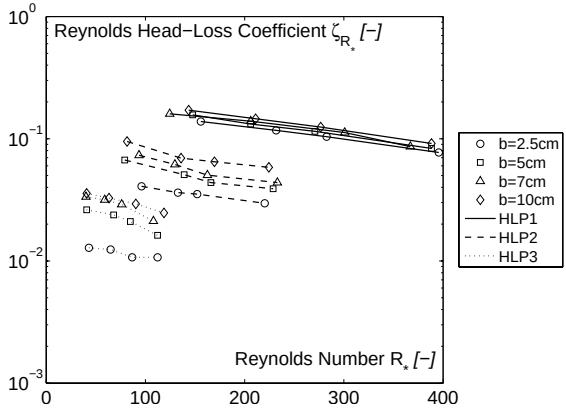

Figure 3.15.: Reynolds heal-loss coefficient ζ_{R_*} of the physical model of brushwood fences as a function on the Reynolds number of the geotextile R_*

The results of the tests are provided in Appendix B, where the minor head loss of the structure Δh_s (in meter) is calculated on the basis of the relationship $Q - \Delta h_l$ obtained by the test series HL0 and expressed by the following equations:

$$\Delta h_l = 3.9338Q + 0.0066 \tag{3.15}$$

where Δh_l is the linear (almost) head-loss between A and B without the structure.

The head-loss due to the structure is thus equal to:

$$\Delta h_s = \Delta h_t - \Delta h_l \tag{3.16}$$

where Δh_t is the measured total head-loss between A and B for test series HLP0 to HLP4.

The minor head-loss coefficient due to the presence of the structure is calculated using the Eq. 3.17 (Idelcik, 1960):

$$R_* \geq 400 \ : \zeta = \frac{\Delta h_s}{\frac{\rho v^2}{2g}} \tag{3.17a}$$

$$R_* < 400 \ : \zeta_{R_*} = \frac{\Delta h_s}{\frac{\rho v^2}{2g}} \tag{3.17b}$$

where ρ is the density of water, and v the flow velocity. The calculation of R_*, the Reynolds number of the geotextile is based on the equation Eq. 3.18 (Idelcik, 1960):

$$R_* = \frac{v\delta_{mean}}{\nu} \tag{3.18}$$

where δ_{mean} is the average line width of the geotextile given in Table 3.3.

Since all the experimental results as presented in Fig. 3.15 and Appendix B corresponds to $R_* < 400$, the calculation of the head-loss coefficient of the structure ζ will be based on Eq. 3.17b. It is expressed as a function of the Reynolds head-loss coefficient by Eq. 3.19 (Idelcik, 1960):

$$\zeta = \frac{\zeta_{R_*}}{k_{R_*}} \tag{3.19}$$

where k_{R_*} is a coefficient given as a function of R_*. Appendix B provides the values of ζ calculated on the basis of Eq. 3.19 and the results provided in Fig. 3.15 for every configuration. The average value of ζ_{R_*} for each configuration with geotextile are given in Table 3.5:

Series/b [cm]	**2.5**	**5**	**7**	**10**
HLP1	0.1092	0.1218	0.1244	0.1333
HLP2	0.0177	0.0251	0.0286	0.0360
HLP3	0.0116	0.0218	0.0288	0.0306

Table 3.5.: Average values of the Reynolds head-loss coefficients of the structure with geotextile ζ_{R_*}

The results of the test series of Table 3.4 are presented in log-normal axis in Fig. 3.15 where the Reynolds minor head-loss coefficient of the structure is calculated as a function of the Reynolds number R_* of the structure.

It can be seen clearly that for a low porosity (P1), the effect of the structure width on the head-loss is minor. This is explained by the very low

ratio of the high porosity of the median element (B in Fig. 3.12b) compared to the porosity of the geotextile. However, when the porosity of the geotextile is high, the effect of the median element becomes significant (P1 compared to P2 and P3).

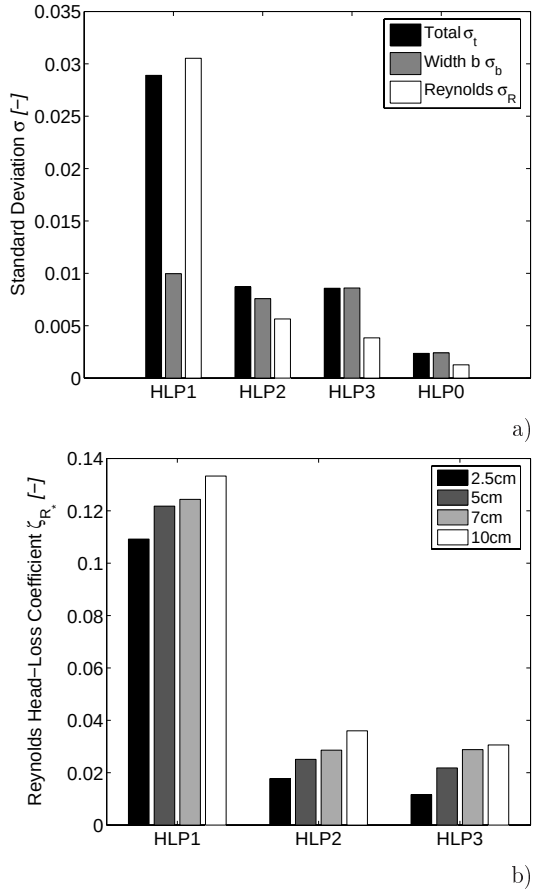

Figure 3.16.: (a) Standard deviation of the head-loss values for three main criteria; (b) Average Reynolds head-loss coefficient for the three configurations with geotextile

In order to separate the effects of the variation of the head-loss due to the increase of the Reynolds number R (of the flow) on one hand and the increase of the structure width on the other hand, the standard deviation for each

case is plotted for the four tests series in Fig. 3.16a. The following conclusions could be verified:

- For a very low porosity (i.e. P1), the increase of the Reynolds number results in significant variations in the structures' head-loss. For HLP1, the standard deviation of the head-loss on the basis of the Reynolds number is at least 6 times higher than the remaining series. This could be explained by the increase in the local drag coefficient due to the very small grid of P1. The increase of the drag coefficient results in a decrease of the flow velocities, and an increase of the minor head-loss coefficient ζ (see Eq. 3.17).
- The ratio of σ_b and σ_t is relevant for revealing the effect of the changing width of the structure on the standard deviation of the minor head-loss. It increases with the porosity of the structure. For P1, this ratio is 0.34. This means that the variation of the width does not influence significantly the minor head-loss of the structure. However, for P2 and P3 and P0 the ratio increases rapidly and tends toward 1.

The average minor head-loss coefficients for each case are calculated in Fig. 3.12b and Table 3.5. The influence of the presence of the geotextile could be clearly seen. The head-loss for HLP1 is at least 12 times higher compared to HLP0. However, when comparing HLP1 with HLP2 and HLP3, this ratio is almost equal to 2 and 4, respectively.

3.3.3. Model compatibility and comparison with prototype

The hydraulic response of above-described materials is compared to experimental results carried out with real brushwood fences at the *Franzius-Institut für Wasserbau und Küsteningenieurwesen* of the *Hannover University* in Germany. During the test a real model of brushwood fences (S1 configuration) is used having a fixed width of $b = 0.25\ m$. It was tested in a channel with a $0.98\ m$ width, $1\ m$ height and $22\ m$ length. Water levels are measured before and after the model for different flow values (von Lieberman et al., 1997).

In order to make a comparison between the tests carried out with a downscaled model and full scaled model, it is proposed to compare minor head-loss due to the presence of the structure as a function of the flow velocities during the tests (see Fig. 3.17). This comparison is found to be relevant since tests are done in two different flow conditions. For the downscaled model, the water flows in pressurized circular pipe, and for the full scaled model the water flows in a rectangular open channel.

It can be seen in Fig. 3.17 that the range of the head-loss due to the physical model covers the entire range of the head-loss due to the real full scaled model *(Hannover University)* and thus for similar flow velocities. This

proves that the response of the material used to construct the small model is comparable to the real material of the brushwood fences for almost the same hydraulic conditions. Unfortunately, no full scaled tests were carried at *(Hannover University)* out for different widths and porosities. Therefore, no further comparison could be undertaken at this level. However, the porosity of the real model is estimated to be comprised between $P1 = 0.16$ and $P2 = 0.36$ when comparing the corresponding values of the minor head-loss. The shape of the relation $\Delta h_s - V$ corresponds to a parabolic fit as proposed in Eq. 3.17. The values of ζ_{R_*} are given in Table 3.5.

On the basis of this analysis, it can be assumed that the response of the small scale-model using geotextile instead of tree branches is comparable to the one with real material. Further tests using the transmission coefficient should also be compared to real response in order to confirm this basic assumption. Section 4.3 shows the experimental results regarding the transmission coefficient of the model for a wide range of water level and proves that it has the same response as a real brushwood fence tested by Mai, Lieberman and Zimmermann (1999).

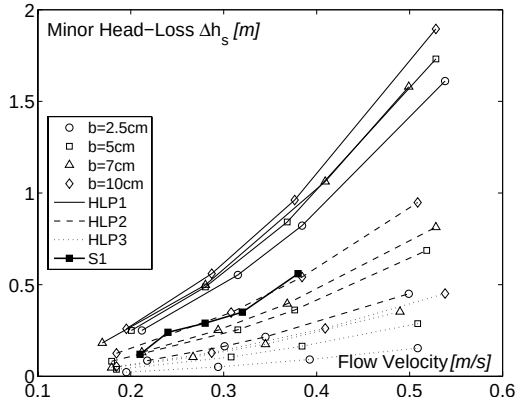

Figure 3.17.: Head-loss of the downscaled physical model of the structure compared to the head-loss of the S1 configuration for full scale experiments carried out at the Hannover University

3.4. Wave characteristics and testing procedures

This section will describe firstly the analysis procedure elaborated for wave measurements and analysis. This procedure is mainly based on data acquisition using LabView® and data analysis using MatLab®. Furthermore, the last two paragraphs describe the tests carried out successively with fixed and mobile bed in the wave tank

3.4.1. Incident, transmitted, and reflected waves

For each configuration tested, at least four arm lengths were considered, and for each one five different wave periods are generated (see Section 3.1.1). The duration of each signal acquisition is not less than 10 min. For each time interval, the following points are applied:

- The sampling frequency of each ultrasonic wave gauge in fixed to 20 Hz. Therefore, since the maximum frequency of the generated waves is almost 1.7 Hz (see Fig. 3.6), the sampling frequency is adequate. It is referred to the sampling theorem stipulating that in order to built an exact representation of the bandlimited signal, the sampling rate (or frequency) should be at least two times higher than the frequency of the original signal (Oppenheim et al., 1983).
- For each frequency, the acquisition time interval is fixed to 2 min. For monochromatic unidirectional waves, this duration is considered as sufficient to obtain a good representation of the signal corresponding to a single wave.
- Non-filtered results are saved in a six column matrix, each one corresponding to the complete signal provided by a single wave gauge.

Filtering of the rough signal

Before proceeding to the analysis of the wave signal, it appeared that using an ultrasonic wave gauge has one major disadvantage. In fact, when measuring the water level, the ultrasonic beam, in function of the distance of the gauge to the water surface, could be reflected away from the gauge, depending on the steepness of the measured wave. When the incoming signal is not entirely captured by the gauge, the measured distance could be very high or could tend to infinity. Such values, commonly called the outliers, should be disregarded or filtered before the calculation of the characteristic of sinusoidal wave signal.

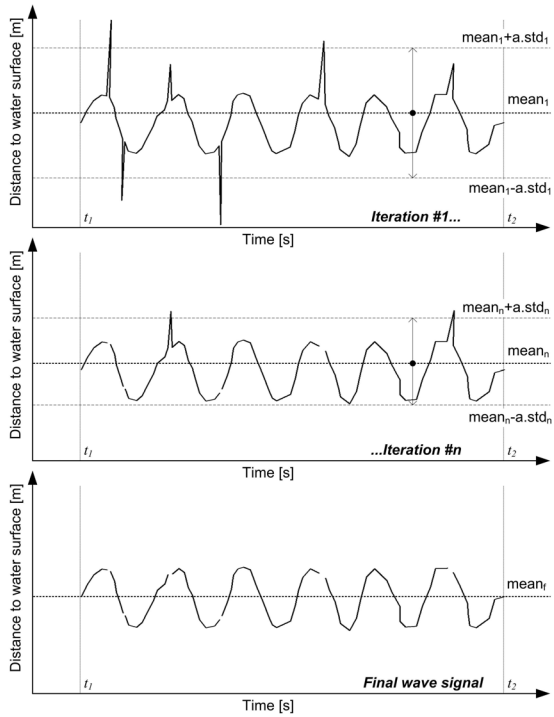

Figure 3.18.: Filtering process of the wave sinusoidal signal

The filtering process is described in Fig. 3.18. Firstly the mean distance z_{it} of the wave gauge to the water level corresponding to iteration number it is calculated using Eq. 3.20:

$$\bar{z_{it}} = \frac{1}{K} \sum_{i=1}^{K} z_i \tag{3.20}$$

where z_i is the instantaneous distance of the wave gauge to the water level, and K the number of measurements between time t_1 and t_2.

At each iteration the values of z_i comprised only in the interval $[z_{it} - a.\sigma_{it} \longrightarrow z_{it} + a.\sigma_{it}]$ are considered. The outliers are replaced by spaces in order to maintain the same time length of the signal. It has to be noted that a is a variable factor equal to 4 for the present filtering process and σ_{it} is the

standard deviation of the iteration number it, calculated as following:

$$\sigma_{it} = \sqrt{\frac{1}{K}\sum_{i=1}^{K}(z_i - \bar{z_{it}})^2} \tag{3.21}$$

The number of iteration varied following the outliers in each wave signal between 2 and 3. A schematic sample of the result is shown in Fig. 3.18 where the *Final wave signal* has a sinusoidal shape and maintaining the initial duration t_2-t_1.

Measuring wave characteristics

The calculation of wave heights are based on the filtered wave signal as described above. A statistical approach is used based on the calculation of the standard deviation as given in Eq. 3.21. Therefore, the wave height considered corresponds to the root mean square of height values and expressed by Eq. 3.22.

$$H_{rms} = 2\sqrt{2}\sigma_f \tag{3.22}$$

where σ_f is the standard deviation of the filtered final wave signal.

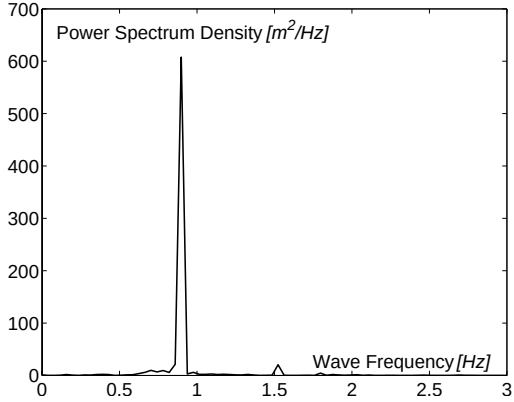

Figure 3.19.: Power spectrum of a single wave filtered signal, generated during experimental tests in the wave tank, corresponding to a wave period of $T = 1.25\ s$

The description of the regular monochromatic wave by the above mentioned statistical value is considered to be most adequate since it represents the total energy of the whole wave height distribution. Additionally, H_{rms} values are used in the numerical model Mike 21 EMS (see Section 6.1.3.

Therefore, since a comparison is to be made between physical and numerical modelling, this selection is the most appropriate.

The calculation of the frequency of the wave signal (see Fig. 3.19) is carried out by using the FFT function (Fast Fourier Transform) developed in MatLab© based on the numerical solution provided by Cooley and Tukey (1965). The Fast Fourier Transform is a widely-used method of extracting useful information from sampled signals. Since the wave signal obtained by the wave gauge is not continuous, the FFT is therefore based on the Discrete Fourier Transform DFT solutions.

To compute the DFT of a signal comprising 2400 samples, this would therefore requires an order of 6 millions calculations. The DFT is therefore an extremely numerically intensive procedure. The direct result of DFT is the power spectrum. For a given signal, the power spectrum (see Fig. 3.19) gives a plot of the portion of a signal's power (energy per unit time) falling within given frequency interval.

Concerning the measurement of the wave length using two consecutive wave gauges, it is based on the calculation of the period and the wave crest velocity between the two wave gauges. Knowing the distance $\Delta x = 30\ cm$ between the two gauges, and the time Δt elapsed between the passage of the wave crest at the two gauges, the wave length will be equal to Eq. 3.23:

$$L = T\frac{\Delta x}{\Delta t} \tag{3.23}$$

During the tests, a comparison was made between this calculations based on Eq. 3.23 and the equation of the wave length provided in Section 2.2.1 and showed good agreements.

Measuring incident and reflected waves

It has to be noted that the above described method for measuring wave characteristics provides the total wave height, more specifically for wave gauges P3 and P4 in Fig. 3.1, which is, in the present case, when a reflective structure is present, the combination of incident and reflected wave over the protection structure. Therefore, in order to separate the two waves a theoretical approach should be applied.

The method of Goda and Suzuki (1976) for the calculation of the reflected waves is commonly used in two-dimensional laboratory experiments, and it provides a valuable technique for examining wave reflection from beaches and coastal structures. The technique is both applicable to regular and irregular trains of waves and assumes that the gauges are placed on an horizontal bottom. Two simultaneous wave records are taken from two adjacent gauges. All the amplitudes of Fourier components are analyzed by the FFT technique that conduct to the calculation of the amplitude of superposed incident and reflected waves, then to the reflection coefficient.

A similar method using three spatially separated gauges for estimating of incident and reflected waves from synoptic time series recorded at the gauges is proposed by Mansard and Funke (1980). In this frequency domain method, spectral analysis of gauge pairs used to calculate incident and reflected wave energy and a noise signal. A least square procedure is used to minimize the noise signal for all three gauges. This frequency domain method concentrates on the phase differences between gauges, and it provides improved stability in the estimates and an increased range of frequency resolution with less sensibility to gauge spacing (compared to previous method). This method as well is a linear theory analysis, and assumes the gauges are placed on a flat bottom.

The two method described above are used for estimation of waves in a flat bottom. Although they were sometimes used for estimating reflected and incident wave in a sloping bottom, they are not considered for the present investigation. The methodology proposed for this purpose is more direct and simple as described in the three following points:

1. Measuring total wave heights during the experimental tests with the presence of the structure

↓

2. Measuring incident wave heights for the same conditions (wave maker adjustment, water depth) without the presence of the structure

↓

3. Calculating reflected wave heights for the similar conditions

The reflected wave equation over an obstacle, when added to the incident wave equation, changes the resulting total wave height but not the resulting wave length and period. Hence, the incident wave has the same wave length as the resulting wave (incident wave + reflected wave).

The transmission of wave period through the brushwood fences is not a major issue when incident waves are regular and considered to be monochromatic. During the tests carried out in the wave tank, waves are considered as regular and monochromatic. Hence, it is assumed that the period transmitted through the structure is equal to the incident wave period. However, changes in the transmission of wave period may occur for irregular incident waves (Mai, Lieberman and Zimmermann, 1999). Although only a slight changes is noticeable, the authors demonstrated that for mean wave periods, the transmission coefficient remains nearly constant and equal to 1.

3.4.2. Testing procedure of brushwood fences on fixed bed

The physical model of brushwood fences was first tested in the wave tank with a fixed bed. By covering the surrounding sandy bottom of the model by plates of ethernite, the sediment movement due to the interaction with incident and diffracted waves is prevented.

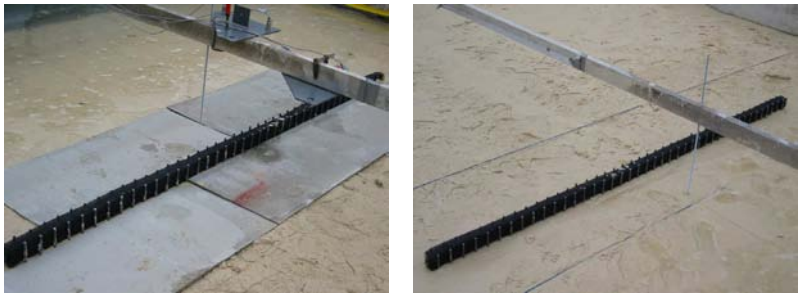

a) b)

Figure 3.20.: Testing brushwood fences in the wave tank with (a) fixed and (b) movable bed

The goal of tests with fixed bed (see Fig. 3.20a) is to evaluate the hydrodynamic response of brushwood fences without the effect of the bed load sediment transport. Based on field observations, the bed load sediment transport occurring in the vicinity of the structure has a significative impact on the transmitted waves through the porous media. Such impact is evaluated later on in Section 5.3.1. Therefore, fixed bed tests allow a better understanding of the wave-structure interaction, independent of any wave-sediment interaction such as formation of ripples, dunes, or even scour beside the structure. They are crucial for the calibration of numerical model where fixed bed is used.

Although the protective plates helped to prevent the bed load sediment transport, some important observations during tests were made:

- Due to specific bed load regimes, the sand is able to move very slowly over the ethernite plates. This implies a modification of the bottom form where the water surface is being measured (behind and after the structure). The measured transmission coefficient is influenced as a consequence
- A systemic "cleaning" of the plaques by removing the sand and re-arranging the bathymetry is crucial in order to create an almost constant bottom form for all the experiments

- Based on the above mentioned observations, it is important to check frequently the slope of the bottom crossectional profile in order to maintain its value as accurately as possible

Section 3.3.3 showed that the geotextile used in the physical modelling of brushwood fences gives sound results and able to reproduce a transmission coefficient comparable to that obtained by using real fascine. The physical model is implemented in the wave tank where incident and transmitted waves are measured. Different configurations of the fascine (varying heights h and porosities p) are tested for a wide range of wave heights (varying approximately between 0.01 m and 0.1 m) and wave periods (varying approximately between 0.5 s and 2 s).

Brushwood fences characteristics			Water depth d [cm]					
porosity p [-]	width b [cm]	height h [cm]	3.5	5	7	10	12.5	15
P1=0.16	5	7	•	•	•	•		
		10		•	•	•	•	
		12.5			•	•	•	•
P2=0.36	5	7	•	•	•	•		
		10		•	•	•	•	
		12.5			•	•	•	•
P3=0.62	5	7	•	•	•	•		
		10		•	•	•	•	
		12.5			•	•	•	•

Table 3.6.: Program of the experimental tests carried out in order to evaluate of the hydraulic performance of brushwood fences with a fixed bed under attack of perpendicular and regular waves

Table 3.6 shows the detailed experimental tests carried out in the wave tank of the Laboratory of Hydraulic Constructions. Based on results of Section 3.3.2, where it is proved that the width b of the physical model does not modify significantly the hydraulic response of the structure, all the tests are carried out with a fixed model width of $b = 5\ cm$. However, different heights h of the structure as well as the three selected model porosities are tested. Concerning the hydraulic conditions, seven different water levels are selected. Compared to the h, this would correspond to the structure in normal and most frequent water depths (emerged and submerged).

3.4.3. Testing procedure of brushwood fences on movable bed

After selecting the appropriate non-cohesive material for the movable bed experiments, it is possible to test brushwood fences, being sure that the bottom will have a response to sediment transport similar to reality.

However, the goal of the movable bed experiments is not to bring out solutions for real case studies. They are carried out in order to answer the following points:

- The variation of the transmission coefficient of brushwood fences in the presence of a movable bed
- The 3D effect of a single detached brushwood fences on the surrounding sand bottom regarding erosion and deposition, and its effect on the evolution of the shoreline
- The 3D effect of a double detached brushwood, separated by a varying gap on the surrounding sandy bottom regarding erosion and deposition, and its effect on the evolution of the shoreline

In principle, the response of a shoreline or bedload transport in the vicinity of shore protection measures is a very slow process. Thus the physical tests duration must be long enough to enable equilibrium conditions. In other terms, every test duration must be long enough so that the evolution of the shoreline and bottom sediment transport becomes almost constant. Therefore, as shown in Table 3.7, the long preliminary tests, helped to estimate the duration a test could take to reach its equilibrium state. In fact, a quasi-equilibrium state was reached after 15 *hours*.

During the long preliminary experiments, observations on the shoreline development are also used as a basis to decide whether equilibrium is reached. To this end, the following criteria were used (Ming and Chiew, 2000):

- At the breaker line, waves are breaking almost simultaneously and normally to the shoreline when the structure is not present
- At the shoreline, wave runup and rundown are perpendicular to the shoreline and do not cause any longshore currents
- There is no noticeable advancement and recession of the shoreline during at least $5h$

The experimental tests carried out with a movable bed are presented in Table 3.7. At first, the preliminary investigation aims to investigate the efficiency of the brushwood fences and their ability in initiating sand deposition. It is followed by a systematic study of the efficiency of a single detached brushwood fence in preventing shoreline erosion. Having a fixed length of 2 m, four distances from the shoreline are considered. In reference

to Section 2.5.1, the ratio B/S for the present experiments is inferior to 1. Therefore, only the formation of salient behind the detached structure is expected. The selection of this interval was based on the following:

- In reality, brushwood fences are not really used as breakwaters intended to induce the tombolo formation. They are actually constructed remotely from the shoreline and intended only to favor sand deposition in their leeside without inducing very high modification of the shoreline
- Since the bottom has a slope of 3%, after carrying some preliminary tests with $B/S >> 1$, it appeared that the incident waves are all breaking before reaching the structure. In fact, the water depth at the structure becomes very shallow (less than 3 cm), which is not really representative to the average conditions found in reality.

The effect of a single gap in a detached structure was investigated in the third experimental test series. Two gap values where considered and tested at different distances to the shoreline. Regular and identical wave characteristics were used during all the tests of both single and double structures. The model of the brushwood fences selected for the experiments used a movable bed is as follows:

- Height $h = 10\ cm$
- Porosity $p = 0.36$

During tests, ultrasonic gauges measured waves characteristics. For a single structure, waves are measured before and behind, and for double structure wave are measured approximately at the axis of the gap. Photos are taken in a regular way and small video sequences were produced to catch interesting phenomenon as wave breaking, wave diffraction, and ripples movement.

The initial (before each test) and the final (after stopping wave generation at the end of each test) bathymetry is to be measured each time. The goal of the two phases measurements is to obtain the same initial bathymetry for all the tests. Furthermore, the initial bottom slope is almost equal to the equilibrium slope corresponding to the selected grain diameter.

In order to reproduce the resulting shoreline accurately, the measurement resolution is very dense in the region R1 (see Fig. 3.21). In the cross-sectional direction of the wave tank, the resolution of R1 varies following the bathymetry changes between 10 and 15 cm. One section is measured every 25 cm. In the region R2, where the structure is located, measurement density remains the same in the cross-sectional direction and could decrease occasionally to 50 cm in the longitudinal direction when there are no significant bottom variations. The lowest measurement density is R3, where dx and dy are almost equal to 50 cm.

Table 3.7.: Experimental tests program defined for the evaluation of effect the brushwood fences on a movable bed for perpendicular incident regular waves

Group	Test Number	Duration [h]	H [m]	T [s]	B [m]	G [m]	S [m]	B/S [m]	h_b [m]
Preliminary investigation	CS1	53	0.055	1.20	-	-	-	-	
	CS2	48	0.055	1.20	1.00	-	1.00	1	
Single structure	SE	12	-	-	-	-	-	-	
	T1	10	0.035	1.16	2.00	-	2.00	1.00	0.040
	T2	10	0.037	1.16	2.00	-	3.00	0.67	0.063
	T3	15	0.040	1.16	2.00	-	3.50	0.57	0.073
	T4	15	0.041	1.16	2.00	-	4.00	0.50	0.084
	T5	15	0.042	1.16	2.00	-	4.50	0.44	0.095
Double structures	T6	15	0.036	1.16	1.00	0.25	2.50	0.050	
	T7	15	0.036	1.16	1.00	0.50	2.50	0.050	
	T8	15	0.040	1.16	1.00	0.25	3.50	0.073	
	T9	15	0.040	1.16	1.00	0.50	3.50	0.073	
	T10	15	0.042	1.16	1.00	0.25	4.50	0.095	
	T11	15	0.042	1.16	1.00	0.50	4.50	0.095	

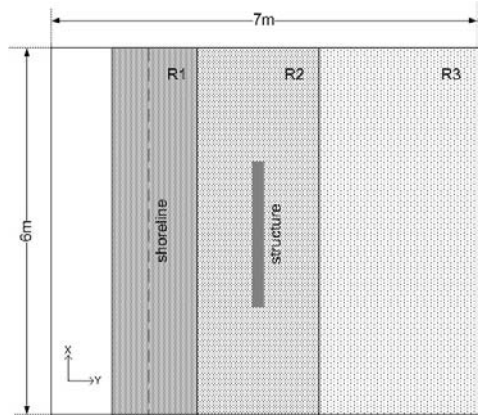

Figure 3.21.: Three different resolutions for the measurement of the bathymetry after each test: R1=[$dx = 10$ *to* 15 *cm*, $dy = 25$ *cm*]; R2=[$dx = 10$ *to* 25 *cm*, $dy = 25$ *to* 50 *cm*]; R3=[$dx = 25$ *to* 50 *cm*, $dy = 50$ *cm*]

It has to be mentioned that the above region definition provides a general description of the measurement density. However, this could be increased as a function as any eventual significant erosion or deposition. A direct measurement of the resulting shoreline is also carried out based on its distance to the rear wall of the wave tank.

The bathymetric data of each test comprises a matrix of three columns, the first two are the abscise X and ordinate Y related to the origin of the wave tank and the third column corresponds to the elevation. A grid is afterwards generated on the basis of this matrix in order to obtain a square matrix where additional points could be added by interpolation.

The detailed steps of the procedure for each run are as follows:

- Molding the beach in order to create a 2% slope based on marks put over the side walls
- Digging holes and securing the model of brushwood fences at the proper location
- Measuring the bathymetry and taking photos
- Filling the wave tank to the proper water level
- Putting in place the wave gauges
- Starting the wave generator with the adequate tuning
- Starting the program LabView© for wave measurements during the entire period of the run
- At the end of the run, shutting down the wave generator and lowering the water level
- Measuring the final bathymetry and taking photos

- Removing the model of brushwood fences

4. Analysis and results of experimental tests with brushwood fences on a fixed bed

The experiments in the wave tank with fixed bed are carried out according to the description in Section 3.4.2. The goal of this chapter is to define the interaction of incident regular waves with the brushwood fences model (scale of 1 : 10). The interaction is mainly described by the transmission coefficient K_T. This allows a better understanding of the effect of the variation of many variables on this coefficient. They are related to the local hydraulic and hydrodynamic conditions (i.e. water depth at the structure and wave height and period) or to the characteristics of the structure itself (i.e. its porosity and height). Therefore, the objectives of this chapter are the following:

- To provide a detailed analysis of the effect of the main dimensionless variables on the transmission coefficient of the brushwood fences
- To propose an empirical relationship for the calculation of the transmission coefficient

4.1. Main results on the interaction of brushwood fences with regular waves

In the following sections, the results concern mainly the transmission coefficient of a brushwood fence obtained by the analysis of the effect of different variables. They are based on regular wave measurements before and behind the obstacle. The wave heights are measured by two couples of wave gauges at B and C as shown in Fig. 3.1. Concerning the investigation of the selected dimensionless variables, it has to be noted the following:

- Its main goal is to define the general trends relating the dimensionless variables to the transmission coefficient. These trends are only used to understand the effect of the selected variable on the transmission coefficient. They are not to be considered as a final result for the calculation of the efficiency of the brushwood fences

- Each investigation for each variable does not separate the effect of others. Therefore, the rough results presented for each variable could show very scattered data. These results are however intermediate ones. Their only goal is to identify the best trend describing the relationship of the variable and the transmission coefficient
- The relationship of the transmission coefficient with all the variables grouped together is the only way to obtain more accurate and relevant results. However, since this relationship is still unknown, it is important to identify separately the effect (and trend) of each variable. The second stage would be to group all the variables together and to take into consideration all these effects

4.1.1. Effect of the freeboard of the structure R_c/H_i

The relative freeboard as described in Eq. 2.27a, is the first important dimensionless variable that relates incident wave heights to the structure height and water depth (the freeboard, R_c, is the difference of these two variables). It has been used by many researcher in several applications related to breakwater efficiency in damping incoming waves such as Mai, Ohle and Daemrich (1999), Daemrich et al. (2001) and Calabrese et al. (2003). They included the relative freeboard in the calculation of the transmission coefficient.

The experimental results for the height $h = 10\ cm$ are plotted in Fig. 4.1. Results of $h = 7$ and $12.5\ cm$ are in Appendix D. It can be seen from the curve fitting plotted for different porosities that the transmission coefficient, $K_T = H_{transmitted}/H_{incident}$, decreases almost linearly when the relative freeboard, R_c/H_i increases ($H_i = H_{rms}$). The use of H_{rms} for the incident waves was found to be most convenient since every generated wave is considered monochromatic in addition to the fact that for the numerical modelling purpose, the boundary condition of waves depends on the "$r$oot $m$ean $s$quare values" of the incoming wave heights.

When the relative freeboard is lower than -1 (a negative value indicates that the structure is totally submerged), K_T seems to reach an upper constant value. This indicates that the structure looses rapidly the efficiency in wave damping when the water depth is higher than the structure height. Independently of the structure height, the maximum values of K_T when the structure is submerged are comprised between 0.8 and 1.1 (with respect to the prediction bounds). For R_c/H_i higher than 1 and when the structure is emerging ($R_c \geq 0$), K_T reaches too almost a constant value.

Fig. 4.1 reveals that a low porosity of brushwood fences increases wave damping. Nevertheless, it does not seem to increase proportionally when the porosity decreases. This could be seen in a reference to the position of the curves related each to a different porosity.

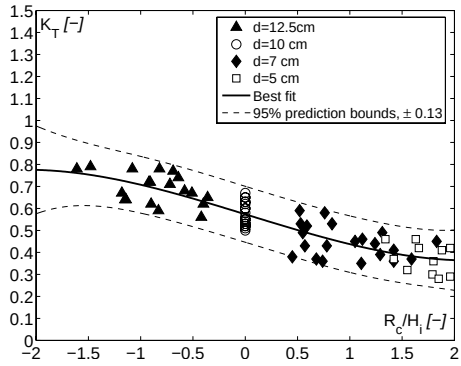

a)

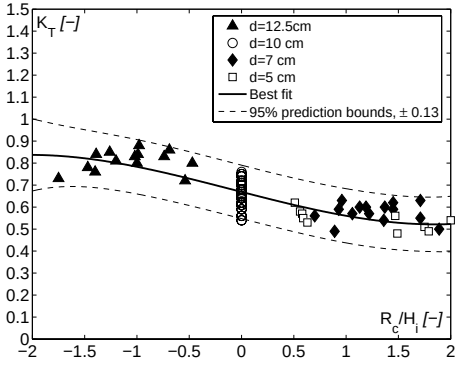

b)

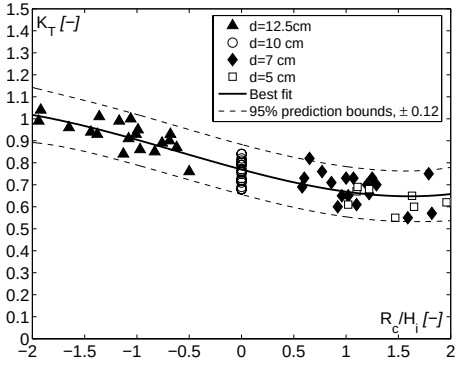

c)

Figure 4.1.: Transmission coefficient K_T for the height $h = 10\ cm$ of the brushwood fences calculated as a function of the relative freeboard: a) $p = 0.16$; b) $p = 0.36$; c) $p = 0.62$

The cubic fitting proposed in Fig. 4.1 is described by the following Eq. 4.1:

$$K_T = a\frac{{R_c}^3}{H_i} + b\frac{{R_c}^2}{H_i} - c\frac{R_c}{H_i} + d \tag{4.1}$$

The values of the variables a to d depend mostly on the porosities of the structure and applicable only for $-2 \leq R_c/H_i \leq 2$. They are given in Table 4.1.

porosity	a	b	c	d	bounds
0.62	0.01	0.02	0.12	0.76	$\pm$0.12
0.36	0.01	0.01	0.12	0.67	$\pm$0.13
0.16	0.01	0	0.14	0.57	$\pm$0.13

Table 4.1.: Average values of the cubic fitting variables in Eq. 4.1 for each porosity and $h = 10\ cm$

The scattered wave data as can be seen in Fig. 4.1 could hardly be improved since they are essentially the consequence of small experimental scale. In addition, such values correspond to the results for different wave period. This could be detrimental for the accuracy of the curve fitting since they suggest that the wave period have no effect on the transmission coefficient, which is probably not the case. Another reason for the scattering could be related to wave measurements gauges. In fact, when the waves are very steep, the reflected ultrasonic signal reaches partially the gauges.

The selection of the cubic fitting appeared to be more adequate in the present case than the linear relationship as proposed by Mai, Lieberman and Zimmermann (1999). The measured data clearly indicate that the transmission coefficient tends almost to a constant value for $R_c/H_i \geq 1$ and $R_c/H_i \leq -1$. Therefore, a linear fitting approach was disregarded. Furthermore, for a cubic fitting, the 95% prediction bounds are the lowest. However, when this fitting is near to the boundary conditions of the experimental tests, the prediction bounds increase slightly (see Fig. 4.1 when $R_c/H_i = 2$). This is mainly due the lack of data at these boundaries.

The three cubic fitting curves are plotted in Fig. 4.2 for the interval $-2 \leq R_c/H_i \leq 2$. The shape of the curves shows the effect of a variable porosity on the transmission coefficient. The difference between each curve is higher when the structure is emerging ($R_c \geq 0$) in comparison to a totally submerged situation. This indicates that the porosity gradually loses its importance when the structure is totally submerged. This effect on wave transmission becomes however more important when the water depth decreases in a totally emerging situation. A detailed analysis of its effect is provided is Section 4.2.1.

Hence, the cubic fitting of the entire collected data suggests the following two observations:

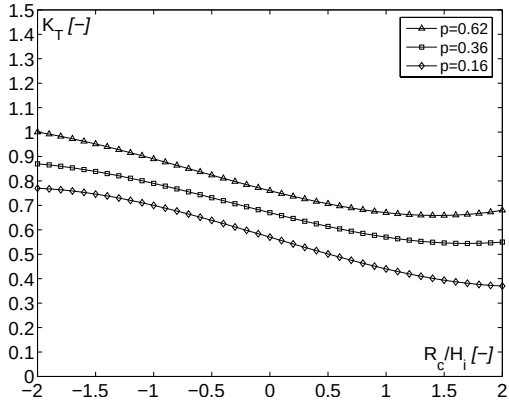

Figure 4.2.: Transmission coefficient K_T calculated as a function of the relative freeboard R_c/H_i for the three tested porosities according to Eq. 4.1 and Table 4.1 for $h = 10\ cm$

- The structure response to the incoming wave is different according to the water depth. When the structure is totally submerged, K_T seems to vary differently as a function of the relative freeboard in comparison to the condition when the structure is emerging. This indicates that a more adequate data treatment would be to separate the conditions related to the two water depths
- Additionally the effect of the structure height seems to play a minor role (see the difference between the heights at Appendix D). This should be proved by adequate selection of dimensionless variables. The effect of the structure height will be shown later in Section 4.1.2

In reference to the first observation, a separate analysis is suggested in the next sections where two series of data are considered. The first series is the 's' series, when the structure is completely submerged, and the second is the 'e' series, when the structure emerges.

In order to compare the present results with the experimental results carried out by Mai, Lieberman and Zimmermann (1999), a linear fitting proposed in Fig. 4.3 is described by the following Eq. 4.2:

$$K_T = -a\frac{R_c}{H_i} + b \tag{4.2}$$

The values of the variables a and b depend mostly on the porosity of the structure and are only applicable for $-2 \leq R_c/H_i \leq 2$. They are given in Table 4.2.

porosity	a	b
0.62	-0.10	0.79
0.36	-0.09	0.67
0.16	-0.12	0.57

Table 4.2.: Values of the linear fitting variables in Eq. 4.2 for the three different porosities and $h = 10\ cm$

The three linear relationships between K_T and R_c/H_i of the interval $-2 \leq R_c/H_i \leq 2$ are plotted in Fig. 4.3. In fact, they almost correspond to the cubic fitting in this same interval as shown in Fig. 4.2. However, some difference in the boundary values are noticed, mainly for the highest porosity of 0.62 where the transmission coefficient in the linear fitting is overestimated.

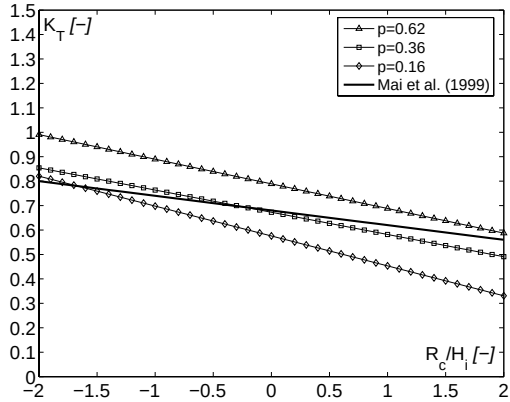

Figure 4.3.: Transmission coefficient K_T calculated as a function of the relative freeboard R_c/H_i for the three different porosities and $h = 10\ cm$ compared to the results of Mai, Lieberman and Zimmermann (1999)

The comparison shows that the values of a (the slope) for the three porosities are very close, however the main difference is in the values of b. A similar and direct linear relationship between the transmission coefficient of the brushwood fences and the relative freeboard was proposed by Mai, Lieberman and Zimmermann (1999) in Eq. 2.29 in Section 2.4.2. It is compared in Fig. 4.3 with the experimental results of this study. Although the comparison shows a difference in the slopes, the average values of K_T are quite similar. The difference in slopes is mainly related to the fact that

Eq. 2.29 was developed without taking into consideration the separation between submerged and emerging situations.

Similar linear relationship was proposed by D'Angremond et al. (1996) for permeable breakwater. The authors suggested to calculate the transmission coefficient using the following Eq. 4.3 (see Section 2.4.2 for further details):

$$K_T = -a\frac{R_c}{H_s} + B \tag{4.3}$$

where the term B is calculated as a function of the width and the face slope of the breakwater. The width is the variable that determines the permeability of the structure.

Since in the present case, as shown in Section 3.3.2, the width of the physical model is not really representative of the permeability of structure, it is assumed that B is calculated as a function of the geometrical porosity of the physical model. This suggestion is confirmed when comparing the values of a and b in Table 4.2.

4.1.2. Effect of the height of the structure h/H_i

Figs. D.4, D.5, and D.6 depict K_T as a function of the relative height of the structure (h/H_i) for the three porosities, 0.16, 0.36, and 0.62, respectively. The water depth d for each height and porosity is given by the value of the relative freeboard of the structure denoted as h/R_c expressed as a function of its height h. The effect of the height of the brushwood fences on the transmission coefficient is investigated for every porosity. A linear best fit of the results is proposed in Fig. 4.4. Results are separated on the basis of the immersion condition of the structure. This direct relationship considered between the transmission coefficient K_T and the structure height h/Hi follows Eq. 4.4:

$$K_T = a\frac{h}{H_i} + b \tag{4.4}$$

Since the structure has different behavior depending on its immersion state (submerging or emerging), as proved in Section 4.1.1, the analysis of the effect of the relative structure height on the transmission coefficient is carried out separately. Therefore, two sets for the variables a and b are proposed. The values are given in Table 4.3:

The highest values of K_T are obtained when the structure in completely submerged. It can be concluded that the efficiency of the brushwood fences decreases when the structure is totally submerged. Moreover, the effect of the porosity in such conditions is less significant (slopes of the curves of Fig. 4.4b are lower than the slopes in Fig. 4.4a).

series 's'			series 'e'	
porosity	a	b	a	b
0.62	0.01	0.69	0.001	0.85
0.36	0.02	0.53	0.009	0.73
0.16	0.04	0.30	0.029	0.52

Table 4.3.: Average values of the variables corresponding to the linear fitting in Eq. 4.4 for each porosity for series 's' and 'e'

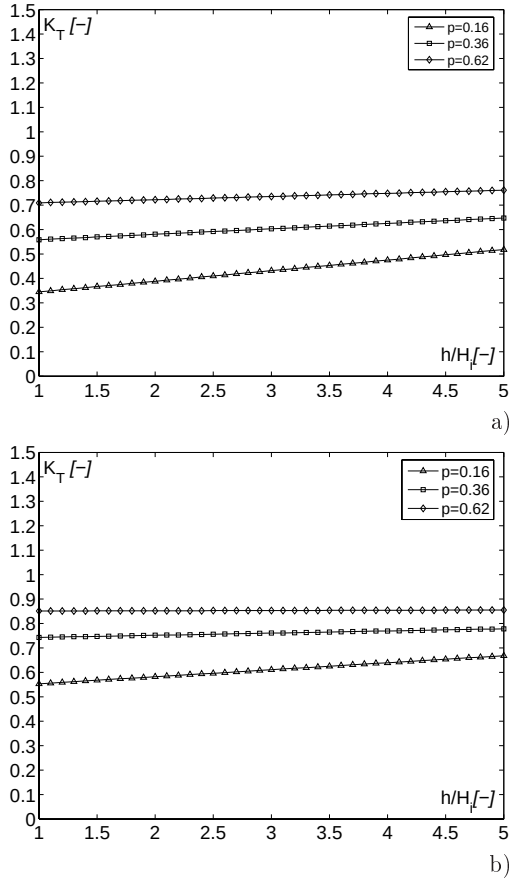

Figure 4.4.: Transmission coefficient K_T calculated as a function of the relative height h/H_i of the structure for different porosities: (a) $1 \leq h/R_c \leq 5$; (b) $-5 < h/R_c \leq 1$

The results show that the height of the structure for each case (emerging or submerged structure) has relatively a small effect on the wave transmission. This can be seen for instance in Fig. 4.4. For a porosity $p = 0.62$ the average value of K_T is 0.75 for $R_c \geq 0$ and 0.85 for $R_c \leq 0$. For the porosity of 0.36, the values are equal to 0.60 and 0.78, respectively. They are equal to 0.42 and 0.61 for the porosity of 0.16.

In Figs. 4.4a and 4.4b the transmission coefficient is given as a function of the structure relative height for both cases, $R_c \geq 0$ and $R_c \leq 0$. At first sight, they prove that the impact of the structure height is less significant than the impact of the sign of R_c of the transmission coefficient. In fact, the positive slopes of the linear relationships appear to be very small. Such observation suggests that a decreasing wave height or an increasing structure height does not really influence the rate of the transmitted waves, for each water level domain.

Disregarding the effect of the structure's relative height, Figs. 4.4a and 4.4b show that when the porosity is almost quadrupled, the transmission coefficient does not increase proportionally. For the interval $R_c \geq 0$ (see Fig. 4.4a), K_T increases on average by almost 30%, and for interval $R_c \leq 0$ (see Fig. 4.4b), K_T increases on average by almost 25%. This result implies that the effect of porosity is slightly higher when the brushwood fences emerge than for a completely submerged situation. It also implies that its variation is not directly proportional to the variation of K_T. In addition, Fig. 4.4b shows that the variation of wave heights has a larger influence on K_T when the structure emerges. This can be seen by comparing the average slopes of the three porosities for each domain (equal to 0.039 for $R_c \geq 0$ and 0.026 for $R_c \leq 0$).

4.1.3. Effect of the wave number kd

The wave number k as explained in Section 2.2.2 depends on the incoming wave length. Since the protection structure is located normally in an intermediate water depth or a shallow region, the wave length depends on the incoming wave period. Therefore, when calculating the wave number, the influence of the wave period on the transmission coefficient is taken into account. The relative dimensionless wave number as proposed for instance in Section 2.4.1 by Sollitt and Cross (1976), Sulisz (1985), Ting et al. (2004), is the product of the wave number k and the water depth d where the incoming waves are being measured.

The transmission coefficient has been calculated as a function of kd for different structure heights and porosities and depicted in Fig. D.7. The results show that the wave transmission remains almost constant when the wave number increases (when R_c is positive). It has to be noted, as mentioned in Section 4.1.1, that the water depth has less influence on the

transmission coefficient especially when the structure is emerging. The trends for a submerged structure are showed in Fig. 4.5. The influence of kd on the transmission coefficient could be seen. This linear fitting is given by the following Eq. 4.5:

$$K_T = akd + b \tag{4.5}$$

The values of the variables a and b depend mostly on the porosity of the structure and are applicable only for $R_c \leq 0$ and when $0.4 \leq kd \leq 1.4$ (approximately). They are given in Table 4.4:

series 's'			series 'e'
porosity	a	b	K_T
0.62	0.865	-0.01	0.75
0.36	0.06	0.73	0.65
0.16	0.17	0.48	0.41

Table 4.4.: Average values of the variables corresponding to the linear fitting in Eq. 4.5 for each porosity for series 's' and the transmission coefficient K_T for series 'e'

Considering the series 'e' (structure emerging), the transmission coefficient tends to a constant values as given in Table 4.4.

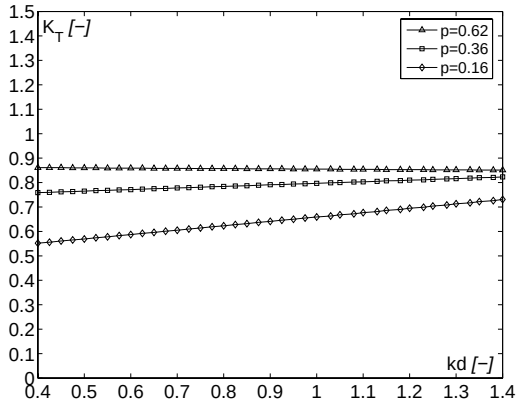

Figure 4.5.: Transmission coefficient K_T calculated as a function of the wave number kd for the three porosities and when the structure is totally submerged according to Eq. 4.5 and Table 4.4

Sollitt and Cross (1976) demonstrated the effect of kd on wave transmission through porous media. They found that for an increasing

wave number, the transmission coefficient decreases rapidly. However, for a structure where the width has very negligible effect on the porosity, Ting et al. (2004) demonstrated that the transmission coefficient tends to increase very slowly with kd. Therefore, the effect of the width in relation to the porosity of the structure contributes significantly to the influence of kd on K_T. In the present case, where the porosity of the brushwood fences plays a major role, the results show a convergence with the results of Ting et al. (2004). Moreover, when the porosity is very low (see $p = 0.16$ in Fig. 4.5), the effect of the wave number becomes higher compared to higher porosities (slopes for $p = 0.36$ and $p = 0.62$ are very low).

4.1.4. Effect of the wave steepness H_i/gT^2

The variation of K_T with wave steepness H_i/gT^2 for different structure heights and porosities is investigated in this section. This form of wave steepness has been used by many researchers, for instance Herbich (1990), Rao et al. (1999). In fact, it is a direct form of wave steepness since it does not use the water depth in order to calculate the wave length (see Section 2.2).

The rough results are provided in Fig. D.8. The general trends are given in Fig. 4.6. The results shows that K_T decreases as H_i/gT^2 increases. This agrees as well with the findings of the researchers mentioned above. The decreasing trend of K_T when H_i/gT^2 increases, can be explained by considering the water particle motions. As the wave steepness increases, the wave frequency increases as well, resulting in an increase of water particle velocity and acceleration. When a wave reaches the porous structure, the water particle velocity and acceleration suddenly change, causing reduction in energy due to the turbulence produced by the sudden change in the water particle motion. Hence, the steeper the wave, the more intense is the turbulence, and the greater the loss, resulting in lower K_T.

The results of the evolution of K_T as a function of the wave steepness for the lowest porosity of 0.16 confirm the above mentioned observations (see Fig. D.8e1, e2, e3 and 4.6a). In fact, when the porosity is very low, the energy reduction increases rapidly with wave frequency due to the increase of the drag coefficient. Section 3.3.2 provides a thorough explanation describing this phenomenon.

The linear fitting used in Fig. 4.6 is given by Eq. 4.6:

$$K_T = a\frac{H_i}{gT^2} + b \tag{4.6}$$

The values of the variables a and b depend mostly on the porosities of the structure and applicable when $0 < H_i/gT^2 < 0.008$ (approximately). They are given in Table 4.4.

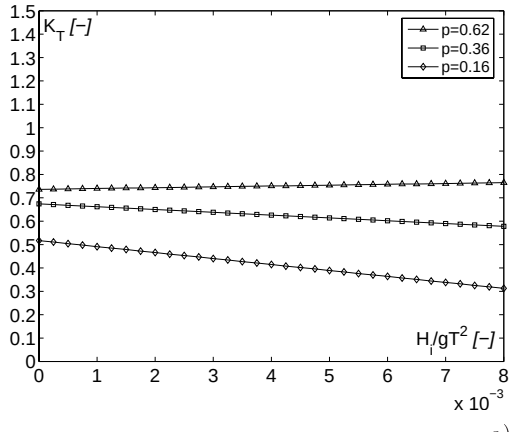

a)

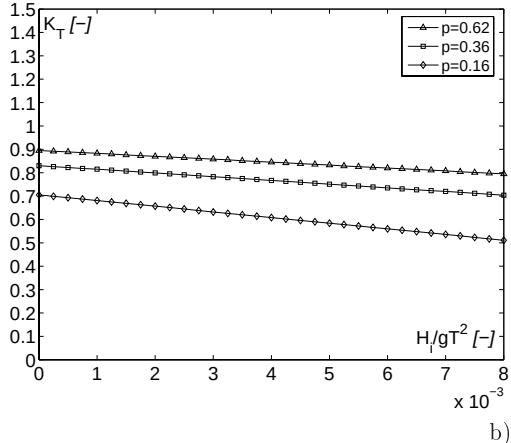

b)

Figure 4.6.: Transmission coefficient K_T calculated as a function of wave steepness H_i/gT^2 for different porosities: (a) $R_c \geq 0$; (b) $R_c \leq 0$

series 's'			series 'e'	
porosity	a	b	a	b
0.62	-12.53	0.89	3.59	0.736
0.36	-15.83	0.83	-12.05	0.674
0.16	-24.21	0.70	-25.55	0.517

Table 4.5.: Average values of the linear fitting variables in Eq. 4.6 for each porosity for series 's' and 'e'

4.2. Behavior and efficiency of the brushwood fences

The analysis of wave transmission through the structure allows on one hand the identification of the most important dimensionless variables when estimating its efficiency. On the other hand, the behavior of the structure when these variables vary can be better understood. Three major conclusions can be derived:

- The efficiency of the structure regarding its transmission coefficient is not the same for the two separate cases related to its immersion condition. Section 4.1 demonstrated that the porous structure has a different behaviors when it is completely submerged in comparison to the condition when the structure emerges.
- Figs. 4.4, 4.5, and 4.6 demonstrate that low porosities have relatively greater influence on the efficiency of the structure with changing hydrodynamics and water level conditions. This could be seen when comparing the absolute values of the slopes of the linear relationships for each porosity
- For both signs of R_c the structure height has little influence. This could be seen in Fig. 4.4 where the slopes of the linear relationship for both conditions are very low in comparison for instance to the slopes of Fig. 4.3 where they are at least 6 times higher
- On the basis of the findings in Section. 4.1.4, the effect of the wave period is to be taken into consideration. The wave period is therefore related to the equation of the wave steepness considered in this section

4.2.1. Influence of the porosity on waves transmission

The porosity of the brushwood fences seems to have a significant influence on its efficiency regarding the transmission coefficient. Although every important dimensionless variable has been analyzed in Section 4.1, the direct influence on the porosity has not yet been identified. Therefore, the aim of this section is to understand the influence of the porosity on wave transmission using the three different porosities considered during the experimental tests.

A direct relationship between K_T and p is proposed in Fig. 4.7 for the two domains, $R_c \geq 0$ in Fig. 4.7a and $R_c \leq 0$ in Fig. 4.7b. In each domain the values of K_T are plotted for each porosity and each structure height. Three straightforward conclusions can be given:

- The average values of K_T for each porosity are different in each domain.
- The values of K_T for each structure height are spread over the same interval for each porosity. This confirms the observations in Section 4.1.2 were it was concluded that the structure height does not really play a major role in the rate of waves transmission

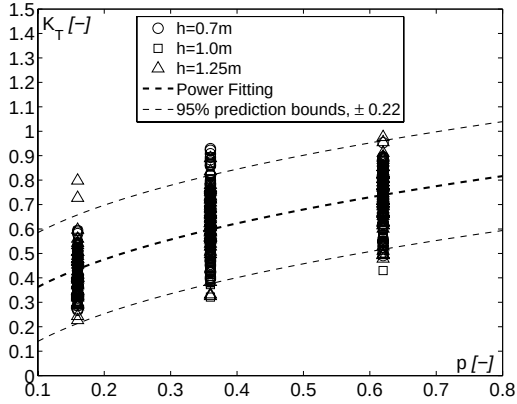

Figure 4.7.: Transmission coefficient K_T calculated as a function of the porosity of the structure for different structure heights: (a) $R_c \geq 0$; (b)$R_c \leq 0$

- The increase of K_T is not proportional to the increase of the porosity of the structure. As shows for instance Fig. 4.7a, when p is multiplied by almost 4 ($p = 0.16/p = 0.62$) the transmission coefficient is multiplied by almost 2 ($K^{ave}_{T,p=0.62}/K^{ave}_{T,p=0.16}$).

In order to evaluate best the trends describing the relationship between K_T and p, several fitting curves are tested. The power fitting corresponds to the highest correlation factor and lowest 95% prediction bounds as shown in Fig. 4.7 according to Eq. 4.7:

$$K_T = a(p)^b \tag{4.7}$$

where a and b are variables given in Table 4.6.

series 's'		series 'e'	
a	b	a	b
0.865	0.172	0.22	0.356

Table 4.6.: Average values of the power fitting variables in Eq. 4.7 for series 's' and 'e'

This relationship is similar to Eq. 2.28 where D'Angremond et al. (1996) proposed a power relationship for the width of the structure. It has to be noted that in the present case the porosity of the structure replaces to some extent its width.

On the basis of the results of this section concerning the effect of the porosity on wave transmission and Sections 4.1.1 to 4.1.4, it may be concluded that the transmission coefficient K_T is appropriately estimated as a function of (see Eq. 4.8):

- The relative freeboard of the structure R_c/H_i with a polynomial relationship (2^{nd} or 3^{th} degree) in order to take into account the difference behavior of the structure regarding its immersion state
- the steepness of incident waves H_i/gT^2 with a linear (supposedly) relationship
- the porosity of the structure p with a non-linear (power) relationship

$$K_T = f(R_c/Hi; H_i/gT^2; p) \tag{4.8}$$

Similar dependences were found by Stamos and Hajj (2001a). Based also on experimental analysis, the authors showed additionally that the transmission and dissipation coefficient as defined in Section 2.4.1 have the same relationships. In the following sections, a more detailed quantitative evaluation of the function f is proposed. This function will have a non-linear form. In the next Section 4.2.2 a short description of the mathematical solution of the non-linear system of equations is provided.

4.2.2. Gauss-Newton algorithm for solving non-linear equations

The "Gauss-Newton algorithm" is used to solve nonlinear least squares problems. It is a modification of "Newton's method" that does not use second derivatives. It provides a numerical analysis solution to the problem of minimizing a sum of squares of several, generally nonlinear functions that depend on a common set of parameters. This minimization problem arises especially in least squares, curve fitting nonlinear programming.

Given m functions $f_1, ..., f_m$ of n parameters $p_1, ..., p_n$ with $m \geq n$, the method proposes to minimize the following sum in Eq. 4.9

$$S(p) = \sum_{i=1}^{m} (f_i(p))^2 \tag{4.9}$$

where, p stands for the vector $[p_1, ..., p_n]$

The 'Gauss-Newton algorithm' suggests an iterative procedure. This means that an initial guess for the parameter vector p, which is called p^0, has to be made. Subsequent guesses p^k for the parameter vector are then produced by the recurrence relation in the Eq. 4.10:

$$p^{k+1} = p^k - (J_f(p^k) J_f(p^k)^T)^{-1} J_f(p^k) f(p^k) \tag{4.10}$$

where $f = (f_1, ..., f_m)$ and $J_f(p)$ denotes the Jacobian of f and p. It has to be noted that the matrix inverse in this calculation is never calculated explicitly in practice. Instead, Eq. 4.11 is used:

$$p^{k+1} = p^k + \delta^k \tag{4.11}$$

where δ^k is computed by solving the linear system in Eq. 4.12:

$$J_f(p^k) J_f(p^k)^T \delta^k = -J_f(p^k) f(p^k) \tag{4.12}$$

The calculations in the following sections is based in the "Gauss-Newton algorithm". The initial guess parameters are inspired by the values proposed by D'Angremond et al. (1996) and Mai, Lieberman and Zimmermann (1999) in Section 2.4.2 and by the fitting results of R_c/H_i, H_i/gT^2, and p found in Section 4.1.1, 4.1.4, and 4.2.1, respectively.

In the following Section 4.2.3, the parameter $[p_1, ..., p_n]$ will be the variables associated with the measured values of each dimensionless coefficient as described in Section 4.2.1. The functions $f = (f_1, ..., f_m)$ will be associated each with the experimental tests results of K_T as a function of this dimensionless parameters.

4.2.3. Empirical relationship for the transmission coefficient of the brushwood fences

The proposed non-linear relationship between K_T and the variables as defined in Eq. 4.8 is given Eq. 4.13:

$$K_{T,f} = \beta_1 \, (\frac{R_c}{H_i})^2 + \beta_2 \, \frac{R_c}{H_i} + \beta_3 \, p^{\,\beta_4} + \beta_5 \, \frac{H_i}{gT^2} \tag{4.13}$$

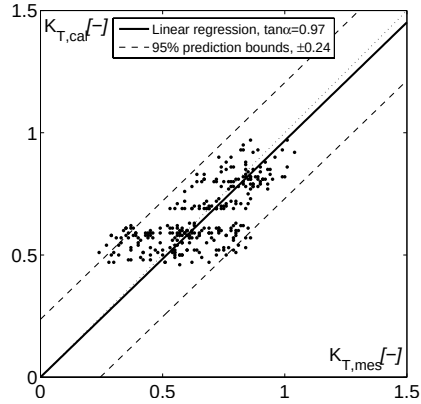

Figure 4.8.: Comparison between measured and calculated transmission coefficients K_T following Eq. 4.13

The "Gauss-Newton algorithm" was able to solve more than 500 non-linear equations where K_T, R_c/H_i, and H_i/gT^2 are provided by the results of the experimental tests carried out using the three selected porosities. Moreover, the best correlation corresponded to the Eq. 4.13 has a value of 0.72 with a 95% prediction bounds of ± 0.24 and a linear regression $tan\alpha = 0.97$ (see Fig. 4.8). The variables β_i for the equation are given in Table 4.7:

	β_1	β_2	β_3	β_4	β_5
Eq. 4.13	0.01	-0.11	0.69	-0.04	-12.40

Table 4.7.: Parameters of the empirical relationship for the transmission coefficient of the brushwood fences

In the following section, some selected results of this relationship are presented. Further explanation concerning the boundary conditions are given in Section 4.3.

4.3. Concluding remarks and discussion on boundary conditions

The effect of the downscaled brushwood fences model of 1 : 10 has been investigated in a wave tank under several hydrodynamic conditions. Using three different porosities covering a large range as it could be found in reality, the transmission coefficient of three heights of the structure has been measured for six water levels each. Incoming wave heights and periods generated in the wave tank were close to prototype conditions.

The response of the structure regarding the transmission coefficient has been evaluated using five dimensionless variables: 1) the relative freeboard of the structure R_c/H_i, 2) its relative height h/H_i, 3) the relative wave number kd, 4) the wave steepness H_i/gT^2, and finally 5) the porosity of the structure p.

At the first stage, an investigation was carried out using the direct results of the experimental tests in order to understand and evaluate qualitatively and quasi-quantitatively the effect of each dimensionless variable on wave transmission. This investigation revealed the following points:

- The response of the structure is different in relation to its immersion condition. When the structure is submerged, every dimensionless variable had a differentiated effect on the transmission coefficient in comparison to the condition when the structure emerges
- The relative freeboard, wave steepness and the porosity played a major role in the response of the structure regarding wave damping. The relative height and wave number were not significant and were disregarded. Their effect is included in the relative freeboard and wave steepness
- A non-linear relationship has to be considered when the effects of the relative freeboard and the porosity of the structure on the transmission coefficient are to be evaluated. The wave steepness seems to have a linear influence

At a second stage, a non-linear relationship between K_T and the selected dimensionless variables was proposed and evaluated for the domain $-2 \leq R_c/H_i \leq 2$. This fundamental quantitative analysis required the use of "Gauss-Newton algorithm" to solve the systems resulting from these relationships and composed each of hundreds of non-linear equations, each equation corresponding to a single experimental result.

The method showed a good convergence of the results and suggested an optimal relationship with good correlations. The proposed relationship in Eq. 4.13 could be used under three constraints:

- The relative freeboard R_c/H_i should be within the interval $[-2;\ +2]$

- The porosity should be reasonably higher than 0
- The wave steepness H_i/gT^2 should be within the interval [0.001; 0.008]

These limitations correspond to the intervals of the experimental tests were carried out. In fact, the more the porosity approaches to zero, the more inaccurate are the results. Therefore, it is recommended to use Eq. 4.13 only for porosities above 0.1. In reality, brushwood fences with such low porosities are impossible to construct. However, when they would be filled with sediment, their porosities could tend to zero. In this case, the transmission coefficient tend to zero (when the diffracted waves are not considered)as well when the structure are emerging.

5. Analysis and results of experimental tests with brushwood fences on a movable bed

The response of the movable bed has been examined during preliminary tests as described in Section 3.2.3. It has been proved in Chapter 3 that the chosen material is able to develop, in response to the experimental wave loading, adequate transport phenomenon. In the next sections, the influence of the brushwood fences on this movable bed is investigated. First, a short investigation of the effect of the brushwood fences in sand trapping is carried out. Therefore, the objectives of this chapter are the following:

- To investigate the effect of a detached single brushwood fence on the evolution of the shoreline and the sand deposition and erosion rates in the sheltered area
- To investigate the influence of a single gap in a detached brushwood fence on the sand deposition and erosion rates in the sheltered area

While the efficiency of the brushwood fences regarding the transmission coefficient was measured in Chapter 4, the present chapter will provide a detailed analysis of their efficiency regarding sediment transport.

5.1. Equilibrium sand profile in the wave tank

Before carrying out the experimental test, the actual beach profile was compared with the equilibrium profile of a beach having identical grain size. The equilibrium profile concept attracted much interest in the past. Many researchers examined the possibility of a simple relation between an equilibrated slope of a profile's sandy beach and the mean sediment diameter of its granulometry. This relationship proposed by Bruun (1954) is independent of the hydrodynamic conditions of a site:

$$h(y) = Ay^{2/3} \tag{5.1}$$

where h is the water depth at a distance y from the shoreline and A is a so-called *'sediment scale parameter'* (in $m^{1/3}$) and depends only on grain size. The values of A are given in Table E.1 in Appendix E.

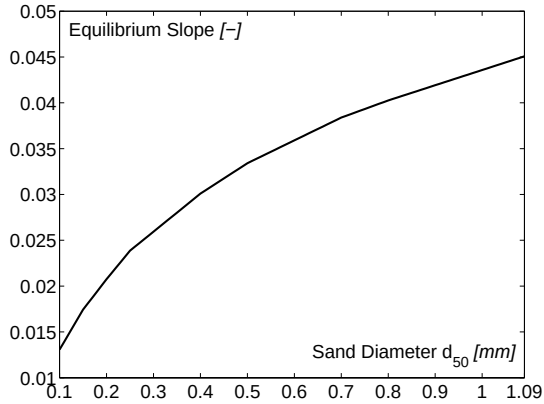

Figure 5.1.: Equilibrium slope according to grain size after Sayah, Boillat and Schleiss (2005)

Using Eq. 5.1 and Table E.1 (Dean, 2002), it is then possible to draw a curve showing the values of the equilibrium slopes according to grain size (see Fig. 5.1).

In Fig. 5.1 it can be seen that the equilibrium profile for $d_{50} = 0.18\ mm$ is almost equal to 2.1%. This indicates that the slope configuration needs to be adjusted in accordance. The following tests will be based on the equilibrium slope as calculated above. Even if the setting of a very precise slope in the wave tank was very time-consuming and difficult to realize accurately, an initial slope as close as possible to the equilibrium slope was prepared (see Fig. E.1), with an error of about $\pm 0.04\%$.

5.2. Effect of single detached brushwood fence under strong waves condition: a preliminary investigation

The present investigation describes mainly the effect of a single protection with a detached brushwood fence on the sand trapping efficiency. It refers to test number CS1 and CS2 as shown in Table 3.7. The first run aims to develop an equilibrium state due to strong incident waves similar to waves generated under major wind events (see Section 3.2.1). After $53h$ test run,

the results concerning the morphological evolution are summarized as follows (see Fig. 5.2):

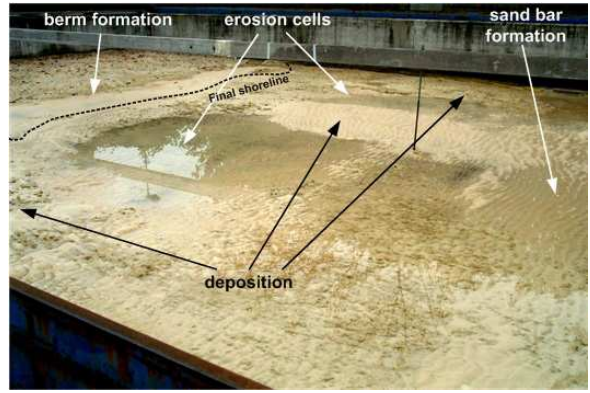

a)

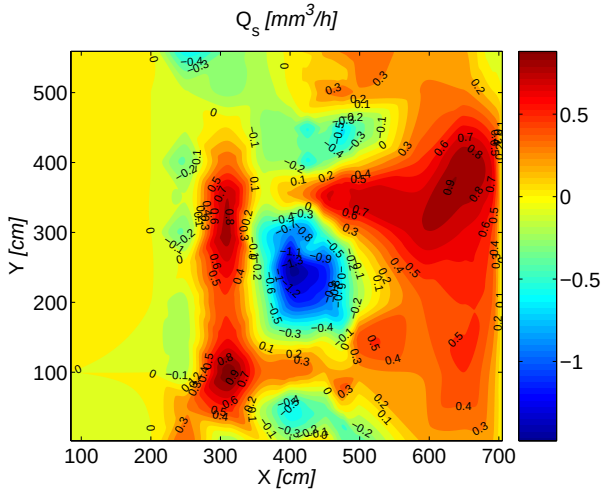

b)

Figure 5.2.: (a) Final bathymetry after $53h$ run of the test CS1; (b) erosion/deposition rates

- The erosion pattern is very similar to the erosion due to rip currents generated by waves propagating perpendicularly to the shoreline. This is demonstrated by the formation of two adjacent erosion cells, separated by a region where sand was deposited. This could be shown clearly

when calculating the gradient of the sediment bed-load (see Fig. E.4 in Appendix E). The two eroded cells can be clearly seen in Fig. 5.2, where in Fig. 5.2b the negative values of the sediment rate (or flow) Q_s indicate erosion

- The formation of a sand bar between $X = 600$ and $X = 700$ (see Fig. 5.2b) indicates that the global sand movement is oriented in the seaward direction, where the average deposition rate is almost $0.5mm/h$
- A berm is created at $X = 300$. It indicates that the shoreline moves seaward. The beach is in fact becoming steeper and the nearshore region flatter
- The berm formed in the swash zone is not continuous (see Fig. E.1a at $Y = 10$ and $Y = 500$ in Appendix E). This could be explained as follows: 1) the initial bathymetry was not uniform; 2) the rugosity of the side wall changes the wave velocity in its vicinity and results in a wave front unevenly propagating towards the shore. Comparing this results with others, it appeared that the first explanation was correct. Additionally, attention should be given to the fact that sediment should be cleared from any organic material coming from the falling leaves of the surrounding trees. The presence of such material at some spots could induce non-uniform bed response

In order to obtain a rough evaluation of the structure capability in sand trapping, at the most eroded place a one meter length detached structure parallel to the shoreline was added having the following characteristics:

- Porosity P2 of 0.36 (see Table 3.3), height $h = 0.1\ m$, width $b = 0.06\ m$, and length $B = 1\ m$
- The corresponding axis are situated at the lowest eroded point at $X = 403$ and $Y = 335$

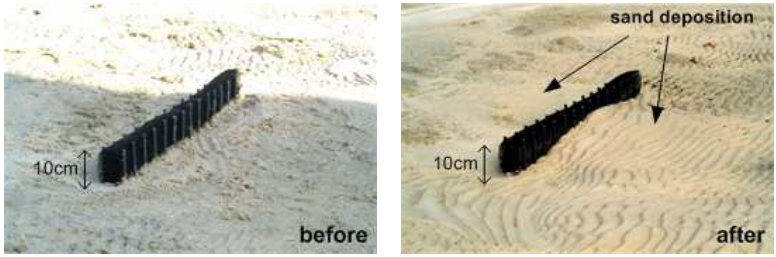

Figure 5.3.: Results of the test CS1 and CS2 where sand deposition occurs in the vicinity of the structure

After a $48h$ test run, the new resulting bathymetry showed that the structure is capable of trapping sand at its front and leeside (see Fig. 5.3). This demonstrates how the bed-load gradient is directed towards the structure. The

results are plotted in Fig. 5.4. The intermediate transport rate (or sediment flow) $Q_{s,i}$, corresponding to the resulting bathymetry for test CS2 compared to test CS1, is shown in Fig. 5.4a. The total transport rate $Q_{s,t}$ comparing the bathymetry of CS2 to the initial one is shown in Fig. 5.4b. The following points are noted:

- The results in Fig. 5.4a, corresponding to $Q_{s,i}$, clearly show the positive effect of the structure in accumulating sand, whereas the average deposition rate is almost equal to $0.5mm/h$. This is probably due to the fact that the porous media decreases the shear-stresses in its vicinity due to wave propagation, and thus orienting the deposition gradient towards its location.
- However, when comparing the total erosion/deposition rate in Fig. 5.4 ($Q_{s,t}$ compared to $Q_{s,i}$), the structure is not able to accumulate enough sediment in order to reach the initial bottom level. Therefore, the total erosion/deposition rate is still negative with an average value of $-0.1mm/h$ at the direct vicinity of the structure.
- Also, the structure does not help to prevent the erosion of the two main deposition areas identified in test CS1 at $Y = 100$ and $Y = 350$. It can be seen that they are being eroded at a maximum rate of $-1.6mm/h$.
- Additionally, erosion occurs between the structure and the shoreline. This could be explained by the diffracted waves through the structure that increases the longshore currents. The berm created by test CS1 is being displaced from $X = 300$ to $X = 220$.
- A global sand migration is identified in Fig. 5.4b, where a sand bar is being formed at $X = 700$.

The bottom depth d (in reference to the water level at $d = 0\ cm$) is shown in Fig. 5.5a at the cross section $Y = 235$ (the middle of the structure). The erosion/depostion values compared to the initial bottom elevation is shown in Fig. 5.5b. Both figures clearly visualize the retreat of the berm created at the end of test CS1, and the increased erosion between the structure and the shoreline (see CS2-CS1 in Fig. 5.5b). Concerning the sand bar elevation, it decreases in test CS2 (compared to its elevation in CS1) and almost reaches the initial elevation.

The main points describing the preliminary investigation could be summarized as follows:

- **Global erosion/deposition behavior**: the morphological evolution of the bathymetry in the wave tank composed of granular sand shows a 3D behavior. Even with regular wave propagation on a uniform initial bed, the erosion/despotion rate could not be described with a simple and average cross-section. Two main cells of erosion has been identified, separated by a region where sand is being deposited. This indicates the influence of the rip-currents generated by the perpendicular incoming waves.

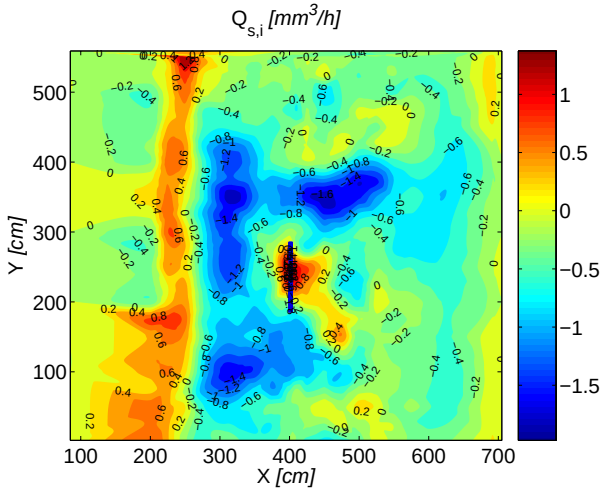

a)

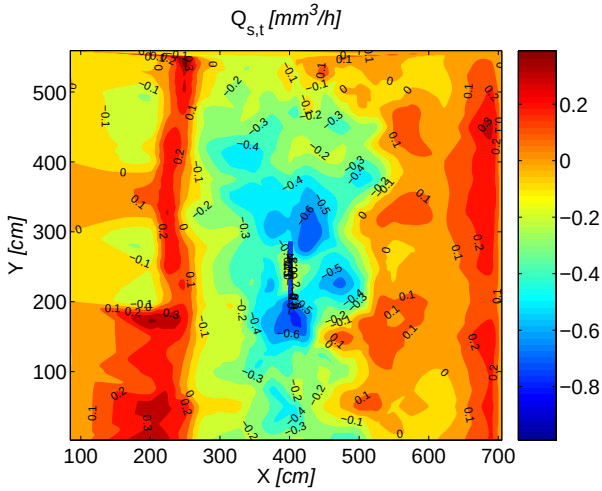

b)

Figure 5.4.: Results of the erosion/deposition rate for the test CS2; (a) Compared the final bathymetry resulting from the test CS1; (b) Compared to the initial bathymetry of the wave tank

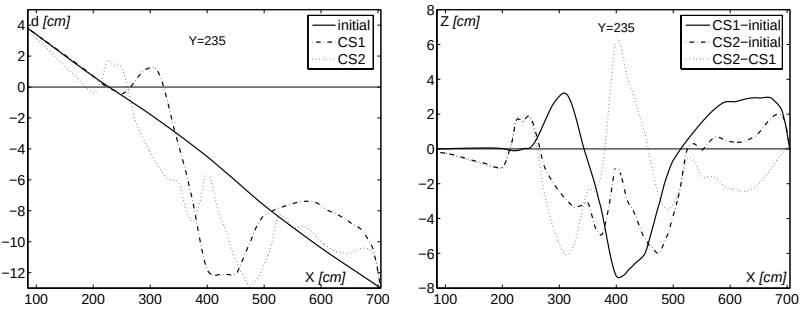

a) b)

Figure 5.5.: Cross section at $Y = 235$ for the tests CS1 and CS2: (a) compared to the MWL; (b) compared to the initial cross section

- **Sand bar formation**: In both tests, with and without the presence of the structure, a sand bar parallel to the shoreline at the seaward end of the bathymetry is created. This sand bar indicates that the bed material is being transported away from the shore. It is not clear enough to identify the influence of the structure on this bar. However, measurements show that this bar tends to decrease with its presence.
- **Shoreline evolution**: A sand berm is being formed due to wave action in the swash zone. Both tests indicate additional sand deposition. The bed-load gradient calculation demonstrates a trend of a sand transport towards the shore. This berm steepens the swash zone and flattens the region in the lee of the structure. This could be an indicator that the initial beach is not in its equilibrium state.
- **Effectiveness of the structure**: The porous structure placed in the most eroded region of the test CS1 was little effective. On one hand, it helped in attracting sand and providing deposition in its vicinity; on the other hand, it did not increase the bottom elevation compared to the initial condition. Moreover, at both of its lateral sides, the structure favored the creation of two erosion cells.

This preliminary investigation highlights the laboratory effect concerning the sediment transport. In fact, since the sandy bottom ends at about $X = 700$, no material movement is allowed beyond that limit. Although no significant volume of sand reached or passed beyond during the tests CS1 and CS2, this remains a major laboratory effect concerning bathymetric evolution. In fact, in order to respect the sediment budget for all the tests, all the material that pass beyond this limit should brought back. Furthermore, since the area is very large, it is impossible to have a precise uniform and symmetric initial bathymetry. This lack of accuracy could results in non-symmetrical

final results as shown in CS1 (the two erosion cells are not symmetrical). Therefore, special attention should be given while putting in place, after each test, the initial bathymetry of the wave tank which should be as symmetrical and uniform as possible.

5.3. Evolution of transmission coefficient and initial shoreline

5.3.1. Evolution of the transmission coefficient

In order to evaluate the effect of the bathymetric evolution, during each test with a movable bed, on the efficiency of the brushwood fence, the transmitted waves through the structure are measured and the transmission coefficients are then plotted as a function of the test duration. This refers to the tests T1 to T5 in Table 3.7, where a single detached structure with no gap is used. Wave gauges were programmed to measure wave characteristics during 3 *min* every 30 *min* interval.

Fig. 5.6 shows the time evolution of K_T for the five selected tests. The following can be observed:

- The general trends show that the transmission coefficient increases with time. The related slopes differ slightly from one test to another, remaining however very near to each other with an average positive value of about $+0.00446$ for all tests.
- The initial water level near the structure h_b does not seem to have a significant influence on the initial values of K_T. Although h_b varies from a test to another, average K_T values remain within the interval $[0.41 - 0.55]$. In fact for the first 3 tests, the structure is emerging; therefore, it is expected to have lower transmitted waves. In average, the transmission coefficient is equal to 0.48 for the tests T1 to T3. Furthermore, when the structure in completely submerged (tests T4 to T5), the average value of K_T is 0.51.

Eq. 5.2 could tentatively be used to describe the evolution of K_T measured at time t after a duration of Δt in hours:

$$K_T(t + \Delta t) = K_T(t) + 0.00446\Delta t \tag{5.2}$$

It has to be noted that this equation could not be used when the incoming wave characteristics are different and when the mobile bed had different grain sizes. The time scale corresponds to the scale of the model. It has to be multiplied my $\sqrt{10}$ for prototype applications.

With time, the structure's efficiency in damping waves decreased. This is mainly due to the bed evolution at its vicinity. In order to understand the

effect of the bed evolution on wave transmission, the incident and transmitted wave heights evolution in time domain is investigated. This investigation is shown in Fig. 5.7.

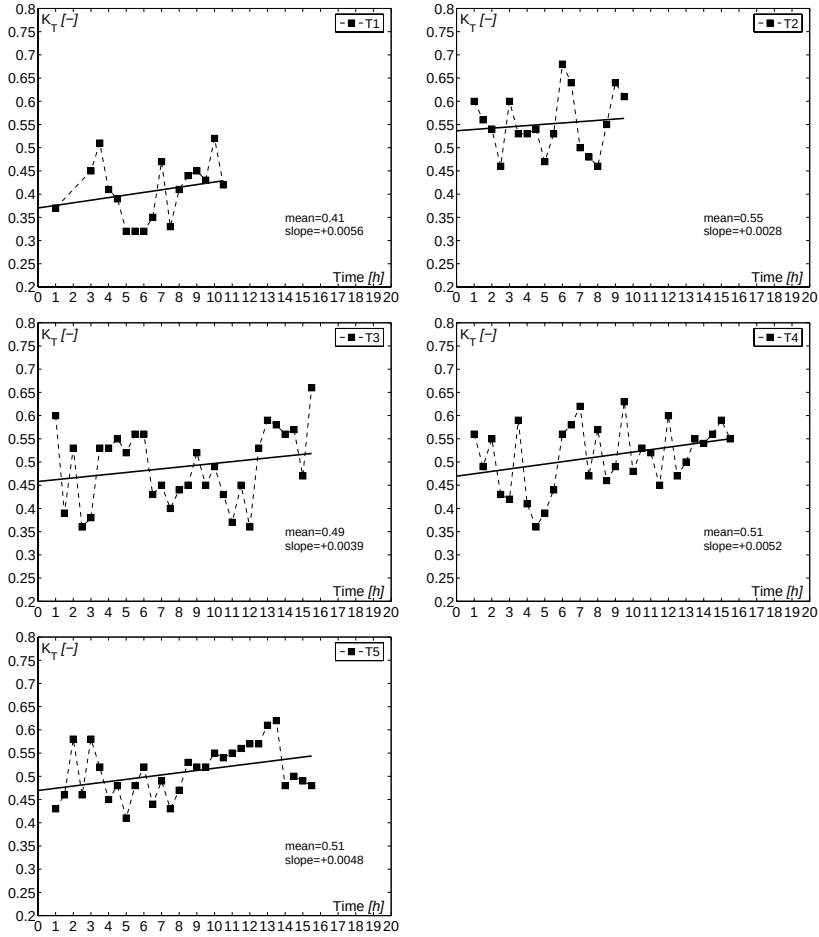

Figure 5.6.: Evolution of the transmission coefficient K_T during tests T1 to T5 (see Table 3.7) with single detached structure

Wave height trends are plotted for every test and, for each trend, the average ratio of the incoming and transmitted is calculated. It appears that this ratio is always less than one, with an average of 0.278. Therefore, with time, the incoming waves are decreasing faster than the transmitted waves. This observation explains why the transmission coefficient increases with time.

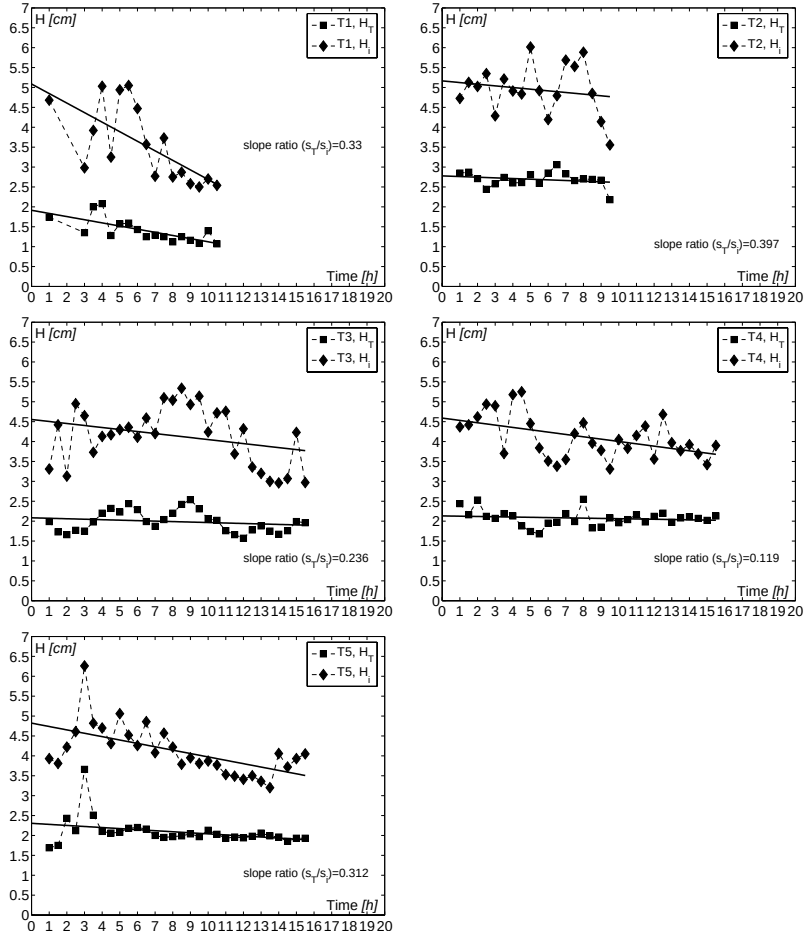

Figure 5.7.: Evolution of the incident and transmitted waves during tests T1 to T5 with single detached structure

Physically, this can only be explained by the fact that the bed at the vicinity of the brushwood fence is flattening.

Initially, the structure is placed in a bathymetry with a average grain-related equilibrium slope. Therefore, the transmitted waves through the structure are increased due to the shoaling coefficient higher than 1. When the bed in the vicinity of the structure becomes flatter than the initial one, the shoaling coefficient decreases. This decreases the transmitted wave heights. It is faster for the incoming waves as visualized in Fig. 5.7. This confirms that the movable bed is becoming flatter or being eroded faster in the seaward compared to the erosion occurring at the leeward of the structure.

5.3.2. Evolution of the shoreline

The shoreline evolution is investigated in the test SE, where the minimum and maximum values of the distance between the initial and new shoreline are measured. The duration of the test SE is equal to 13 h (see Table 3.7). The shoreline development is measured at each hour and the results are plotted in Fig. 5.8a. It can be seen that the shoreline is being accreted with an average of 5 cm/h. However, this accretion is not constant in time. In fact the shoreline development is very fast during the first 4 hours. The average accretion value is almost 12 cm/h. Afterwards, it decreases during the next 9 hours to almost 0.7 cm/h.

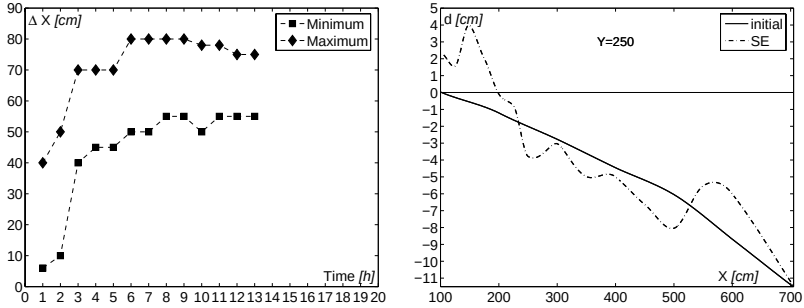

a) b)

Figure 5.8.: Evolution of the shoreline during the test SE; (a) minimal and maximal distances to the initial shoreline; (b) final typical cross-section

During the first 4 hours, the shoreline reaches almost its equilibrium position. The variation during the following hours is very small. This could be clearly seen in Fig. 5.9, where the actual (continuous line) and the initial (dashed line) shoreline are plotted, during the first 7 hours of the test SE. Due

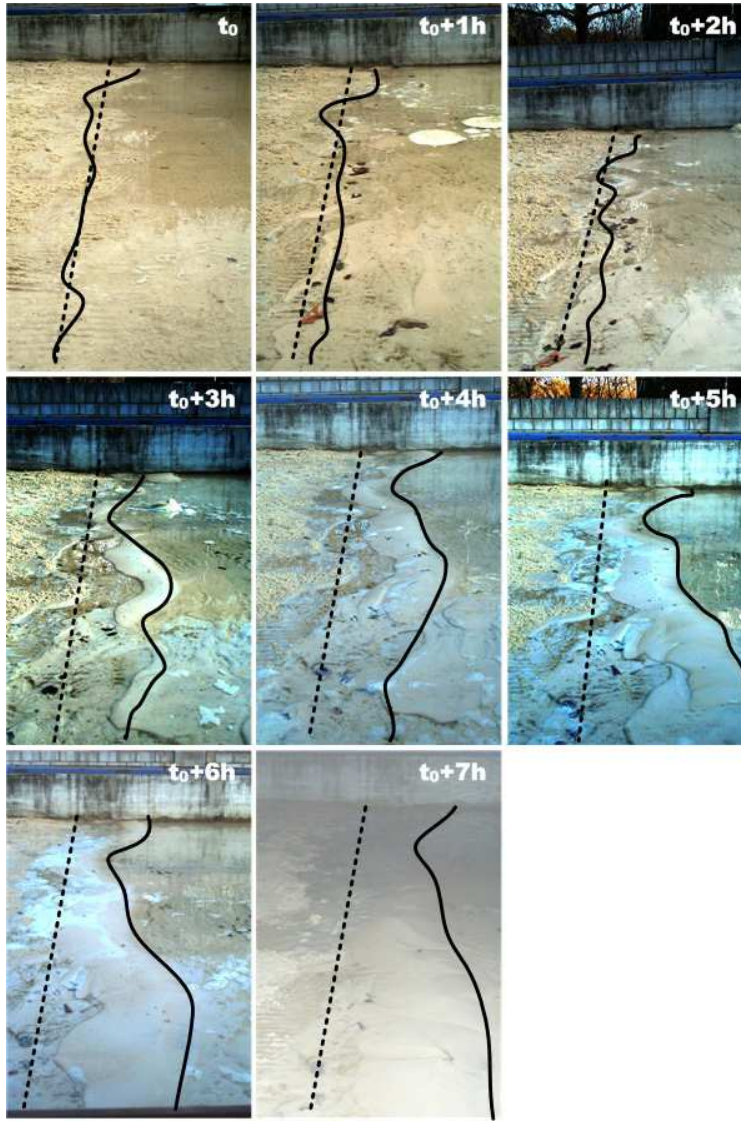

Figure 5.9.: Shoreline evolution in time during the test SE (see Table 3.7): the shoreline is not straight due to two main causes: 1) initial non-uniform shoreline, 2) incident wave fronts are not parallel

to the non-uniformity of the initial bathymetry, the shoreline is not rectilinear. However, with time the shoreline is able to reach a more uniform shape (see $t_0 + 7h$ in Fig. 5.9).

A comparison of a typical final cross-section and the initial one is shown in Fig. 5.8b. The final profile is characterized by a formation of a berm in the swash zone and a sand bar in the nearshore zone. This shape of the beach profile is closely related to the wave motion and conditions. The transport rate presented in Fig. E.11 shows that the cross-shore sediment movement is very active in the nearshore zone. This sediment transport will therefore provide information related to the type and shape of the profile.

Two types of eroded and accreted profiles are described in this section for coarse material (Sunamura and Horikawa, 1974):

- step profile, when $H_0/L_0 < 0.025$: identifying an accreted beach (see Fig. 5.10)
- bar profile, when $H_0/L_0 > 0.03$: identifying an eroded beach (see Fig. 5.10)

where H_0 and L_0 are the wave height and length in deep water, respectively.

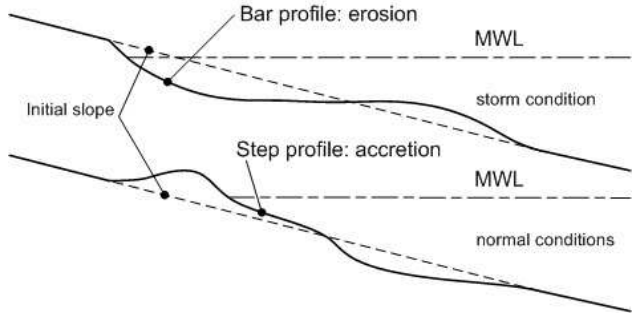

Figure 5.10.: Definition and condition of bar and step profiles after Sunamura and Horikawa (1974)

For values between 0.025 and 0.03, there is a transition zone where either type of profile might exist. In the present case, deep water wave steepness H_0/L_0 is almost equal to 0.016. This indicates that the profile, in reference to the above description, should be a step profile. However, Figs. 5.5a and 5.8b show a profile with both, a berm and sand bar formation indicating a potential typical profile of a transition zone. This in fact, can be related to the following two reasons:

- Indeed, the cross-shore profile obtained in both tests corresponds to a transition zone. Hence, an uncertainty in calculating deep water wave steepness has occurred, and resulted in a smaller value.

- The laboratory effect related to the boundary conditions of the wave tank results in preventing any sediment transport beyond the seaward limit (at $X = 700\ cm$). Hence, the material transported in the seaward direction is being accumulated beside the boundary.

During the first two tests, where strong wave conditions were applied, sand was able to move through this boundary. This indicates that the first assumption, where the cross-shore profile is situated in the transition zone is probably closer to the reality. This could be true since the calculation of H_0/L_0 contains many uncertainties (mainly in wave and water depth exact measurements).

5.4. Effect of detached structures

The effect of detached porous structures like the brushwood fences is investigated in the next sections on the basis of systematic experimental tests carried out in the wave tank with a movable bed. The investigation will focus on two main subjects: firstly the global effect of the structure on the surrounding sandy bed, secondly its effect on the shoreline development. Two types of detached structure are considered, single continuous, and double, separated with a single gap.

5.4.1. Effect of a single detached brushwood fence

The results of the experimental tests with single detached breakwater (T1 to T5) are depicted in Appendix E starting from Fig. E.12 to E.31. For every test, 4 main results related to its final bathymetry are presented as follows:

- The rough final bathymetry elevations Z in $[cm]$ showing the values of the direct measurements of the movable bed zone in the wave tank.
- The erosion/deposition values compared to initial bathymetry ΔZ in $[cm]$, showing the zones in the wave tank where the erosion and deposition occurs. Those values are calculated on the basis of the initial bathymetric elevations measured before each test run.
- The bathymetry of the movable bed zone in the wave tank related to the initial water depth d in $[cm]$, showing mainly the evolution of the shoreline.
- The erosion/deposition rate Q_s in $[mm^3/h]$ calculated as a function of ΔZ and the duration of each test.

Experimental observation

Ripples formation over the sandy bed seems to be the only sediment transport regime that occurs during the present experimental tests with movable bed (see Fig. 5.11a). They present a bed feature whose height and

wave length are small compared to the water depth. In fact, generally, ripples are formed on sandy bed with grain sizes up to 0.8 mm, for flow speeds which are above the threshold of motion but not so intense that the ripples are washed out (Soulsby and Whitehouse, 1997). At very high flow, the ripples are washed out, and a sheet flow sediment transport regime takes place resulting in the formation of a flat bed.

During the tests, ripples are rapidly formed during the first minutes of wave action. They cover the entire surface of the bed and are almost uniformly distributed. Beside the shore, where the water depth is very low, ripples are very small with a height less that 1 cm and a wave length of 3 cm. At the second half of the bottom $X > 350$ cm, ripples become larger, with an average height of 1.5 cm and wave length of 4.5 cm.

a) b)

Figure 5.11.: Experimental observation of ripples and scour: (a) ripples formation during each movable bed test; (b) dune formation at the seaward side of the structure due to reflected waves

Reflected waves over the structure, as described in Section 2.5.2, enhance scour at the nodes of the resulting total wave and accretion at the antinodes. This can be clearly seen in Fig. 5.11b, where erosion and deposition areas reflect the total wave form. The wave length of this intermittence is almost equal to 50 cm with a maximum scour depth (wave height) of 5 cm. This value confirms the description of Sumer et al. (2001) where the length that separates two scour or deposition areas, is equal to half of the wave length. Since the wave length measured at the wave gauge P3, during the test T2 of Fig. 5.11b is equal to 92 cm.

Following the diagram in Fig. 2.17, where the scour depth was related to the wave length, height and water depth for fine and coarse sand, it is possible thereafter to calculate the potential maximum scour depth that occurs at the seaward of a vertical, non-porous structure and to compare it to the actual scour depth that occurs during the experimental tests. For T2, the wave height

and length are equal (on average) to $H = 4.5\ cm$ and $L = 92\ cm$, respectively. The water depth is equal to $h = h_b = 6.3\ cm$. Based on the curve related to fine sand in Fig. 2.17, the calculated maximum scour is equal to 1.1 times the wave height which leads to $S_{cal} = 4.95\ cm$. This corresponds the maximum scour depth measured during tests equal to $S_{meas} = 5\ cm$.

Concerning the shoreline evolution, Fig. 5.12 shows the formation of a beach berm (almost 5 cm above the MWL) during the tests. A salient is formed very clearly when the detached structure is not too far from the beach (tests T1 to T3) as shown in Fig. 5.12a. Furthermore, big erosion and deposition areas with no clear salient structure are formed when the structure is far from the beach (tests T4 to T5) as shown in Fig. 5.12b.

a) b)

Figure 5.12.: Experimental observation regarding berm formation and erosion/deposition cells: (a) berm formation in the swash zone with a small salient during tests T1 to T3; (b) formation of large erosions and deposition cells during tests T4 and T5

Three schematic drawings in Fig. 5.13 describe the evolution of the shoreline form, and the erosion/deposition cells as a function of the structure's distance from the shoreline. They show how the diffracted waves through the porous structure approach the shoreline at a angle. As a result of this slanted wave, a regime of wave run-up and run-down on the shoreline takes place. The observation shows that during a wave cycle, wave run-up is able to carry the sediment particle up the slope (see Fig. 5.12a), and, vice versa, the wave run-down carries the sediment particles down the slope. Although the sediment transport rate during one wave cycle is almost unnoticeable, the cumulative effect over time (more than $10h$) is obvious and significant. This sediment transport due to the wave run-up and run-down motions occur in a zig-zag movement with the net motion directed toward the centerline of the structure. This movement promotes the creation of the middle salient at the center of the shoreline.

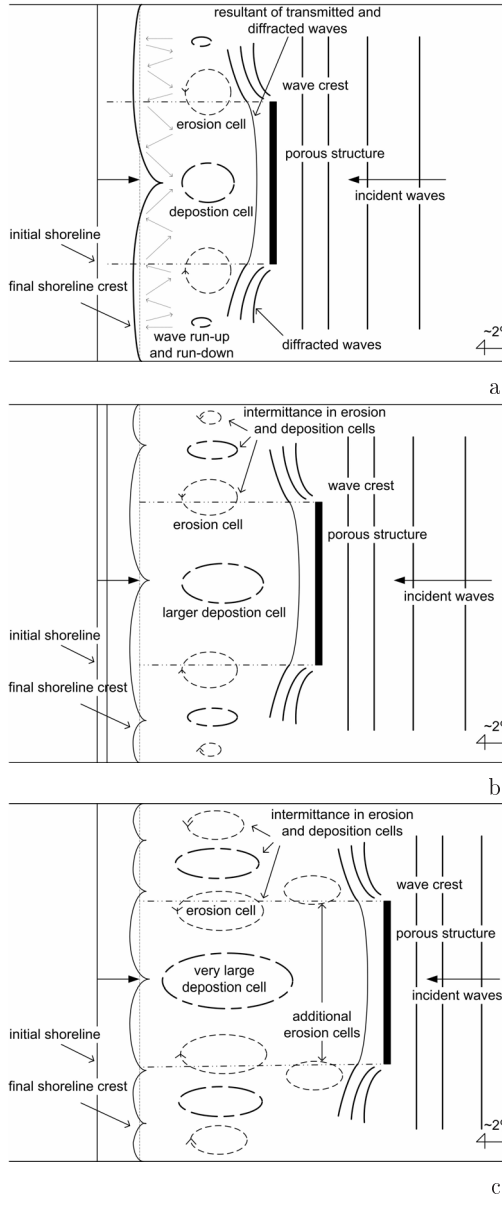

Figure 5.13.: Erosion and deposition analysis during experimental tests with movable bed:(a) T1 and T2 (b) T2, T3 and T4 (c) T4 and T5

When the structure is near the shoreline, as observed in test T1 and T2, the zig-zag motion caused by this wave run-up and run-down contributes directly to the formation of two circulation currents as shown by the two erosion cells in Fig. 5.13a. The formation of those cells results in two longshore currents that move toward each other. They meet at the breakwater centerline and promote the formation of the salient. In parallel, a deposition cell in front of the small salient is formed.

For the three schematized cases (Figs. 5.13a, b and c), a common observation regarding diffracted waves can be made. The diffracted waves at the two edges of the structure are combined with the transmitted waves through the structure and result in wave height field in the sheltered area inferior to that at the both sides of the structure. This variation in the wave height field is capable of initiating a gradient of the mean water level and therefore, promoting the formation of the two circulating, eroded cells.

When the structure is at an average distance from the shoreline as noticed in tests T2 to T4, an additional small deposition cell appears in the wave exposed zones (see Figs. 5.12a and 5.13a). The big erosion cells become narrower and they seem to move toward the center. Beside the wall, small erosion cells also start to form. The shoreline looses its initial form of a single salients and tend to form two small salient at the edge of the sheltered area. The deposition cell at the middle becomes larger and its width decreases.

During tests T4 to T5, this structured small salient formation at the shoreline tends to disappear in favor of the formation of highly intermittent erosion and deposition cells (see Figs. 5.12b and 5.13c). The median deposition cell becomes wider and longer, and, at both sides of its end, two small erosion cells are formed. Erosion and deposition cells become generally larger and longer but their width decrease. As for the shoreline form, no real structure is noticed.

For the three cases, observations show that the combined diffracted and transmitted waves produce a combined motion perpendicular to the shoreline. Since the structure is porous, this wave front in the sheltered area is parallel to the shoreline. This motion is opposite to the salient growth direction. Therefore, it plays a significant role in hindering the salient growth. As for the rate of its growth, it is very high initially and it decreases with time. Finally, at equilibrium, the waves reach the shoreline simultaneously and perpendicularly.

Generally, the size of a salient behind a porous structure is related to the two circulation currents, and to the motion caused by the transmitted and diffracted waves. The former facilitates the growth of the salient, whereas the latter, which is opposite to the direction of the salient growth, deters its development. In the next section, the relation between the salient geometry and the length of the structure and its distance from the shoreline is investigated.

Shoreline evolution

The effect of the distance of the structure from the shoreline, S, and its length, B, are studied as a function of the salient formation. The schematic representation of the variables are provided in Fig. 2.13. The final results of each test with single detached structure in given in Table 5.1. The distance S is calculated following Eq. 5.3:

$$S = S_{fin} = S_{ini} - \alpha \tag{5.3}$$

where S_{fin} is the final distance of the structure from the shoreline to be used for the evaluation estimated without the presence of the structure, S_{ini} is the initial distance of the structure from the shoreline, and α is the shoreline displacement without the presence of the structure, as calculated in Section 5.3.2. According to Fig. 5.8a, the average value at α is estimated at $\alpha = 65\ cm$.

Test number	B [cm]	S_{ini} [cm]	S_{fin} [cm]	X [cm]	B/S_{fin} [-]	$X/Bmeas$ [-]	$X/Bcal$ [-]
T1	200	200	135	135	1.4815	0.6750	0.4208
T2	200	300	235	190	0.8511	0.9500	0.8252
T3	200	350	285	240	0.7018	1.2000	1.0431
T4	200	400	335	330	0.5970	1.6500	1.2695
T5	200	450	385	385	0.5195	1.9250	1.5032

Table 5.1.: Experimental results related to the shoreline evolution and salient formation for a single detached porous structure

The distance X of the structure from the head of the salient is measured at the end of each test. The non-dimensional ratio $X/Bcal$ of the Eq. 2.31 as proposed by Silvester and Hsu (1997) is calculated as a function of the measured values B/S_{fin}. The comparison between the calculated values and measured data of X/B is presented in Fig. 5.14. This comparison shows that the best fit of the measured data with the higher correlation factor is identical to the fitting curve shape proposed by Silvester and Hsu (1997). This curve corresponds to the power law as following:

$$y = ax^b \tag{5.4}$$

For the measured data, the following values for a and b were found:

$$a = 0.80;\ b = -1.26$$

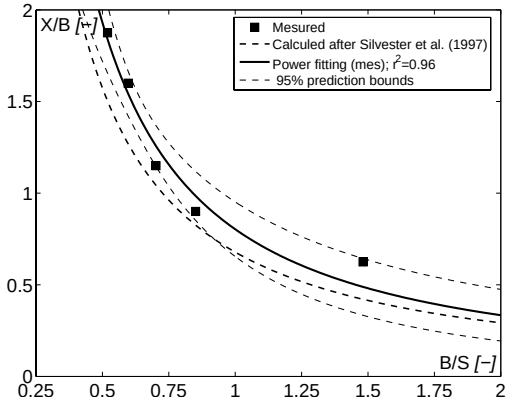

Figure 5.14.: Comparison of measured (tests T1 to T5) and calculated values after Silvester and Hsu (1997)

Fig. 5.14 shows that for a same value of B/S, the X value suggested by the measured data is greater than the calculated one. This observation is due to the fact that the calculated values of X/B correspond to a non-porous vertical breakwater. However, the measured data correspond to the vertical porous structure ($p = 0.36$). In fact, experimental observation showed (see the paragraph before) that the resulting wave motion due to the transmitted and diffracted wave in the sheltered area slows the formation of the salient. This wave motion is lower for the case of a non-porous structure, where only diffracted waves reach the shoreline. Therefore, it implicates the formation of lower width of salient.

Moreover, the power values (b in Eqs. 5.4 and 2.31) are very similar. This indicates that the porous structure has less effect on this value. For the present study, it is proposed to use the same value of b calculated by Silvester and Hsu (1997). Using the Least Square Method (Bevington and Robinson, 1992), the new equation for salient formation proposed for a porous structure would be as follows:

$$\frac{X}{B} = 0.85[\frac{B}{S}]^{-1.21};\ (\pm 0.22) \tag{5.5}$$

It has to be noted that the application domain of this new proposed equation is small, since only a single porosity was tested. Ideally, the porosity of the structure would be included in this same equation. However, a proportional result could be measured with the ratio of the non-linear variation of the transmission of waves with the porosity of the structure as described in Section 4.2.1.

Moreover, the effect of the initial slope (hence, the grain size) has a non-negligible influence on the sand deposition. When S changes, the water depth at the structure h_b changes as a function of the slope. Thus, for the same distance S and the same deep water incoming regular wave, different wave fields are generated near the structure for different slope. This results in different values of deposited and eroded sand.

Total deposited and eroded volumes

In this section, it is proposed to evaluate the total volumes of eroded and deposited sand in the leeside of the structure. The calculation of volumes is based on the results of ΔZ corresponding to tests T1 to T5 as presented in Appendix E. When these values are positive, they indicate deposition, and when they are negative, they indicate erosion. The total positive and negative volumes are consequently calculated following Eqs. 5.6a and b, respectively:

$$deposition: \; V_d = \int_{i=X_{min}}^{X_{max}} \int_{i=Y_{min}}^{Y_{max}} \Delta Z_i^+ dxdy \tag{5.6a}$$

$$erosion \quad : \; V_e = \int_{i=X_{min}}^{X_{max}} \int_{i=Y_{min}}^{Y_{max}} \Delta Z_i^- dxdy \tag{5.6b}$$

where dx and dy the grid width and length, respectively, and the X and Y are the coordinates of the limits of the zone where the volumes are being calculated.

The results of total volumes of eroded and deposited sand in the leeward of the structure are shown in Fig. 5.15. It can be seen that the total volume of deposited sand tends to increase with the distance of the structure from the shoreline, with the maximum value corresponding to the test T5. For the test T1, where the structure is near the shoreline ($B/S = 1.4815$), it appears that a very small volume of sand is trapped behind the structure. As for the volume of eroded sand, the highest value corresponds to test T1. For tests T2 to T5, the eroded volumes are quasi similar (at the exception of the test T3 where a small additional eroded volume takes place) .

Based on the experimental observation as explained before, the sand deposition occurs mainly at the middle of the sheltered area. Erosion occurs however on both sides of this area and beside the structure. Therefore, when the volume of the eroded sand is low, this implies that the erosion cells are not close to the sheltered area. This is not the case for the test T1, where the deposition rate (ratio of V_d and V_e) is very small, and almost equal to

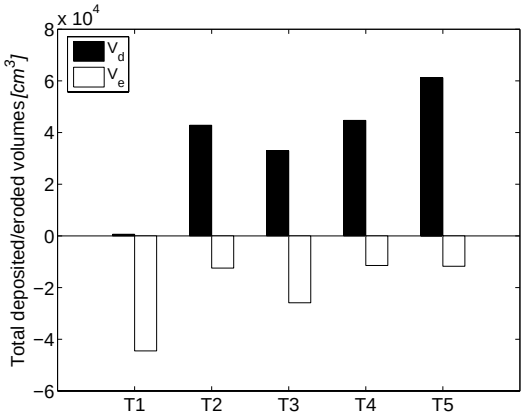

Figure 5.15.: Total deposited and eroded volumes in the sheltered area of the structure for tests T1 to T5

0.01. The highest deposition rate corresponds to the test T5, and is equal to 5.2.

Moreover, the dimensionless value $V_{d,*}$ as proposed in Eq. 2.33 is calculated as a function of B/S and presented in Fig. 5.16. In this case, $V_{d,*}$ is calculated on the basis of the maximum available deposition volume depending on the structure distance from the shoreline and the water depth at the structure (see Section 2.5.1 for more details). The results demonstrate that $V_{d,*}$ increases with B/S to a certain extent. In fact, when $B/\ S$ is high

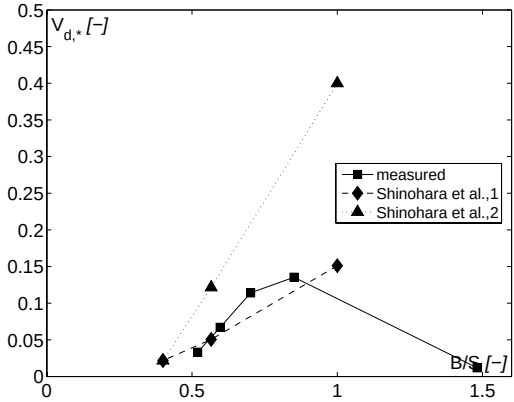

Figure 5.16.: Dimensionless deposited and eroded sand volume in the sheltered area calculated as a function of B/S

(i.e. the structure is near to the shoreline), $V_{d,*}$ decreases rapidly. Although the available deposition volume is very low when B/S is high, which suggests that $V_{d,*}$ increases, the real deposited volume during T1 is so low that a strong decrease in $V_{d,*}$ actually occurs.

This observation seems to be in contradiction with Fig. 2.14 where the results show that with the increase of B/S, the deposited volume behind a breakwater increases since a permanent formation of tombolo could be established. Therefore, the porosity plays a major role in preventing high deposited volumes when B/S is high. This could be explained as presented in the experimental observation, where the wave motion at the leeside of the structure is higher due to the transmitted waves. This prevent the formation of a tombolo.

When B/S is high (structure close to the shoreline), the results show that the volume of deposited sand is relatively low. This volume reaches its highest values during the test T2. For T1, the erosion at the leeside is higher than the deposition. This suggest that when the porous structure is very close to the shoreline ($1.48 \leq B/S$), the sand in the leeside is rather eroded. More detailed analysis with different breakwater length, different distances and grain size should allow the completion of this curve.

The effect of the porosity of the structure is emphasized when compared to the results of Shinohara and Tsubaki (1966). They calculated the deposited sand behind a vertical breakwater with different lengths and distances from the shoreline. The major results of the two main physical experiments are presented in Fig. 5.16. The number 1 series corresponds to incoming regular wave height of 2.55 cm, while the number 2 series to a height of 6.13 cm. This explained why for the former results less sand is deposited than for the latter.

The comparison between the actual results for a porous structure and the results calculated on the basis of Shinohara and Tsubaki (1966) tests does not show significant differences for small value of B/S. The major difference appears when the structure is close to the shoreline ($B/S \geq 0.85$). At this stage, the measured values show, as mentioned above, low volumes of deposited sand, contrary to the other non-porous breakwater results where the deposited volume keeps increasing.

For high distances, the deposited sand in the leeside of the porous structure is almost similar to results with non-porous structure. Although no identical shoreline evolution is observed for the two scenarios, the porous structure seems to favor a more distributed sand deposition over the entire leeside surface.

Following Eq. 2.32, $V_{d,*}$ is calculated as a function of the dimensionless salient width Y_*. The results of the measured and calculated values of $V_{d,*}$ are put together in Fig. 5.17. The curves show on one hand the influence of the salient geometry on the deposited sand, and on the other hand, the influence

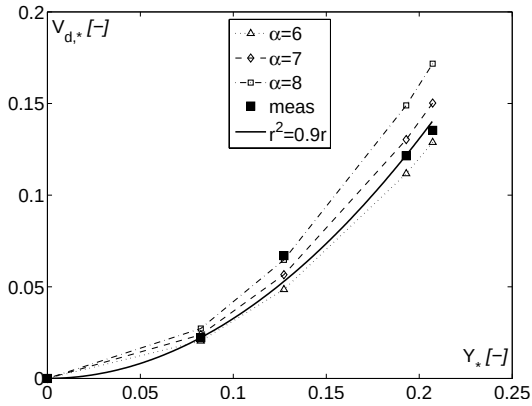

Figure 5.17.: Comparison between measurement and results after Suh and Dalrymple (1986)

due the structure distance from the shoreline. When α is high, it means that for small values of salient width Y_*, the structure is still capable of favoring sand deposition in the leeside. In other words, the deposition is significantly distributed over the entire surface of the leeside. Yet, when the value of α is low, this means, that for the same quantity of trapped sand, the width Y_* is to be higher.

The relationship between $V_{d,*}$ and Y_* is plotted for three values $\alpha = 6$, 7 and 8 in Fig. 5.17. On the same plot, the measured data are also drawn and appear to correspond to an α between 6 and 7. The best fit equation for this data is as following:

$$V_{d,*} = \frac{\alpha Y_*^2}{2};\ \alpha = 6.54;\ r^2 = 0.95 \tag{5.7}$$

Using this equation, it is possible thereafter to estimate, for conditions similar to the experimental tests, the deposited volumes as a function of the salient width. It has to be noted that the wave climate could affect significantly the volume of the deposited sand as Shinohara and Tsubaki (1966) demonstrated and as presented in Fig. 5.16. Therefore, such equation should be applied with caution.

In order to identify more accurately the deposition surface evolution in the leeside of the structure, a detailed analysis is proposed in the following.

Cross-sectional deposited and eroded volumes

The evolution of the deposited sand volumes in the leeside of the structure is given in Fig. 5.18. The dimensionless value of the deposited volume, V_d/S^3,

is calculated as a function of x_l/S, where x_l is the distance of the leeside surface upper limit to the structure. When $x_l = S$, it means that the surface where the volume is calculated covers the entire area where sand can be deposited between the structure and the shoreline. V_d/S^3 is calculated for the five tests expressed as a function of B/S (see Table 5.1).

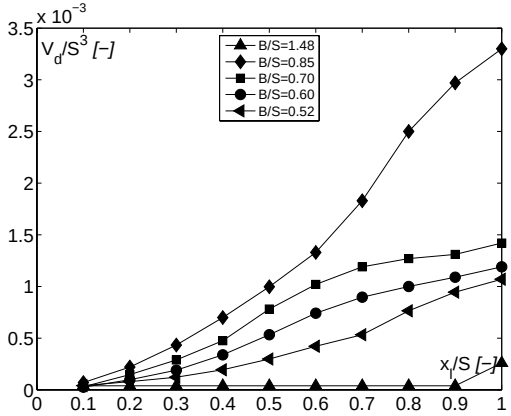

Figure 5.18.: Dimensionless deposited sand volume in the leeside of a single detached structure,V_d/S^3, calculated as a function of the relative distance x_l/S

Except for the curve $B/S = 1.48$, the four remaining curves are associated with a linear fitting as follows:

$$\frac{V_d}{S^3} = a\frac{x_l}{S} \tag{5.8}$$

where a is the calculated slope for each case considered. Its values are presented in Fig. 5.19a as a function of B/S. The correlation factors for this linear fitting ranged between 0.86 and 0.94. The best fit for the values of a as a function of B/S is exponential (see Fig. 5.19a) and corresponds to the following equation:

$$a = 1.42\ 10^{-4} exp(3.55\frac{B}{S});\ r^2 = 0.98 \tag{5.9}$$

The measured values of V_d/S^3 are compared to the calculated values using Eqs. 5.8 and 5.9. These values are presented in Fig. 5.19b with a correlation factor $r^2 = 0.92$.

The same approach is applied on the eroded sand volumes V_e/S^3 in the leeside of the structure. The dimensionless values of the eroded volumes, are thus calculated as a function of x_l/S and presented in Fig. 5.20. Identical

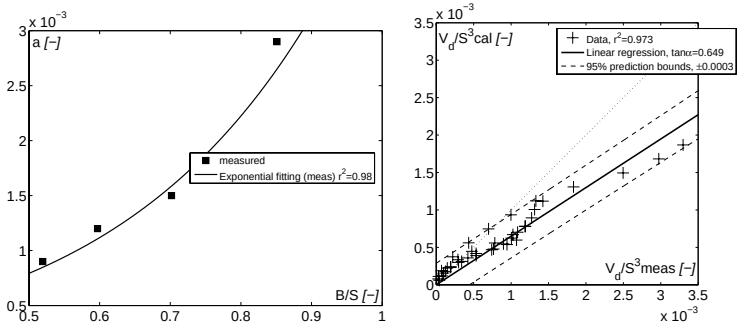

a) b)

Figure 5.19.: (a) Best fit of the slope of V_d/S^3 v/s x_l/S calculated as a function of B/S; (b) Correlation factor between measured and calculated values of V_d/S^3 following Eqs. 5.8 and 5.9

linear fitting is found for the four selected tests and expressed in the following equation:

$$\frac{V_e}{S^3} = b\frac{x_l}{S} \tag{5.10}$$

where b is the calculated slope for each case. Its values are presented in Fig. 5.21a as a function on B/S. The exponential best fit for the values of b as a function of B/S corresponds to the following equation:

$$b = 0.21\ 10^{-4} exp(4.26\frac{B}{S});\ r^2 = 0.99 \tag{5.11}$$

This analysis of deposited and eroded volumes shows two major limitations. The first one concerns the data disregarded at the direct vicinity of the structure (in this present case it is equal to 10% of S), while the second limitation concerns the data of the measured volumes corresponding to the test T1, where $B/S = 1.48$. The first one was intentionally disregarded since the deposited and eroded volumes for each test appeared to be incoherent with the general trend of deposition/erosion in the entire sheltered area. This could be closely related to the scale and laboratory effects. Therefore the trend considered suggests no changes of the level of the bed in the direct vicinity of the structure.

When the structure is close to the shoreline for $B/S = 1.48$, the behavior of the sediment transport is strongly influenced by the structure and its porosity (see the above paragraph "Experimental observation"). This behavior influences directly the deposition and erosion rates and suggests an independent analysis.

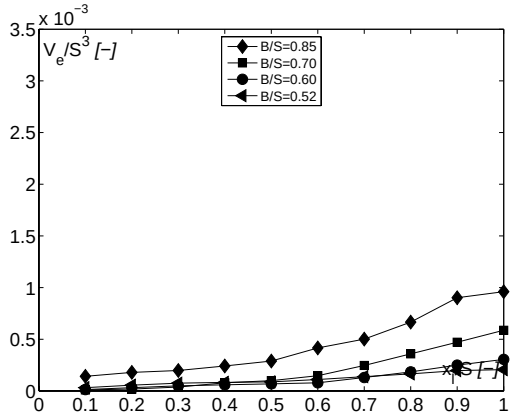

Figure 5.20.: The dimensionless eroded sand in the leeside of a single detached structure,V_e/S^3, calculated as a function of the relative distance x_l/S

The above proposed equations for the calculation of the sediment budget at the leeside of the structure (see Eqs. 5.8, 5.9, 5.10, and 5.11) provide a direct method that leads to a better understanding of the relationship between the deposited and eroded volumes. Thus the erosion ratio V_e/V_d and B/S is analyzed. This is done by dividing Eqs. 5.10 and 5.8. The results follow

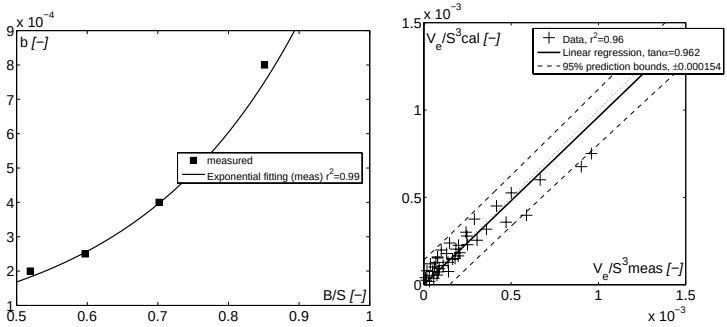

Figure 5.21.: (a) Best fit of the slope of V_e/S^3 vs x_l/S calculated as a function of $B/\ S$; (b) Correlation factor between measured and calculated of V_e/S^3 following Eqs. 5.10 and 5.11

Eq. 5.12:

$$\frac{V_e}{V_d} = 0.15exp(0.76\frac{B}{S});\ r^2 = 0.21 \tag{5.12}$$

The measured and calculated erosion ratios following Eq. 5.12 are compared in Fig 5.22. The correlation factor of such analysis is very low. This is probably due to the added errors at every level related to the definition of Eqs. 5.8 and 5.10. This could be potentially ameliorated by carrying additional tests that cover lower and higher values of B/S and by providing more accurate morphological measurement instrumentation. Moreover, the exponential form proposed in Eq. 5.12 is easily compared to a linear fit when looking at the results of Fig 5.22.

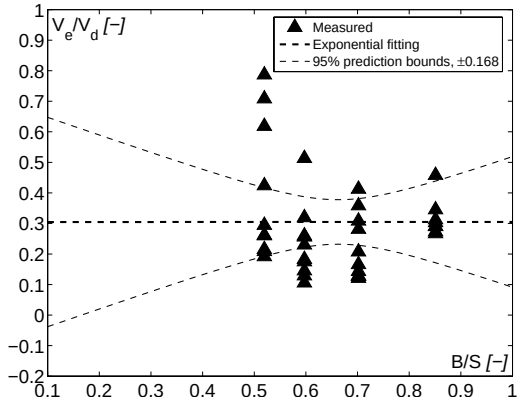

Figure 5.22.: Comparison between measured and calculated values of V_e/V_d as a function of B/S

5.4.2. Effect of detached brushwood fences with a single gap

The results of the experimental tests with double detached breakwater (T6 to T11) are shown in Appendix E starting from Fig. E.32 to E.55. For every test, four main final bathymetry are provided following the explanation in Section 5.4.1.

Experimental observation

Similarly to the observations related to tests with single detached structure, sediment transport regime and ripples formation are identical in

the case of double detached structure with single gap. Furthermore, in the present case, the erosion due to reflected waves on the structure is similar as well. For more details, refer to paragraph 'Experimental observation' in Section 5.4.1.

Waves diffracted through the gap of 50 *cm* are shown in Fig. 5.23a. The bed form in the vicinity of the gap is shown in Fig. 5.23b. It can be clearly seen how the ripples follow the diffracted waves. The figure also shows similar patterns to the wave crests. Ripples form indicates that strong currents are being formed in the gap. Usually, wave ripples correspond more to orbital elliptic currents. In the present case, ripples features are more related to river currents. This suggests the existence of a transport of sand towards the shoreline in the sheltered area in the form of small migrating ripples which finally join the shoreline and widen it.

a) b)

Figure 5.23.: Experimental observation at the gap of two detached brushwood fences, tests T6 to T11: (a) diffraction of waves through the gap; (b) final bed-form showing ripples parallel to the diffracted wave crests

This process of sand migration through the gap can be observed in the descriptive results presented in Fig. 5.24. The three schematic drawings visualize the evolution of the shoreline form and the erosion/deposition cells as a function of the structure's distance to the shoreline and the varying gap width. As mentioned before, a similar process of wave run-up and run down occurs at the swash zone and generate, as a result, a berm quasi identical to the berm with a single detached structure. When the structure is close to the shoreline (see Figs. 5.24a and b) this general run-up and run-down wave movement is hindered by a small similar process with an opposite direction parallel to the gap. This is due to the incoming waves that enter the gap without loosing their energy. This slowing effect slows the formation of salient. The final equilibrium salient width for all the tests is significantly inferior to the one formed behind a single detached structure.

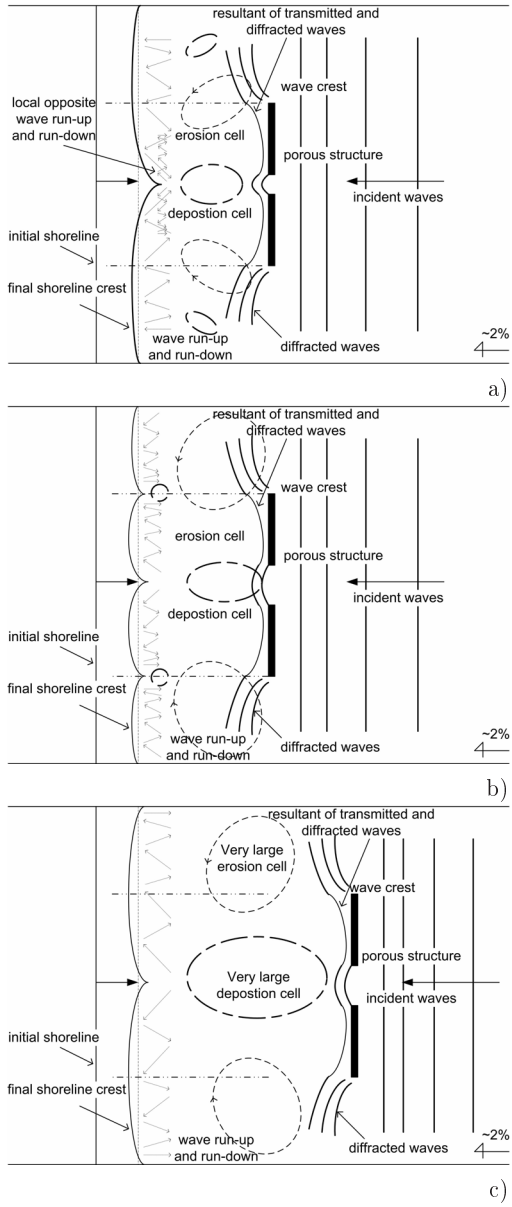

Figure 5.24.: Erosion and deposition analysis during experimental tests with movable bed:(a) T6, T8; (b) T7, T9;(c) T8, T9, T10 and T11

A median deposition cell is recurrently formed during each test. For a small gap width of 25 *cm*, the deposition cell occurs almost near the salient (see Fig. 5.24a). When the gap width is doubled, this cell appears to move seaward in the direction of the gap (see Fig. 5.24b). This is explained by the fact that bottom shear stresses are higher for a small gap than for a wider one. Thus, they are able to transport sediment grains away from the gap in the direction of the shore. When the gap is wide, sediment grains are not able to move over long distances and thus deposit just after entering the gap. A more uniform wave run-up and run-down seems to occur over shorter distances. This is particularly noticed by the new form of the berm on the shore. While, for a small gap, the shoreline presents a single formation of median salient, three small and almost identical salients are formed when the gap becomes wider. It has to be mentioned finally that the experimental observation proved that the evolution of the median salient width with the presence of a gap is not relevant.

The effect of the gap width on the berm patterns diminish with its distance from the shoreline. Therefore, when this distance increases (see Fig. 5.24c), only single median salient is formed independently from the gap width. The deposition cell in the middle of the sheltered area becomes very large as well as the erosion cells at its both sides.

Total deposited and eroded volumes

The effect of gap spacing on sand entrapment was investigated through a series of experimental tests by Harris and Herbich (1986). The authors provided a quantitative approach for the calculation of the sand volume entrapped in the sheltered area of a breakwater (non porous) for different gap spacings and breakwater distances from the shoreline. The main conclusion was that the smaller the gap width is, the more sand is accumulated in the gap.

In this paragraph, a quasi-similar approach for calculating deposited and eroded sand in the sheltered area is considered (the calculations are carried out following Eq. 5.6). This approach consist of dividing the sheltered surface in three ways depending on the structure length B, and the gap width G. The following three analysis cases are considered:

- Case 1: Analysis based on the deposited and eroded sand volumes in the total sheltered area related to the two detached structure and the gap. This case provides a description of the total effect of the detached structure with a single gap
- Case 2: Analysis based on the deposited and eroded sand volumes behind each structure and the half of the gap width. This case shows the effect of a single structure

- Case 3: Analysis based on the deposited and eroded sand volumes behind the gap. This case show the effect of the gap

Sand volumes calculated following case 1 are presented in Fig. 5.25. The results show that the total deposited sand volumes increase with the distance of the structure from the shoreline. This is also true for the total eroded sand. However, when calculating the rates of deposited sand V_d/V_e, it appears that the highest one corresponds to tests T6 and T7 (when the structure is close) and equal to 3.1. This rate decreases when the distance of the structure increases. It is equal to 2.3 and 2.2 for the tests [T8-T9] and [T10-T11], respectively. This indicates, that the efficiency of the system with a single gap decreases with its distance from the shoreline, although the total deposited sand for long distances is higher.

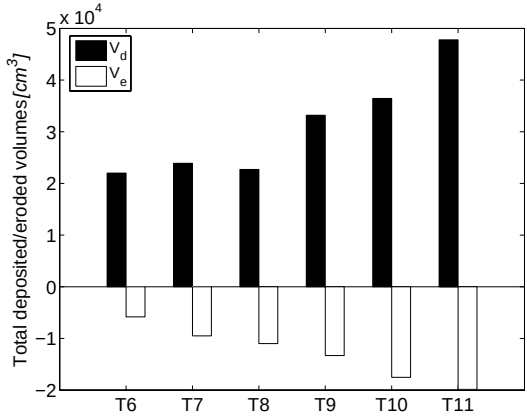

Figure 5.25.: Total deposited and eroded sand volumes in the sheltered area in case 1 of tests T6 to T11

The results of volume calculations for the case 2 are shown in Fig. 5.26. The indices, 1 and 2 for V_d and V_e corresponds to the left and right structures, respectively (while looking to the shore). The deposited and eroded sand volumes in the sheltered area of each structure appear to be very close. These quasi-similar results confirm that the initial bathymetry before each test is almost uniform. The general trend of the deposited volumes shows almost a linear increase with the distance from the shoreline, as shown for case 1.

The deposited and eroded sand volumes at the leeside of the gap are calculated in Fig. 5.27. Very small amounts of eroded volumes can be observed. It is almost equal to zero for the three tests and increases slightly when the structure is far from the shoreline for the tests T10 and T11. The following may be concluded:

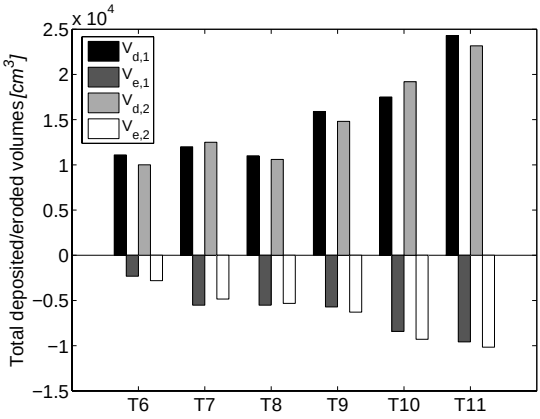

Figure 5.26.: Total deposited and eroded sand volumes in the sheltered area in case 2 of tests T6 to T11

- For the gap width of 50 cm (tests T7, T9 and T11), the deposited volumes are always higher than those corresponding to the gap width of 25 cm (tests T6, T8 and T10). The average ratio of $V_{d,50cm}/V_{d,25cm}$ is equal to 1.6. Hence, when the gap width is doubled, the additional deposited sand volumes are almost 60% higher
- When the gap width is equal to 25 cm, the deposited sand volumes are almost constant, independently of the distance of the structure from the shoreline. This could be easily confirmed with the results of the tests T6,

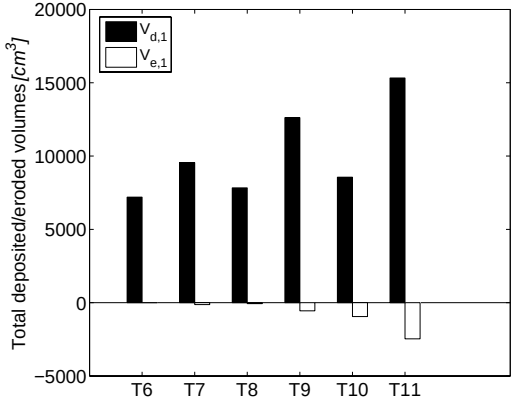

Figure 5.27.: Total deposited and eroded sand volumes in the sheltered area in case 3 of tests T6 to T11

T8 and T10. This suggests that the volume of the deposited sand at the leeside of the gap could depend only of the gap for small width values. For larger gaps, it depends on the gap width and on the structure's distance from the shoreline

In order to evaluate the effect of the gap width, on deposited and eroded sand volume using dimensionless values, the following relationships were used:

$$Case\ 1: \ V_{d,e,*} = \frac{V_{d,e}}{0.5(2B+G)h_b S} \tag{5.13a}$$

$$Case\ 2: \ V_{d,e,*} = \frac{V_{d,e}}{0.5(B+G/2)h_b S} \tag{5.13b}$$

$$Case\ 3: \ V_{d,e,*} = \frac{V_{d,e}}{0.5Gh_b S} \tag{5.13c}$$

Case 1 in Fig. 5.28, shows the sand accreted and eroded behind the total length of the brushwood fences at various distances from the shoreline. This gives some clear indication of the relationship between these values and the gap width. For smaller gap, the accreted sand increases when the structure is close to the shoreline. It slowly decreases with B/S. Regarding the eroded

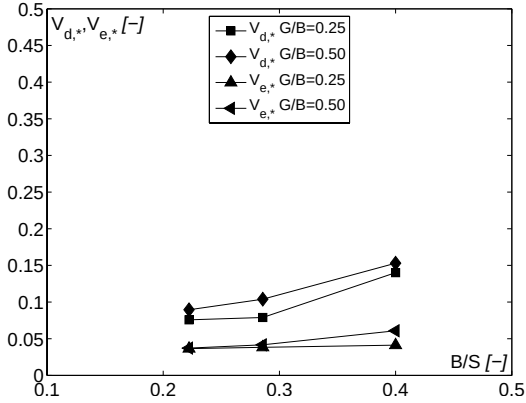

Figure 5.28.: Effect of gap spacing on the deposited (d) and the eroded (e) sand volumes following case 1

sand volumes, they are constant for $G/B = 0.25$ and increase very gently with B/S for $G/B = 0.50$. As for the effect of the width of the gap G/B on the accreted sand, contrary to the finds of Harris and Herbich (1986), it tends to increase for larger gaps. Such result could be expected since the experimental

observation showed a clear ripples regimes at the middle of the gap oriented towards the shore.

The results showed in Fig. 5.29 for Case 2 are very similar to the results of Case 1. The accreted and eroded sand volumes for each structure have almost similar trends and values. It has to be noted that the full lines in Fig. 5.29 are related to the left part of the structure (related volumes have the subscript 1) and the dashed lines are related to the structure on the right (related volumes have the subscript 2). Additionally, that the results related to each structure are also similar. This confirms the observations related to the total deposited and eroded sand volumes for each structure. It was noticed that the uniformity of the initial bathymetry and the regularity of the incident waves results in equivalent values.

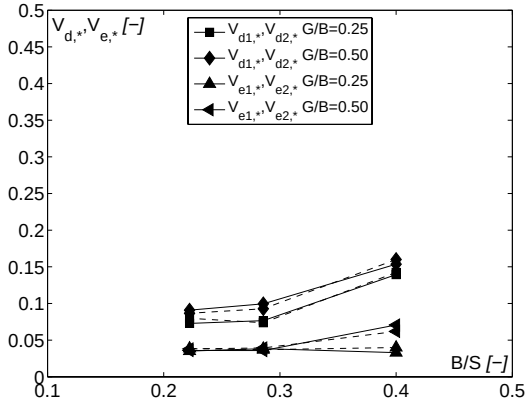

Figure 5.29.: Effect of gap spacing on the deposited (V_d) and the eroded (V_e) sand volumes following case 2

The volumes of accreted and eroded sand at the leeside of the gap for Case 3 are shown in Fig. 5.30. They indicate clearly the highest rate of the deposited sand. For the maximal values, it is three times higher than for cases 1 and 2. More importantly, they reveal that for a small gap, the relative value of the deposited volumes are much higher than for the wider gap. Although the absolute values of the deposited volumes for wider gap are clearly higher. Concerning the eroded volumes, there is almost no erosion at the leeside of the gap since the values of V_e in Fig. 5.30 are very close to zero. Regarding the effect of the distance of the gap from the shoreline, the trends shows that the deposited volumes increase very rapidly (the slope is much higher than for case 1 and 2) when this distance decreases. Hence, it could be concluded that the distance has more effect on the deposited sand at the leeside of the

gap compared to its effect when the entire region sheltered by the structure is considered.

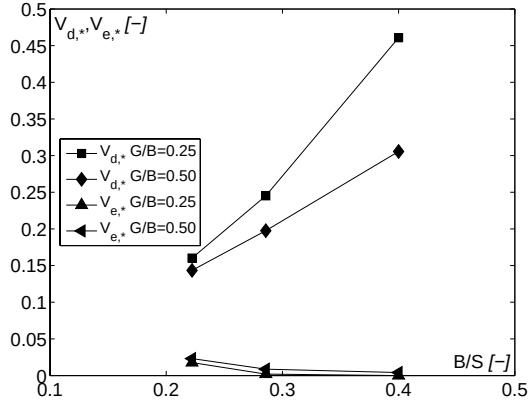

Figure 5.30.: Effect of gap spacing on the deposited (d) and the eroded (e) sand volumes following case 3

The effect of a single structure on the shoreline evolution was of no relevance during the experiments with a single gap. This is due to the very low values of B/S. In reference to the Fig. 2.14, when B/S is less than 0.5 (which was the case for all the tests with single gap), a formation of only incipient to weak salient has occurred. During the experimental tests with single gap, it was not possible to increase the value B/S by decreasing S without having the breaker line at the seaward of the structure. Moreover, using larger structures (higher values of B) was not recommended because this could increase the boundary effect of the sidewalls on the results of the experiments.

5.5. Concluding remarks

The experiments carried out with a movable bed examined mainly the geometrical relationship between a detached porous structure relative length and the volume of the accreted and eroded sand behind it. The use of a fine sand ($d_{50} = 0.18\ mm$) demonstrated its effectiveness, showing adequate morphological evolution. The evolution of the transmission coefficient was also measured in the presence of the movable bed and under constant wave attack. The following main conclusions could be derived:

- **Transmission coefficient and shoreline evolution:** A simple linear fitting demonstrated a clear increase of the values of the transmission coefficient. It was measured for the entire duration of the tests carried

out with single detached structure (average duration equal to 15 *hours*). An empirical relationship of the evolution of K_T was provided. However, it needs to be validated with different incoming wave characteristics. It was demonstrated that time had negative impact on wave damping at least during the period where the bed in the vicinity of the structure evolves to its equilibrium state. Concerning the evolution of the shoreline under regular wave attack without the presence of protection structures, it was proved that the initial shoreline moves seawards only during the first 7 *hours* after which an equilibrium state was reached. A berm was formed in the swash zone. The cross-section was situated between a storm and a normal condition profile.

- **Detached single brushwood fence:** Four different distances of the structure from the shoreline were investigated. Empirical relationship (see Eq. 5.5) was provided for the width of the salient as a function of the structure length B/S. Additionally, the deposited and eroded volumes were measured in the sheltered area by the structure. The deposited volumes were calculated as a function of the salient and B/S. Similarities were noticed when these volumes where compared to the results of Shinohara and Tsubaki (1966). Linear relationships (see Eqs. 5.8, 5.9, 5.10, and 5.11) describing the deposited and eroded volumes in the sheltered area as a function of the distance from the structure were provided.

- **Detached brushwood fences with single gap:** The effect of a single gap was investigated using two gap widths and three different distances of the structure from the shoreline. The experimental observation showed no relevant results concerning the formation of the salient behind the structure. In fact B/S was too small. Three different cases of deposited and eroded sand values were considered. They demonstrated that the influence of each individual structure are similar, which confirmed the uniformity and symmetry of the incoming wave field and the initial bathymetry. It was proven that, for the small gap width, the deposited sand behind the gap are the highest. However, the deposited sand at the leeside of the structure was higher for the wider gap. Almost no erosion occurred behind the gap. It occurred mainly behind the structure at the limits with the exposed zone.

According to observations, the transporting mechanism in the transitional state involves bottom erosion, especially near the head of the porous structure outside the protected area, and transport of sand towards the shore of this area in form of small migrating sand ripples which finally join the shoreline and widen it. The morphological and sedimentological equilibrium are almost reached after 15 *hours*, where, for a single detached structure, the salient equilibrium state is in direct relation with the relative length of the structure.

In fact, when $B/S = 1.48$, the lowest values of the salient width and the deposited sand are reached. This was in contrast to measurements carried out on non-porous breakwaters by other researchers. Moreover, when $B/S = 0.85$, the values of the salient width and the deposited sand are maximal. Concerning the gap width, the smaller the gap ($G/B = 0.25$) the more sand is accumulated in the gap. However for the wider gap ($G/B = 0.5$), the deposited sand in the total sheltered area is slightly higher. Although additional tests are needed for the effect of a single gap, it is suggested to maintain low values of gap width.

It has to be mentioned that sand formation behind a coastal porous structure is a complicated process that depends as it was proven on many variables. As stated before, the bathymetry around the brushwood fences depend on its placement, wave property, and sediment characteristics. The experiments examined only the geometric relationship while holding wave and sediment characteristics constant. Volumes of the deposited and eroded sand was only measured, as accurately as possible, behind and in the gap between the two detached structures. In real cases, the steepness, the period and the angle of approach of incoming waves affect significantly these volumes. Additionally, the sediment grain size, the fall velocity, as well as the beach slope would have also a significant impact. The average of grain size used in the experiments is relatively coarser than the natural sand. Therefore, some scale effect can be expected in this model sediment study. It is recommended in a future stage to compare these experimental results to field data and carry out a numerical modelling after appropriate calibration.

6. Description and calibration of the numerical model

The purpose of this chapter is to describe the numerical model used during the research project. Also, the steps needed in order to carry out an adequate calibration of the different variables provided by the model, based on the experimental results are presented. Therefore, the objectives of this chapter are the following:

- To set-up and calibrate a numerical model of the physical wave tank where experimental tests were carried out
- To provide some general calibration rules to be followed based on a theoretical approach

This chapter is the basis for the numerical modelling of the brushwood fences. It uses the results of the experimental tests with fixed bed without the presence of a protection structures (see Appendix C) in order to define the wave breaking and bottom friction parameters of the numerical model of the wave tank.

6.1. Description of the numerical model

6.1.1. The selected numerical model Mike 21

For the many years, several institutes have been developing numerical models of free-surface water simulation for coastal related applications. Work have been concentrated on two-dimensional, depth-averaged (2DH) schemes. Attention has also been turned to quasi-three-dimensional (Q3D) and three-dimensional (3D) schemes (Briand and Kamphius, 1993) for applications concerning morphological changes under wave attack.

Many researches tried to compare different numerical models on the basis of hydrodynamic (Stoschek and Matheja, 2000) and morphodynamic (Nicholson et al., 1997) output. Although no extensive comparison was undertaken, it was shown that the most well-renowned coastal models results were more or less similar, and reproduces usually the same conditions as physical modelling after sound calibration.

The *Danish Hydraulic Institute* developed an engineering software package containing comprehensive modelling systems for 2D free-surface flows,

Mike 21. It is applicable in situations where stratification is neglected. Mike 21 can be applied to simulate phenomena related to lakes, estuaries, bays, coastal areas and seas (Warren and Bach, 1992). Constructed in a modular manner, Mike 21 is able to provide accurate simulation in the following areas :

- coastal hydraulics and oceanography
- environmental hydraulics
- sediment transport process
- wave generation

Delft3D, developed in the *Netherlands* is a 2D/3D integrated modelling environment capable of simulating conditions in almost the same fields as cited above. One of the major differences is that Mike 21 does not simulate natural phenomenon that may occur along the vertical axis, but only in the two horizontal directions. However, Mike 3 is able to provide the three dimensional aspects complementary to Mike 21.

In the actual research, the commercial 2D Danish software is considered as the main reference for the numerical simulation since major phenomena that are being studied occur essentially in the two horizontal directions. Furthermore, Mike 21 provides a comprehensive panoply of modules for different theories related to wave generation that can be applied differently for each particular case, (*Nearshore and Offshore Spectral Wind-Wave Modules, Parabolic Mild-Slope Wave Module, Elliptic Mild-Slope Wave Module and Boussinesq Wave Module*). In the following sections, the module Mike 21 EMS based on solving the elliptic mild slope equation is described.

6.1.2. The use of the elliptic mild slope module Mike 21 EMS

Mike 21 EMS (EMS stands for *E*lliptic *M*ild *S*lope) can be used to study wave dynamics in coastal areas and in harbors, mainly where a single input could be described by a single wave height, wave period and wave direction. In addition to its utilization for the detection of harbor resonance and seiching caused by long-period waves (i.e swell and tsunamis), this module is mostly used in the presence of porous media such as porous breakwaters, palisades, brushwood fences, etc, used for shore protection against wave induced erosion (DHI, 2001). Many practical applications were realized during the past years confirmed the effectiveness of the mild slope equation and Mike 21 EMS in reproducing valuable results, however, under specific conditions.

Thompson et al. (1996) analyzed, using a numerical model based on the mild slope equations, the wave response of a harbor. Authors focused however the study on short wave validation. They tested the model with several simple domains, in most cases with uniform depth. It is validated with laboratory

data for irregular wave diffraction around a semi-infinite breakwater. The model is also compared to widely accepted curves for regular and irregular wave diffraction through a breakwater gap. Tests demonstrated the effect of the input parameters on the model results and provided some guidelines about the choices of parameter values for a sound and trustful numerical modelling. A non extensive list of the important parameters to be considered is as following:

- Bottom friction
- Boundary reflection
- Coastline reflection
- Depth in infinite region

Although the model was able to reproduce (to a certain extent) the laboratory and field measurements, the authors concluded that the mild slope equation still has some important limitations because it not able to model directly wave currents and wave overtopping.

Mai, Ohle and Zimmerman (1999) evaluated the applicability of three different wave model in shallow coastal waters. The wave models are HISWA and SWAN, from TU Delft university and Mike EMS. Models were tested by comparing the simulation results together with measurements in a wave tank and on site measurements at the North Frisian Coast of Germany. The experimental data on which the model test is based were collected during an investigation on the influence of submerged dikes on wave propagation along a foreland. The authors demonstrated the efficiency of Mike 21 EMS in reproducing the wave conditions similar to that of the wave tank. However, they denoted a standing wave directly in front of the summer dike which is not reasonable for irregular waves. In fact, this is due to the necessity of averaging wave heights since Mike 21 EMS calculates the wave propagation only for regular waves. They were able finally to calibrate the model on the basis of three parameters, the first two related to wave breaking and the third related to the bottom friction.

Concerning wave transmission, Mai, Ohle and Daemrich (1999) calibrated the three numerical model cited above using laboratory wave measurements on a large scale physical model of a summer dike. It was built at natural scale and generated waves similar to those found in reality. The transmission coefficient of the structure was measured afterwards. It was proved that Mike 21 EMS accurately reproduces the shoaling, bottom friction and wave breaking at the structure. The transmission coefficient was reproduced numerically with a correlation factor equal to 0.7. The authors also used the transmission coefficient of the structure measured experimentally to tune the calibration of the wave breaking parameters and the bottom roughness. As a conclusion, Mai, Ohle and Daemrich (1999) stressed that the three models, including Mike 21 EMS are applicable for forecasting of the transmission coefficient at

forelands and summer dikes. The best results in comparison with experimental results were achieved with the model parameters of friction and wave breaking only slightly different from the recommended values in the manuals.

In a direct relation with brushwood fences, Mai, Lieberman and Zimmermann (1999) modelled this porous structures numerically. They calibrated their numerical model on experimental measurements of the transmission coefficient. They also proved the effectiveness of Mike 21 EMS in modelling porous structures.

In a more general application, Tiani et al. (1999) proved the applicability of Mike 21 EMS of a large scale. They examined the wave reflection on the dikes of the harbor and analyzed the harbor agitation. Furthermore, the analysis was also based on experimental downscaled models.

6.1.3. Description of the elliptic mild slope equation

The Elliptic Mild-Slope Wave Module of Mike 21 simulates the propagation of linear time harmonic water waves on a gently sloping bathymetry with arbitrary water depth. The simulation is reproduced by solving the mild-slope wave equation expressed in two horizontal dimensions formulated by Berkhoff (1972). The equations reads:

$$\nabla.(cc_g\nabla\zeta) - \frac{c_g}{c}\frac{\partial^2\zeta}{\partial t^2} = 0 \tag{6.1}$$

where c is the phase velocity of waves, c_g in the group velocity of waves, ζ the surface elevation and ∇ the horizontal gradient operator.

The phase velocity and the group velocity are related to the local still water depth $h = h(x, y)$ following the equations:

$$c^2 = (g/k)tanh(kh) \tag{6.2a}$$

$$c_g = 1/2(122kh/sinh(2kh))c \tag{6.2b}$$

where k is the local wave number.

Copeland (1985a) has rewritten the mild-slope equation (see Eq. 6.1) as a system of first-order differential equations, which are similar to the system of equations governing nearly horizontal flow in shallow water. As a result, a highly efficient and fast algorithm developed for the solution of the latter can be applied. The partial reflection is therefore combined with the mild-slope equation. This combination is based on a porous flow description, which involves the local porosity and a linear dissipation term in the governing first-order differential equations. This leads to the following equations:

$$\lambda_1 \frac{\partial S}{\partial t} + \lambda_2 S + \frac{\partial P}{\partial x} + \frac{\partial Q}{\partial x} = S \tag{6.3a}$$

$$\lambda_1 \frac{\partial P}{\partial t} + \lambda_3 P + c_g^2 \frac{\partial S}{\partial x} = 0 \tag{6.3b}$$

$$\lambda_1 \frac{\partial Q}{\partial t} + \lambda_3 Q + c_g^2 \frac{\partial S}{\partial y} = 0 \tag{6.3c}$$

where $\lambda_1 = c_g/c$,$\lambda_2 = ic_g/c\omega + f_s$, $\lambda_3 = (i + f_p)c_g/c\omega + f_s + e_f + e_b$, P the wave generated flow in X direction, Q the wave generated flow in Y direction, S the source term which generates the incoming wave, i the imaginary unit, ω the wave frequency, f_p the linear friction factor due to energy loss in porous media, f_s the linear friction factor due to energy loss in sponge layers, e_f the energy dissipation due to bed friction, e_b the energy dissipation due to wave breaking, x, y the horizontal and vertical respective cartesian coordinates in a 2D plan and t the time.

By this means, Mike 21 EMS simulates the propagation of linear time harmonic water waves on a gently sloping bathymetry with arbitrary water depth. Furthermore, the module is capable of reproducing the combined effects of shoaling, refraction, diffraction and back-scattering. Energy dissipation, due to wave breaking and bed friction, is included as well as partial reflection and transmission through for instance groyne structures and breakwaters. Sponge layers are applied where full absorption of wave energy is required. In addition, the model includes a general formulation of radiation stresses, based on Copeland (1985b), which is valid in crossing wave trains and in areas of strong diffraction.

6.1.4. Relevant variables for model adjustment

Sections 6.1.2 and 6.1.3 showed on one hand the importance of an appropriate adjustment of the model Mike 21 EMS and some relevant variables related to the adjustment of the model. It appears the adjustment should be made on three levels as follows:

- adjustment related to the generated waves
- adjustment related the boundary conditions of the model, for instance bottom friction
- adjustment related to the porous medias

The goal of the adjustment related to the generated waves is to numerically reproduce wave heights as in reality and similar to laboratory tests. The main variable for this first adjustment is e_b, the energy dissipation due to wave breaking (see Section 6.2.3). The adjustment related to the

boundary conditions of the model concerns two variables. The first one is expressed by e_f, the energy dissipation due to the bed friction (see Section 6.2.4) and the second one, f_s, the linear friction factor due to energy loss in sponge layer (see Section 6.2.2). Furthermore, the variables that concern porous media, instead of being related to its physical characteristics like porosity or permeability, is related to the response of the media to the incident waves, for instance, the reflection and transmission coefficients. A more detailed quantitative analysis is provided in Section 6.2

6.2. Calibration of Mike 21 EMS

This section mainly deals with the suggested methodology followed in order to accomplish an appropriate adjustment of the numerical model Mike 21 EMS. The methodology shows the different variables selected for calibration. It is based mainly on the experimental results carried out in the wave tank. However, a theoretical approach is also provided for a first approximation of the wave breaking variables and the bottom roughness of the numerical model of the wave tank. The suggested methodology is essentially based on the parameter identified in Section 6.1.4. Its corresponding detailed description is provided in Fig. 6.1. It is divided into two main parts:

- Theoretical and experimental input: concerns the results of the experimental tests used for the calibration of some parameter together with a theoretical approach.
- Numerical and experimental comparison: concerns building of an adequate numerical model and comparison of the numerical results with experimental ones.

At a first stage, initial experimental tests with no protection structures provide wave lengths at the most significant wave gauges for an appropriate grid selection of the numerical model of the wave tank. The water depth is taken into consideration when selecting wave heights. Afterwards, the generated numerical model is adjusted on the basis of the calibration of the wave breaking parameters and bottom roughness realized with a theoretical approach combined with physical results.

The first comparison of results is shown for wave heights calculated with the numerical model and compared to experimental results for tests without any structure. This first comparison allows a basic adjusted model where a sponge layer as boundary condition is introduced to the model together with the porous structure. The transmission coefficient is measured in second step and compared to physical results. This comparison will allow a final adjustment of the model. The adjusted numerical model could only then be used is order to test different configurations and geometries of the protection structure.

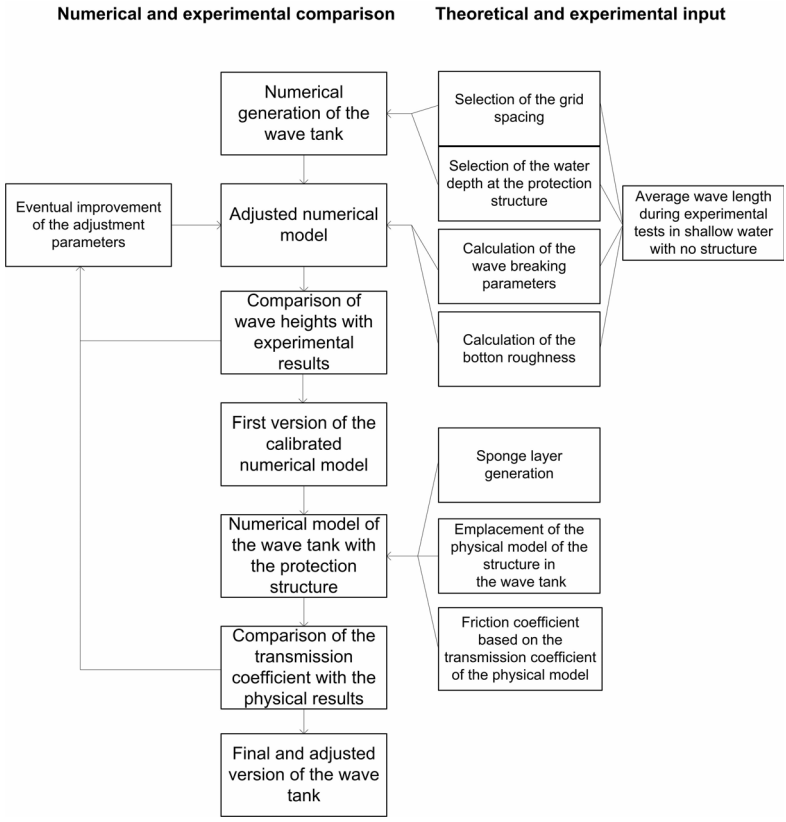

Figure 6.1.: Suggested methodology for the adjustment of the model Mike 21 EMS

6.2.1. Setting up the numerical model of the wave tank

Providing Mike 21 EMS with a suitable model bathymetry is essential for obtaining reliable results from the model. Setting up the bathymetry requires more than just specifying a 2D array of accurate water depths covering the area of interest. It also includes the appropriate selection of the area to be modelled, the grid spacing, location and type of boundaries etc. When setting up the bathymetry it should be kept in mind that shallow water results in small wave lengths which implies small grid spacing which again results in increased CPU time. Therefore, an optimal selection of grid spacing for the bathymetry is very important and requires a very good attention.

The numerical wave tank (see Fig. 6.2) is generated proportionally and identically to the wave tank where the experimental tests are carried out as shown in Fig. 3.1. In order to have more accurate results, and after some preliminary tests, the decision was made to build a numerical model ten times bigger that the wave tank. A square grid is selected for that purpose on the basis of wave lengths generated during experimental tests as shown in Appendix C. The wave length is selected for very shallow water in the wave tank. The results of the wave gauges 5 and 6 are therefore not considered since they measure waves with length 2 to 3 times longer that those at wave gauges 1 to 4.

The grid spacing should be selected to provide adequate resolution of the bathymetry and the waves. Concerning the waves, the grid spacing should allow at least 10 grid points per wave length (Madsen and Larsen, 1987). However, when complicated standing wave patterns can be expected, with combined transmission and reflections, it is recommended to allow up to 15 points per wave length (especially if the automatic selection of time step is applied).

Based on the minimum water depth during experimental results, the grid spacing is selected to be 0.2 m for the big scale numerical model. Which leads to 0.02 m grid spacing at the wave tank scale. Hence, a minimum wave length of 0.3 m is considered. Furthermore, it is required that the grid spacing in combination with the time step is selected to fulfil the CFL criterion (Courant-Friedrichs-Levy), i.e. the Courant number should be less than one. The Courant Number is an expression which describes the number of grid points that wave information will travel in one time step. It is defined following the Eq. 6.4:

$$C_r = c\frac{\Delta t}{\Delta x} \tag{6.4}$$

where c is the wave speed propagation as given in Eq. 6.2a, Δt the selected time step for the numerical calculation and Δx the grid spacing.

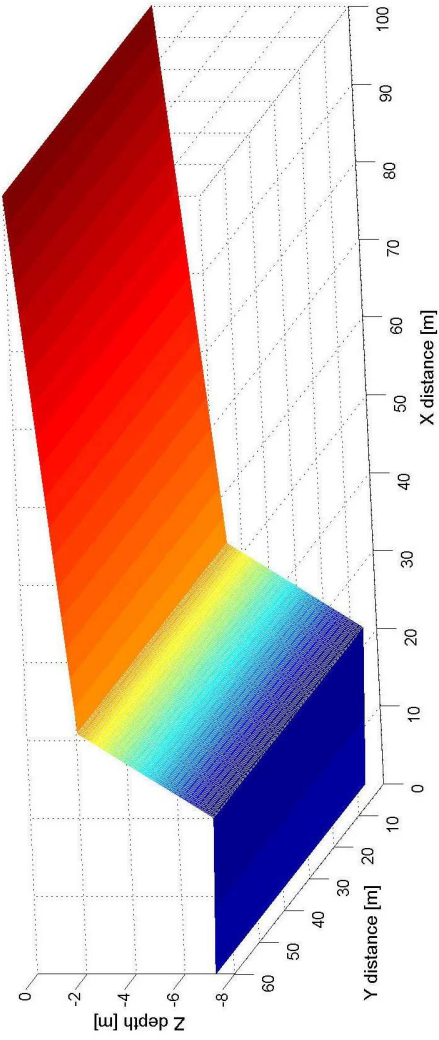

Figure 6.2.: The numerical model of the wave tank with a square grid of 0.2 m

For an average water depth of 0.35 m, wave length of 3 m, the time step considered should be less than 0.07 s. However, the numerical model has the capability of adapting the time step, during the run, when no fixed value is selected, in order to keep the Courant number less or at maximum equal to one.

6.2.2. Boundary conditions of the numerical model

The boundary conditions used at this first stage of the model adjustment are based on experimental tests carried out **without** any protection structure. During these tests wave characteristics are measured at each location of wave gauge shown in Fig. 3.1. The boundary conditions are given in Table 6.1.

number of tests series	depth d *[m]*	wave characteristics
1	0.35	see Table. C.1
2	0.50	see Table. C.2
3	0.70	see Table. C.3
4	1.00	see Table. C.4
5	1.25	see Table. C.5
6	1.40	see Table. C.6
7	1.50	see Table. C.7

Table 6.1.: Boundary conditions for the theoretical calibration and experimental validation

The following sections uses the wave characteristics for each series in Table 6.1 in addition to heights as described in Fig. 6.3.

6.2.3. Wave breaking parameters

The formulation in Mike 21 EMS of wave breaking due to large wave steepness and limiting water depth is based on the formulation of energy dissipation provided by Battjes and Janssen (1978):

$$\frac{dE}{dt} = -\frac{\alpha}{8\pi} Q_b \omega H_{max}^2 \tag{6.5}$$

where E is the energy for monochromatic waves, α a variable fixed to one for Mike 21 EMS, and Q_b the fraction of the breaking waves determined by:

$$\frac{1 - Q_b}{lnQ_b} = -(\frac{H_{rms}}{H_{max}})^2 \tag{6.6}$$

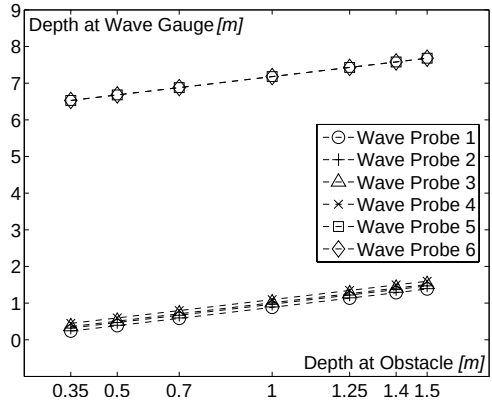

Figure 6.3.: Water depths at each wave gauges according to different depths at obstacle

where H_{max} is the maximum allowable wave height equal to:

$$H_{max} = \frac{\gamma_1}{k} tanh(\frac{\gamma_1}{\gamma_2} kd) \tag{6.7}$$

The two major parameters that define wave breaking characteristics are γ_1 and γ_2 . The first parameter controls the dissipation of energy due to breaking of steep waves, whereas the second controls wave breaking due to limiting water depth conditions. According to Holthuijsen et al. (1989), the value of γ_1 is fixed to 1 in a first step. Battjes and Stive (1985) suggested an expression of γ_2 as following:

$$\gamma_2 = 0.5 + 0.4 tanh(33 S_0) \tag{6.8}$$

where S_0 is the deep water wave steepness. Since the generated waves during the physical experiments are situated at the wave gauge P6 in an intermediate water depth, wave heights and lengths in deep water are to be calculated as follows (see Section 2.2):

$$L_0 = L_i tanh(\frac{2\pi d}{L_i})^{-1} \tag{6.9a}$$

$$H_0 = H_i(\frac{1}{2}\frac{1}{n}\frac{1}{tanh(kd)})^{-\frac{1}{2}} \tag{6.9b}$$

$$\tag{6.9c}$$

where L_i and H_i are wave length and wave height, respectively, measured at the six different wave gauges, d the water height at each wave gauge (see Fig. 6.3).

The values of γ_2 for each wave gauge and each depth are provided in Appendix F.1. The mean values of averages for each water depth and at each wave gauge are presented in Fig. 6.4a and Fig. 6.4b, respectively.

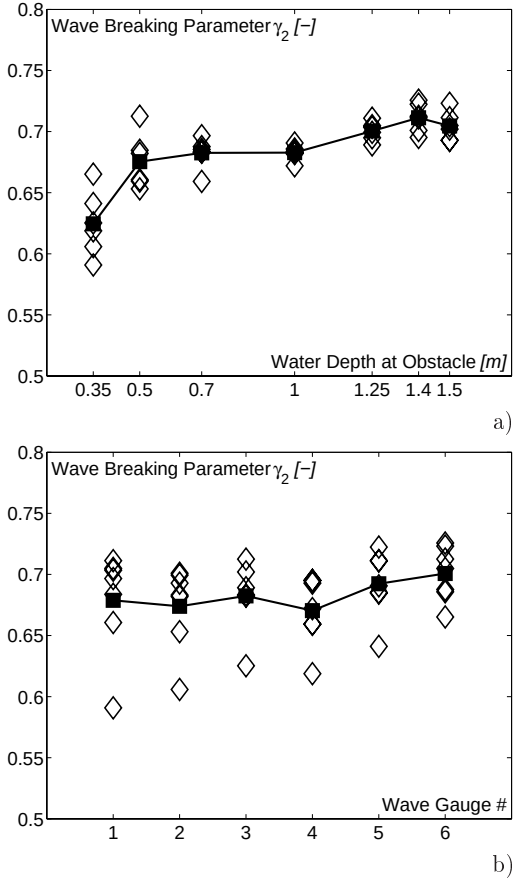

Figure 6.4.: Wave breaking parameter values and averages at (a) different water depths and (b) different wave gauge locations

The average values of γ_2 vary between 0.6 and 0.7. An average value of 0.67 could be considered as a good theoretical approximation for the breaking process at the wave tank. The value of $\gamma_1 = 1$ is considered at this first stage of calibration.

6.2.4. Bottom roughness parameter

Bed friction is the process by which the wave looses (dissipates) some of its energy. The amount of energy dissipated increases with distance, wave height, wave period, and decreases with water depth. In Mike 21 EMS, the formulation of dissipation of energy due to bed friction is based on the quadratic friction law. For monochromatic waves it is expressed by the following:

$$\frac{dE}{dt} = -\frac{1}{6\pi}\frac{0.5 f_w}{g}\left(\frac{wH}{sinh(kd)}\right)^3 \tag{6.10}$$

where f_w is the wave energy loss factor.

The variable for the calibration of the bed friction in Mike 21 EMS is however the Nikuradse roughness parameter k_n. This parameter depends on the wave energy loss factor f_w, as for a hydraulic rough regime according to Jonsson (1966):

$$0.25 f_w^{-0.5} + log(0.25 f_w^{-0.5}) = -0.08 + log(\frac{\hat{A}_\delta}{k_n}) \tag{6.11}$$

where $\hat{A}_\delta$ is the peak value of the orbital excursion given by Eq. 6.12:

$$\hat{A}_\delta = \frac{H}{2sinh(kd)} \tag{6.12}$$

Eq. 6.11 could be rewritten as following:

$$for\ \frac{\hat{A}_\delta}{k_n} > 1.57 :\ \ f_w = exp(-6 + 5.2(\frac{\hat{A}_\delta}{k_n})^{-019}) \tag{6.13a}$$

$$for\ \frac{\hat{A}_\delta}{k_n} \leq 1.57 :\ \ f_w = f_{w,max} = 0.3 \tag{6.13b}$$

The roughness parameter k_n as used in the formulation of Mike 21 EMS (Eqs. 6.13a and 6.13b) is therefore the wave related grain roughness height which is different than the wave related form roughness. In fact, since the bed form is considered as constant during the simulation, the effective wave related bed roughness is the same as the wave related grain roughness k_n.

Rijn (1993) proposed the following values for k_n:

$$ripple\ regime \qquad : k_n = 3d_{50} \tag{6.14a}$$

$$sheet\ flow\ regime \qquad : k_n = 3\theta d_{50} \tag{6.14b}$$

where θ is the peak mobility parameter equal to:

$$\theta = \frac{\tau_w}{(\rho_s - \rho)g d_{50}} \tag{6.15}$$

where τ_w is the wave related bed shear stress provided by Eq. 6.16:

$$\tau_w = \frac{1}{2}\rho f_w U_w^2 \tag{6.16}$$

where U_w, the orbital velocity just above sea bed provided by Eq. 2.11 and f_w is given by the Eqs. 6.13a and 6.13b.

In order to calculate k_n, is it therefore necessary to determine the sediment transport regime as described in Eqs. 6.14a and 6.14b. Using the wave mobility number, Ψ, as proposed by Soulsby (1997). The author suggested the following:

$$\textit{ripple regime} \quad : \Psi < 150 \tag{6.17a}$$
$$\textit{sheet flow regime} \quad : \Psi \geq 150 \tag{6.17b}$$

where Ψ is expressed by Eq. 6.18:

$$\Psi = \frac{U_w^2}{g(s-1)d_{50}} \tag{6.18}$$

The values of the Reynolds number is calculated according to Ψ, in order to evaluate the different type of regimes present during the experiments. The corresponding Reynolds number is equal to:

$$R_w = \frac{U_w \hat{A}_\delta}{\upsilon} \tag{6.19}$$

Concerning the relation between R_w and the type of regime, it is defined as follows:

- laminar range regime : $R_w < 10^4$
- hydraulic smooth regime : $10^4 \leq R_w \leq 10^5$
- hydraulic rough regime : $R_w > 10^5$

Using for each water depth the waves characteristics as described in Table 6.1, it is possible to calculate Ψ and R_w at each wave gauge (since each wave gauge is located at a different water depth, see Fig. 6.3). A representative result at wave gauge P3 and water depth $d = 0.7\ m$ is given in Fig. 6.5. The wave mobility number, ψ is plotted with a logarithmic scale according to the wave related Reynolds number R_w.

It appears that ψ increases with R_w, however, it remains less than 200 for almost all the cases. The wave mobility number decreases when water depth increases. This could be clearly shown when comparing all the results of the calculation of ψ and R_w provided in Appendix F.2. The same is applied for the wave related Reynolds number. It decreases when water depth increases. Furthermore, the values of R_w are almost equal to one, for wave gauges P5 and

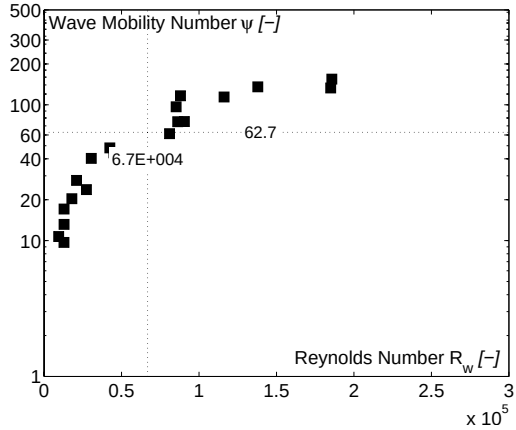

Figure 6.5.: Wave mobility number ψ according to Reynolds number R_w at wave prove P3, for $d = 0.7\ m$

P6 where water depth is very high compared to water depth at wave gauges P1 to P4. The values of R_w provided in Appendix F.2 shows that they are generally less than 10^5 although some waves for some water depths showed high values. Such values however remained always less than $2.5E+5$.

The average values of ψ and R_w are given in Fig. 6.6. Each white point corresponds to the average value at a wave gauge for each water depth as described in Table 6.1. The dark points correspond to the total average values at each wave gauge for the combined water depths. The values of the wave mobility number, ψ (see Fig. 6.6a), indicate the wave general sediment transport regime in the wave tank in a ripple regime since they are less than the threshold value of 150 (see Eq. 6.17a). These results are easily confirmed by the experiments carried out with a mobile bed (see Chapter 5) where it is shown that the main sediment transport regime is assured by the formation of a small ripple over the bed formed with finer granular sand. The wave mobility number at gauge P5 and P6 is almost equal to 0. At this location the water depth is very high, in addition to the fact that no sediment are present at this location.

Concerning the wave related Reynolds number, R_w (see Fig. 6.6a), the total average values are comprised between $4E+4$ and $7E+4$. This confirms that the main hydraulic regime is a transitional one, or hydraulic smooth range as expressed above. This regime usually excludes the sediment transport with sheet flow regime. Hence, this brings additional confirmation concerning the values found for the wave mobility number.

The results can be summarized as follows:

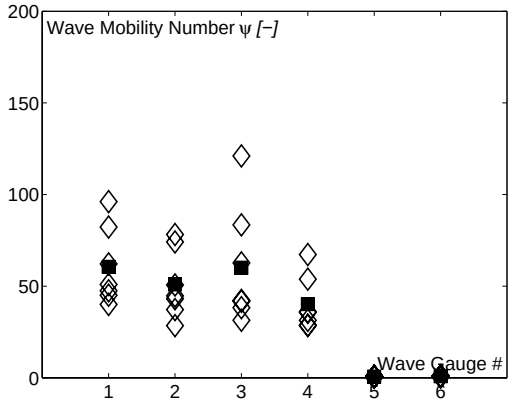

a)

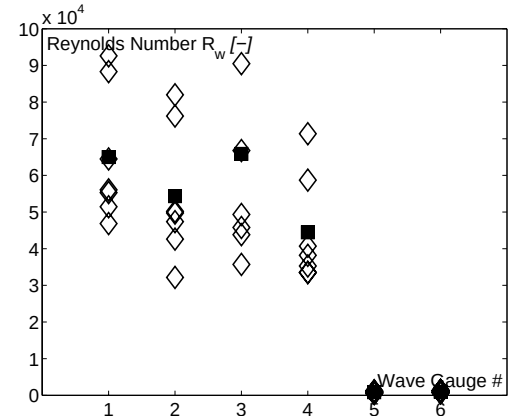

b)

Figure 6.6.: Mean values of (a) the wave mobility number ψ and (b) the wave related Reynolds number R_w at each wave gauge

- $\psi < 150 \Rightarrow$ sediment transport with ripple regime
- $R_w < 10^5 \Rightarrow$ laminar or hydraulic smooth range

It is possible afterward to calculate Nikuradse roughness parameter k_n. For the case of ripple regime, and for $d_{50} = 0.18\ mm$, the proposed adjusted value to be used in Mike 21 EMS is as follows:

$$k_n = 3d_{50} = 0.00054\ m \tag{6.20}$$

6.2.5. Agreement of the numerical model with experimental tests

The comparison between experimental and numerical tests provides the "first version of the calibrated numerical model" as described in Fig. 6.1. This comparison is carried out on the basis of the results of wave heights during the experimental tests, for water depth $d = 0.35\ m$ and at each wave gauge as described in Table 6.1 and Fig. 6.3. A verification is then required for another water depth (for instance $d = 0.7\ m$).

Using the numerical model of the wave tank described in Section 6.2.1, and the boundary conditions for waves measured at gauge P6, it is possible to calculate the standing wave field in the wave tank based on the calibrated values as described above. In order to better understand the wave field morphology resulting from the numerical modelling, an example is provided in Fig. 6.7.

A wave absorbing sponge layer is put all along the Y axis at $X = 0$. Waves are being generated at $X = 50$, the location of the wave gauge P6, in order to get the exact boundary condition as in experimental tests. When the propagation starts, waves move in both directions $X-$ and $X+$. Waves propagating in $X-$ direction, are absorbed by the boundary sponge layer provided by Mike 21 EMS and they are not capable to reflect on the wave tank walls and disturb the waves propagating in the $X+$ direction.

When approaching the beach, incoming waves (wave propagating in the $X+$ direction) are firstly being reflected by the transitional steep slope of 50%. This explains why the wave heights vary significantly when $X < 150$. This phenomenon is due to the superposition of reflection and incident wave in that area. After passing the steep bottom, the wave running on the 3% bottom slope are being loosely damped and decay slowly until breaking.

The morphology of the wave field in Fig. 6.7 is almost the same for all the modelled cases (i.e. all the wave in series in Table 6.1), however, the main variable remains the wave height at each point that depend on the wave used as a boundary condition.

Many values of the calibration variables (breaking parameters) have been tested in order to obtain the best correlation factors as shown in Table 6.2. The

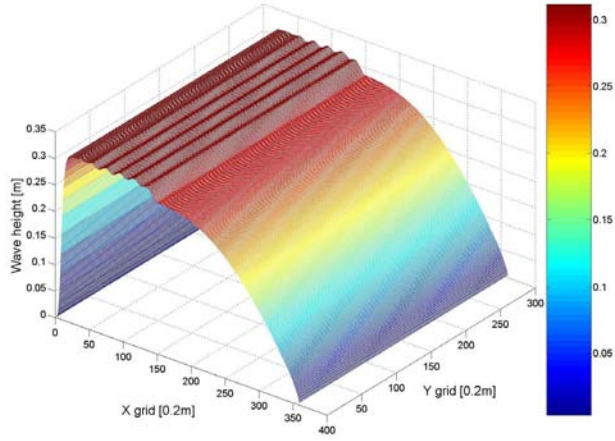

Figure 6.7.: Waves generated with Mike 21 EMS in the numerical model of the wave tank for $d = 0.35\ m$, the wave 20, and adjusted parameters N ° 6

first test considered in with the default variable recommended by Battjes and Janssen (1978). The best correlation factors obtained for such values are for the wave heights at wave gauges P5 and P6. This result was expected, since, at this level of the wave tank, propagating waves are not yet significantly affected by the bottom roughness and breaking. This is confirmed by the fact that the correlation factors at these two gauges remain constant when γ_1 and γ_2 varies.

N °	γ_1	γ_2	k_n	P1	P2	P3	P4	P5	P6
1	0.88	0.88	0.00054	0.625	0.514	0.856	0.867	0.967	0.997
2	0.88	0.67	0.00054	0.669	0.545	0.907	0.905	0.967	0.997
3	0.7	0.67	0.00054	0.663	0.557	0.892	0.895	0.967	0.997
4	1.2	0.67	0.00054	0.701	0.584	0.875	0.881	0.967	0.997
5	1.5	0.67	0.00054	0.656	0.553	0.868	0.875	0.967	0.997
6	**1.06**	**0.67**	**0.00054**	**0.71**	**0.599**	**0.909**	**0.907**	**0.967**	**0.997**

Table 6.2.: Correlation factors for different values of wave breaking parameters

For very low water depth, i.e. at wave gauges P1 and P2, correlation factors are the lowest (see Table 6.2 or $d = 0.35\ m$ in Appendix F.3). This could be explained by the fact that the calibration parameter at this level has

a very strong effect on wave heights. Hence, a slight decrease in γ_2, in scenario N$^\circ$1 and 2, increases the correlation factor at gauges P1 to P4. Additionally, a decrease in γ_1 results in lower correlation values. It has to be noted that a strong increase in γ_1 decreases too the correlation factor. Hence, no specific rule could be issued. However, systematic variations of γ_1 lead to the best correlation that could be obtained for wave heights which is scenario N$^\circ$6 in Table 6.2. In their calibration effort, Mai, Ohle and Daemrich (1999) found the best correlation factors for $\gamma_1 = 1.05$

A verification of the adjusted model is carried out for the average water depth of $d = 0.7\ m$. The results shown in Appendix F.3 prove that for higher water depths, it is much easier to obtain better correlation factors mainly at wave gauges P1 and P2. The adjustment carried out with the inclusion of the porous protection structure as described in Fig. 6.1 is proposed in Chapter 7.

The calibration of the numerical model allowed the following results. They will be used thereafter in order to carry out the numerical modelling of the brushwood fences:

- Setting up the numerical model of the wave tank with adequate grid size
- Calculation of the wave breaking parameters
- Calculation of the bottom roughness of the wave tank

7. Numerical modelling of brushwood fences

After the calibration of some major variables in Mike 21 EMS related to bottom roughness and wave breaking (see Chapter 6), one important variable remains to be calibrated which is the porous media. In the following sections, a detailed analysis of the related calibration in presented, based on relevant experimental results. Afterwards, a numerical analysis will be provided describing the effect of a single and double gap in a protective porous media and the resulting wave field in the enclosed area. Therefore, the objectives of this chapter are the following:

- To adjust the numerical model of the brushwood fences based on the experimental results of Chapter 4
- To suggest some design rules for the gaps in the brushwood fences on the basis of the wave field calculation in the sheltered area

The effect of a single gap in a brushwood fence on sediment transport was investigated in Chapter 5. However, no detailed description of the diffracted wave field in the sheltered area was provided. Therefore, this chapter aims to provide a dimensionless analysis of the wave field for different gap dimensions and gaps spacing.

7.1. Adjustment and modelling of a porous media

7.1.1. Input based on experimental results

The experimental results presented in Chapter 4 are used in order the select the transmission coefficients related to each water depth, porosity of the structure, and other variables if needed. In Mike 21 EMS, the porous media is always considered as emerging, hence specific attention should be given to experimental results where the brushwood fences are emerging ($R_c \geq 0$). The different numerical tests shown in Table 7.1 are to be considered based on similar conditions during experimental tests.

For each scenario, a transmission coefficient is evaluated relative to water depth, three corresponding porosities, and five periods. Although the

N °	porosity p [-]	depth d [m]	wave period T [s]
1	0.16-0.36-0.62	0.35	2.38-2.79-3.11-3.68-4.05
2	0.16-0.36-0.62	0.50	2.38-2.79-3.11-3.68-4.05
3	0.16-0.36-0.62	0.70	2.38-2.79-3.11-3.68-4.05
4	0.16-0.36-0.62	1.00	2.38-2.79-3.11-3.68-4.05
5	0.16-0.36-0.62	1.25	2.38-2.79-3.11-3.68-4.05

Table 7.1.: Water levels and periods considered of the calibration tests of the porous media based in experimental conditions

structure height has an influence on the transmission coefficient, this influence is relatively low when compared to the influence of porosity. Hence, the transmission coefficient calculated by the experimental tests is a simple and rough average for each porosity and each water depth corresponding to $R_c \geq 0$. The results of are presented in Fig 7.1.

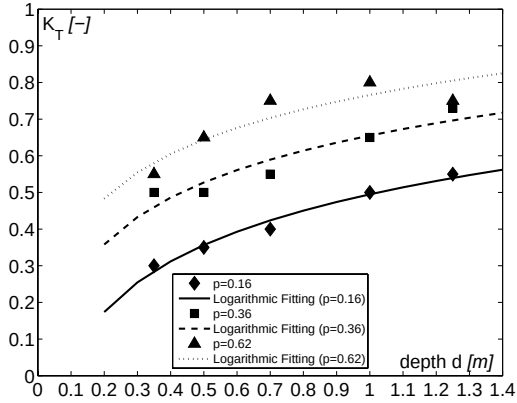

Figure 7.1.: Transmission coefficients related to experimental tests for the use in the numerical modelling

The transmission coefficients are evaluated in Fig 7.1 according to the water depth at the structure and its porosity. It can be seen that the logarithmic fit corresponds to the higher correlation factor. The effect of porosity is clearly shown. For higher ones, the waves are less damped and the transmission coefficient is high. Additionally the water depth variation seems to have the same influence with a lower rate. Hence, K_T increases with d. This could be explained by the fact that a wave is less damped by the bottom friction and more easily transmitted by the structure. Furthermore, the results show the importance of selecting appropriate transmission values in

direct relation with water depth. For numerical modelling, when selecting the porous media, K_T needs to be changed every time the water depth varies.

The above-mentioned results will be used in the calibration of the porous media and the selection of the correspondent friction coefficient, the K_T being related in Mike 21 EMS to a friction coefficient.

7.1.2. Friction factor used as a porous media

Modelling of partial reflection and transmission of waves, from e.g. porous rubble mound breakwaters or brushwood fences, is specified through a friction factor describing the frictional loss in the Elliptic Mild-Slope Wave Module, Mike21 EMS. For the calculation of the friction factor, it is only needed to specify the water depth and wave period as presented in Table 7.1.

The porous structure is therefore replaced by a "wave absorber" with a defined width, stone characteristics, and laminar and turbulent resistance parameter. It must be equal to the width of the brushwood fences in the present case. As in physical modelling, the width considered is equal to $b = 0.6\ m$.

The most comprehensive work that introduced the friction factor term describing the energy loss inside the absorber was made by Madsen (1983). The author presented a theoretical solution for the reflection of linear shallow water waves from a vertical porous wave absorber on a horizontal bottom. The analytical expression for the reflection coefficient is therefore determined as function of the porosity, the friction factor, the wave number multiplied by the width of the absorber, and the water depth. Additionally, the friction factor is related to parameters describing the incoming waves and the absorber characteristics. The reflection coefficient and the friction factor are related by applying the Lorentz' principle stating that the average rate of energy dissipation should be identical whether evaluated using the true non-linear resistance law or its linearized equivalent. The expression is defined using Eq. 7.1:

$$\int_0^b \int_0^T f \frac{\omega}{n} U^2 \, dt dx = \int_0^b \int_0^T (\alpha + \beta |U|) U^2 \, dt dx \tag{7.1}$$

where f is the friction factor, n the porosity of the wave absorber, α and β are variables depending on water depth, porosity and kinematic viscosity, and U is the main variable that depends on incident and reflected wave heights, more specifically, the reflection coefficient, and the water depth.

Mike 21 EMS has included a solver of Eq. 7.1 that calculates the values of K_R (K_T is then calculated using Eq. 2.20) and as a function of the friction factor for a defined wave period and water depth. A first result of the scenario N ° 3 in Table 7.1 is shown in Figs. 7.2 and 7.3. The friction factor is firstly

calculated as a function of the transmission and reflection coefficients for different wave periods (see Fig. 7.2). For a fixed friction factor, the wave period increases with the transmission coefficient. However, the reflection coefficient decreases when the wave period increases.

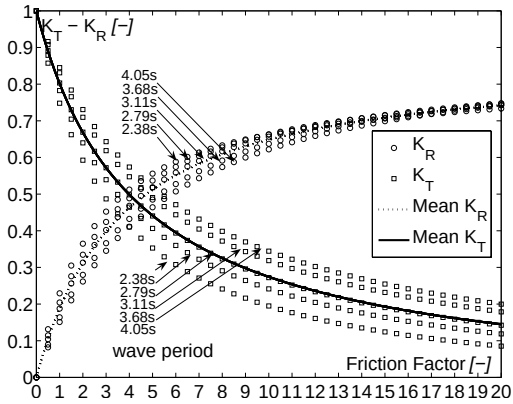

Figure 7.2.: Calculation of the friction factor according to reflection and transmission coefficient by Madsen (1983) for $d = 0.7\ m$ and variable wave period

Concerning the effect of water depth, the results shown in Fig. 7.3 prove that the transmission coefficient increases with water depth. This could be easily confirmed by the results of the physical modelling. As a result, the reflection coefficient decreases when the water depth increases. The curves shown in Fig. 7.3 are the mean values of K_T and K_R calculated for every water depth and wave period as presented in Appendix F.4.

The variation of the friction factor is also proved to be larger for small values of K_T since its curves tends to zero when f tends to infinity. Hence, when K_T is low, the influence of the variation of the wave period or the water depth on the values of the friction factor becomes greater. It is therefore recommended to change the value of f when different values of water depths or wave periods are selected as a function of K_T.

For the present investigation, the friction factor f will be changed as a function of the water depth only. The variation of the wave period and its influence on the transmission coefficient is going to be considered in the comparison between the experimental and numerical results.

On the basis of the above mentioned results, it is possible afterwards to select the friction factor after defining K_T and the water depth. This follows 3 steps:

- selection of a water depth

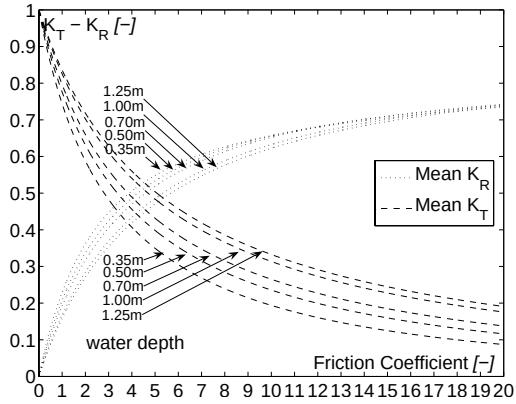

Figure 7.3.: Calculation of the friction factor according to reflection and transmission coefficient by Madsen (1983) for mean values of wave periods and variable water depth at the structure

- selection of the structure porosity and related K_T
- selection of wave period and the friction factor, or direct selection of the friction factor for a mean K_T value

The selected water depth for the following calculations will be $d = 0.7\ m$, and the selected porosity will be $p = 0.36$. Using Fig. 7.1, the corresponding transmission coefficient based on experimental tests is equal to $K_T = 0.6$. The friction factor, based on results presented in Fig. 7.3 is equal to $f = 2.85$.

7.1.3. Comparison with experimental results

The comparison of experimental and numerical results is based on wave heights ($H1$ for experimental and $H2$ for numerical) measured and modelled at every location of wave gauge. Therefore, the correlation factors are calculated at each location for the selected water depth $d = 0.7\ m$ and for two different structure height, $h = 0.7\ m$ and $h = 1\ m$.

When comparing the results corresponding to the two structure heights, results of related to the water depth $d = 0.7\ m$ provides lower correlation factors for $h = 0.7\ m$ than for $h = 1\ m$, with an average value for $h = 0.7\ m$ of 0.72. The lowest correlation factor is given by the results of wave gauge P5 and equal to 0.524. The highest one at gauge P6 equal to 0.902. However the results for $h = 1\ m$ are the most satisfactory with an average correlation of 0.84. The lowest one are at wave gauge P5 as well and equal to 0.676. The highest one at gauge P6 as well and equal to 0.954.

The difference in the results for the two structure heights is mainly due to the water depth compared to the structure height. For the first comparison, the structure height is equal to water depth. Hence the transmission of wave during experimental results is not similar to the transmission of wave when the porous structure is much higher than the water depth. In fact, for the first condition, and for small wave periods and big wave heights, the transmission could occur by overtopping. This is not the case for a structure much higher than the water depth (i.e. $h = 1\ m$), where the wave are mainly transmitted through the structure and not overtopping the structure.

It has to be noted that the structure height in Mike 21 EMS could not be modelled and the porous media is consequently considered as a screen with a height that tends to infinity. Therefore, the experimental results provided for $h = 1\ m$ are nearer to the numerical conditions in comparison to the results for $h = 0.7\ m$. This explains why the correlation factors are much higher for $h = 1\ m$.

Concerning the highest and lowest values of correlation factors, it appears as mentioned above that they are located, for both water depth conditions, at the same wave gauges. The lowest at wave gauge P5, and the highest at wave gauge P6. In fact, for the numerical modelling, the initial wave characteristics are introduced at the same location of the wave gauge P6 during experimental tests. They are equal as well to the waves measured by P6. Hence, it is logical that the best correlation factors are located at gauge P6.

However, for the wave gauge P5, the only explanation that could be provided is that the reflected waves during the experimental tests on the wave maker are not numerically reproduced, the absorbing sponge layer being located at this place. Hence no reflection occurs numerically. It seems that the reflected waves do not have enough energy to propagate for the next locations of wave gauges P1 to P4 where correlation factors increase again.

7.1.4. The use of gaps in coastal protection structures

This following sections will discuss the effect of gaps on the wave field behind the structure. In lakes, as well as in seas, besides providing useful passages for small boats, such gaps enhance better exchange of aquatic fauna and flora between the nearshore shallow region and the enclosed protected area. Furthermore, by the diffraction of waves and the variation of bottom induced currents, gaps may allow better circulation of water mainly during low water level regimes.

Therefore, it is advantageous to create gaps in the offshore protection system, rather than one single long structure. The gaps in the "segmented" structure allow a constant proportion of wave energy to enter the protected

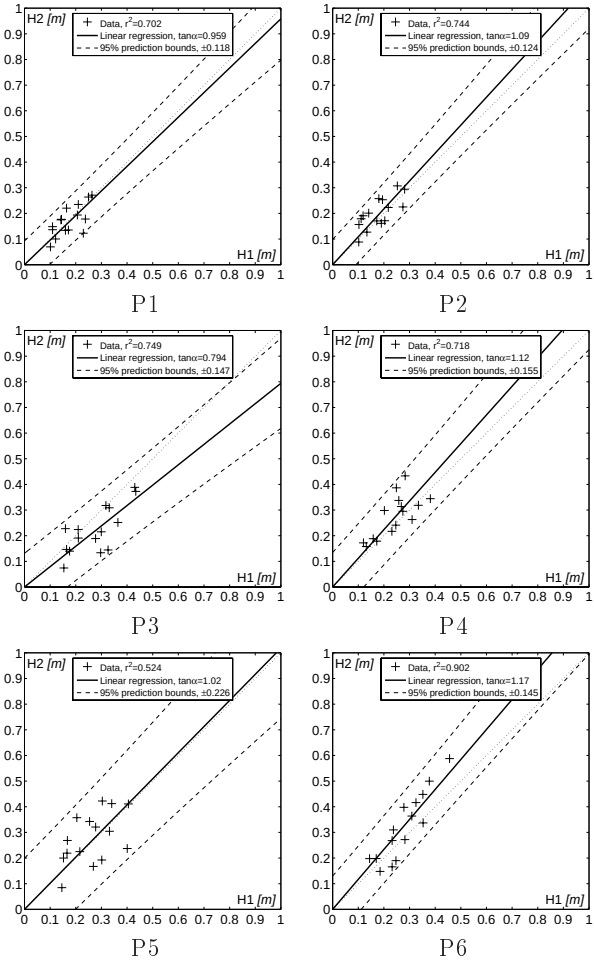

Figure 7.4.: Comparison of experimental results and numerical modelling for $d = 0.7\ m$, $h = 0.7\ m$ and $p = 0.36$

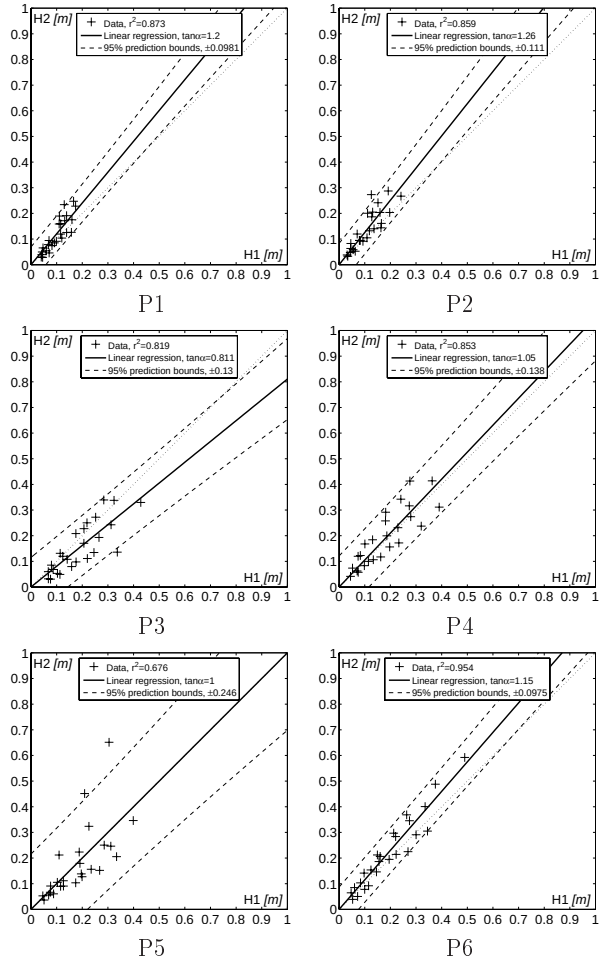

Figure 7.5.: Comparison of experimental results and numerical modelling for $d = 0.7\ m$, $h = 1\ m$ and $p = 0.36$

region. This feature contributes to a better longshore transport, and assists in maintaining water quality in the sheltered region. However, the evaluation of the impact of such gaps in this porous structure remains difficult to predict.

In the mid $80's$, Pos (1985) presented an experimental and numerical analysis of wave height variations when entering a single gap in a non-permeable breakwater. Using photogrammetric techniques, the author calibrated a numerical model (called *Wave*) on the basis of experimental results. An interesting aspect in his research was the use of a enclosed area behind the structure. The area was surrounded by beaches used as wave absorbers. Although the author's work seem to be comprehensive, he did not provide a detailed analysis on the effect of varying gap width, and multiple gaps, on the wave field in the shadow of the structure. However, he highlighted the existence of a wave height peak at the entrance of the gap.

Pos and Kilner (1987) provided a detailed analysis on the effect of the relative gap width, compared to wave length, on the diffraction coefficient at different locations at the entrance of the gap in the shadow zone. For different gap widths and wave lengths, the author demonstrated the effectiveness of the linear wave theory in providing reliable results when calculating wave field due to a breakwater gap in the protected area (shadow zone).

In his numerical modelling based as well on the linear wave theory, Porter and Evans (1996) described the transmission and reflection coefficient through periodic arrays of breakwaters. They studied the effect of gap variation for one and two arrays of parallel breakwater on the transmitted wave energy using the dimensionless wave number. Although they didn't include any wave field investigation in the protected area, they introduced a new approach relating to transmitted and reflected wave to gaps geometry.

Filianoti (2000) analyzed for a detached breakwater and a single gap configuration, the diffraction of wind-generated waves in the shadow zone. After a brief comparison with results of the diffracted periodic waves, the author demonstrated that random (wind generated) waves could generate exceptionally large wave heights in the area behind the breakwater or at the entrance of the gap. He used the general theory of three-dimensional wave groups for that purpose. The author concluded that the unexpectedly high waves are due to the fact that they have a short crest and large directional spread.

A comprehensive experimental investigation on the diffracted and refracted random wave through breakwater single gap configuration was carried out by Yu et al. (2000). The authors studied the effect of varying gap widths in a non-permeable breakwater for different wave periods, heights, and directions. They demonstrated that the diffraction coefficient for regular waves outside the shadow zone is higher than the one for random waves. However, in the shadow zone, the diffraction coefficient is mostly influenced by

the directional spreading of the waves. Similarly to Filianoti (2000), Yu et al. (2000) proved experimentally that diffraction coefficient in the shadow zone increased with the directional spreading of the incident random waves.

In an attempt to compare solid and permeable breakwaters, Bowen and Mclver (2002) analyzed the effect of a gap in infinite breakwaters, on diffracted waves with variable incidence angle. He proved that with permeable barrier the diffraction coefficient is almost 30% lower than for a solid barrier. The authors numerical investigation was followed later on with very similar research conducted by Mclver (2005). Instead of using one single gap, the author, using the same numerical technique, analyzed the effect of segmented breakwater on diffracted wave. Both numerical investigations were not able to provide neither easy tools for evaluating the wave field in the sheltered area, nor suggesting a simple dimensionless analyzes for calculating the diffracted wave heights.

Furthermore, many physical experiments were carried out by several researchers that concerned segmented breakwaters such as Abul-Azm and Williams (1997), Stamos and Hajj (2001b) and Bowman and Pranzini (2003) of normal and oblique waves. None on them suggested comprehensive description of the wave field behind the structure. However, it was proved that such experiments could helps in identifying optimal widths of gaps and breakwaters.

Based on the above description, the following conclusions are suggested:

- Concerning the protected zone (also called the sheltered zone), there is no detailed description of the entire region (from the structure to the shore) and how wave field varies as a function of gap width and number.
- The approach suggested by Pos (1985) could therefore be used in order to provide a detailed wave field description for a *permeable* structure.
- All the described researches does not provide a comprehensive investigation of the effect of different variables like wave period and length, gap width and number, structure permeability, etc.
- Concerning a gap in a permeable structure, Bowen and Mclver (2002) and Mclver (2005) did not consider the effect of the variables. In addition, no basic rules and recommendations for gap design were provided.

Since the brushwood fences are more commonly used to encircle or surround the entire part of an eroded zone, the approach for studying the wave field and the gap effect will be based on the numerical model of the wave tank as described in Section 6.2.1.

7.2. Effect of a single gap on the wave field in the protected area

As previously mentioned, gaps are advantageous in the brushwood fences for many environmental reasons. They would allow a constant proportion of wave energy to enter the protected region. This feature contributes to a better longshore transport and assists in maintaining water quality in the sheltered region.

However, the evaluation of the impact of such gaps in a porous structure such as brushwood fences on the wave field in the shadow zone remains difficult to predict. In order to better understand such impact, the effect of one single gap will be assessed first. Since the problem is two dimensional, the calibrated 2D numerical model Mike 21 EMS will be used. Using this module, it is possible to calculate a modified wave field, since the combined effects of shoaling, refraction, diffraction, and partial reflection and transmission are included for a gently sloping bathymetry.

7.2.1. Boundary conditions and effect of linear infinite protection

The numerical investigation of the wave field is carried out in an enclosed area corresponding to the area of the wave tank behind the structure as described in Fig. 3.1. In a reference to Fig. 6.2 and Fig. 6.7, the porous structure is included in the numerical model at $Xdistance = 30\ m$ or $Xgrid = 300$.

The wave field in the enclosed area is shown in Fig. 7.6. In order to simplify the notation, the new origin of the X axis is brought to the X coordinate of the structure in the wave tank as described above. The enclosed area is limited on the two lateral sides by a sponge layer ($X = 1$ to 250, $Y = 0$; $X = 1$ to 250, $Y = 300$) in order to absorb the diffracted waves and to prevent any lateral reflection that may influence the wave field.

Before reaching the structure in the seaward direction, the incident wave height is equal to 0.25 m with a 2.31 s period. This corresponds to waves during an average wind event on Lake Biel (see Section 1.2). Fig. 7.6 shows that the generated waves are capable to propagate and decay smoothly on the 3% beach slope. The decay is due to the wave breaking process that starts at $X = 100$. At both sides of the protected area, wave decay abruptly due to the presence of the sponge layer. This could be seen at $Y = 0$ and $Y = 300$.

Therefore, in the following sections, the wave heights considered correspond to $21 \leq Y \leq 269$. Hence, the maximum "valuable" width of the protected area is equal to $W_{max} = 52\ m$. Noting that the sponge layer width is $20grids \times 0.2m = 4\ m$.

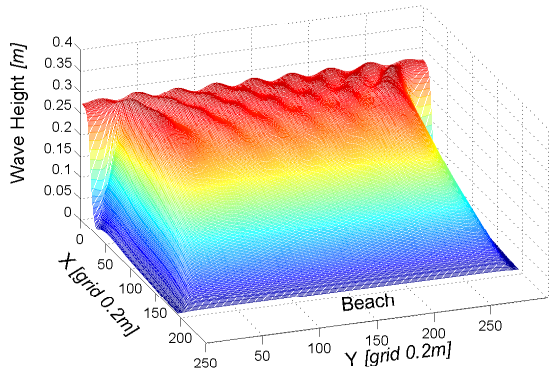

Figure 7.6.: Numerical modelling of the enclosed area in the wave tank with the absence of any protection structure

Fig. 7.7 shows the wave field after adding the porous structure at $X = 0$; $Y = 0$ to $Y = 300$. It is first tested without gaps. The wave field is uniform and waves begin to decay due to breaking at $X = 150$. Along the lateral sides, the waves decay as explained above due to the absorbing sponge layer. The effect of the porous media on wave damping without gaps can be clearly seen.

Before wave decay (or breaking), the wave field is almost uniform and wave heights are constant and almost the half of incident waves when no porous structure is added. This corresponds to the selected transmission coefficient equal to $K_T = 0.6$.

7.2.2. Wave field morphology in the vicinity of a single gap

In order to describe the wave field morphology in the enclosed area, a single gap is placed in the middle of the structure. Six gap widths are considered: $G = 1,\ 2,\ 4,\ 6,\ 8$, and $10\ m$. Fig. 7.8 clearly shows the two dimensional behavior due to the presence of a gap in the protection structure. The pattern of the transmitted and diffracted waves is totally different even for a very small gap width, when compared to a structure with no gap (Fig. 7.8 compared to Fig. 7.7).

Furthermore, the surface of the most affected area behind the structure at the middle of the gap does not increase significantly when the gap is four times wider (see Fig. 7.8b). This high wave area, with a "tongue" form, reaches a maximum width of 20 m at a distance almost 30 m away from the structure,

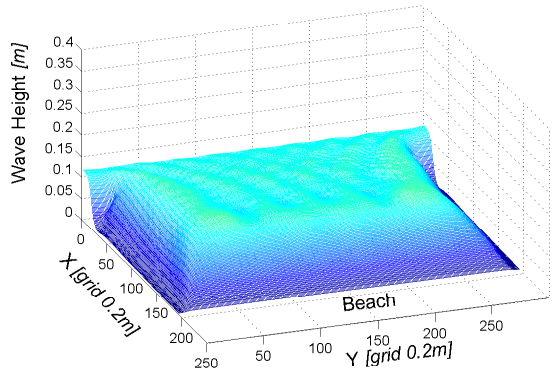

Figure 7.7.: Wave field in the enclosed area for a linear brushwood fence

independently of the gap width. In fact, wave heights are higher in the middle when the gap width increases (maximum height equal to initial incident wave height) and decay continuously while approaching the shore. On both sides of the highly affected area, wave heights and patterns are almost constant, for all the gap widths. This can be explained by the fact that the wave energy entering the gap is concentrated in the middle which allows a higher extent of high waves towards the shore and not in the Y direction. However, high waves are formed on both sides of the tongue only in the middle of the protected area (for $X = 150$). The results of all the gap widths are provided in Appendix G.1

The same pattern of wave diffraction was observed by Yu (1995). The authors presented an implicit description of the wave field behind a very thin porous semi-infinite breakwater due to long-crested waves, propagating in the normal direction (in similarity with the present case). He used the linear wave theory for his numerical modelling. Contrary to a non-permeable breakwater, the calculated wave field is proved not to be constant and the diffraction coefficient is proved to change significantly. Later on, McIver (1999) showed the same pattern using very similar approach but for variable angle of wave incidence.

7.2.3. Longitudinal and crossectional analysis of waves

The wave heights $H/H0$ in the protected area are calculated according to the distance to the shoreline $D/Dmax$ (see Fig. 7.9) and to the width of the protected area $W/Wmax$ (see Fig. 7.9) for different values of gap widths

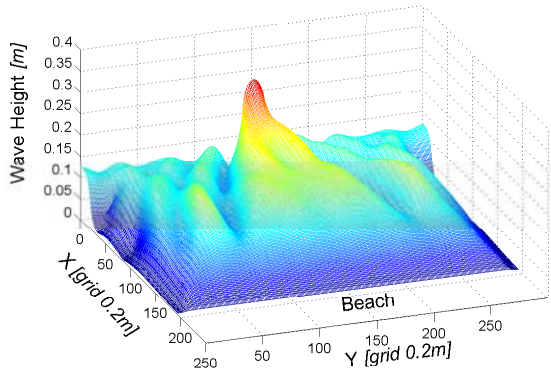

a)

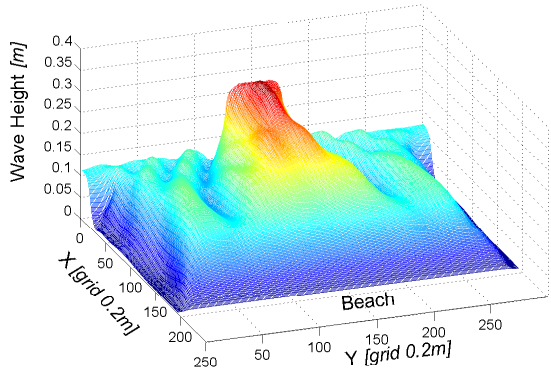

b)

Figure 7.8.: Wave field in the vicinity of a single gap in the porous shore protection structure for a gap width of (a) $G = 4\ m$ and (b) $G = 10\ m$

$G/Wmax$. The latter is considered in relation to the total width of the structure $Wmax = 52\ m$ as implemented in the numerical wave tank and explained in Section. 7.2.1.

Along the X direction at $Y = 150$ (see Fig. 7.6 for axes references), in the middle of the gap, the wave heights increase with the increase of the gap width (see Fig. 7.10). However, near the shoreline, the wave heights become almost identical (starting at $D/Dmax = 0.8$). After this threshold, the wave heights are equal as well to waves for the configuration with no gap. Furthermore, It has to be noted that the variation between wave heights is not identical along

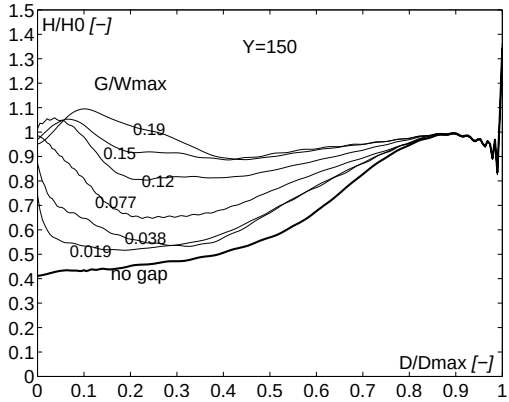

Figure 7.9.: Wave height $H/H0$ in single gap configuration and different gap widths $G/Wmax$ as a function of its the distance to the shoreline $D/Dmax$

the distance of the structure to the shoreline when compared to corresponding variation of gap widths. Hence, when the gap width $G/Wmax$ increases from 0.019 to 0.038 the wave heights increase until $D/Dmax = 0.3$. After this, wave heights are identical. However, when the gap width $G/Wmax$ increases from 0.038 to 0.077, wave heights are identical only after $D/Dmax = 0.8$. This shows that wave diffraction along the X axis could not be considered as proportional to the gap width.

For wide gaps ($G/Wmax \geq 0.12$), and when $D/Dmax < 0.2$, waves are up to 10% higher than the initial incident wave. This result brings out the effect of the diffracted and reflected waves on the edges of the gap that may increase the wave height in the protected area. This phenomenon has been identified as well by Pos (1985).

A typical cross-section, at mid-distance to the shoreline for $X = 100$, of the values of wave heights variation is provided at Fig. 7.10. This variation seems to have an identical pattern for all the gap width. The highest values of wave height variation are situated as expected at the middle of the section for $0.3 < W/Wmax < 0.7$.

Therefore, as far as the gap width is concerned, it may be concluded that the wave field in the protected area is mainly influenced in the middle, and less at the sides of the gap. The gap width has less effect on the influenced area and more effect on the wave heights in the middle.

When comparing wave heights $H/H0$ for different gap widths with wave heights with a no gap configuration, results show that in the strongly affected area, wave heights are 10 to 40% higher. They decrease rapidly towards the

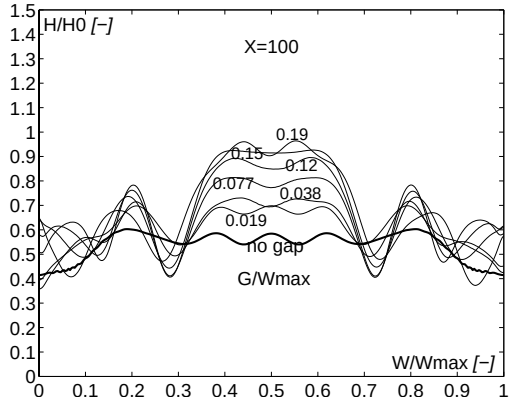

Figure 7.10.: Wave height $H/H0$ in single gap configuration and different gap widths $G/Wmax$ as a function of the width of the protected area $W/Wmax$

shore. At both sides of the gap, the wave heights are up to 20% higher.

The combined diffraction and refraction coefficients $K_{d,r}$ in the enclosed area are provided in Fig. 7.11 for two gap widths $G = 2$ and 10 m (see Appendix G.2 for all the results). They show mainly the impact of a big increase in the gap width on wave field near the gap. For $G = 2$ m, $K_{d,r}$ reaches its highest values (above 0.9) as expected at the entrance of the gap. In front on this area, $K_{d,r}$ decreases strongly (less than 0.7 before it decreases when approaching the shore. However, for a wide gap of $G = 10$ m, the peak values of $K_{d,r}$ shift toward the shadow zone inside the protected area almost 10% with a value greater than 1.05.

The analysis of combined diffraction and refraction coefficients proves as mentioned above that at a distance from the shoreline of almost 0.8, the wave field is no longer influenced by the gap.

7.3. Effect of two gaps on the wave field in the protected area

In the following simulations, the wave field behind the protection structure is analyzed for two gaps with a constant width of $G = 4$ m. The main variable considered is the spacing between two consecutive gaps, Es. The values tested are: $Es = 4,\ 8,\ 12,\ 16,\ 20,\ and\ 24$ m. Boundary conditions are the same as presented under Section 7.2.1.

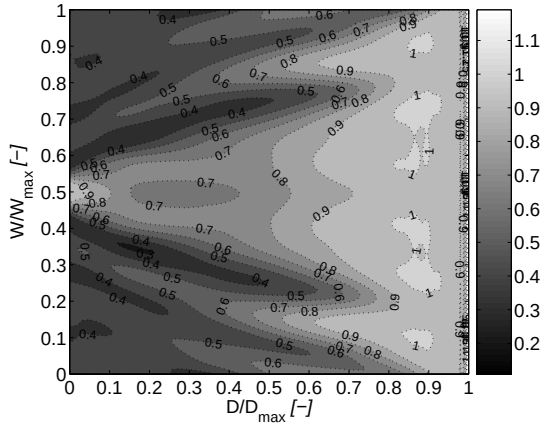

a)

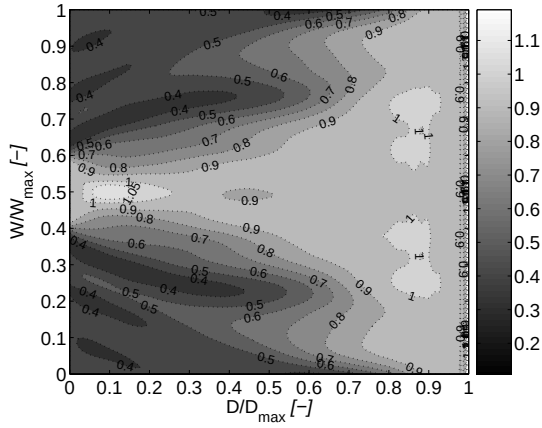

b)

Figure 7.11.: Combined diffraction and refraction coefficients $K_{d,r}$ in the enclosed area for a gap width of (a) $G = 4\ m$ and (b) $G = 10\ m$

7.3.1. Wave field morphology in the vicinity of two gaps

The wave field resulting from two gaps in the protection structure is shown in Fig. 7.12 (see Appendix G.3 for all the results). Compared to the wave field due to a single gap, the highly affected area by incident waves is almost twice as large, even for a small gap spacing of $Es = 4\ m$ (see Fig. 7.12a). The wave pattern on both sides of the protected area is similar to the wave pattern due a single gap. However, the wave field in the middle of the enclosed area is different because of the interaction of the diffracted waves entering the gaps.

For a small spacing peak values of wave heights occur between the two gaps. For a very large spacing, for instance 6 times the gap width ($Es = 24\ m$), this pattern disappears completely as shown in Fig. 7.12b. Therefore, an optimal gap spacing must exist, where the combined diffracted and refracted waves in each gap have no negative impact on wave field between the gaps as will be shown below.

7.3.2. Longitudinal and crossectional analysis of waves

The wave heights $H/H0$ in the protected area are calculated according to the distance to the shoreline $D/Dmax$ (see Fig. 7.13) and to the width of the protected area $W/Wmax$ (see Fig. 7.14) and thus for different values of gap spacing Es/G. When comparing wave heights for different gap spacing and wave heights with no gap configuration for $Y = 150$, it appears that for small spacings, the maximum wave heights are almost 50% higher than the waves with no gap. This corresponds to $Es/G = 1$ and 2 for $0.1 \leq D/Dmax \leq 0.5$ in Fig. 7.13.

However for larger spacing ($Es/G = 3\ to\ 6$), the maximum wave heights are only 20% higher. However, contrary to the values for a single gap configuration, where all the waves are higher than the waves with no gap configurations, it appears that the interference of the two diffracted wave fields in the two gaps generates wave heights even smaller than those for no gap configuration.

This could be clearly seen in Fig. 7.14 where for $Es/G = 5$, and 6, the waves in the middle and the second half of the protected area are smaller than the waves behind the structure with no gaps. This may be considered as detrimental to the uniformity of the wave field. Hence, Es/G values between 3 and 4 appear to be more adequate. Fig. 7.14 reveals as well this strong and rapid decrease in wave heights for $Es/G = 5$ and 6.

Furthermore, for $Es/G = 1$ and 2, the variation of wave heights on both sides are higher. Although waves are higher at the middle, for $Es/G = 3$, and

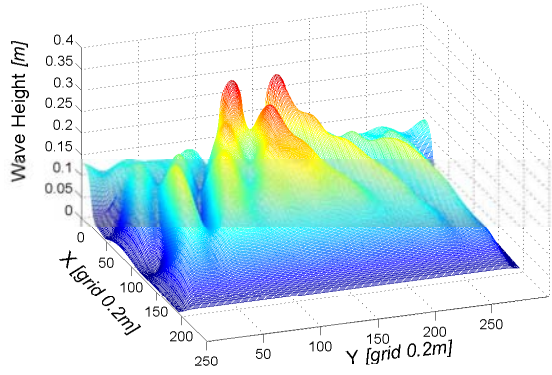

a)

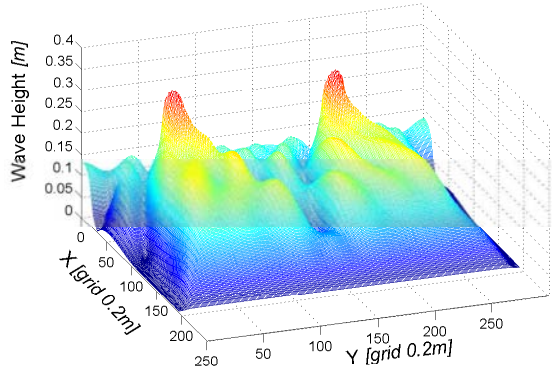

b)

Figure 7.12.: Wave field in the vicinity of two gaps in the porous shore protection structure for a gap width of $G = 4\ m$ and spacing between gaps of (a) $Es = 4\ m$ and (b) $Es = 24\ m$

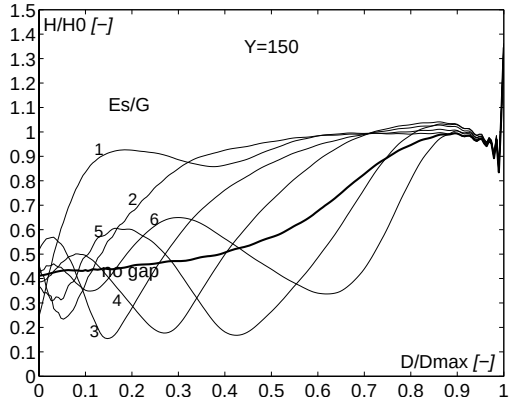

Figure 7.13.: Wave height $H/H0$ in two gap configuration and different gap spacing Es/G in the protection structure as a function of its the distance to the shoreline $D/Dmax$

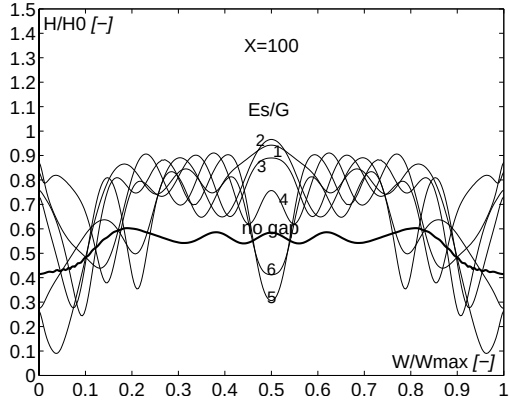

Figure 7.14.: Wave height $H/H0$ in two gap configuration and different gap spacings Es/G in the protection structure as a function of the width of the protected area $W/Wmax$

4 wave field seems to be more 'uniform'. Therefore, such values could be used as the basis of an optimal design.

The combined diffraction and refraction coefficients $K_{d,r}$ in the enclosed area are provided in Fig. 7.15 for spacing values of $Es = 4$ and 24 m (see Appendix G.4 for all the results). They show mainly the impact of a big increase in the gap spacing on wave field near the gap. For $Es = 4\ m$, $K_{d,r}$ reaches it highest values (above 0.9) between the gaps as a result of the superposition of diffracted waves. Very low values of $K_{d,r}$ are obtained between the gaps along the structure.

For $Es = 24\ m$, the wave field seems to be less influenced by the diffracted wave at each gap. No high waves are present between the gaps as for $Es = 4\ m$. However, at $D/Dmax = 0.3$, two areas of small waves are formed.

The threshold of $D/Dmax = 0.8$ where waves heights almost starts to be equal to those corresponding to the no gap configuration appears to be highest for a two gap configuration at $Y = 150$. The graphics in Figs. 7.13 and 7.15 show that wave beside the shoreline remains higher until $D/Dmax > 0.9$.

7.4. Analysis of some major variables

7.4.1. Influence of the wave period

The effect of the variation of the wave period on wave transmission is showed in Fig. 7.16. The transmitted waves tend to increase with the the period. For very small periods, the transmission waves are very low. This can be explained by the experimental results of fixed bed where it was demonstrated that the high wave frequency tend to dissipate their energy in the porous structure due to the drag coefficient. This numerical results could also be explained by the fact that the wave breaks before reaching the structure. Therefore, the residual energy that reach the structure becomes non-relevant. For high wave periods, although transmitted waves are very high, however, the transmission coefficient remains less than 1. No further investigation is provided in this current research. This issue needs to be treated systematically in the future.

7.4.2. Analysis of total energy loss variation

The total average energy per unit surface area of the wave behind the structure in the protected area, is the sum of the potential (PE) and kinetic energy (KE). The total energy per unit surface of the enclosed area E is calculated following the Eq. 7.2 (Dean and Dalrymple, 2002):

$$E = \overline{KE} + \overline{PE} = \frac{1}{8}\rho g H^2 \tag{7.2}$$

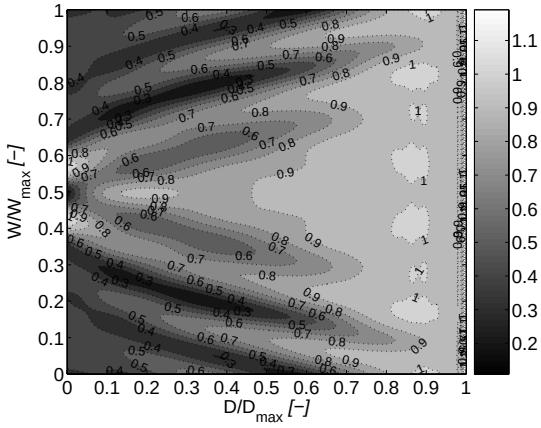

a)

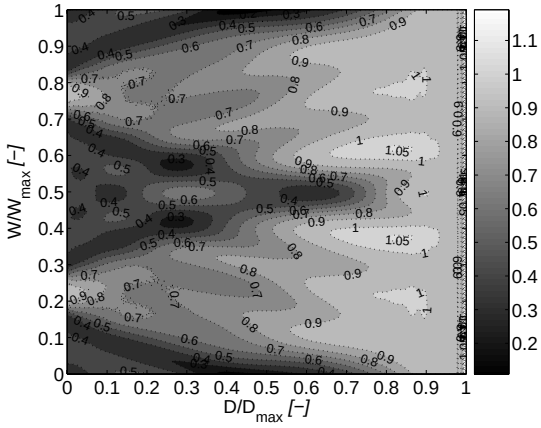

b)

Figure 7.15.: Combined diffraction and refraction coefficients $K_{d,r}$ in the enclosed area for a spacing of (a) $Es = 4\ m$ and (b) $Es = 24\ m$

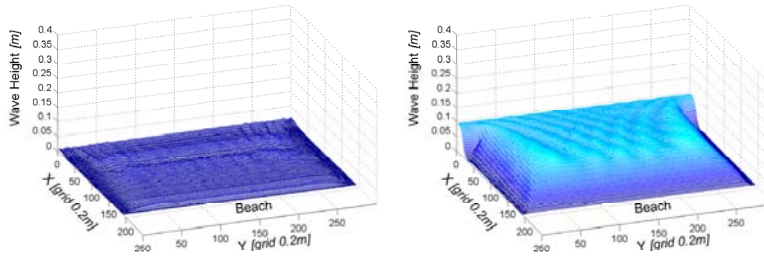

$T = 1.155\ s$ $T = 2\ s$

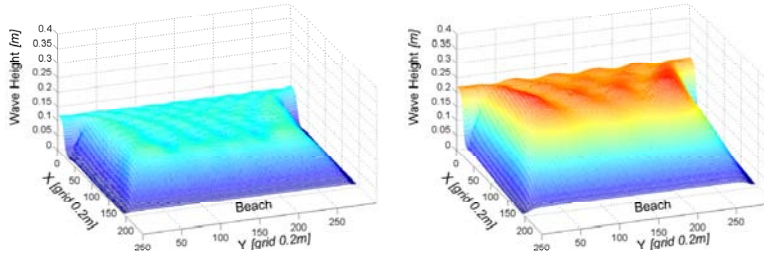

$T = 2.31\ s$ $T = 3.5\ s$

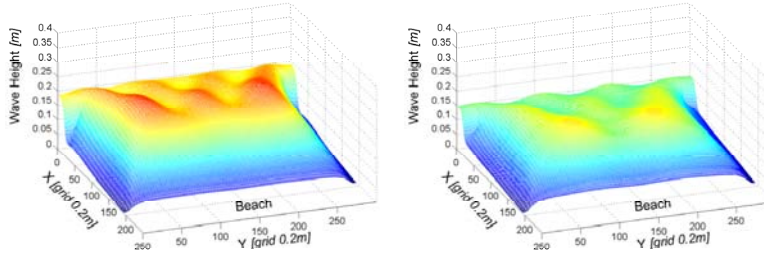

$T = 4.625\ s$ $T = 5.5\ s$

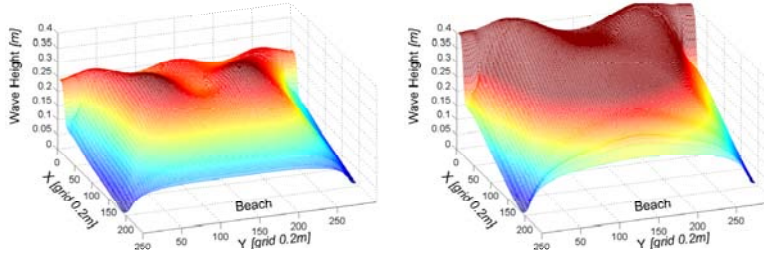

$T = 7\ s$ $T = 10\ s$

Figure 7.16.: Effect of wave period on the wave field behind a linear porous structure for $d = 0.7\ m$, $h = 1\ m$ and $p = 0.36$

where ρ and g are the water density and the acceleration of the gravity, respectively.

The dimensionless total average energy $E/E0$ for a single gap configuration is shown in Fig. 7.17, according to $G/Wmax$. The total energy of the wave field with no structure is expressed by $E0$. $E/E0$ increases linearly with the gap width. However, such increase is not directly proportional to the gap width. For a maximum value of 10 m gap width ($G/Wmax = 0.19$), the energy is only 1.5 times higher than the energy corresponding to a 1 m gap width ($G/Wmax = 0.019$).

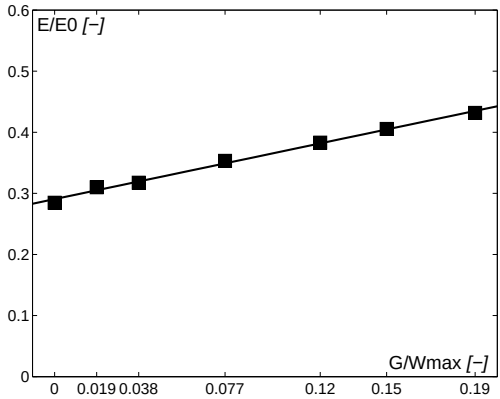

Figure 7.17.: Total average wave energy in the enclosed area behind the brushwood fences for one gap configuration

As shown in Fig. 7.18, the wave energy for two gaps is independent of the gap spacing, since the gap width for the second case is constant. This energy is almost equal to a constant value of 0.42. Furthermore, since the selected gap width for the two gaps configuration is equal to 2x4 m, the total energy entering the protected area for such configuration should be almost twice the total energy corresponding to a single gap of 4 m width.

This energy according to Fig. 7.17 is equal to 0.39. This shows that doubling the number of gaps corresponds to an average increase of only 7% of wave energy entering the enclosed area instead of 100%. Such result is directly related to the wave height reduction in the enclosed area behind the structure, due to the interferences of the diffracted waves behind the two gaps. This phenomenon appears to favor the reduction of the total energy of waves in the enclosed area.

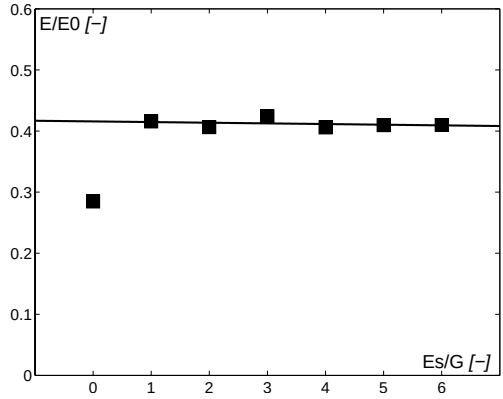

Figure 7.18.: Total average wave energy in the enclosed area behind the brushwood fences for two gaps configuration ($G = 4\ m$)

7.5. Conclusions for gap design

The numerical modelling of the wave field for a single gap configuration proved that high waves are concentrated in the middle of the protected area along the axis of the gap. On both sides of this area, wave heights are less influenced by the gap width. However, for high values of $G/Wmax$ (=0.12), wave heights are higher than the initial wave heights without any protection. A rule was proposed to use a relative gap width $G/Wmax$ less then 0.12.

Wave field for two gaps is different and significantly influenced by the spacing between the gaps. For low spacing values ($Es/G = 2$), waves in the middle of the protected area are high along the structure are very low when approaching the shore. For high spacing values ($Es/G = 5$), the wave field is also significantly deformed. However, values of Es/G comprised between 3 and 4 seem to be most appropriate since the corresponding wave field is less deformed. The two gaps configuration does not significantly increase the residual total energy behind the structure. It is relatively constant with the variation of the spacing between two gaps and increase slowly with the increase of a single gap width.

Since no numerical tests have been carried out with a movable bed, it was not possible to carry out further comparison of the experimental tests with movable bed. However, the wave field behind the brushwood fences modelled numerically would constitute the basis for setting-up the radiation stresses that are used as a boundary condition for modelling sediment transport.

8. Case Study: efficiency of brushwood fences field at Mörigen in Lake Biel

The objective of the case study is to model a real situation where brushwood fences were used in order to provide adequate protection of shore against erosion induced by wind-waves. Many of the numerical approaches as proposed in Chapters 6 and 7 will be utilized. This chapter doest not aim to provide any engineering solution for potential existent problems. However, it will describe the present real phenomenon based on the numerical modelling with Mike 21 EMS. Moreover, it will demonstrate how numerical tools could be used in order to model the wave field behind the protection structures. Boundary conditions (wave climate) are calculated on the basis of wind velocities and directions measured *in situ* over water and over land.

8.1. Site description and numerical model

8.1.1. General introduction and field measurements

The site selected as a case study is located at the South-Eastern shore of Lake Biel at almost 6 km South of Biel city. The location is called Mörigen (see Fig. A.1). The selection of this site was based on three main reasons:

- Many field surveys were carried out in this site: wind, waves, and bathymetric measurements
- This site is located almost at the middle of the shore side of Lake Biel where erosion is most active
- More than ten brushwood fences segments are located at this site used for wave damping

The segmented brushwood fences in Mörigen are shown in Fig. 8.1. Each extremity of a single structure was located using GPS technique that provided the Swiss coordinates X and Y. The altitude Z for each segment was measured locally. In addition to the positions of brushwood fences, wind velocities over water are measured at almost 2 m above the water level together with wave characteristics and the transmission coefficient of one single segment of brushwood fences at the upper part.

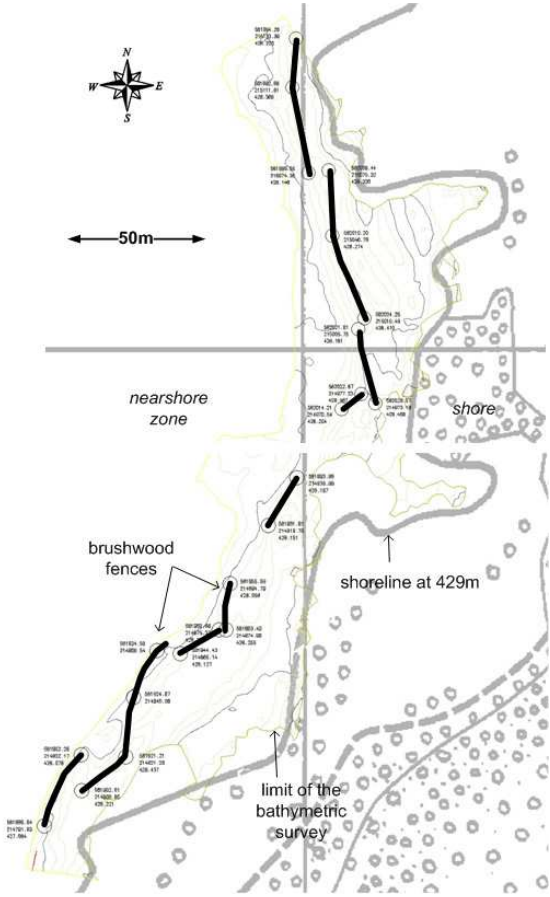

Figure 8.1.: Segmented brushwood fences at Mörigen in Lake Biel (Berne University for Applied Sciences)

Field Measurements of wind at Mörigen

In situ wind measurements at Lake Biel have been realized in several other localities. However, the measurements of wind at the site of Mörigen (see Fig. 8.2b), selected for the present case study, show substantial results concerning wind velocities for the two major regimes over Lake Biel (see Section 1.2). Instant over water wind velocities U_W and directions are measured during 6 months period (from first of October 2004 until the end of March 2005) with a Young anemometer (see Fig. 8.2b). Velocities and

directions are averaged at 10 minutes intervals, and presented in Fig. 8.3. Furthermore, the wind is measured at Neuchâtel ANETZ wind station (wind over land) for the same period and shown in Fig. 8.4. .

a)

b)

Figure 8.2.: (a) *In situ* wind and wave measurement platform at Mörigen; (b) Wind anemometer powered by solar panels

The comparison of over water (see Fig. 8.3) and over land wind (see Fig. 8.4) speeds and events shows relevant similarities. The events are selected when wind speed is significantly higher than 2.5 m/s and lasting at least 1 hour. Figs. 8.3 and 8.4 clearly show that events at Neuchâtel (at almost 5 km South of Lake Biel) occur at the same period and almost for the same direction trends as at Mörigen. However, the measured wind speeds are not similar for every event.

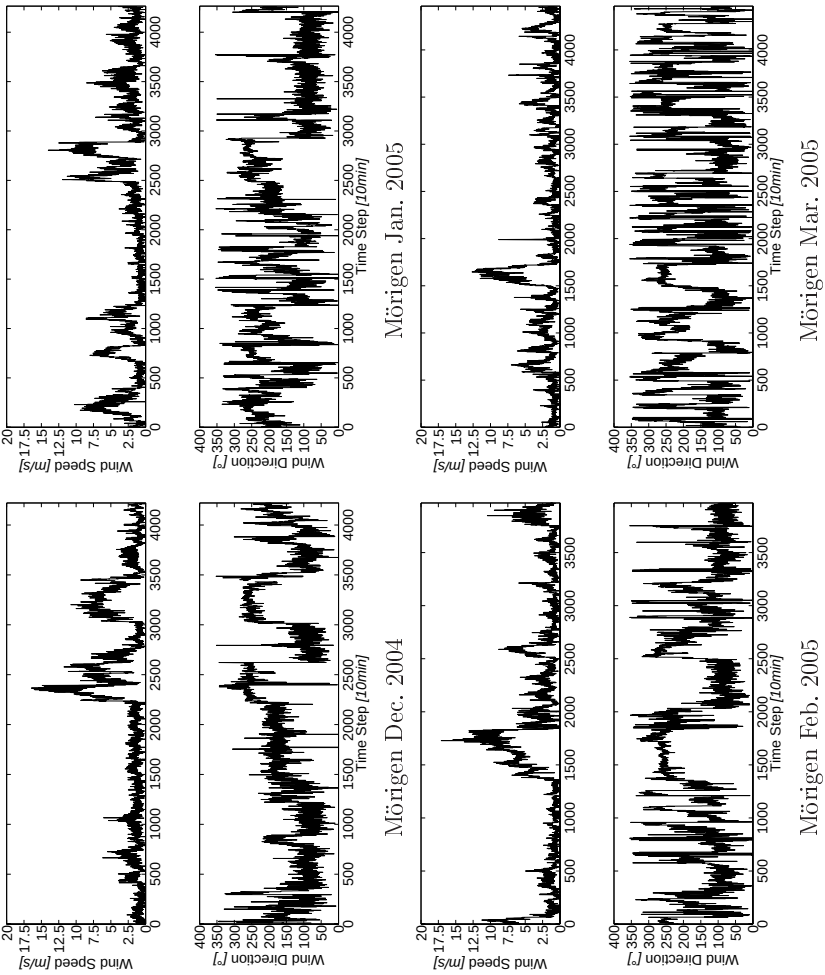

Figure 8.3.: Wind velocities and directions (over water) measured at Mörigen during the period [Dec. 2004 - Mar 2005]

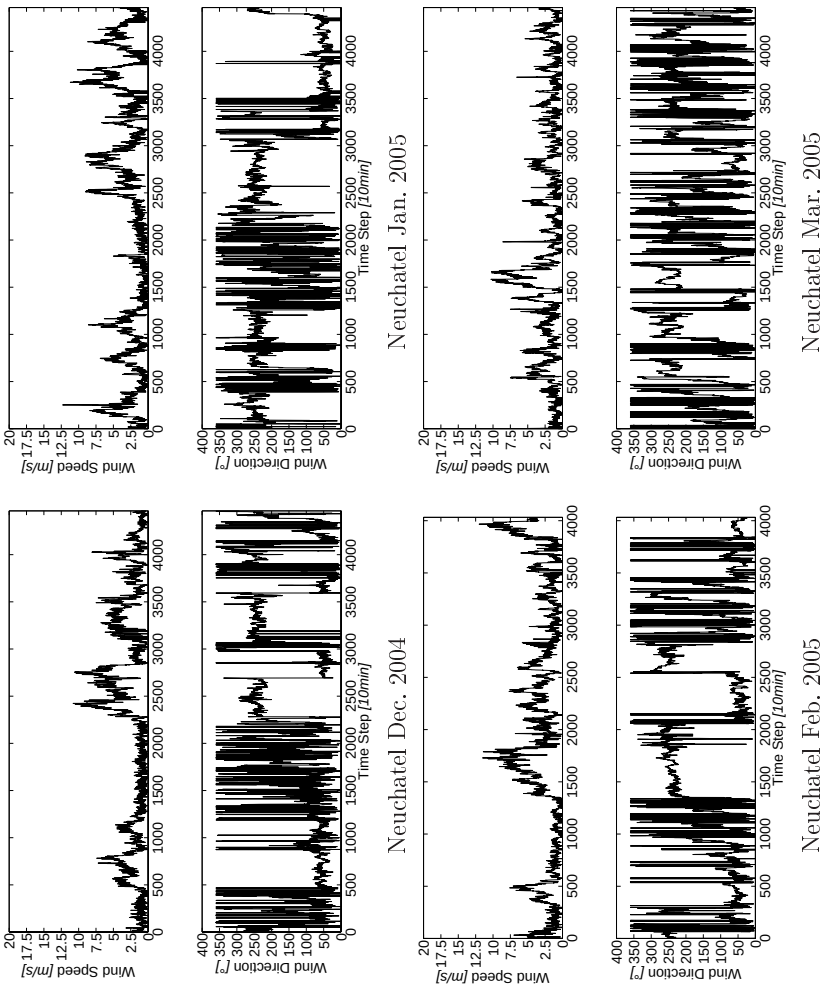

Figure 8.4.: Wind velocities and directions (over land) measured at Neuchâtel wind station, almost 15 km South of Lake Biel, during the period [Dec. 2004 - Mar 2005]

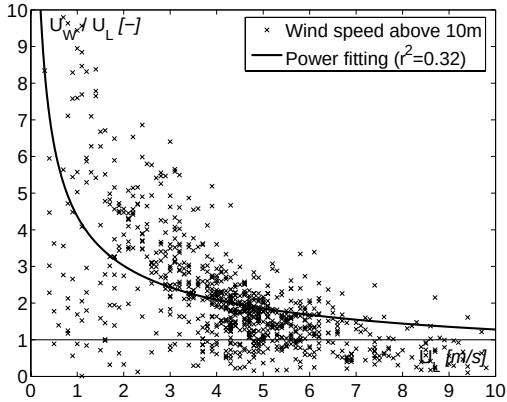

Figure 8.5.: Ratio of wind speed over water U_W at Mörigen to wind speed over land U_L at Neuchâtel according to U_L, for a wind sector [210 °-240 °] during the period [Dec. 2004 - Mar 2005]

Fig. 8.5 highlights the effect of wind speed variation due to transition from land to water. The data shown corresponds to wind speeds for the South-western wind events during the period [Dec. 2004 - Mar 2005]. It includes measurement during more than 10 wind events as shown in Fig. 8.3. Thus, wind speed tends to increase after a transition from a land surface. However, due to the behavior of water roughness as a function of wind speed, the ratio of over water wind speed at a fixed level to over land wind speeds (U_W/U_L) is not constant, but varies nonlinearly.

Fig. 8.5 provides the trend for the form of such variation. The exact magnitude and characteristics of the transition depend on the roughness properties of the terrain and vegetation on one hand, and on the stability of the air flow on the other hand. Resio and Vincent (1982) presented a simple approximation of this wind speed variation based on a logarithmic fitting curve to the asymptotic over land and over water wind speed values.

Furthermore, trends in Fig. 8.5 indicate, as expected, that wind speeds over water follow a power law. The ratio U_W/U_L tends to infinity when U_L tends to zero and to almost 1 when U_L tends to infinity. The latter fitting depends mostly on the location of on water measurement station and on the wind regime. For "mean" wind speeds (roughly varies between 6 and 10 m/s in Switzerland), corresponding to recurrent wind events, such fitting provides a rough ratio of U_W/U_L equal to 1.35. Thus, wind over water is 35% stronger than wind over land for average wind events. This rough estimation strongly depends on the nature of vegetation beside the lake and the local topographic

conditions. Therefore it could be not used for general applications.

Field measurements of the transmitted waves at Mörigen

The field measurements of waves was carried out at the upper part of the brushwood fences field in Mörigen. Waves were measured before and behind a typical segment of brushwood fences. Waves were measured during the same period as the wind measurements and the waves selected for analysis correspond to significant waves heights H_s greater than 0.15 m. Results of K_T according to the dimensionless freeboard R_c/H_s are provided in Fig. 8.6. During field measurements, the lake water level was always lower than the top of the brushwood fences. Therefore, the structure was always emerging and the transmission coefficient calculated is considered as maximal. The mean K_T value could be estimated for such conditions equal to $K_{T,mean} = 0.32$.

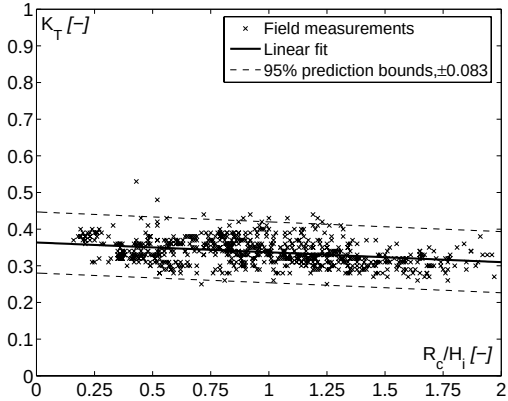

Figure 8.6.: Transmission coefficient K_T of typical brushwood fences at Mörigen according the relative freeboard R_c/H_s for a structure height $h = 1.12$ m (Berne University of Applied Sciences)

Bathymetric survey and grain distribution

The bathymetry of the nearshore region of Mörigen was measured accurately. Many sediment samples were analyzed and shown that the bottom is mainly constituted of granular sand and gravel. The samples were taken at the lakeshore during the winter 2000 from both bed material and from the cover layer. The thickness of the cover layer observed is almost 0.05 m without a clear distinction with the bed material. The bottom granulometric characteristics, are as follows:

- 72.34% sand, 27.66% gravel
- $d_{50} = 0.342\ mm$, $d_{60} = 0.393\ mm$, and $d_{10} = 0.119\ mm$

As shown in Fig. 8.7, the bathymetric survey was very dense and allows a precise numerical interpolation of the nearshore region without loosing information.

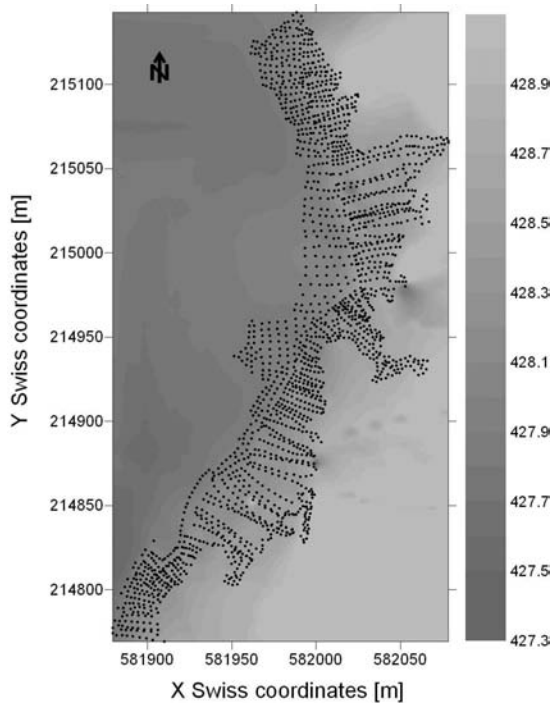

Figure 8.7.: In situ bathymetric measurements of the bottom nearshore region at Mörigen (Berne University for Applied Sciences)

8.1.2. Anemometric and hydrodynamic conditions

The long term statistical analysis of the wind in the region of Lake Biel is described in Section 1.2. For the present case study, it is proposed to calculate incoming wave in the region of Mörigen using the numerical analysis by Swan model (Booij et al., 1996). Since the time of wave measurements in the nearshore region of Mörigen is too short, a long term analysis of incoming waves could not be carried out. Therefore, the proposed methodology described in Section 1.2 is used.

Three main wind regimes are considered for Mörigen as following:

- South-Western wind (sector [210 °-240 °]) "Le Vent": $fetch = 7000\ m$
- North-Eastern wind (sector [30 °-60 °]) "La Bise": $fetch = 4500\ m$
- North-Western wind (sector [300 °-330 °]) "Le Joran": $fetch = 3500\ m$

By using the long term statistical analysis for the three regimes, a calculation of wind velocities for every wind sector and return period could be made. Afterwards, the calculation of waves is carried out in Swan, using as input wind velocities and directions. Since waves are refracting near Mörigen, incoming wave directions are different than wind directions. Therefore special attention should be given to wave direction used afterwards in Mike 21 EMS, when calculating wave field in the brushwood fences location. Hence, two points for boundary waves are considered for the numerical input as following:

- $P1(X = 581800; Y = 215200)$: "Bise" and "Joran" wind regimes
- $P2(X = 581600; Y = 214800)$: "Vent" wind regime

By calculating wave heights, periods and directions at points $P1$ and $P2$ in Swan, it is possible to introduce these values as boundary conditions for the modelling of the wave field at Mörigen. Tables H.1, H.2, and H.3 provide wave characteristics for each wind regime. An example of the results is given in Table 8.1.They depend mainly on wind speeds. The wind duration does not play a major role since the condition for the selection of wind velocities is defined when the duration is long enough to produce a fetch limited condition (Kamphuis, 2000). Furthermore, the wind speed depends mainly on the selected return period T_r.

The return periods of waves are the same as the return periods of winds. Although many return periods were considered, for the present case study, only 3 return periods are selected as follows: $T_r = 1$, 5, and 20 *years*. For each return period, three water levels of the Lake Biel are selected:

- $MHWL = 429.60\ m$
- $MWL = 429.20\ m$
- $MLWL = 428.8\ m$

8.1.3. Set-up of the numerical model and calibration values of the bathymetry at Mörigen

The numerical model of the bathymetry used in Mike 21 EMS for the calculation of the nearshore wave field is based on two inputs:

- bathymetric measurements carried out during the field investigation as described in Section 8.1.1

Water level [m]	Return period [$year$]	Duration for F.L. [min]	Wind speed [m/s]	H_s [m]	T_m [s]	Direction [$^\circ$]	Directional spreading [$^\circ$]
429.80	1	120	8.77	0.26	1.86	233.95	18.68
	2	120	9.44	0.29	1.94	233.92	18.56
	5	90	10.87	0.34	2.06	234.98	18.76
	10	90	11.59	0.36	2.10	235.89	19.01
	20	90	12.30	0.38	2.16	236.41	19.17
	50	90	13.25	0.42	2.27	236.40	19.21
429.60	1	120	8.77	0.26	1.85	233.99	18.66
	2	120	9.44	0.29	1.93	234.07	18.58
	5	90	10.87	0.33	2.05	235.21	18.79
	10	90	11.59	0.35	2.10	236.10	19.02
	20	90	12.30	0.37	2.16	236.68	19.15
	50	90	13.25	0.41	2.27	236.91	19.16
429.40	1	120	8.77	0.26	1.85	234.13	18.67
	2	120	9.44	0.29	1.93	234.30	18.62
	5	90	10.87	0.33	2.05	235.45	18.84
	10	90	11.59	0.35	2.09	236.28	19.06
	20	90	12.30	0.37	2.16	236.93	19.17
	50	90	13.25	0.41	2.26	237.47	19.10
429.20	1	120	8.77	0.26	1.84	234.40	18.68
	2	120	9.44	0.28	1.92	234.69	18.64
	5	90	10.87	0.33	2.04	235.79	18.89
	10	90	11.59	0.35	2.09	236.49	19.12
	20	90	12.30	0.37	2.15	237.17	19.21
	50	90	13.25	0.41	2.26	238.00	19.07
429.00	1	120	8.77	0.26	1.84	234.78	18.72
	2	120	9.44	0.28	1.92	235.20	18.67
	5	90	10.87	0.33	2.04	236.20	18.94
	10	90	11.59	0.35	2.09	236.74	19.19
	20	90	12.30	0.37	2.15	237.40	19.28
	50	90	13.25	0.40	2.26	238.50	19.08
428.80	1	120	8.77	0.26	1.84	235.24	18.68
	2	120	9.44	0.28	1.91	235.76	18.65
	5	90	10.87	0.33	2.04	236.68	18.94
	10	90	11.59	0.35	2.09	237.09	19.20
	20	90	12.30	0.37	2.15	237.73	19.28
	50	90	13.25	0.40	2.26	238.99	19.08

Table 8.1.: Wind waves calculation at Mörigen during the "Le Vent" wind regime for the sector [210 $^\circ$-240 $^\circ$] based on long term analysis of wind data at Neuchâtel station

- bathymetric data of Lake Biel provided by the Swiss Federal Office of Topography

By combining the two above mentioned data, it is possible to define an accurate numerical model of the region of Mörigen. However, in order to have reliable results, this numerical model as described in Section 6.2.2, should respect some criteria. The first one depends on mesh generation and the second one define the limits of the model. As explained before a typical wave length should be at least 12 times longer than a grid width. Based of wave values in Section 8.1.2, the average wave length is almost equal to 7 m. Therefore, a square grid of 0.5 m seems to be appropriate. Special attention should be given to this point since, by selecting very small grid, calculation time tends to increase significantly. An optimal grid width should be selected carefully in order to optimize the calculation time.

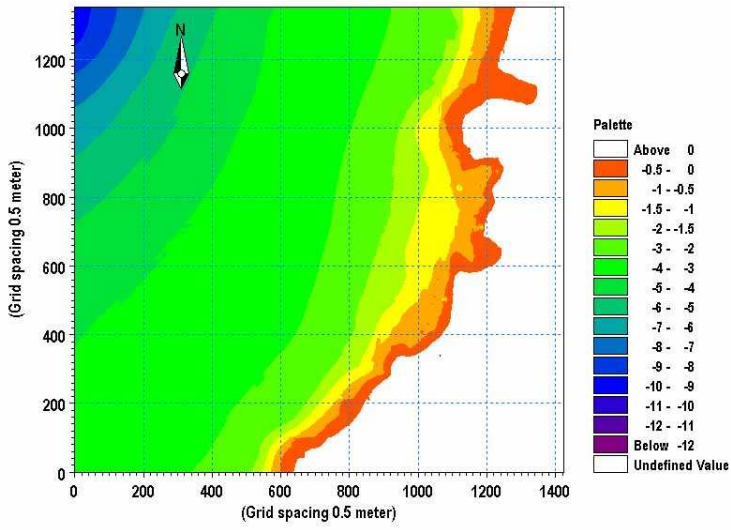

Figure 8.8.: Numerical bathymetry of the nearshore region at Mörigen for the use in Mike 21 EMS showing the limits of the model for the MWL

On the basis of the calibration described in Chapter 6 and *in situ* measurements of waves and sediment as described in Section 8.1.1, the values selected for wave breaking parameters and bottom roughness are as follows:

- wave breaking parameter: $\gamma_1 = 1.05$ and $\gamma_2 = 0.8$
- nikuradse roughness: $k_n = 0.00081$

8.2. Efficiency of the brushwood fences field in shore protection

As previously mentioned, the following sections highlights the effect of the present nearshore brushwood fences field at Mörigen on the incoming waves. They are based on numerical modelling carried out by Mike 21 EMS. Using the numerical model of the local bathymetry described above, it is possible to calculate the wave field without introducing any structures. In the next step, the wave field is calculated with the presence of the protection structures as described in Section 8.1. This will allow an accurate description of the effect of the protection system on the nearshore hydrodynamics and will constitute the basis of any protection enhancement proposals.

8.2.1. Selection of adequate friction factors

Based on Fig. 8.6, the mean value of the transmission coefficient for at typical brushwood fences at Mörigen is as following:

$$K_{T,mean} = 0.32 \tag{8.1}$$

This value is based on field measurements of waves before and behind brushwood fences. It is carried out during a period where the water level of Lake Biel oscillated around the value of 429.08 m. Since the top of the brushwood fences measured at this location is at 429.35 m, this means that the measured K_T corresponds to an emerging condition where the brushwood fences contribute most efficiently in wave damping. As described in Chapter 4, the brushwood fences have different behavior when they are totally submerged. Knowing that $MHWL = 429.6$ m (see Section 8.1.2), the brushwood fences at Mörigen could in fact be totally submerged. Therefore, it is proposed to estimate $K_{T,sub}$ of the brushwood fences when they are totally submerged.

The estimation of $K_{T,sub}$ would be based on the results of the experimental tests. Knowing that the structure height $h_p = 1.12$ m (p for $p$rototype and m for $m$odel), and defining the relative freeboard for both submerged (sub) and emerged situations (eme) as follows:

$$fr_{sub} = \frac{h_p}{R_{c,p,sub}} = \frac{1.12}{429.35 - 429.6} = -4.48 \tag{8.2a}$$

$$fr_{eme} = \frac{h_p}{R_{c,p,eme}} = \frac{1.12}{429.35 - 429.08} = 0.27 \tag{8.2b}$$

and assuming that:

$$K_{T,p}(fr_{eme}) = K_{T,m}(fr_{eme}) \tag{8.3}$$

the following condition should be respected:

$$\frac{K_{T,m}(fr_{sub})}{K_{T,m}(fr_{eme})} = \frac{K_{T,p}(fr_{sub})}{K_{T,p}(fr_{eme})} \tag{8.4}$$

This comparison between experimental and field measurements leads to the definition of two transmission coefficients as follows:

$$K_{T,MLWL} = K_{T,MWL} = K_{T,eme} = 0.35 \tag{8.5a}$$
$$K_{T,MHWL} = K_{T,sub} = 0.7 \tag{8.5b}$$

It is possible to estimate the friction factors for each water level condition and return period as selected in Section 8.1.2. The calculation of the friction factor is based on Section 6.2.4. Figs. H.1, H.2, and H.3 shows the variation of K_T and K_R as a function of the friction factor for different return periods. The values of the friction factor could be estimated for the selected transmission coefficients according to Eqs. 8.5.

Water level	429.60	429.20	428.80
Wind sector	$[m]$	$[m]$	$[m]$
[210 °-240 °]	1.5	4.5	3.7
[30 °-60 °]	1.0	2.9	2.3
[300 °-330 °]	1.0	3.9	3.0

Table 8.2.: Values of friction factors of brushwood fences to be used in Mike 21 EMS for each wind sector and water level condition

8.2.2. Wave field for three selected wind regimes

The numerical calculation of the wave field is carried out for every wind regime, water level and return period. For both cases with and without the presence of the structure, the total number of run is 54. For each run the following points are applied:

- the calculations are made using a PC pentium(R) 4 with a $2.40GHz$ CPU speed and $1.00GB$ RAM
- the selected time step is 0.5 s and number of time step is 1000
- the time for each calculation is 8 $hours$
- final file size is $592MB$

The results are presented in Figs H.4 to H.9. An example of the wave field for the South-Western wind regime is given in Fig. 8.9. Wave field is presented using H_{rms} wave height values, based on X and Y axis using the grid width of 0.5 m as a unit. The efficacy of brushwood fences could be explained on the following basis.

Effect of the water level variations

The variation of the water level influences significantly the shoreline position. Therefore, for $MHWL$ the shoreline moves in the landward direction and for $MLWL$, it moves in the seaward direction. At some shallow places, for a water level variation of 0.80 m, the shoreline displacement could reach 25 m ($X = 350; Y = 500$). Furthermore, for shallower regions ($X = 450; Y = 900$), the shoreline displacement is almost 75 m. Such high values bring out the effect of the distance of brushwood fences from the shoreline. This distance should be long enough in order to enable a good performance of the structure during low water regimes. Results show that this criteria is practically fulfilled in almost all the cases. Even for $MLWL$, all brushwood fences structures are still in water and able to damp efficiently the incoming waves (see Figs H.5, H.7 and H.9).

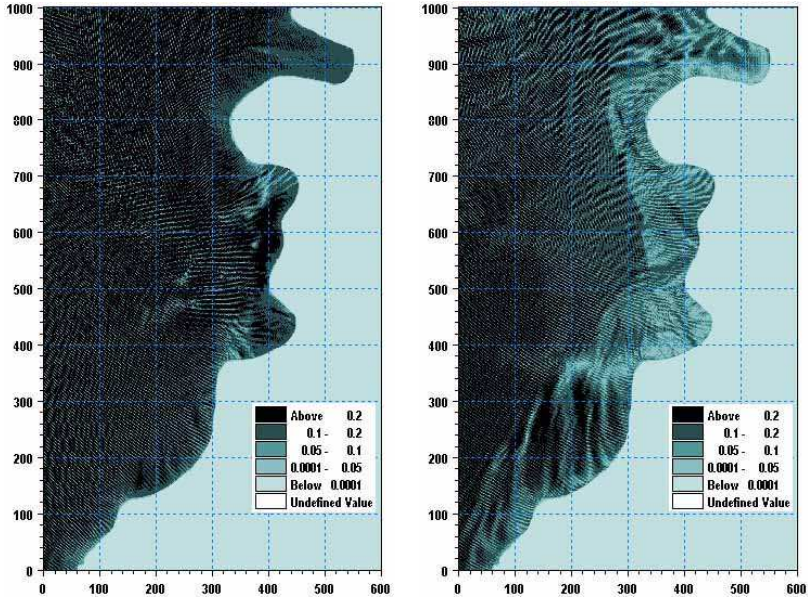

Figure 8.9.: Wave field (H_{rms}) at Mörigen during a South-Western wind regime for the $MHWL$ and $T_r = 1$ *year*: a) without the presence of the brushwood fences; b) with the presence of the brushwood fences

Additionally, the wave damping effect decreases significantly for all the modelled wind regimes when the water level is high. Therefore, when

comparing in Figs. H.5, H.7 and H.9 wave heights behind the brushwood fences field for the three modelled water levels of the lake, it is apparent that during a $MHWL$ period, the incoming waves are almost equal before and behind the protection structures. It has to be noted that during this water level regime, the structures are totally submerged.

For MWL , waves in the protected area at the leeside of the brushwood fences are much smaller than waves corresponding to the $MHWL$. However, when compared to waves during $MLWL$, they do not appear to be much higher, although the water level variation is the same. This is probably due to the fact that for both water level regimes, the structure in emerging. For this condition, its efficiency is almost constant. Concerning the wave field width at the leeside of the protection structure, the results show that for MWL, the protected region is much wider than the one corresponding to $MLWL$.

Effect of the wind regimes

The wind regime has a clear effect on the nearshore wave field at Mörigen. When comparing Figs. H.4, H.6 and H.8 it appears that waves tends to be higher for the South-Western regime. This could be clearly seen for the return period $Tr = 20\ years$. Such high waves are essentially due to the fact that the fetch of this wind regime is almost twice as large as the fetches of the two other main wind regimes (see Section 8.1.2). Moreover, wind speeds for South-Western wind are the highest. The comparison of wave fields without the presence of the structure also shows that the incoming waves for the North-Western wind are the smallest. In addition to the fact that this wind regime corresponds to the smallest fetch, it seems that waves are being significantly damped by the the strong refraction process since wave propagation during the North-Western regime is almost parallel to the shoreline.

With the presence of the brushwood fences, wind regimes influences significantly the wave field at the leeside of the protection structures. Therefore, when comparing wave fields in Figs. H.5, H.7 and H.9 for MWL, it appears clearly that for both North-Eastern and Western wind regimes, waves reach more easily the shore by diffraction through the wide gaps in the brushwood fences field (see ($X = 350$; $Y = 450$) in Figs. H.7 and H.9). However, during a South-Western wind regime, although waves are higher, it seems that the present geometrical disposition of the structures protects the shoreline very efficiently.

Furthermore, the efficacy of the brushwood fences geometrical disposition during a South-Western wind regime is clearly shown for the $MHWL$. When comparing the wave field in Figs. H.5, H.7 and H.9, it appears that the average wave heights in the lee of the structures are almost twice smaller for the South-Western wind.

8.3. Conclusion and recommendations

The brushwood fences field at Mörigen in Lake Biel have been modelled using Mike 21 EMS. The wave field at the leeside of the fences is obtained for the three main lake water levels, and for the three main wind regimes. The statistical analysis of in-situ over-land wind measurements permitted the identification of three main wind directions, North-East, North-West and South-West. After adjustment of wind velocities based on the ratio of over-water and over-land wind speeds (equal to 1.35), waves statistics for each regime were determined using the numerical model of the entire lake based on Swan application. In average, for a wind return period of $T_r = 20\ years$, corresponding to an average wind velocity of 12 m/s, the waves at Mörigen are almost 0.4 m height and 2.2 s period. The introduction of the transmission values of the brushwood fences and bottom characteristics into the numerical model of nearshore region of Mörigen are provided through in-situ measurements and depends on water level variation.

For each wind regime, eighteen cases have been investigated. In order to evaluate the effectiveness of the brushwood fences field related mainly to their geometrical distributions, nine cases are considered without the presence of the structures, and nine cases with the presence of the structures.They correspond to the three selected return periods, $T_r = 1,\ 5$ and $20\ years$, for each, three selected water levels, $MHWL,\ MWL$ and $MLWL$ are considered.

The comparison of the results permitted the following conclusions:

- When the water level of the lake is $MHWL$, the effectiveness of the brushwood fences field is very low. The transmission of the incoming waves is almost 100%
- Although during the South-Western wind regime, incoming waves reaches their highest values, they are efficiently damped by the particularly adapted geometrical configuration of the brushwood fences field. For the two other wind regimes, waves are able to reach the shore through wide gaps between the fences

The present study demonstrated the effectiveness of the use of Mike 21 EMS to model real cases, where porous structures are built. The input of the results obtained by the Swan model for wind-wave data appeared to be very relevant and adequate. Further detailed numerical analysis of currents and bedload sediment transport is crucial, and should reveal significant nearshore phenomenon that contributes to a better understanding of the hydrodynamics of the brushwood fences field in order to suggest resolute enhancement of the protection system.

9. Concluding summary and proposals for future investigations

Adequate scientific basis for the design of soft techniques such as brushwood fences used in shallow coastal zones are still lacking. Thus, protections often do not provide efficient results, like stopping shoreline from moving backward, or substantially damping waves during major wind events or high water levels. By the mean of physical and numerical modelling, the main goal of the research was therefore to study the interactions of a selected soft shore protection measure (i.e. brushwood fences), with the incident waves and evaluate its effect on sediment transport. The former is measured by the transmission coefficient of the structure, and the latter by its efficiency in promoting sand deposition and shoreline accretion. This approach provided a better understanding of its behavior and, as a result, helped to establish technical recommendations for its design basis. In the next sections, a concluding summary of the main results is given.

9.1. Summary and recommendations

9.1.1. Downscaled model and experimental tests

Physical tests were conducted in the wave tank at the *Laboratory of Hydraulic Constructions (LCH)*. It is 10 m long, 6 m wide, and 1.3 m deep. A pneumatic wavemaker was used to generate monochromatic unidirectional waves. A realistic typical bathymetry found commonly in the shallow zones of the major confined water bodies in Switzerland was designed inside the wave tank. The brushwood fences model with a scale of $1:10$ consisted of building the fascine (the main porous media of the brushwood fences) by enrobing a highly porous media with a geotextile. It is assumed that the overall porosity of the fascine is approximately the same as the geometrical porosity of the geotextile. A comparison of this model with tests carried out on real full scaled brushwood fences showed convergent results. The first series of tests was carried out on a fixed bed. Three different porosities of the structure were tested $p = 0.16 - 0.36 - 0.62$ for three different heights $h = 0.7 - 1.0 - 1.25$ m

(full scale values). The transmission coefficient K_T was measured for several wave periods and several water depths. The second series of tests focused on the effect of the structure built on a movable bed. The granular fine sand used had an average diameter $d_{50} = 0.18\ mm$. The measured effect of the distance of the structure from the shoreline, and a varying gap width, concerned mainly the evolution of the shoreline and the deposited and eroded sand volumes at the leeside of the structure. The impact of the movable bed on the transmission coefficient was also evaluated.

9.1.2. Interaction of brushwood fences and waves

The response of the structure regarding the transmission coefficient has been evaluated using five dimensionless variables: 1) the relative freeboard of the structure R_c/H_i, 2) its relative height h/H_i, 3) the relative wave number kd, 4) the wave steepness H_i/gT^2, and finally 5) the porosity of the structure p. The following observations are noted:

- The response of the structure is different in relation to its immersion condition. It was shown that the efficiency of the brushwood fences decreases rapidly when they are totally submerged.
- The relative freeboard, the wave steepness and the porosity play a major role in the response of the structure regarding wave damping. The effect of the relative height and the wave number is not significant and can be disregarded.
- The effect of the relative freeboard and the porosity of the structure on the transmission coefficient are non-linear while the effect of the wave steepness could be considered as linear.

In the second step, a non-linear relationship between K_T and the selected dimensionless variables was proposed and tested. It reads as follows (see Eq. 9.1):

$$K_T = 0.01\ (\frac{R_c}{H_i})^2 - 0.11\ \frac{R_c}{H_i} + 0.69\ p^{\ -0.04} - 12.40\ \frac{H_i}{gT^2}\ (\pm 0.24) \qquad (9.1)$$

The method showed a quite good agreement with the physical results; 95% of the data fall within a confidence interval for K_T of ± 0.24. The empirical equation is to be applied only when the relative freeboard R_c/H_i is within the interval $[-2, +2]$. The porosity should be higher than 0, and the wave steepness H_i/gT^2 should be within the interval $[0.001, 0.008]$. Finally, it has to be mentioned that these intervals correspond to the ones used during the experimental tests. This relationship could be used tentatively for other values of R_c/H_i and H_i/gT^2, however after thorough experimental investigations. As

for the porosity, the more it approaches zero, the more inaccurate the results provided by the equation become. Therefore, it is recommended to stay above 0.1.

9.1.3. Interaction of brushwood fences and sediments

Experimental tests carried out with the brushwood fences (fixed porosity of 0.36) on a movable bed examined mainly their effect on the deposited and the eroded volumes in the sheltered area. The tests proved that the geometrical placement of the structure has a direct correlation with these volumes. The use of a fine sand ($d_{50} = 0.18\ mm$) demonstrated its effectiveness, showing adequate morphological evolution. Moreover, the evolution of the transmission coefficient was also measured under constant wave attack.

It was demonstrated that the transmission coefficient K_T increased with time due to the flattening of the bed in the vicinity of the structure. An empirical equation was derived (see Eq. 9.2) that describes this evolution. However, this equation is only applicable for the defined wave characteristics and the grain size ($d_{50} = 0.18\ mm$) during the tests.

$$K_T(t + \Delta t) = K_T(t) + 0.014\Delta t \tag{9.2}$$

Using four different distances of the structure from the shoreline, an empirical relationship was provided for the width of the salient Y as a function of the structure length B/S (see Eq. 9.3):

$$\frac{X}{B} = 0.85[\frac{B}{S}]^{-1.21};\ (\pm 0.22) \tag{9.3}$$

The deposited and eroded volumes were measured in the sheltered area by the structure. The deposited volumes were calculated as a function of B/S. Similarities were noticed when these volumes where compared to the results of Shinohara and Tsubaki (1966). The deposited sand could be calculated tentatively at the distance x_l behind the structure by Eq. 9.4:

$$\frac{V_d}{S^3} = 1.42\ 10^{-4} exp(3.55\frac{B}{S})\frac{x_l}{S};\ (\pm 0.0003) \tag{9.4}$$

The effect of a single gap was investigated using two gap widths and three different distances of the structure from the shoreline. The experimental observation showed no relevant results concerning the formation of the salient behind the structure. In fact B/S was too small. However, it seems that the smaller the gap ($G/B = 0.25$) the more sand is accumulated in the gap. However for the wider gaps is ($G/B = 0.5$), the deposited sand in the total sheltered area was slightly higher. Although additional tests were needed for the effect of a single gap, it was suggested to choose a low gap width $G/B < 0.5$.

In real cases, the steepness, the period, and the angle of approach of incoming waves affect significantly the erosion and the deposition of sand initiated by a coastal structure. Since constant wave characteristics were used, it is recommended to carry out additional experimental tests covering other wave and sediment characteristics, and to investigate the effect of a varying porosity.

9.1.4. Numerical modelling

Mike 21 EMS (EMS stands for *E*lliptic *M*ild *S*lope) simulates the propagation of linear time harmonic water waves on a gently sloping bathymetry with arbitrary water depth. The simulation is reproduced by solving the mild-slope wave equation. By this means, Mike 21 EMS was utilized to simulate the combined effects of shoaling, refraction, diffraction and transmission in the presence of a porous structure in a numerical model similar to the physical wave tank. Energy dissipation, due to wave breaking and bed friction, is included as well as partial reflection and transmission through the brushwood fences. Sponge layers were applied where full absorption of wave energy is required. Based on a theoretical approach, the wave breaking and bottom roughness parameters were calculated. Afterwards, the results of the physical experiments without the brushwood fences were simulated numerically. The results of wave heights were compared to experimental results obtained with similar boundary conditions. This process led to an acceptable calibration of the numerical model of the wave tank to be used in a next step for further modelling.

9.1.5. Gaps in porous media

In order to include the porous media in the numerical model, the experimental results of the transmission coefficient for variable water depths and porosities were used. This process enabled a direct adjustment of the numerical model. A comparison of the transmitted wave during the experimental tests and numerical modelling showed a good agreement.

In order to describe the wave field morphology in the enclosed area, surrounded by brushwood fences, a single gap was placed in the middle of the structure. Six gap widths were considered: $G = 1,\ 2,\ 4,\ 6,\ 8,$ and $10\ m$. It was shown that the presence of a gap in the protection structure has mainly a 2D dimensional behavior. The pattern of the transmitted and diffracted waves is totally different even for a very small gap width when compared to a structure with no gap. Furthermore, the surface of the most affected area behind the structure at the middle of the gap did not increase significantly when the gap was four times wider. This high wave area, with a "tongue" form, reached a maximum width independently of the gap width. It was shown that, for single

gap, wave heights are higher in the middle for an increasing gap width and decay continuously when approaching the shore. On both sides of the highly affected area, wave heights and patterns were almost constant for all the gap widths. This can be explained by the fact that the wave energy entering the gap was concentrated in the middle, which allowed a higher extent of high waves towards the shore and not in the lateral direction.

Moreover, the wave field behind the protection structure was analyzed for two gaps with a constant width of $G = 4\ m$. The main variable considered was the spacing between the gaps, Es. The values tested are: $Es = 4,\ 8,\ 12,\ 16,\ 20$, and $24\ m$. Compared to the wave field due to a single gap, the highly affected area by incident waves proved to be almost twice as large, even for a small gap spacing of $Es = 4\ m$. The wave pattern on both sides of the protected area was similar to the wave pattern due a single gap. However, the wave field in the middle was significantly different because of the interaction of the diffracted waves entering the gaps. In fact, for a small spacing, peak values of wave heights occurred between the two gaps. For a very large spacing, for instance 6 times the gap width ($Es = 24\ m$), this pattern disappeared completely. Therefore, an optimal gap spacing is supposed to exist, where the combined diffracted and refracted waves in each gap have no negative impact on the wave field between the gaps.

For a single gap, a rule was suggested to use a relative gap width $G/Wmax$ less then 0.12 ($Wmax$ is the width of the protected area) since for higher values, diffracted waves were proved to be higher than the incident wave without the presence of the structure. For low spacing values ($Es/G = 2$), waves in the middle of the protected area were high along the structure and very low when approaching the shore. For high spacing values ($Es/G = 5$), the wave field was also significantly deformed. However, values of Es/G between 3 and 4 appear to be most appropriate since the corresponding wave field was less deformed. Finally, it was shown that the two gaps configuration does not significantly increase the residual total energy behind the structure. It was relatively constant with spacing between two gaps and increase slowly with the increased of a single gap width.

9.1.6. Application on a real-life case

The model Mike 21 EMS was used successfully to set up a numerical model of the brushwood fences field at Mörigen in Lake Biel. The wave field at the leeside of the fences is obtained for the three main lake water levels, MHWL, MWL and MLWL, and the three prevailing wind regimes North-East, South-West, and West. After adjustment of wind velocities based on the ratio of over-water and over-land wind speeds (equal to 1.35), waves statistics for each regime were determined using the numerical model Swan of the entire lake. For each wind regime, eighteen cases were investigated. In order to evaluate the

effectiveness of the brushwood fences field, related mainly to their geometrical distributions, nine cases are considered without the presence of the structures and nine cases with the presence of the structures. It was proved that the efficiency of the brushwood fences field decreased dramatically for $MHWL$. It was the most efficient during the South-Western wind regime, although incoming waves during this regime are the highest. For the two other regimes, it was proved that the waves are capable of reaching the shore through the wide gaps in the brushwood fences field. Finally, the case study demonstrated the effectiveness of the use of Mike 21 EMS to model real-life cases where porous structures are built.

9.2. Proposed future investigations

The main goals fixed at the beginning of this research project were achieved. However, many other interesting issues were encountered during the study, and some were partially investigated. If any follow up of this research is to be done, it is suggested to address the following points:

- Comprehensive investigation of the numerical modelling (using Mike 21 HD) of the brushwood fences in the wave tank by adding the hydrodynamic effects that enables the understanding of the influence of gaps on the wave generated nearshore currents. Additionally, it is proposed to use the experimental results with movable bed for the calibration of the sediment transport numerical model (using Mike 21 ST) and model the effect of other geometrical dispositions on the nearshore morphology.
- During the thesis, *in situ* measurements were carried out by the *Berne University of Applied Sciences* on different locations at the shores of Lake Biel. It is proposed to carry out numerical analysis of the wave field and sediment transport in these locations where different soft shore protections are used. The case study proposed in this research suggest the appropriate methodology. The model adjustment should be based of the results of the field campaigns.
- Risk analysis of the effect of wind-waves on shores using the measured extreme wind events. At present, a first step is being investigated by the author by building statistical codes that treat the wind data measures by ANETZ wind stations network. The results could then be used in Swan in order to generated wave risk maps for some major confined water surfaces.

Acknowledgements

Without the help and support of many people, the present study would have never been realized. Therefore, I would like to express my big gratitude to the assistance of many persons I profoundly respect. I firstly acknowledge the technical and scientific guidance of the supervisor of my research project, Prof. Dr Anton Schleiss. By providing the best work conditions, he contributed generously in raising my motivation. Additionally, I would like to thank him for encouraging me to participate in several international conferences that widened my vision as a researcher and provided me the opportunity to present and discuss my work. I am very grateful for the advices provided by Dr Jean-Louis Boillat during my experimental tests. Moreover, with working under his supervision on applied researches, he showed me the right way to follow, for solving engineering water-related problems. I would like to thank Dr Stephan Mai from the *Bundesanstalt für Gewässerkunde, Germany*, invited as academic guest at *LCH-EPFL*, who offered me in addition to a great friendship, a relevant help in numerical modelling and theoretical support. No experimental tests would have been carried out without the help of the technical stuff, to whom I send my best and thankful thoughts: Louis Schneiter; Eric Pantillon; René Fontanellaz and Michel Teuscher. A special thanks to Caroline Etter and Stephanie Rochat who helped in several logistic issues.

Many members of the EROSEE research group were always present to answer questions concerning on field investigations: Mr Christoph Iseli and Mrs Baerbel Mueller. Moreover, I would like to send my respect to Dr Andreas Huber, to whom I acknowledge a great experience (generously shared) in Swiss lakes. I had the opportunity to carry out long and scientific conversations with Dr Andreas Matheja from *Franzius Institut für Wasserbau und Küsteningenieurwesen, University of Hannover, Germany*, during his visit as an academic guest at *LCH-EPFL*, Dr Jean-Michel Fallot and Dr Jacques-André Hertig from the *Laboratory of Environmental Fluid Mechanics and Hydrology, EPFL*, Dr Karsten Mangor and Dr Henrik Kofoed-Hansen and Mrs Valérie Carles from the *Danish Hydraulic Institute, DHI-Denmark*, Prof. Dr William Kamphuis from *Queen's University, Kingston, Canada*.

I would like to address a special thank for Mr Keith Dalton and Dr Elie Bou-Zeid who helped me in proof reading my final report, to my colleagues

and special dear friends from the *LCH* with whom I shared fruitful experiences on technical and personnel levels, and without them the 3 years of the thesis would have been passed slowly.

I would like to thank the *Swiss Federal Commission for Grants to Foreign Students* and express my gratefulness to Mrs Catherine Vinckenbosch and Mrs Annette Jaccard for they support. I acknowledge the financial support of the *KTI/CTI Innovation Promotion Agency* provided under the grant N ° KTI 5670.1, together with other research partners.

I would like to thank my dear brother Habib, who was always available and ready to act for any help needed. Last but not least, I express my gratitude to my beloved Valérie, for her long patience, continuous encouragement, and persistent love and support.

References

Abul-Azm, A. G. and Williams, A. N. (1997). Oblique wave diffraction by segmented offshore breakwaters, *Ocean Engineering* **24**: 63–82.

Aso, Y. (1998). Restoring japan's rivers to ecological vibrance, *Technical report*, Ministry of Land, Infrastructure and Transport Government of Japan.

Bagnold, R. A. (1963). *The physics of sediment transport*, ASCE, New York.

Battjes, J. and Janssen, J. P. F. M. (1978). Energy loss and set-up due to breaking of random waves, *16th Intertnational Conference on Coastal Engineering*, Hamburg, pp. 569–587.

Battjes, J. and Stive, M. (1985). Calibration and verification of a dissipation model for random breaking waves, *Journal of Geophysical Research* (90): 9159–9167.

Beltrami, G. M., Bellotti, G., Girolamo, P. D. and Sammarco, P. (2001). Treatment of wave breaking and total absorption in a mild-slope equation fem model, *Journal of Waterway, Port, Coastal and Ocean Engineering* **127**(5): 263–271.

Berkhoff, J. (1972). Computation of combined refraction-diffraction, *in* ASCE (ed.), *13th Coastal Engineering Conference*, Vol. 1, Vancouver, pp. 471–490.

Bevington, P. R. and Robinson, D. K. (1992). *Data Reduction and Error Analysis for the Physical Sciences*, 2nd edn, WCB/McGraw-Hill, Boston.

BFH (2002). Development of contructional techniques and dimensioning principle by the example of lake biel, *Progress Report 1*, Berner Fachhoschule, Burgdof.

Biezen, S. v. d., Graaf, J. v. d. and Later, J. d. (1999). 3d model tests of the influence of submerged breakwaters on a beach profile exposed to regular waves, pp. 1–5.

Bonnefille, R. (1992). *Cours d'hydraulique maritime*, 3ème edn, Masson.

Booij, N., Holthuijsen, L. H. and Ris, R. C. (1996). The swan wave model for shallow water, *in* ASCE (ed.), *15th International Conference on Coastal Engineering*, Orlando, Florida, USA, pp. 668–676.

Bowen, M. K. and Mclver, P. (2002). Diffraction by a gap in an infinite permeable breakwater, *Journal of Waterway, Port, Coastal and Ocean Engineering* **128**(1): 2–9.

Bowman, D. and Pranzini, E. (2003). Reversed responses within a segmented detached breawater, the tuscany coast italy - a case study, *Coastal Engineering* (49): 263–274.

Breusers, H. N. C. and Raudkivi, A. J. (1991). *Scouring*, Balkema, Rotterdam.

Briand, M. and Kamphius, J. W. (1993). Sediment transport in the surf zone: a quasi 3-d numercial model, *Coastal Engineering* **20**: 135–156.

Bruschin, J. and Falvey, H. (1980). Vagues de vent sur un plan d'eau confiné : Considérations générales et application au léman(petit-lac), *Bulletin technique de la Suisse romande* .

Bruschin, J. and Schneiter, L. (1978). Caractéristiques des vagues dans les lacs profonds, *Bulletin technique de la Suisse romande* (19): 269–276.

Bruun, P. (1954). Coast erosion and the development of beach profiles.

Calabrese, M., Vicinanza, D. and Buccino, M. (2003). Low-crested and sumberged breakwaters in presence of broken waves, *in* HydroLab (ed.), *Towards a balanced methodology in european hydraulic research*, Budapest.

Colenutt, A. (2001). Saltmarsh management techniques, *Technical report*, New forest district council coast protection group.

Cooley, J. W. and Tukey, J. W. (1965). An algorithm for the machine computation of the complex fourier series, *Mathematics of Computation* **19**: 297–301.

Copeland, G. J. M. (1985a). A practical alternative to the "mild-slope" wave equation, *Coastal Engineering* **9**: 125–149.

Copeland, G. J. M. (1985b). Practical radiation stress calculations connected with equations of wave propagation, *Coastal Engineering* **9**: 195–219.

Daemrich, K.-F., Mai, S. and Ohle, N. (2001). Wave transmission at submerged breakwaters, *4th International conference on ocean wave measurement and analysis*, San Francisco, USA.

D'Angremond, K., Meer, J. W. v. d. and Jong, R. J. d. (1996). Wave transmission at low-crested structures, *25th International Conference on Coastal Engineering*, Kobe, Japan.

Dean, R. G. (2002). *Beach Nourishment - Theory and Practice*, Vol. 18 of *Advanced Series on Ocean Engineering*, 2002 edn, World Scientific, Singapore.

Dean, R. G. and Dalrymple, R. A. (2002). *Water Wave Mechanics for Engineers and Scientists*, Vol. 2 of *Advanced Series on Ocean Engineering*, 1st edn, World Scientific, Singapore.

Debaillon, P., Sergent, P. and Zhang, B. (2001). Morphological evolution bebind a detached shore-parallel breakwater, *Coastal Dynamics '01*, pp. 46–54.

DHI (2001). Mike 21.

Eurovision (2004). *Living with coastal erosion in Europe: sediment and space for sustainability - A guide to coastal erosion management practices in Europe*, European Commission, RIZK, EUCC, IGN, UAB, BRGM, IFEN, EADS, Bruxelles.

Filianoti, P. (2000). Diffraction of random wind-generated waves by detached breakwater or breakwated gap, *Ocean Engineering* (27): 1249–1263.

Goda, Y. and Suzuki, Y. (1976). Estimation of incident and reflected waves in random wave experiments, *15th Coastal Engineering Conference*, Hawaii.

Harris, M. M. and Herbich, J. B. (1986). Effect of breakwater spacings on sand entrapment, *Journal of Hydraulic Research* **24**(5).

Herbich, J. B. (1990). *Handbook of coastal and ocean engineering*, Gulf publishing compagny.

Holthuijsen, L., Booij, N. and Herbers, T. (1989). A prediction model for stationnary, short-crested waves in shallow water with ambient currents, *Coastal Engineering* **13**: 23–54.

Hudson, R. Y., Herrmann, F. A., Sager, R. A., Whalin, R. W., Keulegan, G. H., Chatham, C. E. and Hales, L. Z. (1979). Coastal hydraulic models, *Special Report 5*, US Army Engineer Waterways Experiment Station, Vicksburg, Mississippi.

Hughes, S. A. (1993). *Physical Models and Laboratory Techniques in Coastal Engineering*, Vol. 7 of *Advanced Series on Ocean Engineering*, World Scientific.

Idelcik, I. E. (1960). *Memento des pertes de charges*, Eyrolles, Paris.

Ippen, A. (1966). *Estuary and Coastaline Hydrodynamics*, McGraw-Hill.

Iseli, C. (1992). Ingenieurbiologische Schilf- und Uferschutzmassnahmen am Bielerse, *Ingenieurbiologie (Zürich)* **1**: 11–14.

Iseli, C. and Wherli, M. (1995). Zehn Jahre Schilf- und Uferschutzmassnahmen am Bielersee, *VBS Schriftenreihe* **4**.

Jonsson, I. (1966). Wave boundary layers and friction factors, *10th International Conference on Coastal Engineering*, Tokyo, Japan, pp. 127–148.

Kamphuis, J. W. (1996). Physical modeling of coastal processes, *in* P. L.-F. Liu (ed.), *Advances in coastal and ocean engineering*, Vol. 2, World Scientific, Singapore, pp. 79–114.

Kamphuis, J. W. (2000). *Introduction to Coastal Engineering and Management*, Vol. 16 of *Advanced Series on Ocean Engineering*, 1st edn, World Scientific.

Komar, P. and Miller, M. (1975). Sediment threshold under oscillatory waves, *14th Conference on Coastal Engineering*, ASCE, New York, pp. 756–775.

Lee, C. (2005). Techniques of internally generating waves on a curve in a rectangular grid system, *XXXIth International Association for Hydraulic Research IAHR Congress*, IAHR, Seoul, Korea, pp. 4134–4143.

Lencastre, A. (1984). *Manuel d'Hydraulique Générale*, Collection de la direction des études et recherches d'Electricité de France, 9ème edn, Eyrolles.

Losada, I. J., Dalrymple, R. A. and Losada, M. A. (1998). Wave-induced mean flows in vertical rubble mound structures, *Coastal Engineering* **35**: 251–281.

Losada, I. J., Losada, M. A. and Martin, F. L. (1995). Experimental study of wave-induced flow in porous structure, *Coastal Engineering* **26**: 77–98.

Madsen, P. (1983). Wave reflection from a vertical permeable wave absorber, *Coastal Engineering* **7**: 381–396.

Madsen, P. and Larsen, J. (1987). An efficient finite-difference approach to the mild-slope equation, 1st edn, Danish Hydraulic Institute, Denmark, pp. 329–351.

Mai, S., Lieberman, N. v. and Zimmermann, C. (1999). Interaction of foreland structures with waves, *in* W. Franzius-Intitute for Hydraulic and G. Coastal Engineering, University of Hannover (eds), *XXVIII-IAHR Conference*, Graz.

Mai, S., Ohle, N. and Daemrich, K.-F. (1999). Numerical simulation of wave propagation compared to physical modeling, *HYDRALAB-Workshop*, Hannover, Germany.

Mai, S., Ohle, N. and Zimmerman, C. (1999). Applicability of wave models in shallow coastal waters, *5th In. COPEDEC*, Cape Town, South Africa, pp. 170–179.

Mangor, K. (2001). *Shoreline Management Guidelines*, Vol. 1st, Danish Hydraulic Institute.

Mansard, E. P. D. and Funke, E. R. (1980). The measurement of incident and reflected spectra using least square method, *Coastal Engineering* **1**: 154–172.

Matumoto, H., Imai, K. and Koike, T. (1991). Similarity relation between site and laboratory scour phenomenon, *XXIV IAHR Congress Madrid*, Ministerio de Obras Publicas y Transportes, España, pp. B–531–B538.

McIver, P. (1999). Water-wave diffraction by thin porous breakwater, *Journal of Waterway, Port, Coastal and Ocean Engineering* **125**(2): 66–70.

McIver, P. (2005). Diffraction of water waves by a segmented permeable breakwater, *Journal of Waterway, Port, Coastal and Ocean Engineering* **131**(2): 69–76.

Ming, D. and Chiew, Y.-M. (2000). Shoreline changes behind detached breakwater, *Journal of Waterway, Port, Coastal and Ocean Engineering* **126**(2): 63–70.

Mizumura, K. and Shiraishi, N. (1981). Laboratory study on the shoreline changes behind a coastal structure, *Coastal Engineering* (5): 51–81.

Müller, B., Sayah, S. M., Wyler, E. and Schmoker, P. (2005). Shore protection in swiss lakes: Physical modelling and in-situ measurements, *Waves2005*, Madrid, Spain, pp. 34–45.

Nicholson, J., Borker, I., Roelvink, J. A., Price, D., Tanguy, J. M. and Moreno, L. (1997). Intercomparison of coastal area morphodynamic models, *Coastal Engineering* **31**: 97–123.

Nir, Y. (1982). Offshore artificial structure and their influence on the israel and sinai mediterranan beaches, *18th Conference on Coastal Engineering*, ASCE, Reston, Va, pp. 1837–1856.

Oehy, C. (2003). *Effects of obstacles and jets on reservoir sedimentation due to turbidity currents (2684)*, PhD thesis, Ecole polythechmique fédérale de Lausanne.

Oppenheim, A. V., Wilsky, A. S. and Young, I. T. (1983). *Signals and Systems*, Prentice-Hall International Editions.

Ostendorp, W., Iseli, C., Krauss, M., Krumscheid-Plankert, P., Moret, J.-L., Rollier, M. and Schanz, F. (1995). Lake shore deterioration, reed management and bank restoration in some central european lakes, *Ecological Engineering* **5**: 51–75.

Porter, R. and Evans, D. V. (1996). Wave scaterring by periodic arrays of breakwaters, *Wave Motion* **23**: 95–120.

Pos, J. D. (1985). Asymetrical breakwater gap wave diffraction using finite and infinite elements, *Coastal Engineering* **9**: 101–123.

Pos, J. D. and Kilner, F. A. (1987). Breakwater gap wave diffraction: an experimental and numerical study, *Journal of Waterway, Port, Coastal and Ocean Engineering* **113**(1): 1–19.

Rao, S., Rao, N. B. S. and Sathyanarayana, V. S. (1999). Laboratory investigation on wave transmission through two rows of perforated hollow piles, *Ocean Engineering* **26**: 675–699.

Requejo, S., Vidal, C. and Losada, I. J. (2002). Modelling of wave loads and hydraulic performance of vertical permeable structures, *Coastal Engineering* **46**: 249–276.

Resio, D. T. and Vincent, C. L. (1982). A comparison of various numerical wave prediction techniques, *11th Annual offshore technology conference*, Houston, USA, pp. 2471–2485.

Rijn, L. C. v. (1993). *Principles of sediment transport in rivers, estuaries and coastal seas*, Delft Hydraulics, The Netherland.

Rijn, L. C. v. (1998). *Principle of Coastal Morphology*, Delft Hydraulics, The Netherland.

Rosen, D. S. and Vajda, M. (1982). Sedimentological influences of detached breakwater, *18th Conference on Coastal Engineering*, ASCE, Reston, VA, pp. 1837–1857.

Sayah, S. M., Boillat, J.-L. and Schleiss, A. (2004). The use of soft shore protection measures in shallow lakes: Research methodology and case study, *Limnologica* **34**(1-2): 65–74.

Sayah, S. M., Boillat, J.-L. and Schleiss, A. J. (2005). Analysis and rehabilitation of a severely eroded sand beach at lake geneva in switzerland, *3rd International Conference on Asian and Pacific Coasts*, Hanrimwon Publishing Co., Ltd, Jeju, Korea, pp. 713–728.

Sayah, S. M., de Cesare, G., Fallot, J.-M. and Schleiss, A. J. (2006). Long-term analysis of wind data based on idf curves for wave risk evaluation in swiss lakes, *Journal of Coastal Research* (in preparation).

Sayah, S. M., Mai, S., Boillat, J.-L. and Schleiss, A. J. (2005). Field measurements and numerical modelling of wind-waves in lake biel: a basic tool for shore protection projetcs, *XXXIth International Association for Hydraulic Research IAHR Congress*, IAHR, Seoul, Korea, pp. 4332–4343.

Sayah, S. M., Metral, M., Boillat, J.-L. and Schleiss, A. J. (2005). Effet de la repartition géométriques des pieux de palissades sur la transmission des vagues, *Génie biologique* **3-4**: 8–11.

Scarlatos, P. D. and Singh, V. P. (1987). Long-wave transmission through porous breakwater, *Coastal Engineering* **11**: 141–157.

Shields, A. (1936). *Anwendung der Ähnlichkeits-Mechanik und der Turbulenz-forschung auf die Geschiebebewegung*, Vol. 16, Versuchsanstalt für Wasserbau und Schiffbau, Berlin.

Shinohara, K. and Tsubaki, T. (1966). Model study on the change of shoreline of sandy beach by the offshore breakwater, *in* ASCE (ed.), *10th Coastal Engineering Conference*, Vol. 1, pp. 550–563.

Silvester, R. and Hsu, J. R. C. (1997). *Coastal Stabilization*, Vol. 14 of *Advenced Series on Ocean Engineering*, 1st edn, World Scientific.

Sollitt, C. K. and Cross, R. H. (1976). Wave reflection and transmission at permeable breakwaters, *Technical Report 76-8*, US army corps of engineers - Coastal engineering research center.

Soulsby, R. (1997). *Dynamics of marine sands*, 1th edn, Thomas Telford.

Soulsby, R. L. and Whitehouse, R. J. S. W. (1997). Threshold od sediment motion in coastal environment, *Pacific Coasts and Ports '97 Conference*, Christchurch, New Zealand, pp. 149–154.

Stamos, D. G. and Hajj, M. R. (2001a). Reflection and transmission of waves over submerged breakwaters, *Journal of Engineering Mechanics* **127**(2): 99–105.

Stamos, D. G. and Hajj, M. R. (2001b). Reflection and transmission of waves over submerged breakwater, *Journal of Engineering Mechanics* **127**(2): 99–105.

Stoschek, O. and Matheja, A. (2000). Sensitivity analysis of numerical solving techniques for modelling sediment transport under tidal conditions, *in* W. Franzius-Intitute for Hydraulic and G. Coastal Engineering, University of Hannover (eds), *4th International Conference on Hydroinformatics*, Lowa city, USA.

Suh, K. and Dalrymple, R. A. (1986). Offshore breakwaters in laboratory and fields, *Journal of Waterway, Port, Coastal and Ocean Engineering* **113**(2): 105–121.

Sulisz, W. (1985). Wave reflection and transmission at permeable breakwater of arbitrary cross-section, *Coastal Engineering* **9**: 371–386.

Sumer, B. M. and Fredsoe, J. (2000). Experimental study of 2d scour and its protection at rubble-mound breakwater, *Coastal Engineering* (40): 59–87.

Sumer, B. M., Whitehouse, R. J. S. and Torum, A. (2001). Scour around coasal structures: a summary of recent research, *Coastal Engineering* (44): 153–190.

Sunamura, T. and Horikawa, K. (1974). Two-dimensionnal beach transformation due to waves, *14th International Conference on Coastal Engineering*, pp. 810–819.

Thompson, E. F., Chen, H. S. and Hadley, L. L. (1996). Validation of numerical model for wind waves and swell in harbors, *Journal of Waterway, Port, Coastal and Ocean Engineering* **122**(5): 245–257.

Thornton, E. B. and Calhoun, R. J. (1972). Spectral resolution of breakwater reflected waves, *Journal of Waterway, Harbour and Coastal Engineering Division* **98**(4): 443–446.

Tiani, G., Gonella, M. and Polo, P. (1999). Environmental impact assessment study of a marina with mike 21 numercial model simulations, *3rd DHI Software Conference*, Denmark, pp. 1–11.

Ting, C.-L., Lin, M.-C. and Cheng, C.-Y. (2004). Porosity effects on non-breaking surface waves over permeable submerged breakwaters, *Coastal Engineering* **50**: 213–224.

USACE (2001). *Coastal Egineering Manual*, Vol. 1, 1th edn, Engineer Manual 1110-2-1100, U.S. Army Corps of Engineers, Washington, D.C.

von Lieberman, N., Matheja, A., Schwarze, H. and Zimmermann, C. (1997). Optimierung von Küstensicherungsarbeiten im Küstenvorfeld der Nordseeküste, *Technical report*, Franzius-Institut für Wasserbau und Küsteningenieurwesen, Universität Hannover.

Warnock, J. E. (1950). *Hydraulic Similitude*, Engineering Hydraulics, John Wiley & Sons, New York.

Warren, I. R. and Bach, H. K. (1992). Mike 21: a modelling system for estuaries, coastal and seas, *Environmental Software* **7**: 229–240.

Wood, A. M. M. and Fleming, C. A. (1969). *Coastal Hydraulics*, seconde edition 1981 edn, John Wiley.

Yalin, S. (1971). *Theory of Hydraulic Models*, Macmillan Civil Engineering Hydraulics, 1th edn, Macmillan.

Yu, X. (1995). Diffraction of water waves by porous breakwaters, *Journal of Waterway, Port, Coastal and Ocean Engineering* **121**(6): 275–282.

Yu, Y.-X., Liu, S.-X. and Wai, O. W. H. (2000). Refraction and diffraction of random waves through breakwater, *Ocean Engineering* **27**: 489–509.

Zanuttigh, B., Guerrero, M. and Lamberti, A. (2003). 3d experimetal analysis and numerical simulation of hydrodynamics around low crested structures, *XXX IAHR Congress*, Thessaloniki, Greece, pp. 369–376.

Zyserman, J. A., Broker, I., Jorgensen, K., Christensen, E. D. and Jensen, J. H. (2000). Morphological modelling around detached breakwater, *Publication Topic 2.2 Projet 4*, Danish Hydraulic Institute.

List of Tables

List of Figures

A. Protection measures used for shore protection at Lake Biel

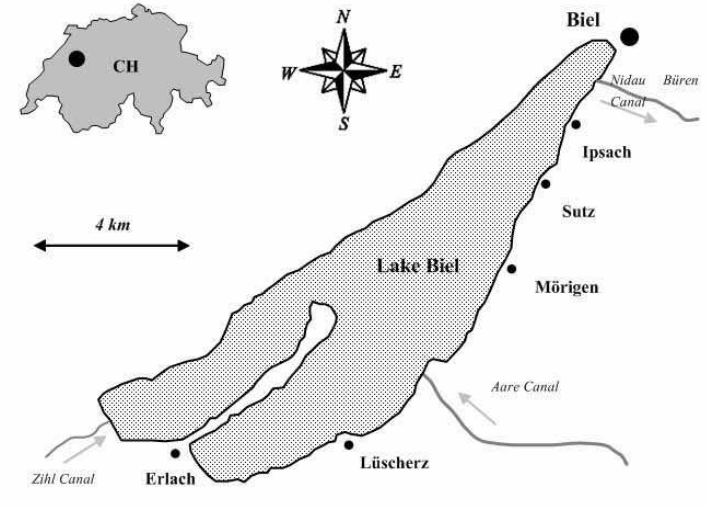

Figure A.1.: Lake Biel (Switzerland)

Protection measure	Description	Location
Armour layer of gravel 	Measure integrated into lake banks.It consists on coarse sand filling in order to protect finer sand erosion against waves attack and littoral currents	Biel, Ipsach, Sutz, Lüscherz, Erlach
Brushwood fences 	Fences constructed with two parrallel wooden pile rows, where wooden sticks come between in order to dissipate the energy of incoming waves.	Ipsach, Sutz, Mörigen, Täuffelen, Lüscherz, Erlach
Palisades 	One or two parallel pile rows facing the shore in order to dissipate the energy of incoming waves.	Ipsach, Lüscherz, Erlach
Breakwater 	Rip-rap embankments constructed parallel to the shore in order to dissipate the energy of incoming waves.	Biel, Ipsach
Groyne made of tree trunks 	Built perpendicularly to the shore, they are made essentially with tree trunks, used to stop shore-parallel sediment transport.	Ipsach, Täuffelen, Lüscherz, Erlach, La Neuveville

Table A.1.: Five main shore protection measures, most commonly used in Lake Biel after Iseli and Wherli (1995)

B. Results of the head-loss experiments on the model of the brushwood fences

Structure width b	Flow Q	Flow velocity	Pressure A	Pressure B	Total head-loss	Structure head-loss	Structure head-loss coefficient
[cm]	[m/s]	[m/s]	[m]	[m]	[m]	[m]	[-]
2.5	0.0033	0.1846	0.0995	0.0935	0.0060	-	-
	0.0062	0.3526	0.1570	0.1450	0.0120	-	-
	0.0086	0.4896	0.2040	0.1995	0.0045	-	-
	0.0112	0.6433	0.2925	0.2725	0.0200	-	-
5.0	0.0038	0.2177	0.1270	0.0950	0.0320	0.0103	0.0078
	0.0073	0.4177	0.2035	0.1605	0.0430	0.0076	0.0066
	0.0082	0.4664	0.3450	0.1835	0.1615	0.1228	0.0060
	0.0112	0.6433	0.4010	0.2620	0.1390	0.0883	0.0050
7.0	0.0034	0.1899	0.1260	0.0885	0.0375	0.0177	0.0096
	0.0057	0.3225	0.1670	0.1300	0.0370	0.0081	0.0087
	0.0078	0.4439	0.2835	0.1715	0.1120	0.0749	0.0079
	0.0106	0.6106	0.3400	0.2330	0.1070	0.0586	0.0064
10.0	0.0040	0.2295	0.1500	0.1020	0.0480	0.0255	0.0125
	0.0063	0.3604	0.2670	0.1470	0.1200	0.0886	0.0116
	0.0089	0.5087	0.3890	0.2035	0.1855	0.1440	0.0106
	0.0106	0.6106	0.4600	0.2495	0.2105	0.1621	0.0097

Table B.1.: Results of the head-loss tests for the series HLP0

Table B.2.: Results of the head-loss tests for the series HLP1

Structure width b	**Flow Q**	**Flow velocity**	**Pressure A**	**Pressure B**	**Total head-loss**	**Structure head-loss**	**Geotextile Reynolds number**	**Reynolds head-loss coefficient**	k_{R_*}	**Structure head-loss coefficient**
[cm]	[m/s]	[m/s]	[m]	[m]	[m]	[m]	[-]	[-]	[-]	[-]
2.5	0.0037	0.2119	0.3350	0.0100	0.3250	0.3169	155.8420	0.1384	1.1242	0.1231
	0.0055	0.3152	0.6000	0.0470	0.5530	0.5378	231.7626	0.1170	1.0546	0.1109
	0.0067	0.3843	0.7900	0.0250	0.7650	0.7451	282.6064	0.1040	1.0139	0.1026
	0.0094	0.5381	1.2100	0.0400	1.1700	1.1397	395.6503	0.0772	1.0096	0.0765
5.0	0.0035	0.2007	0.3530	0.0060	0.3470	0.3397	147.5980	0.1568	1.1204	0.1400
	0.0049	0.2803	0.6100	0.0350	0.5750	0.5622	206.0916	0.1320	1.0751	0.1228
	0.0065	0.3683	0.8670	0.0170	0.8500	0.8312	270.7834	0.1150	1.0234	0.1124
	0.0092	0.5282	1.2530	0.0380	1.2150	1.1853	388.3641	0.0834	1.0088	0.0826
7.0	0.0030	0.1693	0.2730	0.0460	0.2270	0.2218	124.4584	0.1600	1.0278	0.1557
	0.0049	0.2803	0.4870	0.0300	0.4570	0.4442	206.0916	0.1392	1.0751	0.1295
	0.0072	0.4092	0.8950	0.0350	0.8600	0.8384	300.9127	0.1124	1.0001	0.1124
	0.0087	0.4991	1.1500	0.0280	1.1220	1.0943	366.9909	0.0862	1.0067	0.0856
10.0	0.0034	0.1953	0.3280	0.0050	0.3230	0.3160	143.5765	0.1714	1.1043	0.1552
	0.0050	0.2871	0.5930	0.0370	0.5560	0.5428	211.0816	0.1457	1.0711	0.1360
	0.0066	0.3763	0.8600	0.0230	0.8370	0.8177	276.6570	0.1245	1.0187	0.1222
	0.0092	0.5282	1.3670	0.0360	1.3310	1.3013	388.3641	0.0915	1.0088	0.0907

Table B.2.: Results of the head-loss tests for the series HLP2

Structure width b	**Flow Q**	**Flow velocity**	**Pressure A**	**Pressure B**	**Total head-loss**	**Structure head-loss**	**Geotextile Reynolds number**	**Reynolds head-loss coefficient**	k_{R_*}	**Structure head-loss coefficient**
[cm]	[m/s]	[m/s]	[m]	[m]	[m]	[m]	[-]	[-]	[-]	[-]
2.5	0.0038	0.2177	0.0810	0.0100	0.0710	0.0493	96.0391	0.0204	1.2024	0.0170
	0.0053	0.3009	0.1490	0.0380	0.1110	0.0836	132.7663	0.0181	1.0611	0.0171
	0.0060	0.3449	0.1450	0.0080	0.1370	0.1066	152.1684	0.0176	1.1278	0.0156
	0.0087	0.4991	0.2553	0.0260	0.2293	0.1884	220.1945	0.0148	1.0638	0.0140
5.0	0.0032	0.1794	0.1210	0.0470	0.0740	0.0549	79.1455	0.0335	1.0611	0.0316
	0.0055	0.3152	0.2030	0.0460	0.1570	0.1286	139.0575	0.0254	1.0862	0.0234
	0.0066	0.3763	0.2320	0.0180	0.2140	0.1815	165.9942	0.0219	1.1140	0.0197
	0.0090	0.5184	0.4050	0.0310	0.3740	0.3318	228.6954	0.0195	1.0570	0.0184
7.0	0.0037	0.2119	0.1050	0.0050	0.1000	0.0787	93.5052	0.0366	1.1783	0.0311
	0.0052	0.2940	0.1820	0.0300	0.1520	0.1251	129.6860	0.0308	1.0487	0.0294
	0.0065	0.3683	0.2200	0.0140	0.2060	0.1740	162.4700	0.0252	1.1175	0.0225
	0.0092	0.5282	0.3850	0.0310	0.3540	0.3111	233.0184	0.0219	1.0536	0.0208
10.0	0.0033	0.1846	0.1140	0.0120	0.1020	0.0826	81.4395	0.0475	1.0637	0.0447
	0.0054	0.3080	0.2210	0.0380	0.1830	0.1551	135.8901	0.0347	1.0736	0.0323
	0.0067	0.3843	0.3120	0.0350	0.2770	0.2439	169.5639	0.0324	1.1104	0.0292
	0.0089	0.5087	0.4730	0.0460	0.4270	0.3855	224.4208	0.0292	1.0605	0.0276

Table B.4.: Results of the head-loss tests for the series HLP3

Structure width b	**Flow Q**	**Flow velocity**	**Pressure A**	**Pressure B**	**Total head-loss**	**Structure head-loss**	**Geotextile Reynolds number**	**Reynolds head-loss coefficient**	k_{R_*}	**Structure head-loss coefficient**
[cm]	[m/s]	[m/s]	[m]	[m]	[m]	[m]	[-]	[-]	[-]	[-]
2.5	0.0034	0.1953	0.0910	0.0460	0.0450	0.0248	43.0729	0.0128	1.2460	0.0103
	0.0052	0.2940	0.0960	0.0120	0.0840	0.0571	64.8430	0.0124	1.2470	0.0099
	0.0069	0.3925	0.1180	0.0100	0.1080	0.0744	86.5896	0.0107	1.1126	0.0096
	0.0089	0.5087	0.2010	0.0190	0.1820	0.1405	112.2104	0.0107	1.0996	0.0097
5.0	0.0033	0.1846	0.1130	0.0480	0.0650	0.0456	40.7197	0.0262	1.1802	0.0222
	0.0054	0.3080	0.1780	0.0350	0.1430	0.1151	67.9450	0.0238	1.2067	0.0197
	0.0067	0.3843	0.2130	0.0220	0.1910	0.1579	84.7819	0.0210	1.0954	0.0191
	0.0089	0.5087	0.3180	0.0250	0.2930	0.2515	112.2104	0.0162	1.0996	0.0147
7.0	0.0032	0.1794	0.0740	0.0000	0.0740	0.0549	40.1000	0.0335	1.1628	0.0288
	0.0047	0.2670	0.1700	0.0300	0.1400	0.1149	58.8978	0.0316	1.3243	0.0239
	0.0060	0.3449	0.2360	0.0300	0.2060	0.1756	76.0842	0.0290	1.1009	0.0263
	0.0086	0.4896	0.3200	0.0210	0.2990	0.2588	108.0082	0.0212	1.1479	0.0184
10.0	0.0033	0.1846	0.0780	0.0000	0.0780	0.0586	40.7197	0.0357	1.1802	0.0302
	0.0050	0.2871	0.1850	0.0380	0.1470	0.1206	63.3245	0.0327	1.2668	0.0258
	0.0072	0.4092	0.2960	0.0370	0.2590	0.2242	90.2738	0.0293	1.1476	0.0255
	0.0094	0.5381	0.4500	0.0420	0.4080	0.3645	118.6951	0.0247	1.0250	0.0241

C. Wave characteristics during experimental tests without the brushwood fences

Wave number	T	P1		P2		P3		P4		P5		P6	
		H	L	H	L	H	L	H	L	H	L	H	L
	[s]	[cm]	[cm]	[cm]	[cm]	[cm]	[cm]	[cm]	[cm]	[cm]	[cm]	[cm]	[cm]
1	1.41	0.92	64.13	0.62	74.60	0.81	78.90	0.75	87.65	0.52	260.22	0.71	260.22
2	1.28	0.87	55.22	0.91	64.16	0.87	67.83	0.70	75.27	0.71	203.97	0.78	203.97
3	1.12	0.53	46.51	0.73	53.94	0.67	56.98	0.73	63.11	0.76	150.09	0.89	150.09
4	1.27	0.77	41.53	0.86	48.09	0.75	50.76	0.63	56.14	0.85	121.39	0.79	121.39
5	1.39	0.51	34.08	0.70	39.33	0.57	41.45	0.50	45.66	0.83	83.52	0.72	88.50
6	0.78	0.86	60.87	1.02	70.78	1.30	74.84	1.03	83.12	1.10	239.66	1.28	239.66
7	0.71	1.29	55.22	1.28	64.16	1.23	67.83	1.25	75.27	1.21	203.97	1.40	203.97
8	0.63	1.09	46.51	1.28	53.94	1.17	56.98	1.16	63.11	1.45	150.09	1.58	150.09
9	0.68	1.11	40.08	1.39	46.40	1.39	48.96	1.17	54.12	1.10	113.53	1.48	113.53
10	0.65	0.97	34.08	1.01	39.33	0.94	41.45	1.02	45.66	1.11	83.52	1.53	83.52
11	0.48	1.46	60.87	0.81	70.78	2.39	74.84	1.92	83.12	1.70	239.66	2.09	239.66
12	0.40	1.70	55.22	1.76	64.16	2.23	67.83	2.09	75.27	1.96	203.97	2.53	203.97
13	0.36	1.21	46.51	1.88	53.94	2.29	56.98	2.10	63.11	2.60	150.09	2.81	150.09
14	0.40	1.90	40.08	1.89	46.40	1.98	48.96	1.56	54.12	1.90	113.53	2.53	113.53
15	0.40	1.90	34.08	1.91	39.33	1.75	41.45	1.54	45.66	1.66	83.52	2.50	83.52
16	0.35	1.80	64.13	0.94	74.60	2.81	78.90	2.48	87.65	2.43	260.22	2.85	260.22
17	0.35	1.52	55.22	1.63	64.16	3.23	67.83	3.36	75.27	2.75	203.97	2.85	203.97
18	0.25	1.27	46.51	2.07	53.94	3.31	56.98	3.03	63.11	3.19	150.09	4.01	150.09
19	0.29	1.41	41.53	1.84	48.09	2.70	50.76	2.11	56.14	2.64	121.39	3.44	121.39
20	0.32	2.11	34.08	2.26	39.33	2.43	41.45	2.22	45.66	2.17	83.52	3.11	83.52

Table C.1.: Wave characteristics for $d = 3.5$ *cm* provided by the six wave gauges P1 to P6 for tests without structure

Wave number	T	P1		P2		P3		P4		P5		P6	
		H	L	H	L	H	L	H	L	H	L	H	L
	[s]	[cm]	[cm]	[cm]	[cm]	[cm]	[cm]	[cm]	[cm]	[cm]	[cm]	[cm]	[cm]
1	0.93	0.58	77.42	0.92	85.24	1.20	88.56	0.43	95.48	1.03	240.64	1.08	240.64
2	0.84	0.99	70.15	1.34	77.17	1.28	80.15	0.73	86.34	1.01	204.54	1.19	204.54
3	0.69	1.31	58.90	0.84	64.68	1.15	67.12	1.24	72.17	1.03	150.23	1.46	150.23
4	0.62	1.09	50.58	1.00	55.43	1.19	57.46	0.73	61.65	0.93	113.55	1.62	113.55
5	0.90	0.73	44.16	0.94	48.27	1.49	49.99	0.83	53.50	1.07	88.50	1.11	88.50
6	0.53	2.06	77.42	2.15	85.24	1.47	88.56	1.64	95.48	1.56	240.64	1.89	240.64
7	0.54	2.65	70.15	2.16	77.17	2.20	80.15	1.79	86.34	1.76	204.54	1.84	204.54
8	0.38	2.15	56.59	2.22	62.12	1.89	64.45	1.75	69.26	2.49	139.67	2.60	139.67
9	0.39	1.69	50.58	1.40	55.43	1.65	57.46	1.46	61.65	1.97	113.55	2.57	113.55
10	0.39	1.70	42.77	1.60	46.73	1.51	48.37	1.32	51.73	1.73	83.52	2.53	83.52
11	0.37	2.89	0.00	2.47	85.24	2.07	88.56	2.51	95.48	2.36	240.64	2.69	240.64
12	0.35	2.30	70.15	2.36	77.17	2.95	80.15	2.81	86.34	2.54	204.54	2.89	204.54
13	0.25	2.81	58.90	2.78	64.68	3.01	67.12	2.61	72.17	3.05	150.23	3.93	150.23
14	0.31	2.53	52.45	2.56	57.51	2.51	59.64	2.40	64.02	2.77	113.55	3.24	113.55
15	0.28	2.52	44.16	2.86	48.27	2.68	49.99	2.60	53.50	2.57	88.50	3.56	88.50
16	0.29	2.88	81.62	1.68	89.90	4.07	0.00	3.31	100.75	3.17	261.46	3.48	261.46
17	0.27	2.38	33.91	2.08	77.17	3.91	80.15	3.36	86.34	3.66	204.54	3.70	204.54
18	0.20	2.44	58.90	2.50	64.68	7.58	67.12	3.43	72.17	3.98	150.23	5.07	150.23
19	0.22	2.22	52.45	3.33	57.51	4.07	59.64	3.33	64.02	4.02	121.43	4.47	121.43
20	0.20	2.24	44.16	3.10	48.27	4.02	49.99	3.83	53.50	2.89	88.50	4.90	88.50

Table C.2.: Wave characteristics for $d = 5\ cm$ provided by the six wave gauges P1 to P6 for tests without structure

Wave number	T	P1		P2		P3		P4		P5		P6	
		H	L	H	L	H	L	H	L	H	L	H	L
	[s]	[cm]	[cm]	[cm]	[cm]	[cm]	[cm]	[cm]	[cm]	[cm]	[cm]	[cm]	[cm]
1	1.06	1.85	94.64	0.99	100.92	0.94	103.64	0.86	109.41	0.86	241.86	0.94	241.86
2	0.73	1.38	81.64	1.70	86.95	1.50	89.25	1.01	94.10	1.13	189.44	1.37	189.44
3	0.84	0.97	68.68	1.05	73.01	1.15	74.88	0.97	78.79	1.29	139.78	1.19	139.78
4	0.82	0.77	61.15	1.06	64.89	1.07	66.50	1.02	69.85	1.32	113.58	1.22	113.58
5	0.95	0.90	51.33	1.09	54.30	1.43	55.55	1.08	58.16	0.98	83.52	1.05	83.52
6	0.61	2.41	94.64	1.77	100.92	1.80	103.64	1.73	109.41	1.70	241.86	1.64	241.86
7	0.44	2.36	81.64	1.89	86.95	2.67	89.25	1.90	94.10	1.92	189.44	2.29	189.44
8	0.51	1.86	71.56	2.12	76.11	2.10	78.07	1.71	82.20	2.27	150.40	1.97	150.40
9	0.64	1.55	61.15	1.77	64.89	1.48	66.50	1.33	69.85	2.27	113.58	1.56	113.58
10	0.58	1.62	51.33	1.53	54.30	1.83	55.55	1.46	58.16	1.68	83.52	1.71	83.52
11	0.41	2.46	94.64	2.22	100.92	2.36	103.64	1.63	109.41	2.24	241.86	2.42	241.86
12	0.40	2.66	85.59	2.16	91.20	2.65	93.63	2.13	98.76	2.08	205.24	2.51	205.24
13	0.31	2.42	71.56	3.54	76.11	3.37	78.07	2.35	82.20	3.33	150.40	3.25	150.40
14	0.42	2.23	61.15	2.53	64.89	2.27	66.50	1.85	69.85	3.05	113.58	2.39	113.58
15	0.41	1.98	51.33	2.21	54.30	2.20	55.55	2.17	58.16	2.06	83.52	2.41	83.52
16	0.31	3.63	45.18	3.68	106.52	3.46	109.42	2.90	115.55	3.05	263.02	3.25	263.02
17	0.25	4.62	37.85	3.56	91.20	3.80	93.63	3.30	98.76	2.82	205.24	3.93	205.24
18	0.25	7.34	71.56	5.68	76.11	3.67	78.07	3.05	82.20	4.16	150.40	4.02	150.40
19	0.26	3.49	61.15	4.42	64.89	3.22	66.50	2.75	69.85	3.80	113.58	3.79	113.58
20	0.32	2.60	51.33	3.41	54.30	3.74	55.55	2.75	58.16	2.63	83.52	3.17	83.52

Table C.3.: Wave characteristics for $d = 7$ *cm* provided by the six wave gauges P1 to P6 for tests without structure

Wave number	T	P1		P2		P3		P4		P5		P6	
		H	L	H	L	H	L	H	L	H	L	H	L
	[s]	[cm]	[cm]	[cm]	[cm]	[cm]	[cm]	[cm]	[cm]	[cm]	[cm]	[cm]	[cm]
1	0.93	1.01	114.93	0.95	119.89	0.97	122.07	1.01	126.75	0.99	243.52	1.08	243.52
2	1.19	0.94	103.65	0.94	108.04	1.08	109.96	0.84	114.08	0.95	206.16	0.84	206.16
3	0.80	0.94	86.10	0.91	89.57	0.88	91.09	0.59	94.32	0.98	150.61	1.24	150.61
4	1.10	0.80	75.96	0.93	78.89	0.77	80.16	0.84	82.86	0.86	121.52	0.91	121.52
5	1.33	1.16	62.78	0.78	64.99	0.85	65.94	0.75	67.92	0.89	88.51	0.75	88.51
6	0.59	2.01	114.93	1.59	119.89	1.82	122.07	1.80	126.75	2.04	243.52	1.69	243.52
7	0.49	2.53	98.72	1.94	102.85	1.90	104.66	1.63	108.54	1.31	190.10	2.04	190.10
8	0.53	1.92	82.49	1.64	85.77	1.48	87.20	1.97	90.24	2.35	139.92	1.87	139.92
9	0.59	1.44	73.00	1.60	75.77	1.62	76.97	1.45	79.51	2.11	113.61	1.70	113.61
10	0.96	1.47	62.78	1.56	64.99	1.23	65.94	1.23	67.92	1.55	88.51	1.04	88.51
11	0.39	2.32	114.93	2.45	119.89	2.23	122.07	2.71	126.75	2.38	243.52	2.58	243.52
12	0.40	2.37	98.72	2.82	102.85	2.65	104.66	2.20	108.54	1.87	190.10	2.53	190.10
13	0.33	2.86	86.10	2.31	85.77	2.31	87.20	2.71	94.32	3.36	139.92	3.07	139.92
14	0.42	2.16	73.00	2.31	75.77	2.41	76.97	2.41	79.51	3.08	113.61	2.40	113.61
15	0.63	1.62	60.56	1.66	62.64	1.93	63.54	1.46	65.40	1.81	83.52	1.60	83.52
16	0.31	2.95	121.43	2.95	126.71	2.70	129.04	3.29	134.03	2.90	265.18	3.22	265.18
17	0.29	3.67	103.65	3.15	108.04	3.68	109.96	2.64	114.08	3.45	206.16	3.51	206.16
18	0.31	3.30	89.99	2.55	93.67	4.07	95.27	2.85	98.70	3.68	162.45	3.19	162.45
19	0.27	2.94	75.96	3.00	78.89	2.76	80.16	2.56	82.86	2.36	121.52	3.77	121.52
20	0.52	2.44	62.78	2.64	64.99	2.63	65.94	2.46	67.92	2.86	88.51	1.93	88.51
21	0.24	3.83	114.93	3.96	119.89	3.58	122.07	4.28	126.75	3.91	243.52	4.18	243.52
22	0.24	4.31	103.65	4.43	108.04	4.35	109.96	3.38	114.08	3.91	206.16	4.18	206.16
23	0.20	4.31	86.10	4.30	89.57	4.26	91.09	2.77	94.32	3.83	150.61	4.94	150.61
24	0.31	2.52	73.00	2.78	75.77	2.44	76.97	2.37	79.51	3.55	113.61	3.26	113.61
25	0.45	3.14	62.78	3.20	64.99	3.01	65.94	2.79	67.92	2.99	88.51	2.24	88.51

Table C.4.: Wave characteristics for $d = 10\ cm$ provided by the six wave gauges P1 to P6 for tests without structure

Table C.5.: Wave characteristics for $d = 12.5\ cm$ provided by the six wave gauges P1 to P6 for tests without structure

		P1		P2		P3		P4		P5		P6	
Wave number	T	H	L	H	L	H	L	H	L	H	L	H	L
	[s]	[cm]	[cm]	[cm]	[cm]	[cm]	[cm]	[cm]	[cm]	[cm]	[cm]	[cm]	[cm]
1	1.04	1.57	128.77	1.18	133.01	1.59	134.89	1.11	138.95	1.42	244.77	1.04	244.77
2	1.38	1.36	115.86	1.01	119.58	1.05	121.22	1.00	124.76	1.23	206.83	1.38	206.83
3	1.52	2.09	0.00	1.09	98.58	0.67	99.85	1.06	102.56	1.62	150.75	1.52	150.75
4	1.00	0.95	84.01	0.66	86.39	0.53	87.43	0.78	89.64	1.08	121.55	1.00	121.55
5	0.78	1.20	68.76	0.69	70.46	0.66	71.20	0.44	72.75	0.72	88.51	0.78	88.51
6	1.98	1.88	136.19	1.55	140.73	1.70	142.75	1.83	147.10	2.00	266.81	1.98	266.81
7	2.40	1.96	115.86	1.76	119.58	1.80	121.22	1.76	124.76	1.69	206.83	2.40	206.83
8	2.24	1.72	95.70	1.71	98.58	1.25	99.85	1.88	102.56	2.34	150.75	2.24	150.75
9	1.83	1.41	80.59	1.72	82.82	1.42	83.80	1.66	85.86	1.89	113.63	1.83	113.63
10	0.95	1.36	68.76	1.10	70.46	1.38	71.20	0.95	72.75	1.49	88.51	0.95	88.51
11	2.72	2.23	136.19	2.19	140.73	2.15	142.75	1.83	147.10	2.55	266.81	2.72	266.81
12	3.03	2.55	115.86	2.37	119.58	2.46	121.22	2.44	124.76	2.13	206.83	3.03	206.83
13	2.72	2.22	95.70	2.13	98.58	1.75	99.85	2.42	102.56	2.83	150.75	2.72	150.75
14	2.15	1.85	80.59	2.19	82.82	1.67	83.80	2.16	85.86	2.38	121.55	2.15	113.63
15	1.48	1.52	68.76	1.73	70.46	1.71	71.20	1.35	72.75	1.73	88.51	1.48	88.51
16	3.45	3.36	136.19	3.27	140.73	3.24	142.75	3.14	147.10	3.57	266.81	3.45	266.81
17	3.84	3.25	110.20	3.27	113.69	3.45	115.23	3.07	118.54	3.82	190.56	3.84	190.56
18	3.07	2.54	95.70	2.41	98.58	2.32	99.85	2.81	102.56	3.20	150.75	3.07	150.75
19	2.74	2.46	80.59	3.10	82.82	2.30	83.80	2.76	85.86	3.02	113.63	2.74	113.63
20	1.45	1.92	68.76	2.04	70.46	2.39	71.20	1.93	72.75	2.25	88.51	1.45	88.51
21	4.34	4.66	128.77	4.43	133.01	4.40	134.89	4.36	138.95	4.55	244.77	4.34	244.77
22	4.79	3.96	115.86	3.82	119.58	3.80	121.22	3.89	124.76	3.17	206.83	4.79	206.83
23	4.90	3.80	95.70	3.71	98.58	2.85	99.85	4.06	102.56	4.56	150.75	4.90	150.75
24	3.26	2.95	80.59	3.39	82.82	2.47	83.80	3.15	85.86	3.88	113.63	3.26	113.63
25	2.21	3.12	68.76	3.07	70.46	2.96	71.20	2.35	72.75	3.03	88.51	2.21	88.51
26	5.88	4.89	136.19	5.19	140.73	5.60	142.75	4.80	147.10	4.88	266.81	5.88	266.81
27	5.69	4.75	115.86	4.81	119.58	4.69	121.22	5.08	124.76	4.33	206.83	5.69	206.83
28	6.30	4.71	95.70	5.05	98.58	4.20	99.85	4.36	102.56	5.05	150.75	6.30	150.75
29	3.99	3.80	80.59	4.41	82.82	3.44	83.80	4.15	85.86	5.36	113.63	3.99	113.63
30	2.24	4.68	68.76	4.94	70.46	4.74	71.20	4.07	72.75	4.96	88.51	2.24	88.51

Wave number	T	P1		P2		P3		P4		P5		P6	
		H	L	H	L	H	L	H	L	H	L	H	L
	[s]	[cm]	[cm]	[cm]	[cm]	[cm]	[cm]	[cm]	[cm]	[cm]	[cm]	[cm]	[cm]
1	0.55	1.87	136.12	1.92	140.03	2.39	141.77	1.64	145.53	2.41	245.46	1.81	245.46
2	0.58	1.49	122.30	1.93	125.71	1.65	127.22	1.47	130.47	1.87	207.19	1.74	207.19
3	0.56	1.49	100.68	1.15	103.28	1.42	104.43	1.13	106.88	2.32	150.82	1.78	150.82
4	0.73	1.38	84.43	1.68	86.41	1.50	87.27	1.43	89.10	1.58	113.64	1.37	113.64
5	0.94	1.18	68.90	0.74	70.26	0.80	70.85	0.86	72.07	1.04	83.53	1.07	83.53
6	0.42	2.41	136.12	2.68	140.03	3.17	141.77	2.31	145.53	3.00	245.46	2.39	245.46
7	0.36	2.25	122.30	2.63	125.71	2.56	127.22	2.06	130.47	2.61	207.19	2.75	207.19
8	0.45	2.08	100.68	1.60	103.28	1.86	104.43	1.61	106.88	2.68	150.82	2.24	150.82
9	0.42	1.90	88.11	1.51	90.23	1.84	91.16	1.38	93.13	1.88	121.57	2.37	121.57
10	0.71	1.17	68.90	0.95	70.26	1.13	70.85	1.27	72.07	1.78	83.53	1.40	83.53
11	0.26	3.08	144.07	2.44	148.26	3.26	150.13	3.06	154.17	3.52	267.73	3.79	267.73
12	0.28	2.98	122.30	2.87	125.71	3.26	127.22	2.46	130.47	2.73	207.19	3.57	207.19
13	0.25	2.43	100.68	2.69	103.28	2.24	104.43	2.67	106.88	3.42	150.82	4.04	150.82
14	0.36	2.35	88.11	1.88	90.23	2.18	91.16	1.76	93.13	2.33	121.57	2.78	121.57
15	0.63	1.67	68.90	1.51	70.26	1.71	70.85	1.81	72.07	1.91	83.53	1.59	83.53
16	0.20	4.36	136.12	3.79	140.03	4.51	141.77	4.29	145.53	4.80	245.46	4.96	245.46
17	0.21	4.12	122.30	3.67	125.71	4.37	127.22	3.37	130.47	3.66	207.19	4.77	207.19
18	0.21	2.94	100.68	3.48	103.28	2.83	104.43	3.05	106.88	3.56	150.82	4.81	150.82
19	0.26	3.30	88.11	2.63	90.23	3.36	91.16	2.74	93.13	2.81	121.57	3.90	121.57
20	0.39	2.66	74.61	2.58	76.19	2.74	76.88	2.59	78.33	2.11	93.95	2.59	93.95
21	0.18	5.73	136.12	5.68	140.03	6.14	141.77	5.32	145.53	6.14	245.46	5.70	245.46
22	0.16	5.29	122.30	4.65	125.71	5.52	127.22	4.50	130.47	5.05	207.19	6.22	207.19
23	0.18	4.24	100.68	4.58	103.28	4.23	104.43	3.51	106.88	4.62	150.82	5.59	150.82
24	0.24	3.85	84.43	3.15	86.41	3.36	87.27	3.03	89.10	4.12	113.64	4.09	113.64
25	0.43	3.99	71.68	3.88	73.15	3.16	73.79	2.63	75.12	5.06	88.51	2.33	88.51

Table C.6.: Wave characteristics for $d = 14\ cm$ provided by the six wave gauges P1 to P6 for tests without structure

Wave number	T	P1		P2		P3		P4		P5		P6	
		H	L	H	L	H	L	H	L	H	L	H	L
	[s]	[cm]	[cm]	[cm]	[cm]	[cm]	[cm]	[cm]	[cm]	[cm]	[cm]	[cm]	[cm]
1	0.46	1.77	140.71	1.12	144.42	1.49	146.08	1.75	149.65	1.80	245.90	2.17	245.90
2	0.65	1.72	126.29	1.58	129.52	1.36	130.95	1.89	134.04	1.70	207.42	1.54	207.42
3	0.56	1.23	103.72	1.54	106.16	1.28	107.24	1.14	109.55	1.58	150.86	1.78	150.86
4	0.57	1.21	90.59	0.79	92.55	1.27	93.42	1.17	95.25	1.58	121.58	1.75	121.58
5	1.05	1.05	73.40	0.87	74.73	0.94	75.31	0.86	76.51	1.26	88.51	0.95	88.51
6	0.34	3.05	140.71	2.28	144.42	2.96	146.08	2.88	149.65	3.27	245.90	2.97	245.90
7	0.41	2.52	126.29	2.12	129.52	2.07	130.95	2.40	134.04	1.71	207.42	2.45	207.42
8	0.38	2.03	103.72	2.21	106.16	2.45	107.24	1.45	109.55	2.50	150.86	2.62	150.86
9	0.58	1.44	90.59	1.58	92.55	1.24	93.42	1.33	95.25	1.70	121.58	1.74	121.58
10	0.74	1.44	73.40	1.32	74.73	1.27	75.31	1.24	76.51	1.29	88.51	1.34	88.51
11	0.26	3.43	140.71	2.51	144.42	3.08	146.08	3.39	149.65	3.49	245.90	3.88	245.90
12	0.30	3.22	126.29	2.50	129.52	2.64	130.95	2.80	134.04	2.07	207.42	3.37	207.42
13	0.30	2.23	103.72	2.51	106.16	2.06	107.24	2.28	109.55	3.01	150.86	3.34	150.86
14	0.33	2.45	86.74	1.74	88.57	2.74	89.37	2.04	95.25	2.85	113.64	3.05	113.64
15	0.67	1.59	73.40	1.44	74.73	1.81	75.31	1.27	76.51	1.77	88.51	1.50	88.51
16	0.22	4.64	140.71	3.54	144.42	4.14	146.08	4.49	149.65	4.80	245.90	4.48	245.90
17	0.22	3.92	126.29	3.27	129.52	3.43	130.95	3.45	134.04	2.97	207.42	4.57	207.42
18	0.25	2.90	103.72	3.13	106.16	2.89	107.24	2.50	109.55	3.68	150.86	4.01	150.86
19	0.38	2.33	90.59	2.56	92.55	2.08	93.42	2.11	95.25	2.49	121.58	2.62	121.58
20	0.38	2.07	76.46	2.82	77.91	2.74	78.54	2.30	79.86	2.63	93.95	2.67	93.95
21	0.16	6.00	140.71	4.78	144.42	4.96	146.08	5.81	149.65	5.78	245.90	6.09	245.90
22	0.17	5.17	126.29	4.64	129.52	4.74	130.95	4.67	134.04	4.33	207.42	5.97	207.42
23	0.19	4.08	103.72	4.06	106.16	4.38	107.24	2.89	109.55	4.74	150.86	5.15	150.86
24	0.22	3.42	90.59	2.94	92.55	3.84	93.42	3.57	95.25	5.05	121.58	4.63	121.58
25	0.20	3.20	76.46	3.82	77.91	3.99	78.54	3.50	79.86	4.87	93.95	5.12	93.95

Table C.7.: Wave characteristics for $d = 15\ cm$ provided by the six wave gauges P1 to P6 for tests without structure

D. Results of the experimental tests with fixed bed

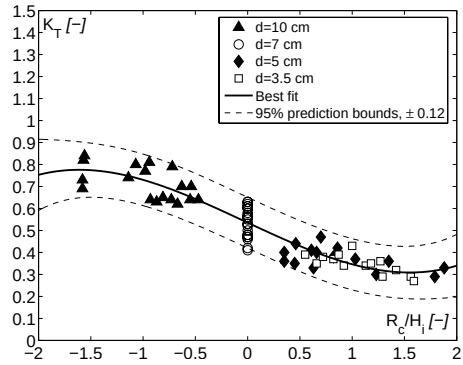

a)

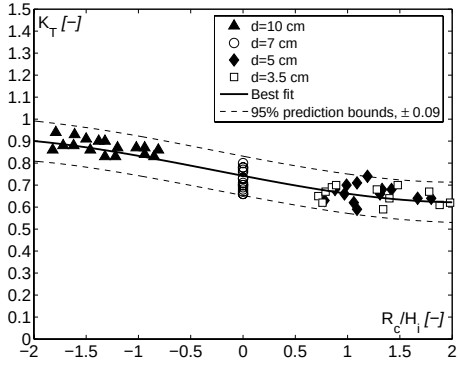

b)

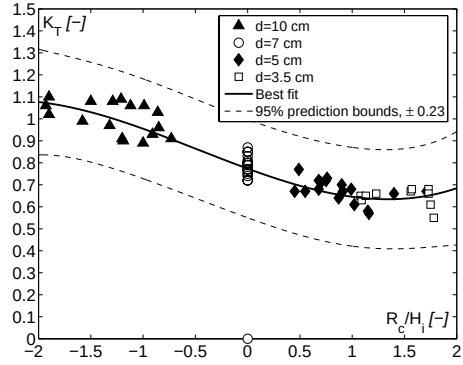

c)

Figure D.1.: Transmission coefficient K_T for the height $h = 7\ cm$ of the brushwood fences calculated as a function of the relative freeboard: a) $p = 0.16$; b) $p = 0.36$; c) $p = 0.62$

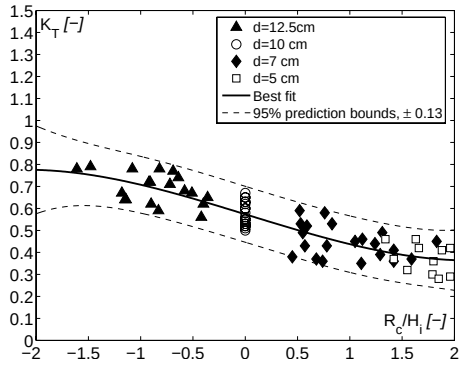

a)

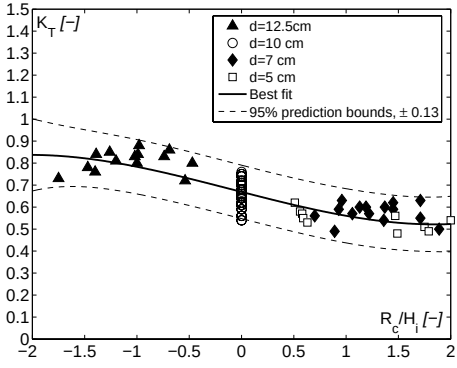

b)

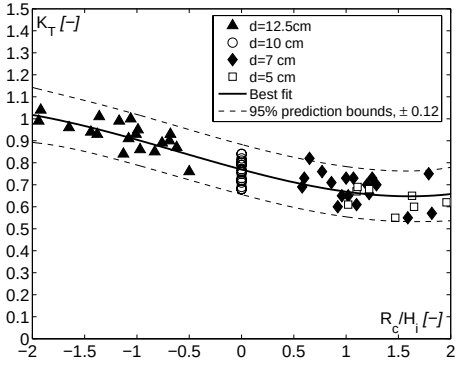

c)

Figure D.2.: Transmission coefficient K_T for the height $h = 10\,cm$ of the brushwood fences calculated as a function of the relative freeboard: a) $p = 0.16$; b) $p = 0.36$; c) $p = 0.62$

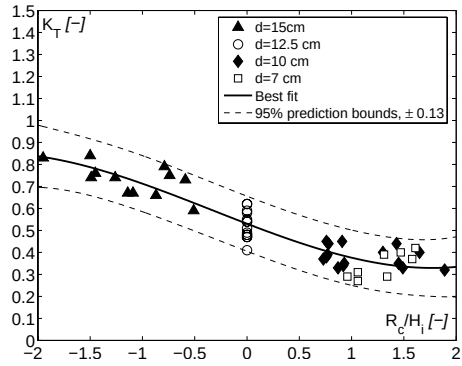

a)

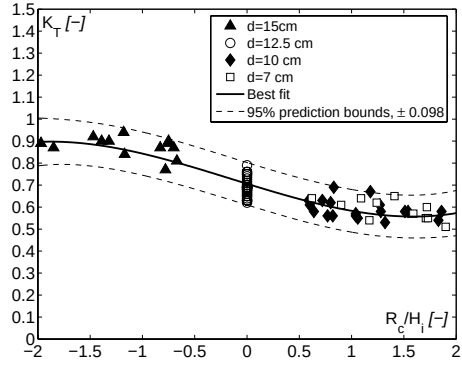

b)

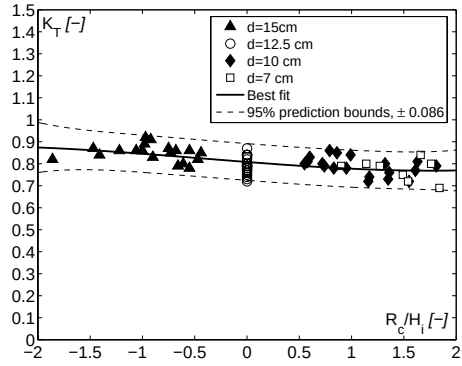

c)

Figure D.3.: Transmission coefficient K_T for the height $h = 12.5\ cm$ of the brushwood fences calculated as a function of the relative freeboard: a) $p = 0.16$; b) $p = 0.36$; c) $p = 0.62$

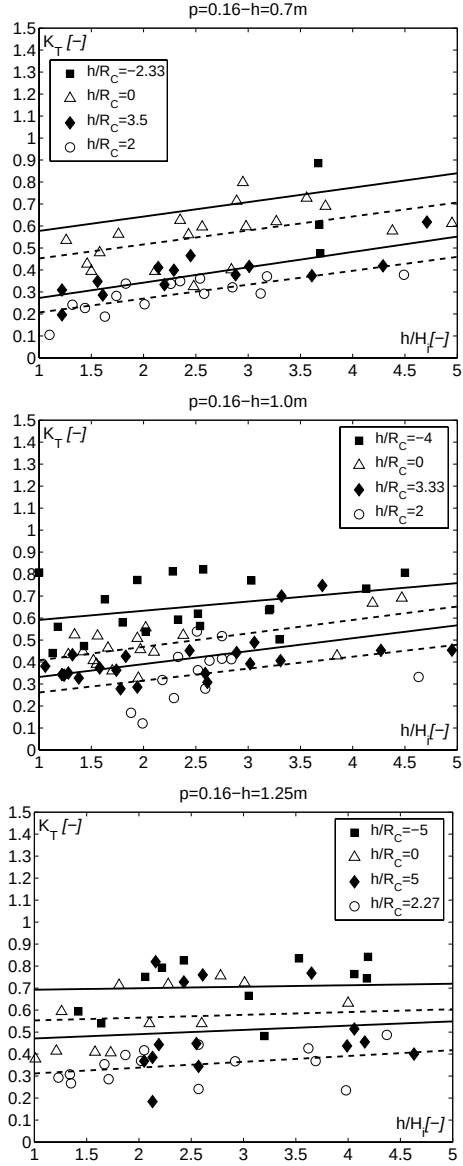

Figure D.4.: Transmission coefficient K_T for different heights h of the brushwood fences and for a porosity $p = 0.16$ calculated as a function of the relative height h/H_i

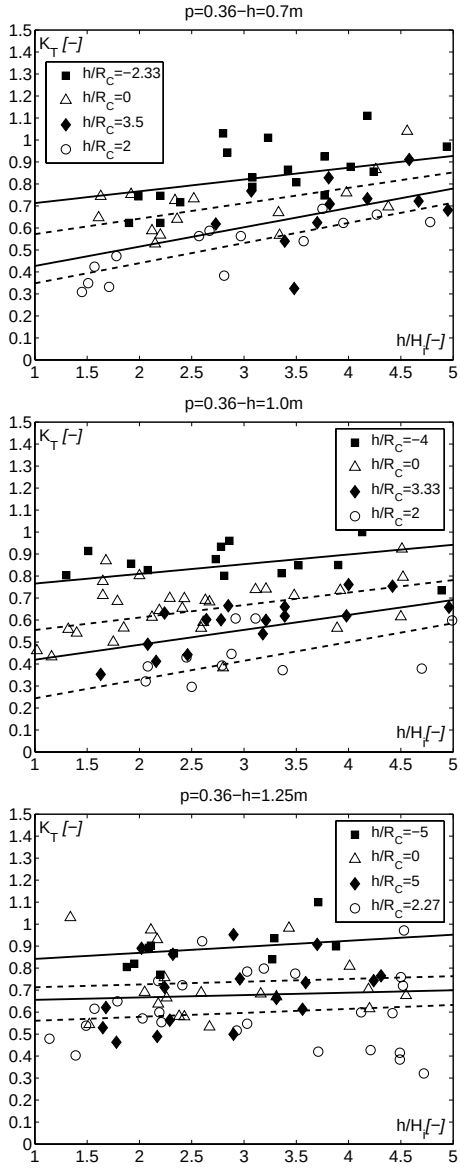

Figure D.5.: Transmission coefficient K_T for different heights h of the brushwood fences and for a porosity $p = 0.36$ calculated as a function of the relative height h/H_i

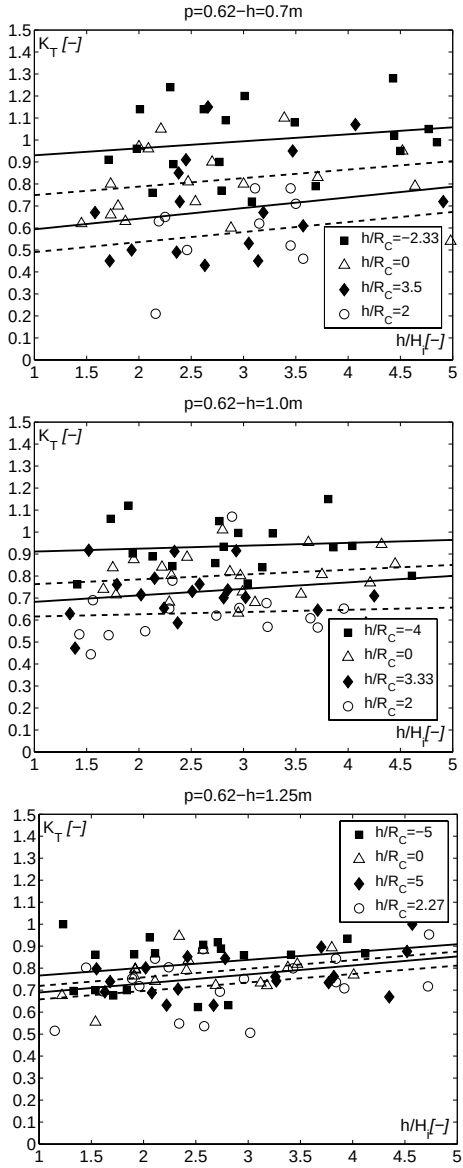

Figure D.6.: Transmission coefficient K_T for different heights h of the brushwood fences and for a porosity $p = 0.62$ calculated as a function of the relative height h/H_i

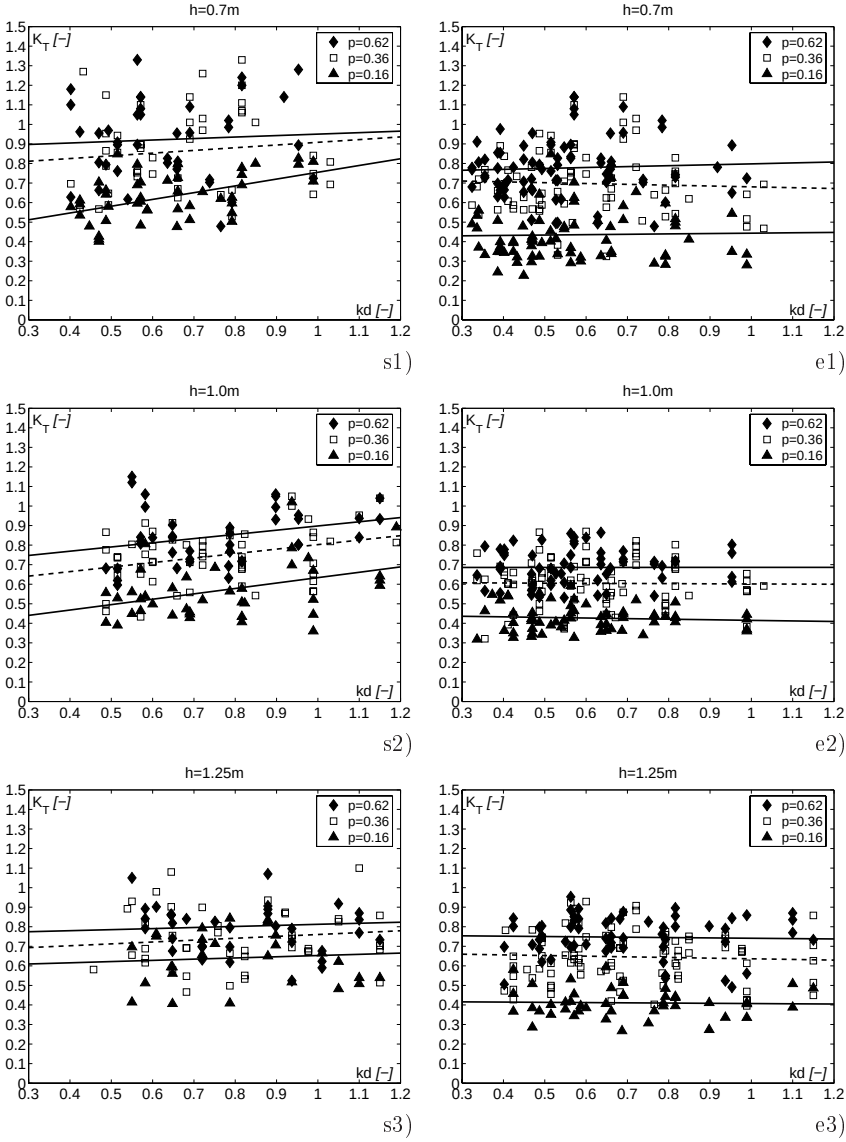

Figure D.7.: Transmission coefficient K_T for different heights h of the brushwood fences calculated as a function of the relative wave number kd when the structure is completely submerged (series 's') and completely emerging (series 'e')

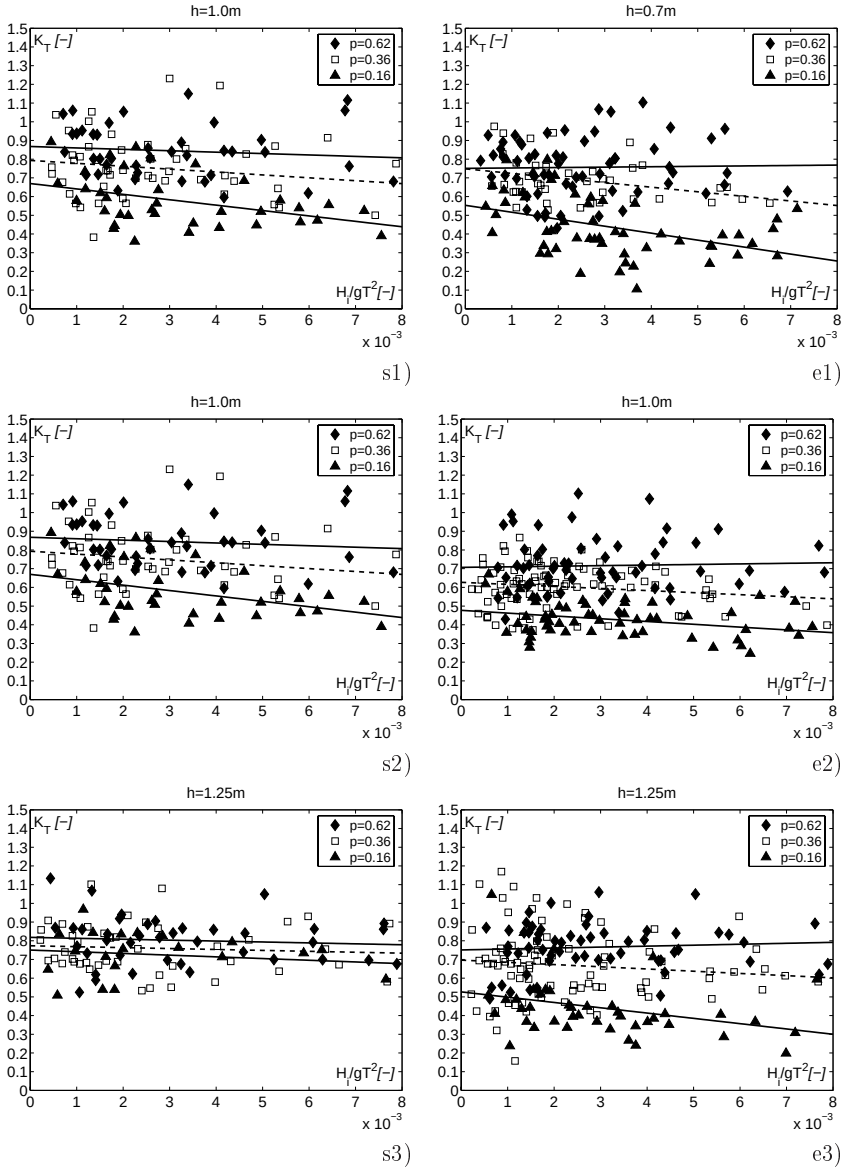

Figure D.8.: Transmission coefficient K_T for different heights h of the brushwood fences calculated as a function of the wave steepness H_i/gT^2 when the structure is in completely submerged (series 's') and in a completely emerging situation (series 'e')

E. Results of the experimental tests with movable bed

$D[mm]$	0.00	0.01	0.02	0.03	0.04	0.05	0.06	0.07	0.08	0.09
0.10	0.0630	0.0672	0.0714	0.0756	0.0798	0.0840	0.0872	0.0904	0.0936	0.0968
0.20	0.1000	0.1030	0.1060	0.1090	0.1120	0.1150	0.1170	0.1190	0.1210	0.1230
0.30	0.1250	0.1270	0.1290	0.1310	0.1330	0.1350	0.1370	0.0139	0.1410	0.1430
0.40	0.1450	0.1466	0.1482	0.1498	0.1514	0.1530	0.1546	0.1562	0.1578	0.1594
0.50	0.1610	0.1622	0.1634	0.1646	0.1658	0.1670	0.1682	0.1694	0.1706	0.1718
0.60	0.1730	0.1742	0.1754	0.1766	0.1778	0.1790	0.1802	0.1814	0.1826	0.1838
0.70	0.1850	0.1859	0.1868	0.1877	0.1886	0.1895	0.1904	0.1913	0.1922	0.1931
0.80	0.1940	0.1948	0.1956	0.1964	0.1972	0.1980	0.1988	0.1996	0.2004	0.2012
0.90	0.2020	0.2028	0.2036	0.2044	0.2052	0.2060	0.2068	0.2076	0.2084	0.2092
1.00	0.2100	0.2108	0.2116	0.2124	0.2132	0.2140	0.2148	0.2156	0.2164	0.2172

Table E.1.: Summary of recommended A values after Dean (2002)

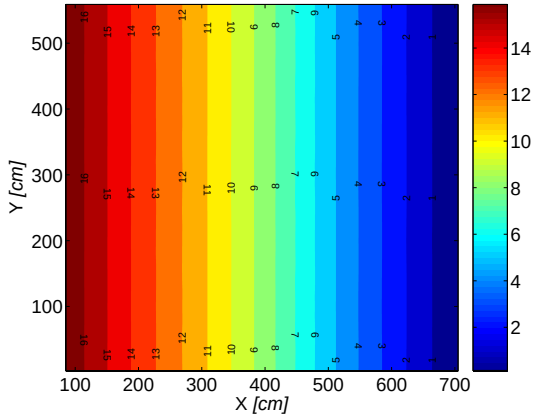

Figure E.1.: Initial bathymetry of the wave tank

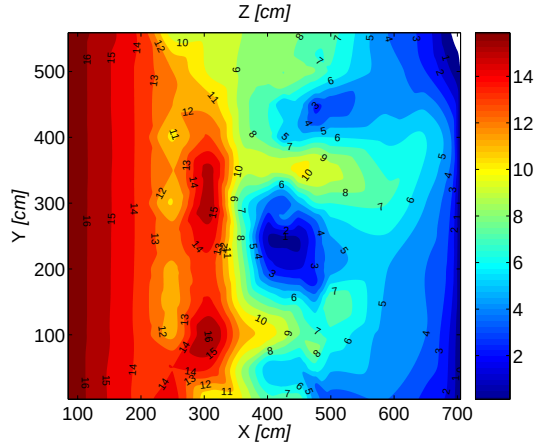

Figure E.2.: Results of the test CS1: final bathymetry

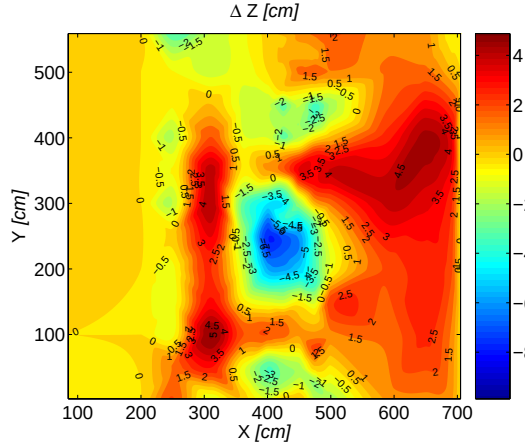

Figure E.3.: Results of the test CS1: erosion/deposition values

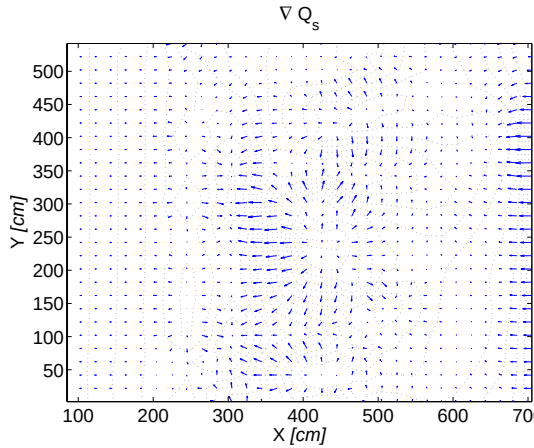

Figure E.4.: Results of the test CS1: bedload gradient

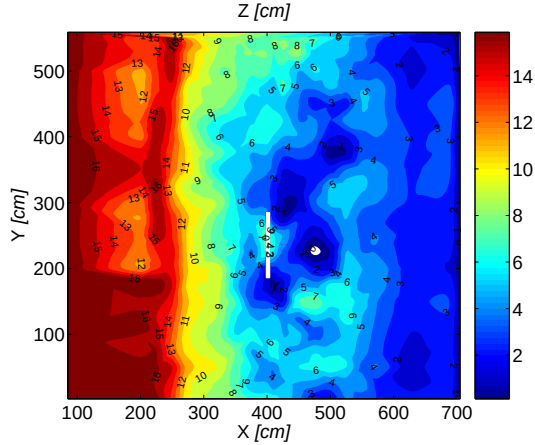

Figure E.5.: Results of the test CS2: final bathymetry

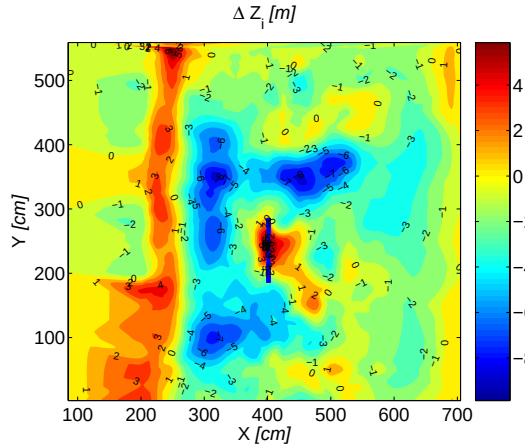

Figure E.6.: Results of the test CS2: erosion/deposition intermediate values compared to initial bathymetry resulting of the test CS1

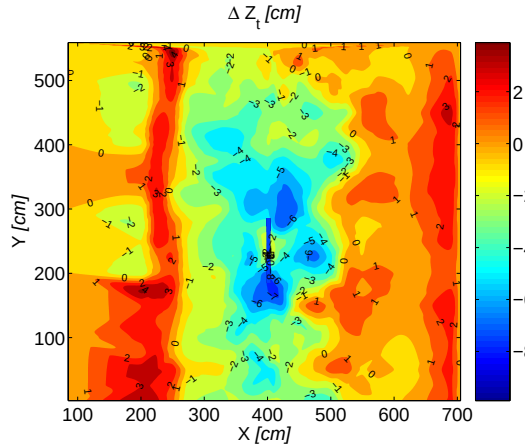

Figure E.7.: Results of the test CS2: erosion/deposition total values compared to initial bathymetry of the wave tank

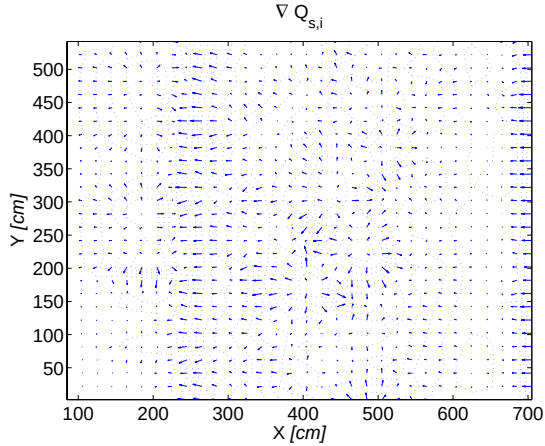

Figure E.8.: Results of the test CS2: bedload gradient

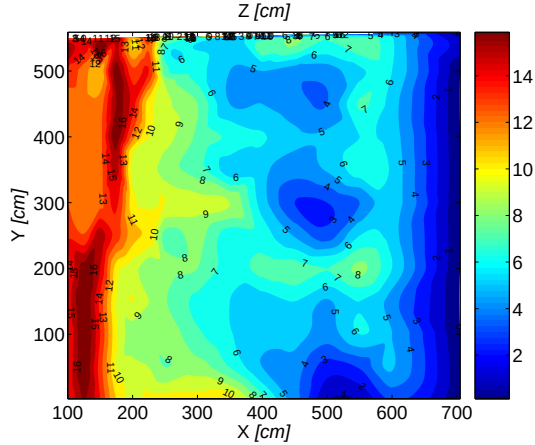

Figure E.9.: Results of the test SE: final bathymetry

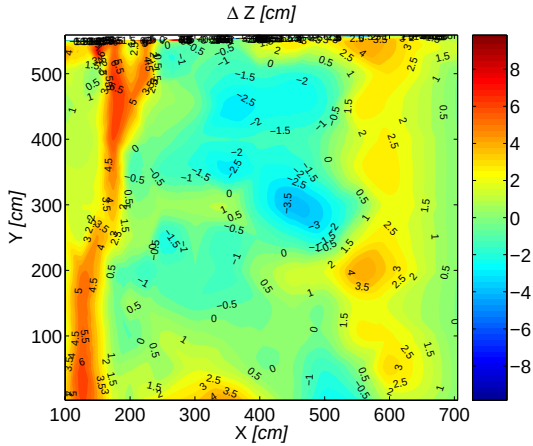

Figure E.10.: Results of the test SE: erosion/deposition values compared to initial bathymetry

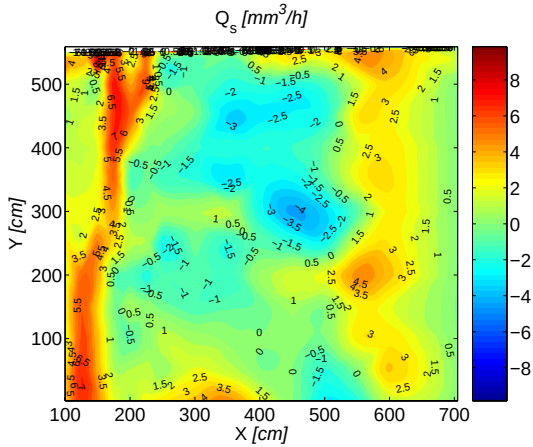

Figure E.11.: Results of the test SE: erosion/deposition rate

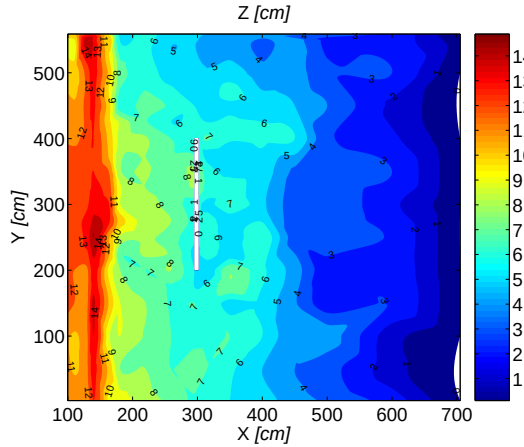

Figure E.12.: Results of the test T1: final bathymetry

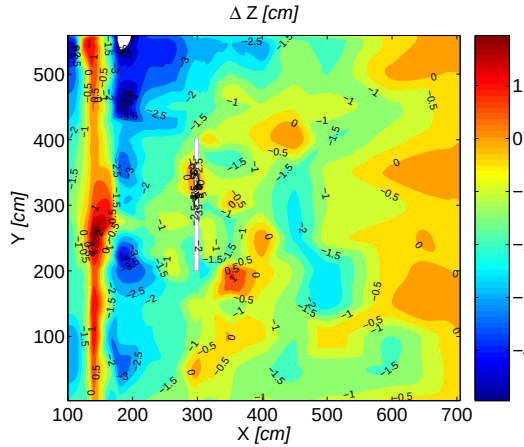

Figure E.13.: Results of the test T1: erosion/deposition values compared to initial bathymetry

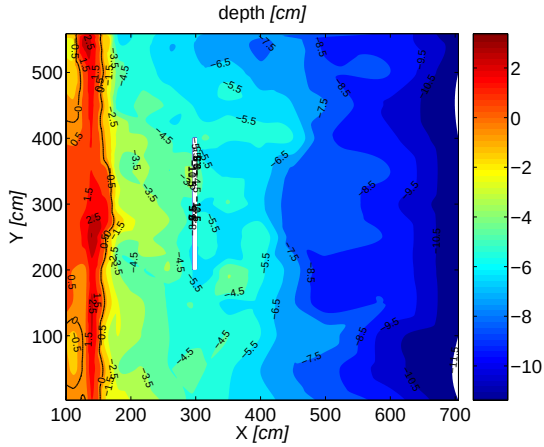

Figure E.14.: Results of the test T1: bathymetry related to initial water depth

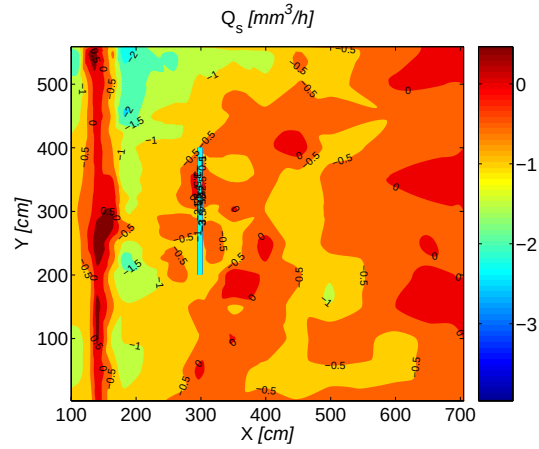

Figure E.15.: Results of the test T1: erosion/deposition rate

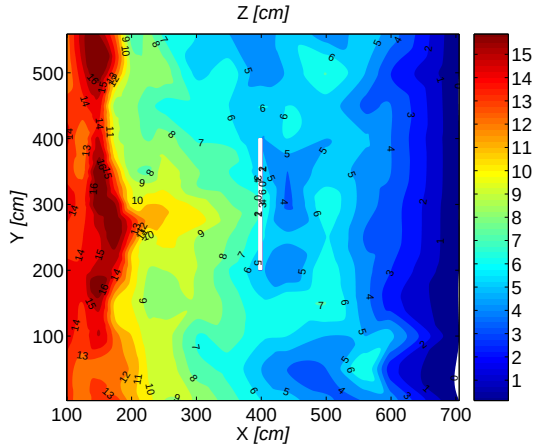

Figure E.16.: Results of the test T2: final bathymetry

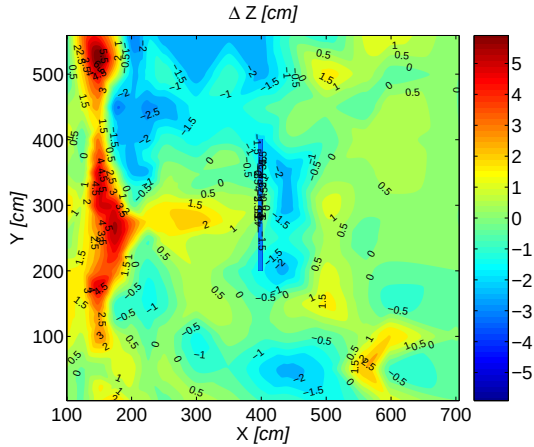

Figure E.17.: Results of the test T2: erosion/deposition values compared to initial bathymetry

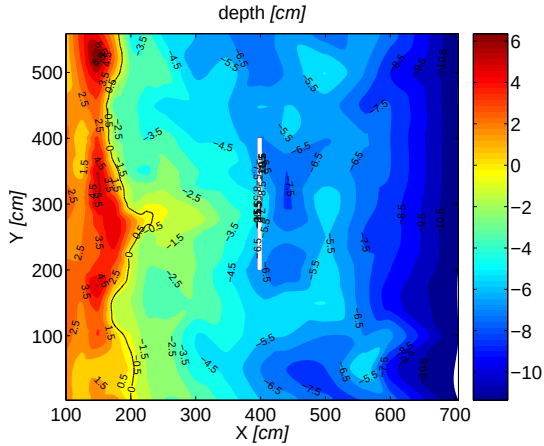

Figure E.18.: Results of the test T2: bathymetry related to initial water depth

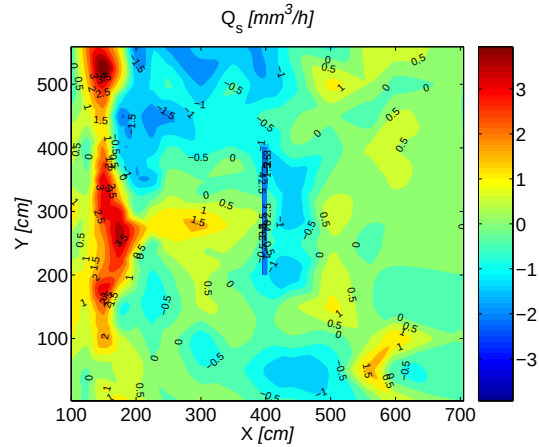

Figure E.19.: Results of the test T2: erosion/deposition rate

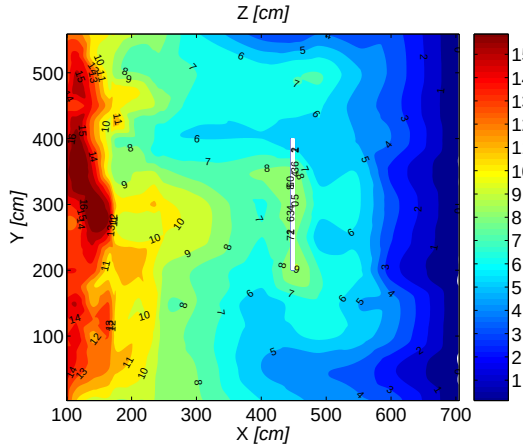

Figure E.20.: Results of the test T3: final bathymetry

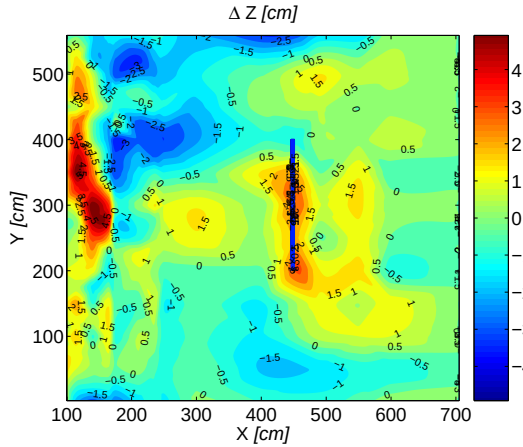

Figure E.21.: Results of the test T3: erosion/deposition values compared to initial bathymetry

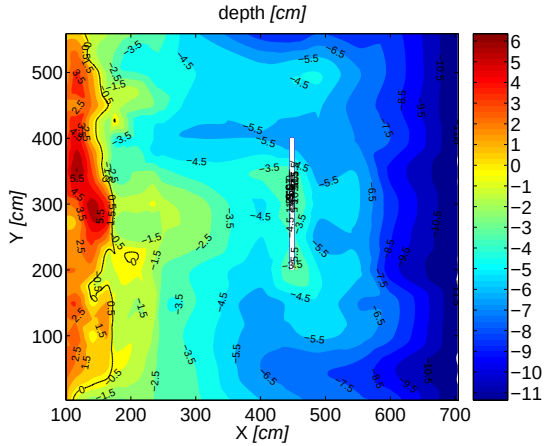

Figure E.22.: Results of the test T3: bathymetry related to initial water depth

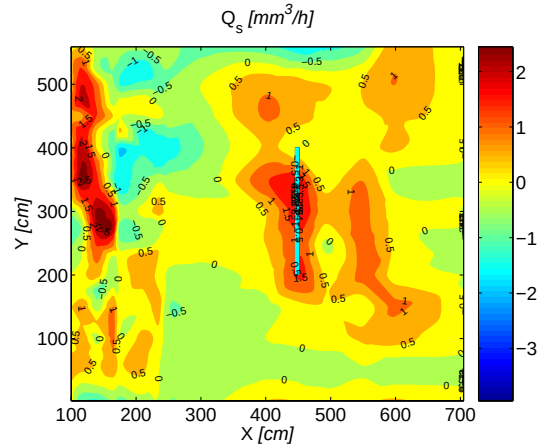

Figure E.23.: Results of the test T3: erosion/deposition rate

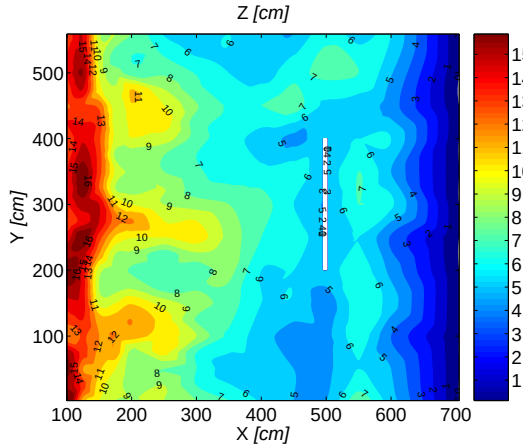

Figure E.24.: Results of the test T4: final bathymetry

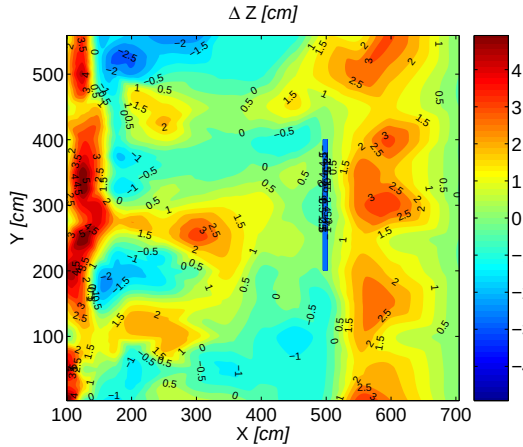

Figure E.25.: Results of the test T4: erosion/deposition values compared to initial bathymetry

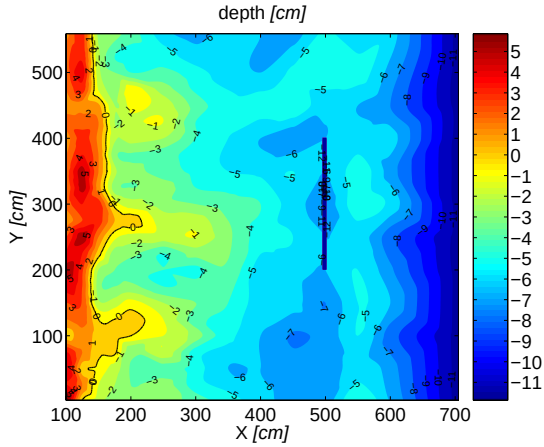

Figure E.26.: Results of the test T4: bathymetry related to initial water depth

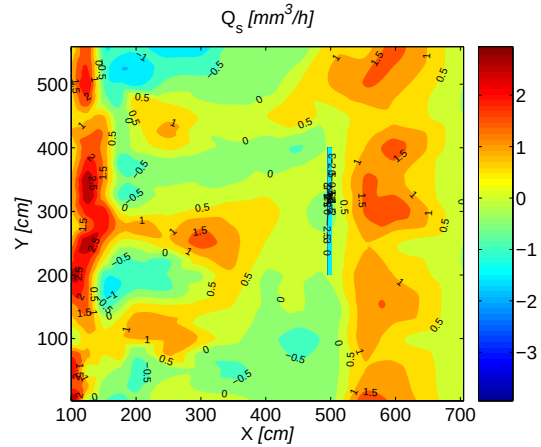

Figure E.27.: Results of the test T4: erosion/deposition rate

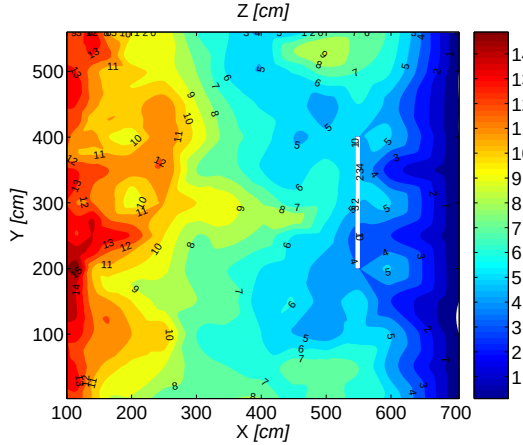

Figure E.28.: Results of the test T5: final bathymetry

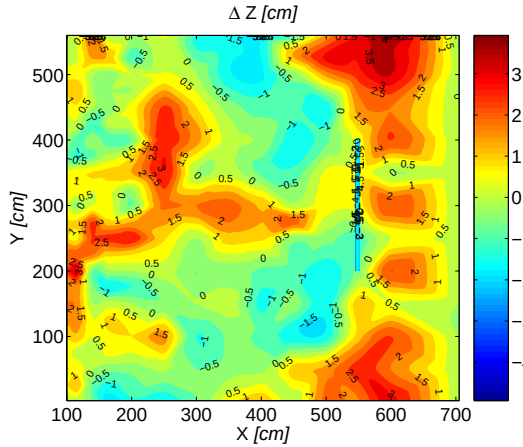

Figure E.29.: Results of the test T5: erosion/deposition values compared to initial bathymetry

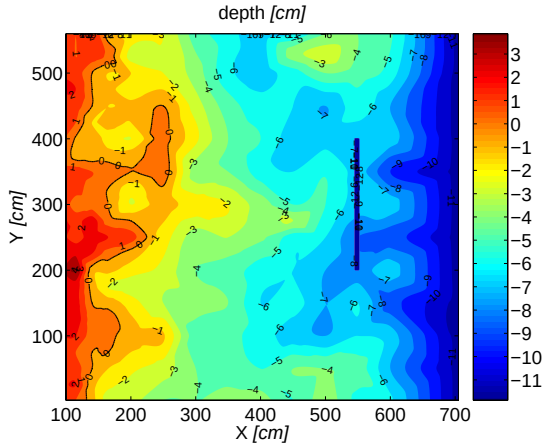

Figure E.30.: Results of the test T5: bathymetry related to initial water depth

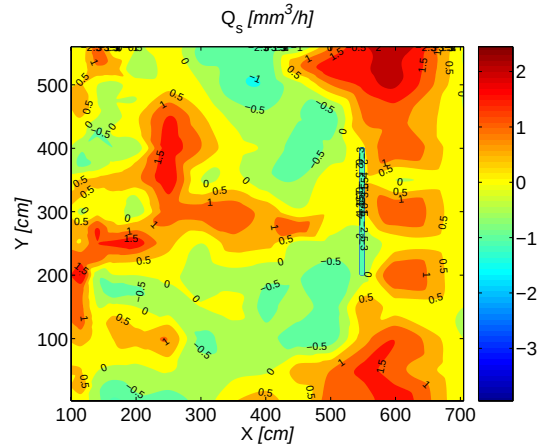

Figure E.31.: Results of the test T5: erosion/deposition rate

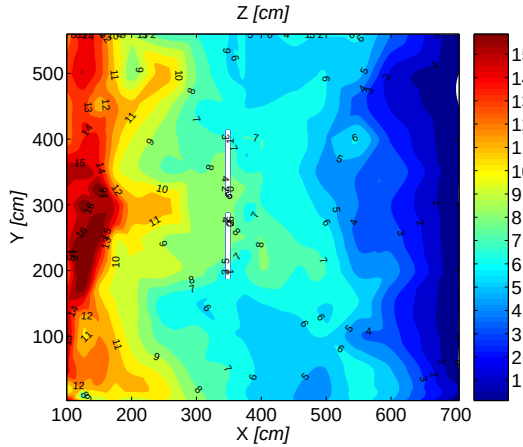

Figure E.32.: Results of the test T6: final bathymetry

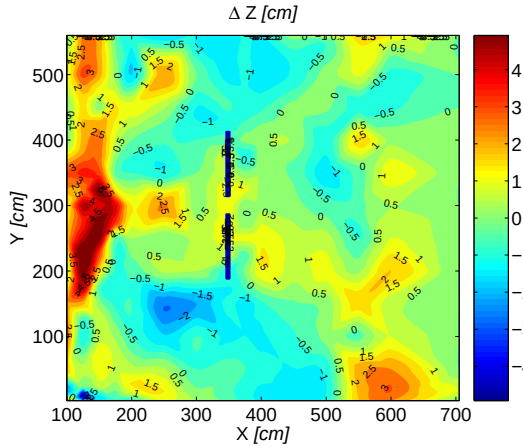

Figure E.33.: Results of the test T6: erosion/deposition values compared to initial bathymetry

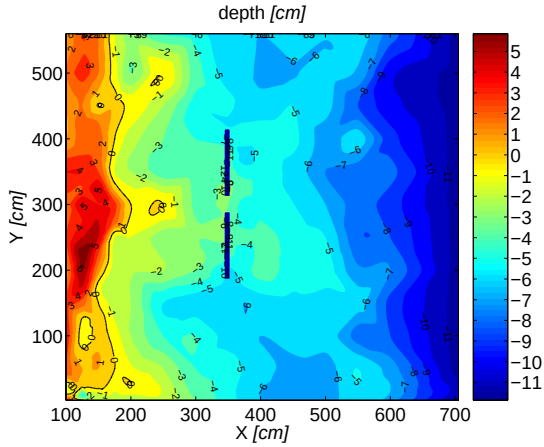

Figure E.34.: Results of the test T6: bathymetry related to initial water depth

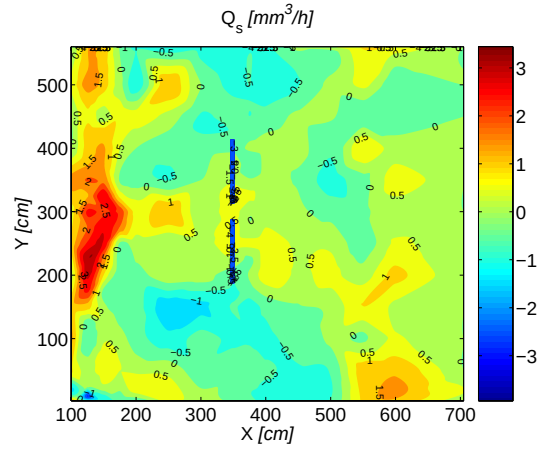

Figure E.35.: Results of the test T6: erosion/deposition rate

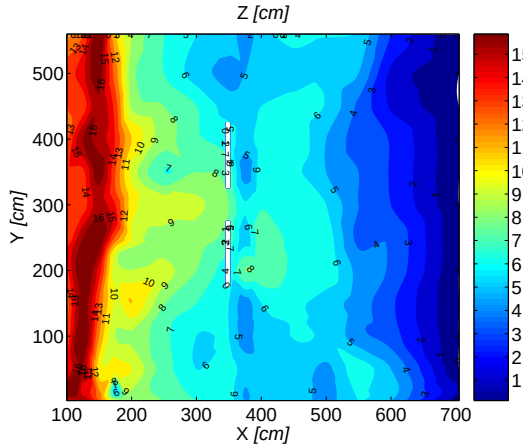

Figure E.36.: Results of the test T7: final bathymetry

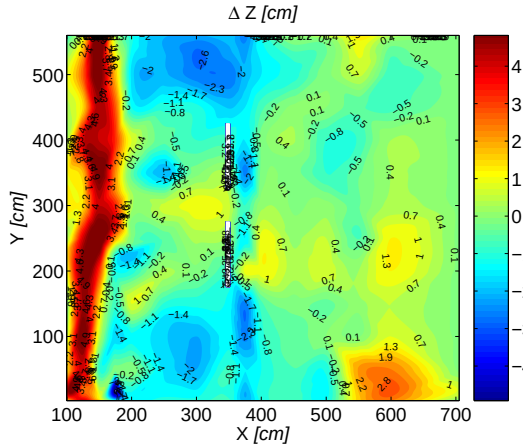

Figure E.37.: Results of the test T7: erosion/deposition values compared to initial bathymetry

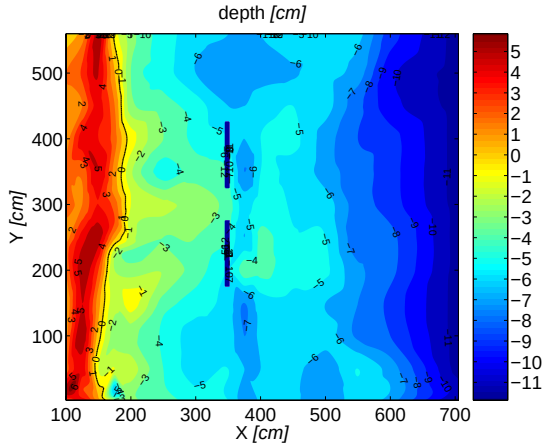

Figure E.38.: Results of the test T7: bathymetry related to initial water depth

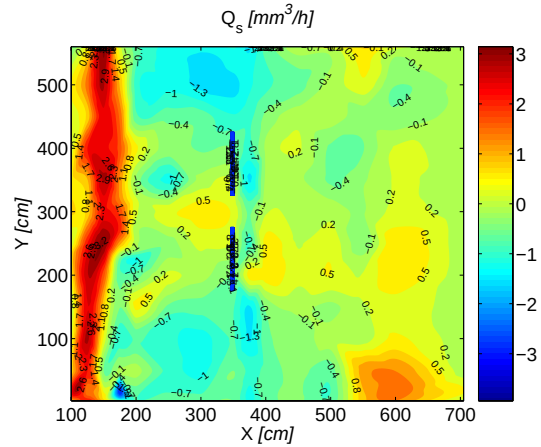

Figure E.39.: Results of the test T7: erosion/deposition rate

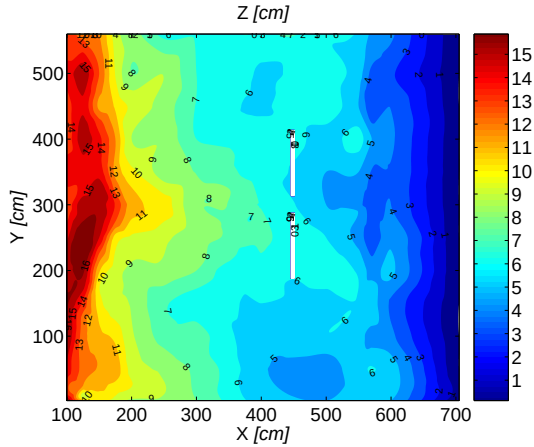

Figure E.40.: Results of the test T8: final bathymetry

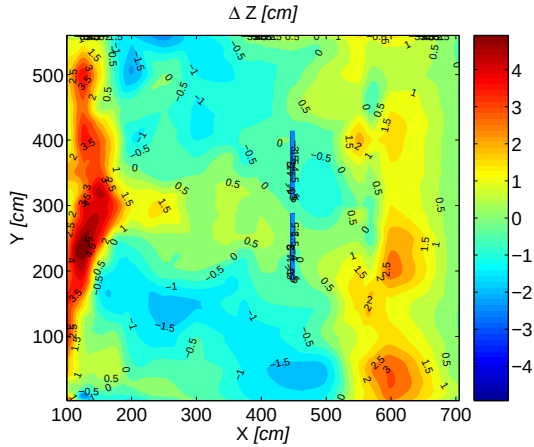

Figure E.41.: Results of the test T8: erosion/deposition values compared to initial bathymetry

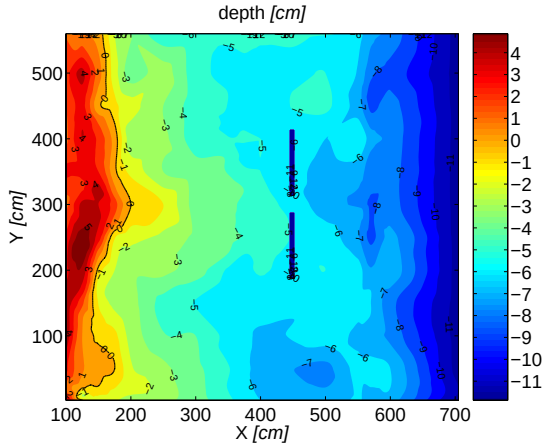

Figure E.42.: Results of the test T8: bathymetry related to initial water depth

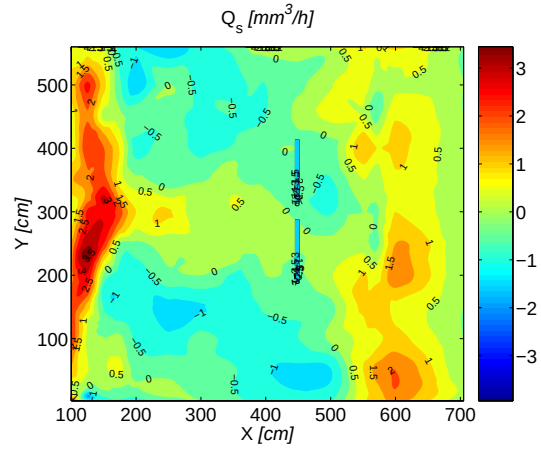

Figure E.43.: Results of the test T8: erosion/deposition rate

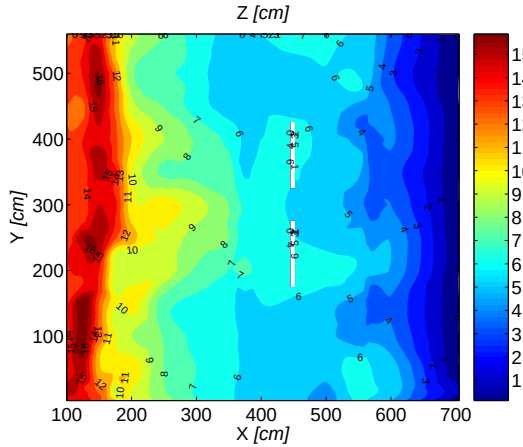

Figure E.44.: Results of the test T9: final bathymetry

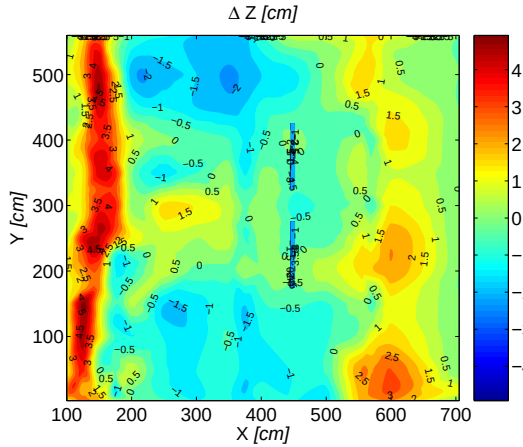

Figure E.45.: Results of the test T9: erosion/deposition values compared to initial bathymetry

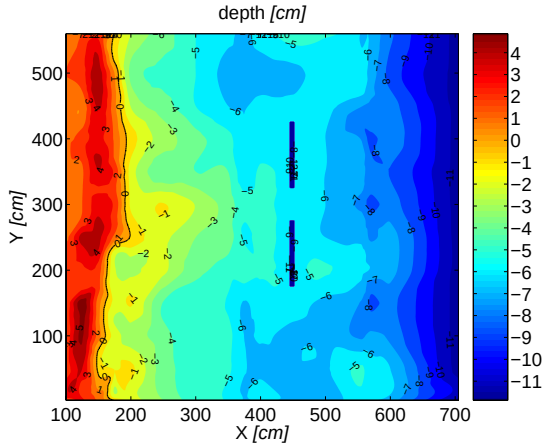

Figure E.46.: Results of the test T9: bathymetry related to initial water depth

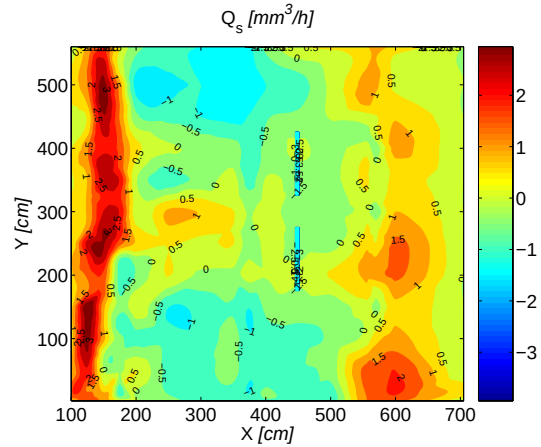

Figure E.47.: Results of the test T9: erosion/deposition rate

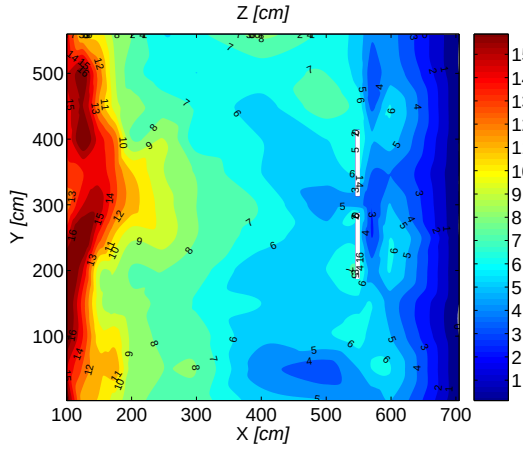

Figure E.48.: Results of the test T10: final bathymetry

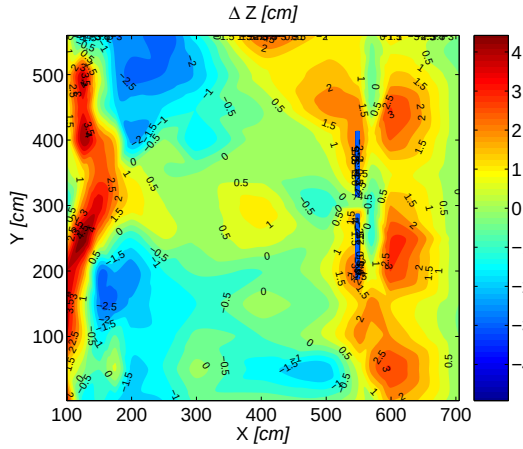

Figure E.49.: Results of the test T10: erosion/deposition values compared to initial bathymetry

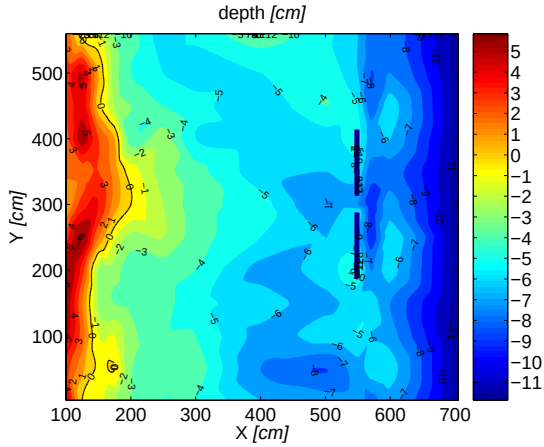

Figure E.50.: Results of the test T10: bathymetry related to initial water depth

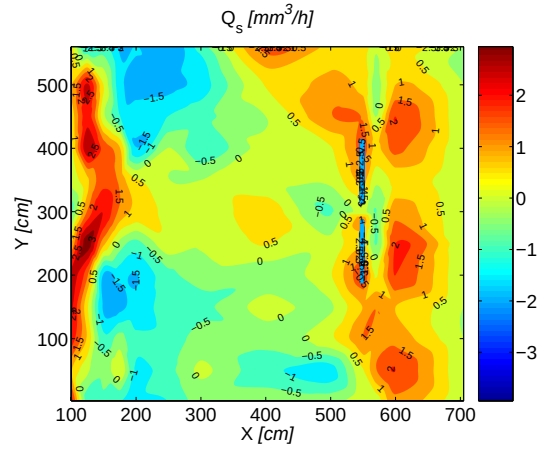

Figure E.51.: Results of the test T10: erosion/deposition rate

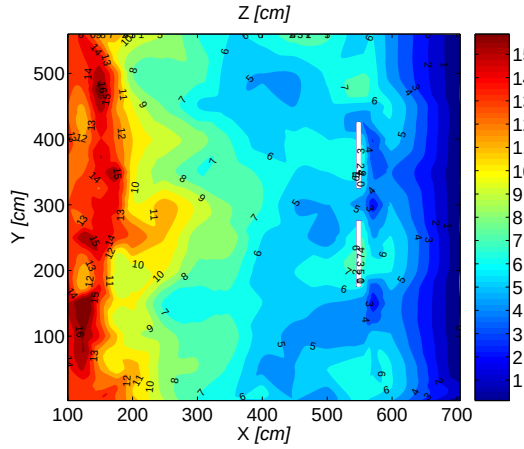

Figure E.52.: Results of the test T11: final bathymetry

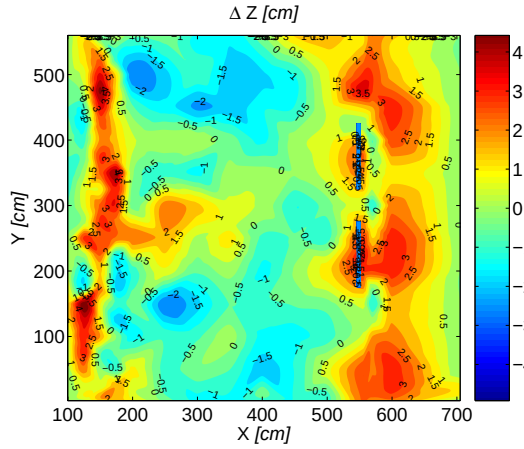

Figure E.53.: Results of the test T11: erosion/deposition values compared to initial bathymetry

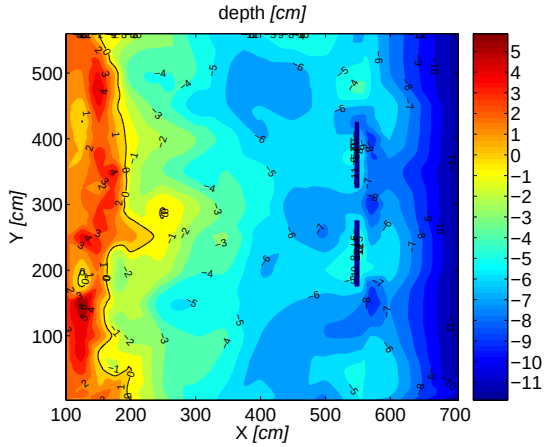

Figure E.54.: Results of the test T11: bathymetry related to initial water depth

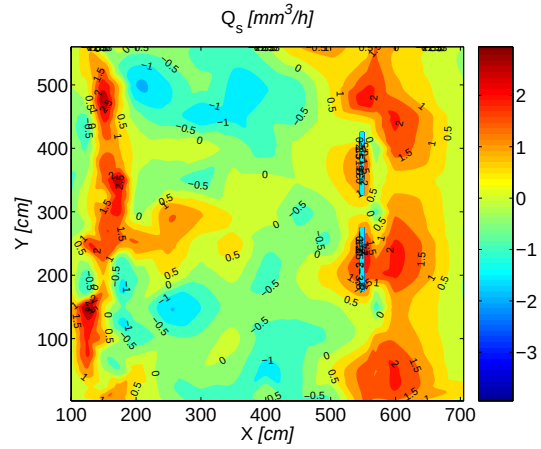

Figure E.55.: Results of the test T11: erosion/deposition rate

F. Results of the adjustment of the numerical model

F.1. Theoretical calculation of the wave breaking parameter γ_2

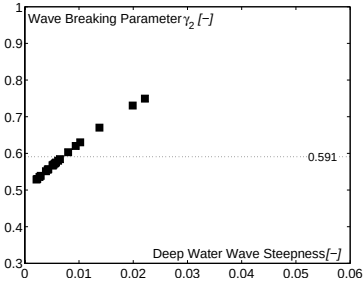

$d = 0.35\ m$ - P1

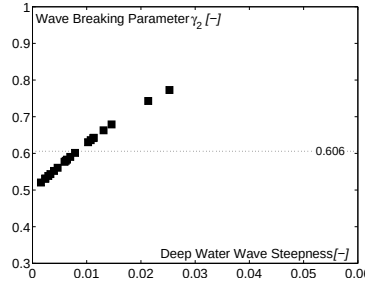

$d = 0.35\ m$ - P2

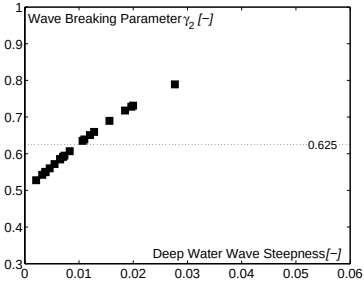

$d = 0.35\ m$ - P3

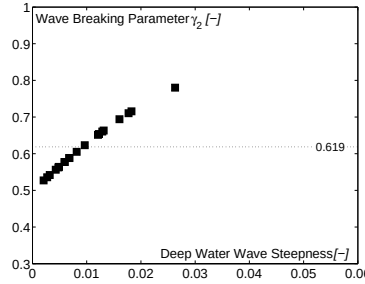

$d = 0.35\ m$ - P4

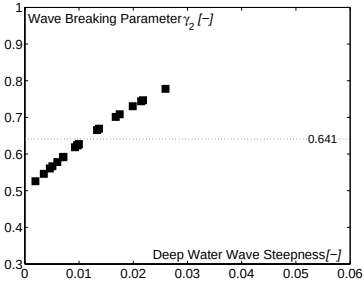

$d = 0.35\ m$ - P5

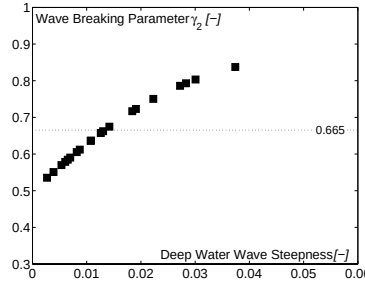

$d = 0.35\ m$ - P6

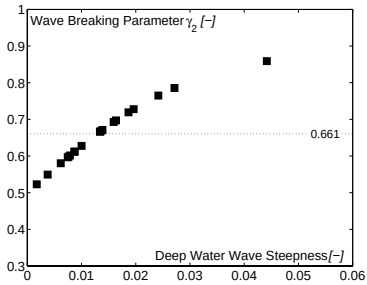

$d = 0.5\ m$ - P1

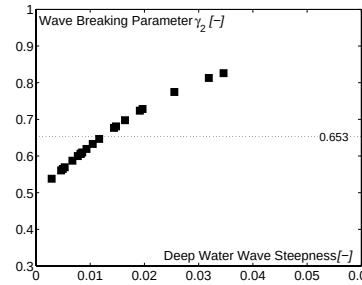

$d = 0.5\ m$ - P2

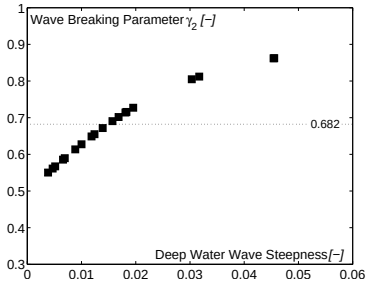

$d = 0.5\ m$ - P3

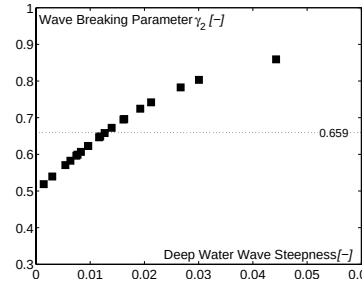

$d = 0.5\ m$ - P4

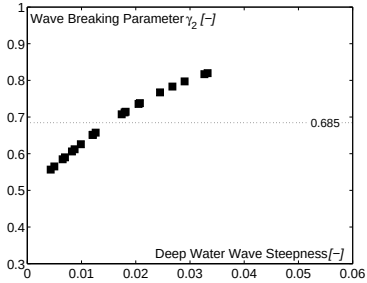

$d = 0.5\ m$ - P5

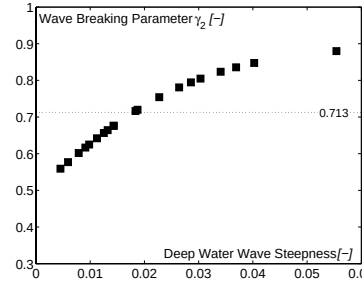

$d = 0.5\ m$ - P6

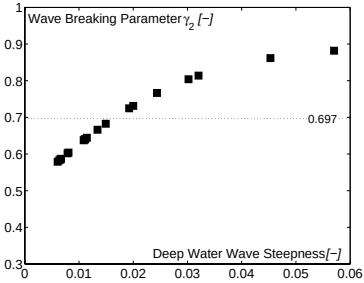

$d = 0.7\ m$ - P1

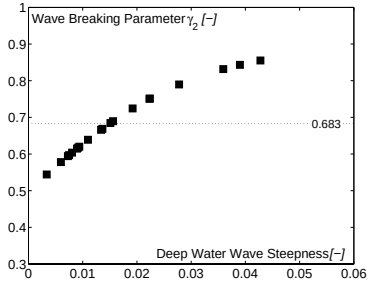

$d = 0.5\ m$ - P2

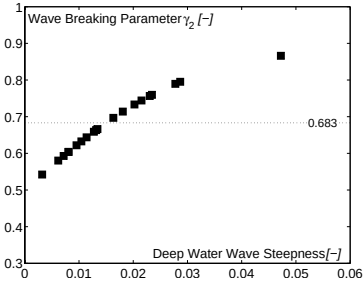

$d = 0.7\ m$ - P3

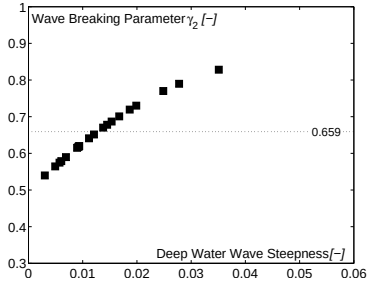

$d = 0.7\ m$ - P4

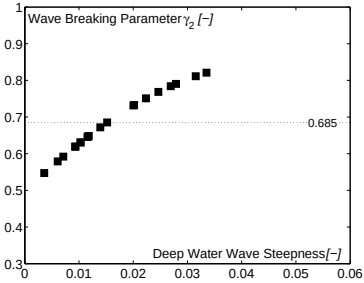

$d = 0.7\ m$ - P5

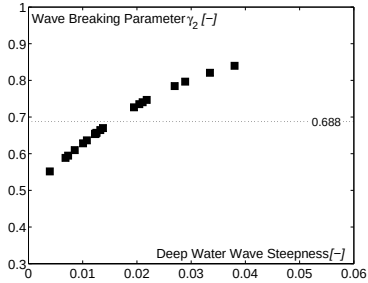

$d = 0.7\ m$ - P6

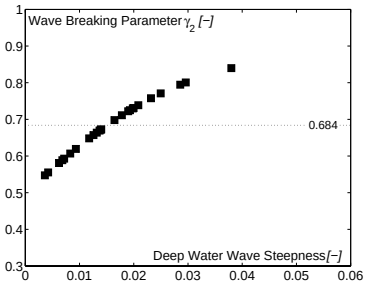

$d = 1.0\ m$ - P1

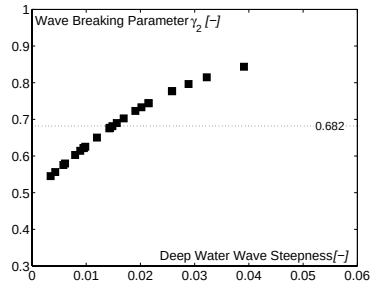

$d = 1.0\ m$ - P2

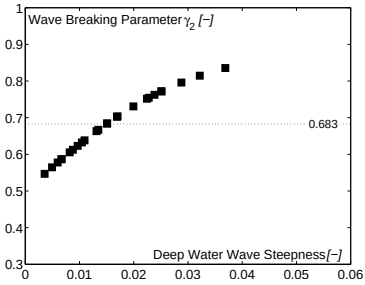

$d = 1.0\ m$ - P3

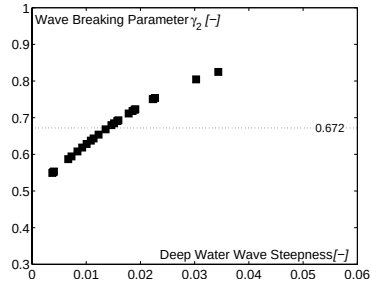

$d = 1.0\ m$ - P4

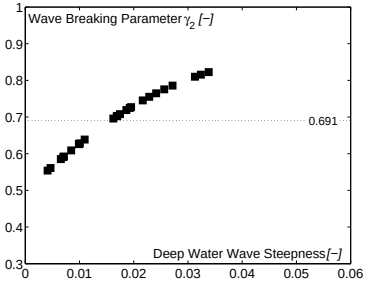

$d = 1.0\ m$ - P5

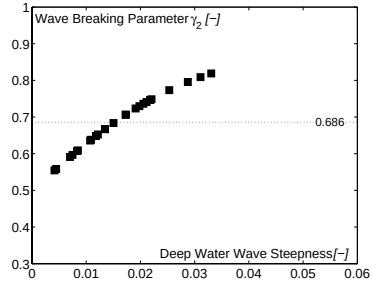

$d = 1.0\ m$ - P6

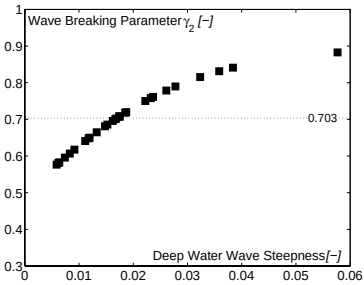

$d = 1.25\ m$ - P1

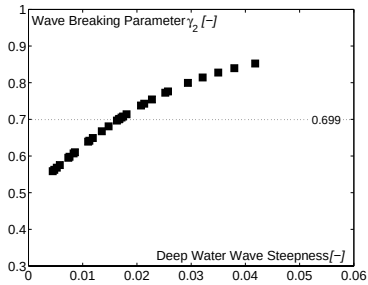

$d = 1.25\ m$ - P2

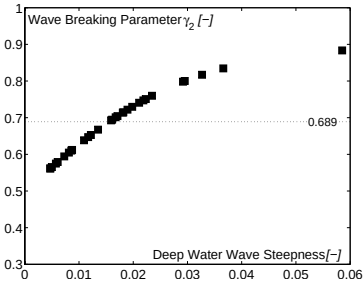

$d = 1.25\ m$ - P3

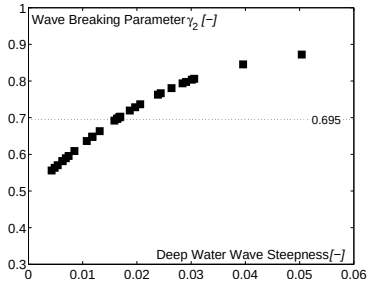

$d = 1.25\ m$ - P4

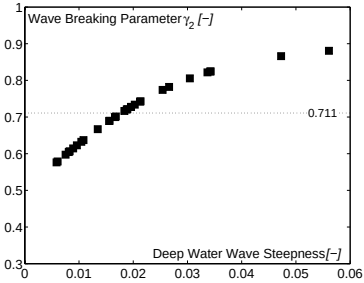

$d = 1.25\ m$ - P5

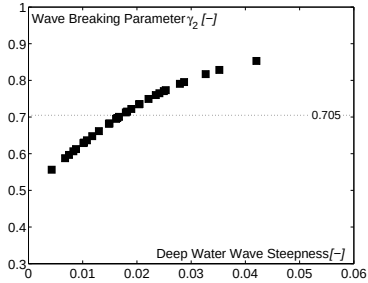

$d = 1.25\ m$ - P6

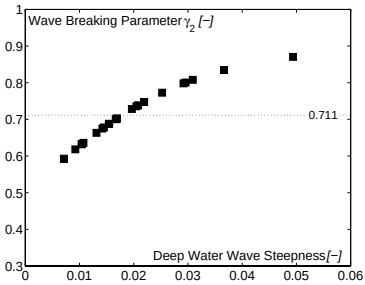

$d = 1.4\ m$ - P1

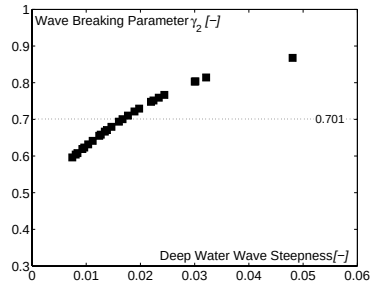

$d = 1.4\ m$ - P2

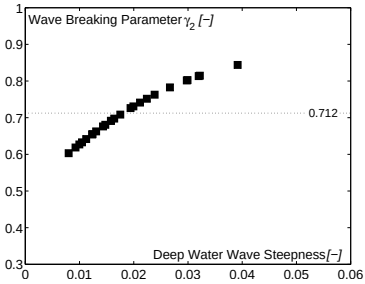

$d = 1.4\ m$ - P3

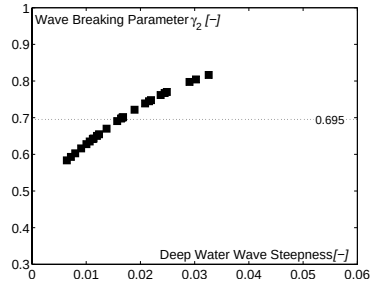

$d = 1.4\ m$ - P4

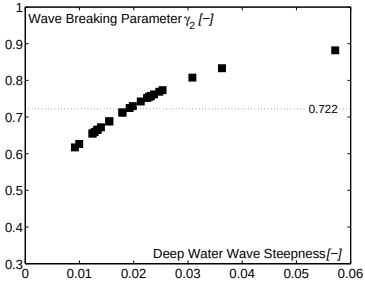

$d = 1.4\ m$ - P5

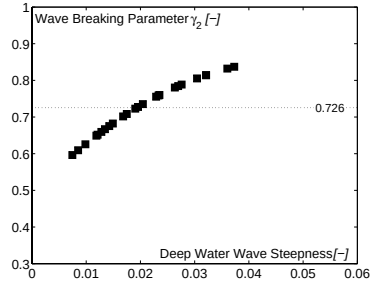

$d = 1.4\ m$ - P6

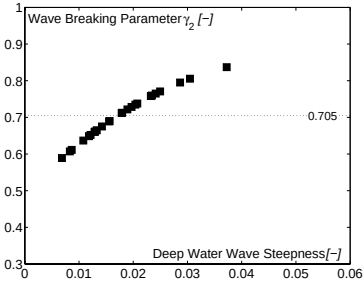

$d = 1.5\ m$ - P1

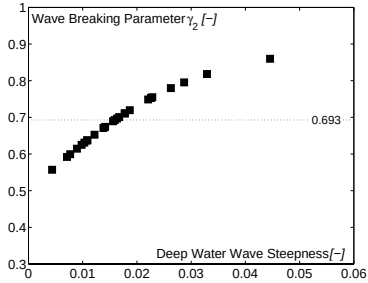

$d = 1.5\ m$ - P2

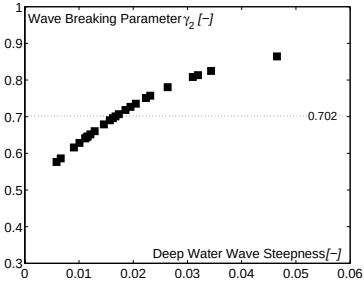

$d = 1.5\ m$ - P3

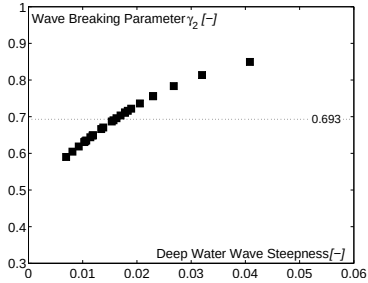

$d = 1.5\ m$ - P4

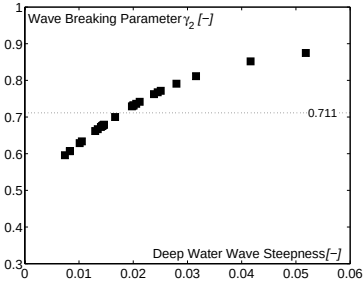

$d = 1.5\ m$ - P5

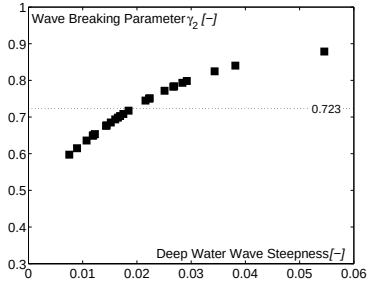

$d = 1.5\ m$ - P6

F.2. Theoretical calculation of the wave related Reynolds number and the wave mobility number

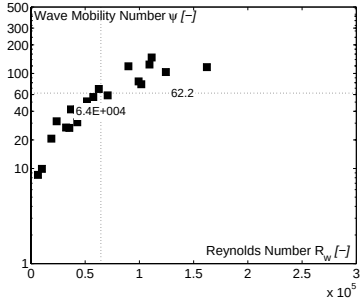

$d = 0.35\ m$ - P1

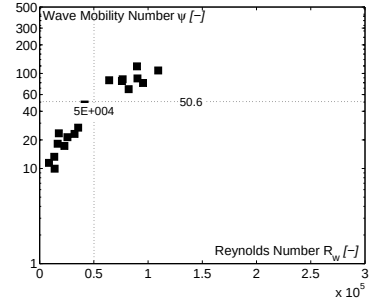

$d = 0.35\ m$ - P2

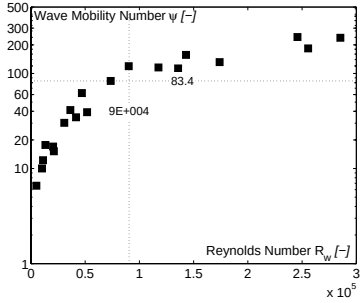

$d = 0.35\ m$ - P3

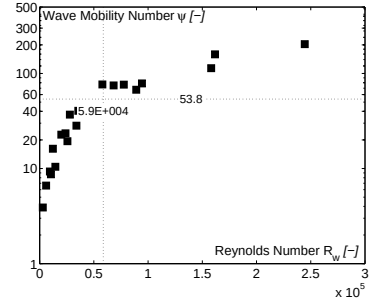

$d = 0.35\ m$ - P4

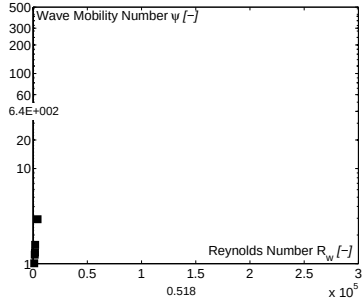

$d = 0.35\ m$ - P5

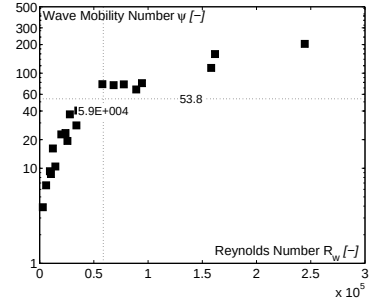

$d = 0.35\ m$ - P6

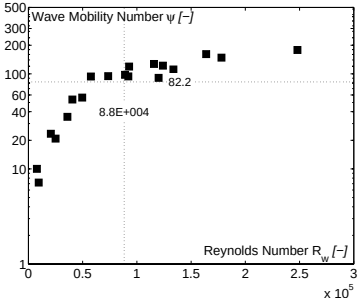

$d = 0.5\ m$ - P1

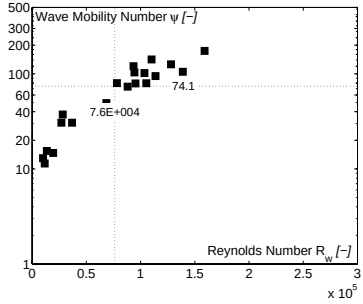

$d = 0.5\ m$ - P2

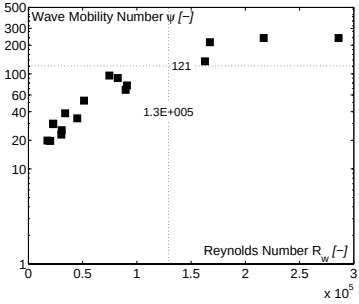

$d = 0.5\ m$ - P3

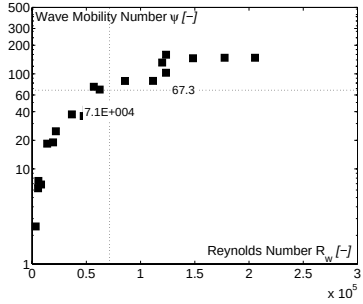

$d = 0.5\ m$ - P4

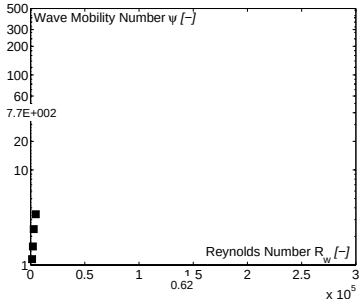

$d = 0.5\ m$ - P5

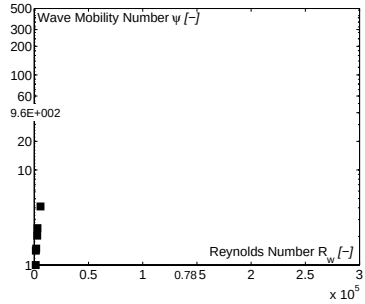

$d = 0.5\ m$ - P6

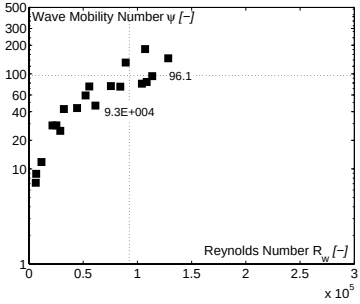

$d = 0.7\ m$ - P1

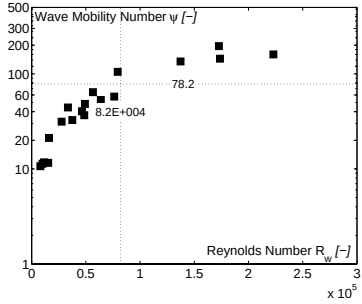

$d = 0.7\ m$ - P2

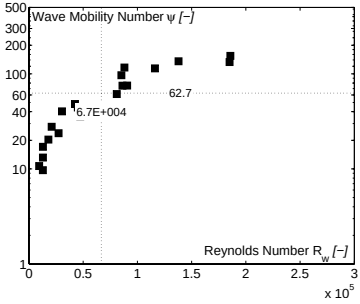

$d = 0.7\ m$ - P3

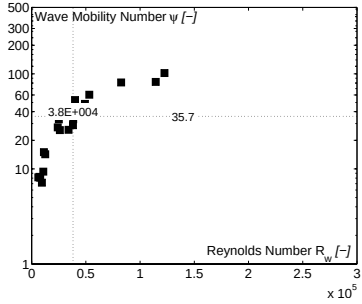

$d = 0.7\ m$ - P4

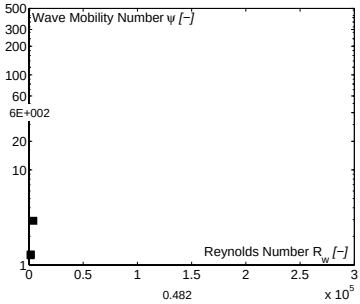

$d = 0.7\ m$ - P5

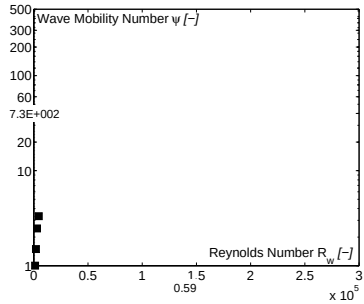

$d = 0.7\ m$ - P6

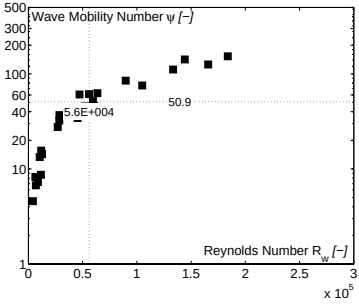

$d = 1.0\ m$ - P1

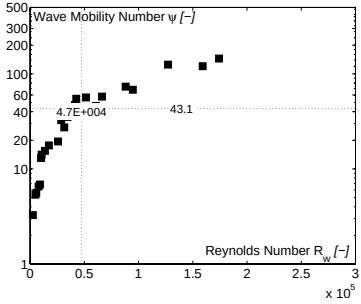

$d = 1.0\ m$ - P2

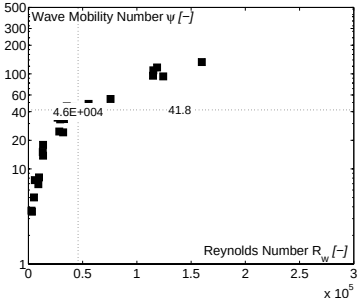

$d = 1.0\ m$ - P3

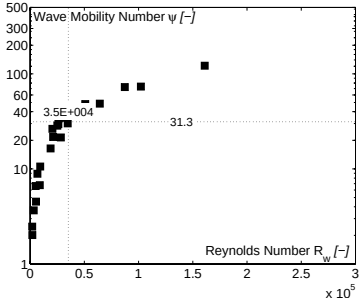

$d = 1.0\ m$ - P4

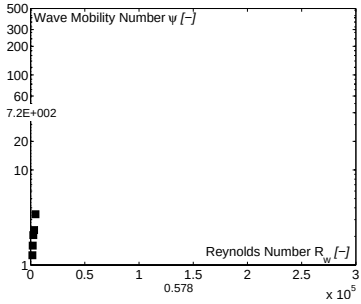

$d = 1.0\ m$ - P5

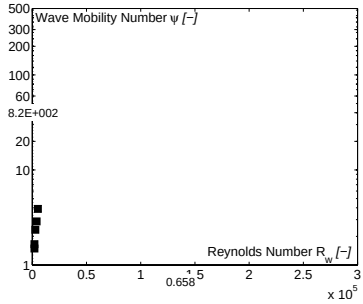

$d = 1.0\ m$ - P6

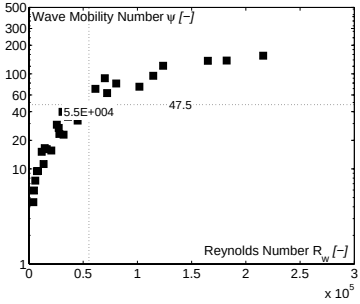

$d = 1.25\ m$ - P1

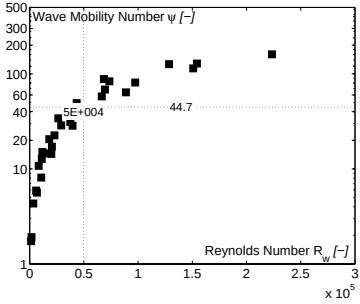

$d = 1.25\ m$ - P2

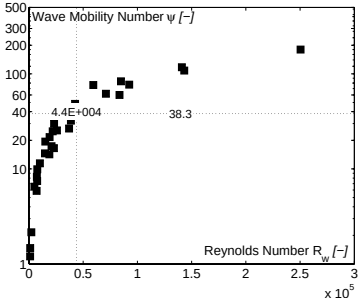

$d = 1.25\ m$ - P3

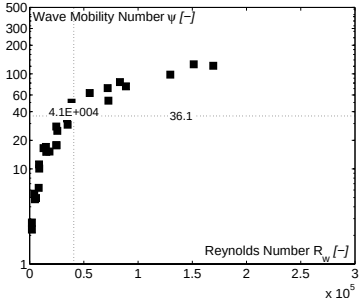

$d = 1.25\ m$ - P4

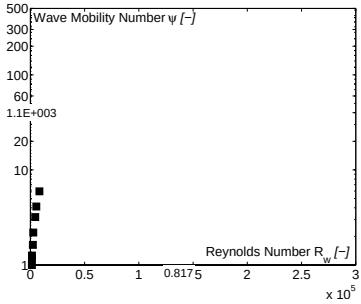

$d = 1.25\ m$ - P5

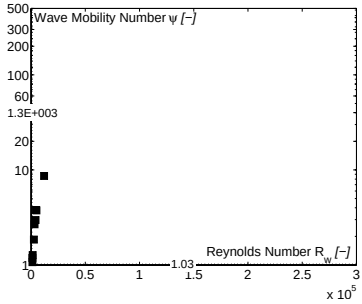

$d = 1.25\ m$ - P6

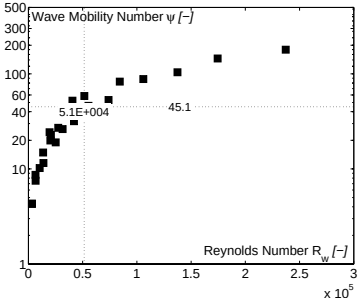

$d = 1.4\ m$ - P1

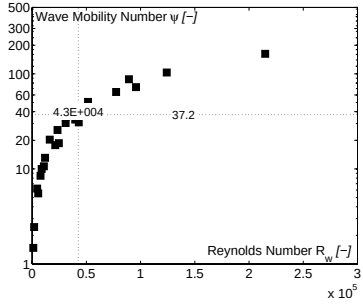

$d = 1.4\ m$ - P2

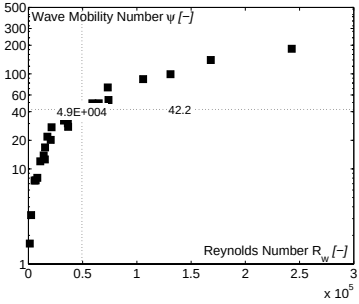

$d = 1.4\ m$ - P3

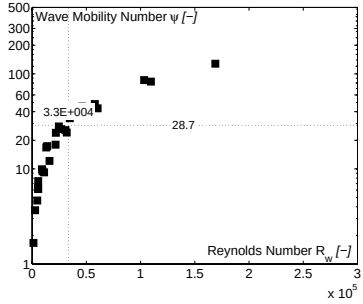

$d = 1.4\ m$ - P4

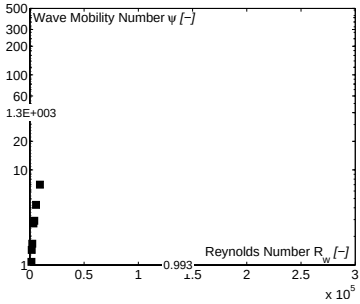

$d = 1.4\ m$ - P5

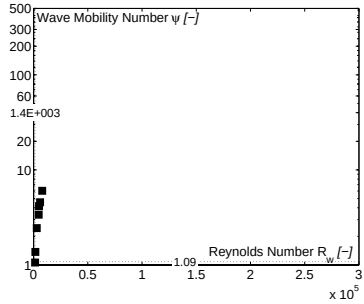

$d = 1.4\ m$ - P6

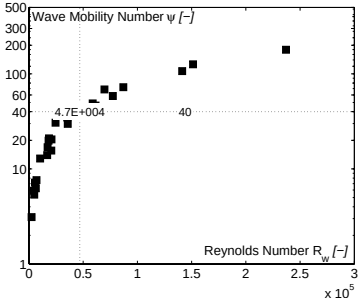

$d = 1.5\ m$ - P1

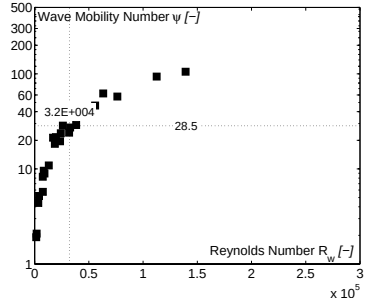

$d = 1.5\ m$ - P2

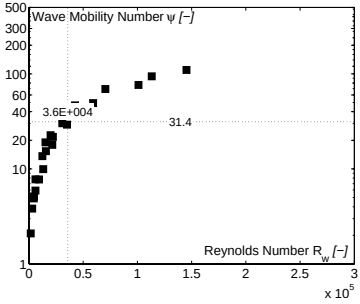

$d = 1.5\ m$ - P3

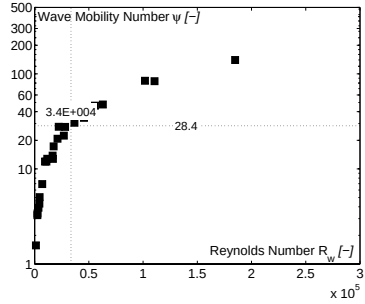

$d = 1.5\ m$ - P4

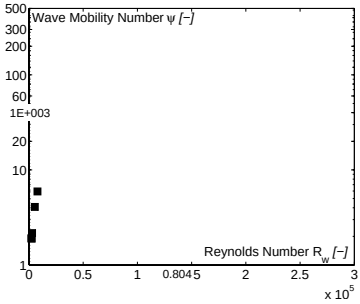

$d = 1.5\ m$ - P5

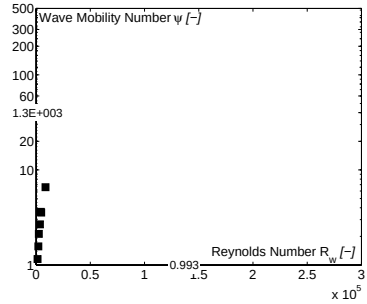

$d = 1.5\ m$ - P6

F.3. Correlation factors of the calibrated variables

The following correlation factors corresponds to the adjustment N ° 6 in Table 6.2.
H1 = wave height measured during the experimental tests
H2 = wave height of the numerical modelling

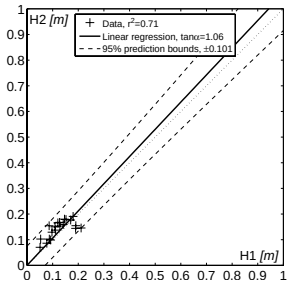

$d = 0.35\ m$ - P1

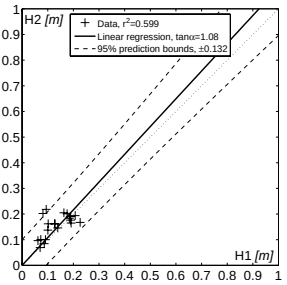

$d = 0.35\ m$ - P2

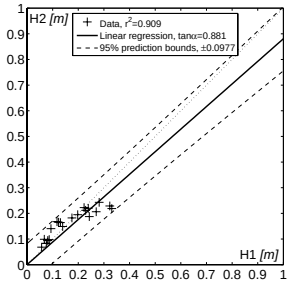

$d = 0.35\ m$ - P3

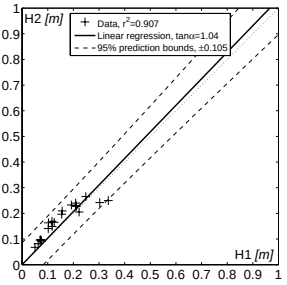

$d = 0.35\ m$ - P4

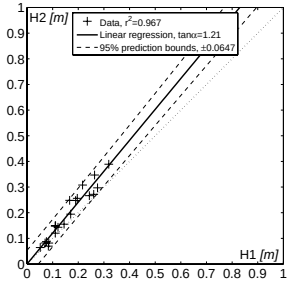

$d = 0.35\ m$ - P5

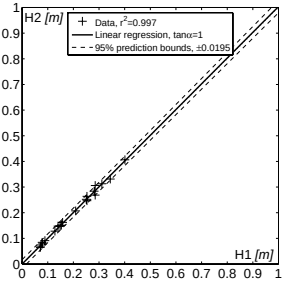

$d = 0.35\ m$ - P6

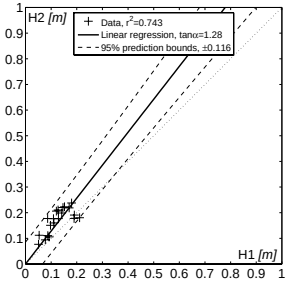

$d = 0.7\ m$ - P1

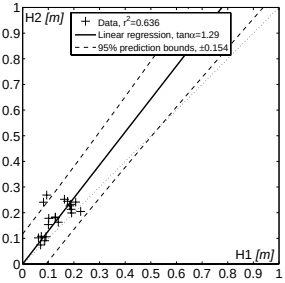

$d = 0.7\ m$ - P2

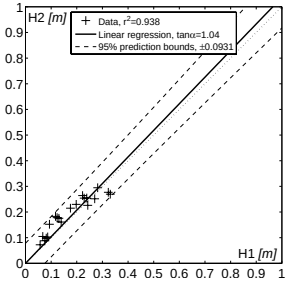

$d = 0.7\ m$ - P3

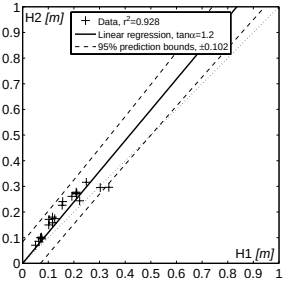

$d = 0.7\ m$ - P4

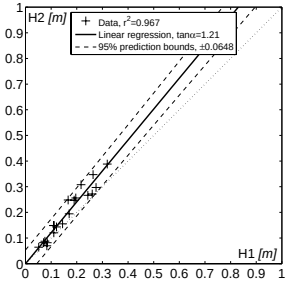

$d = 0.7\ m$ - P5

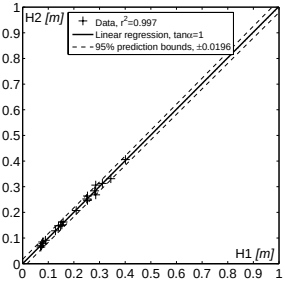

$d = 0.7\ m$ - P6

F.4. Friction factor as a function of K_T and K_R for variable wave period

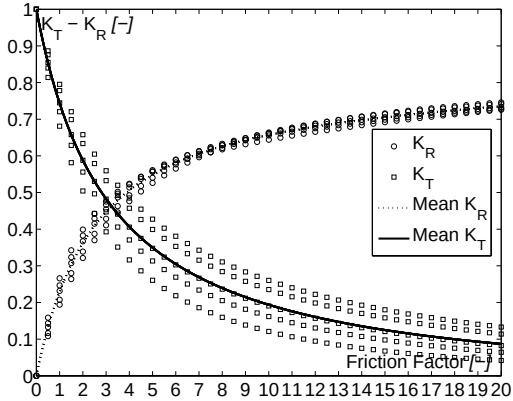

$d = 0.35\ m$

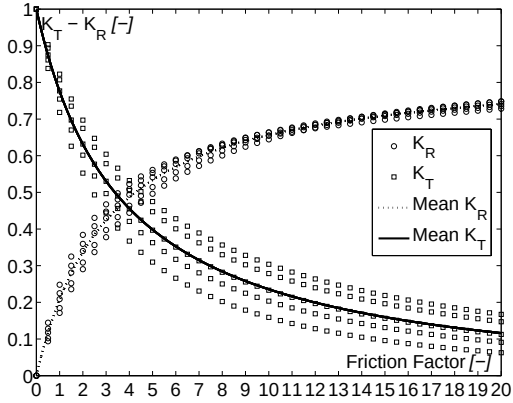

$d = 0.5\ m$

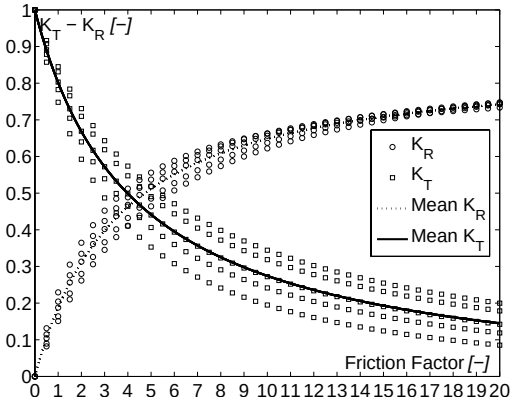

$d = 0.7\ m$

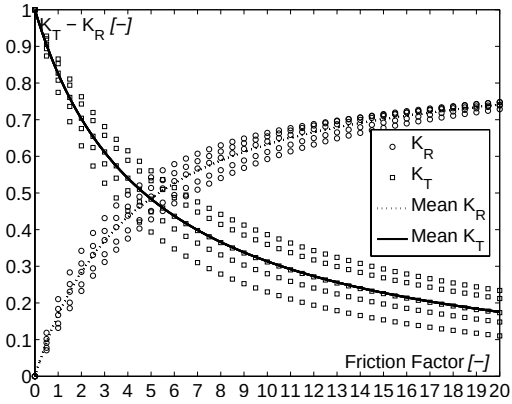

$d = 1\ m$

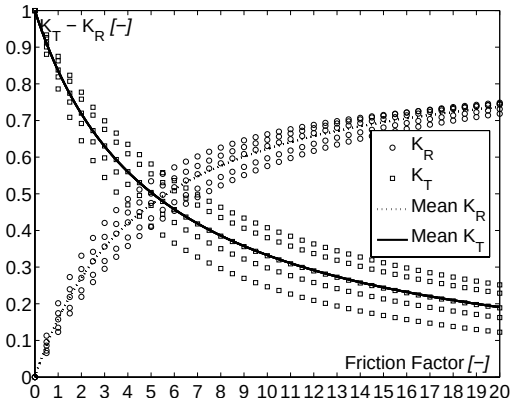

$d = 1.25\ m$

G. Results of the numerical modelling

G.1. Wave field in the vicinity of a single gap configuration

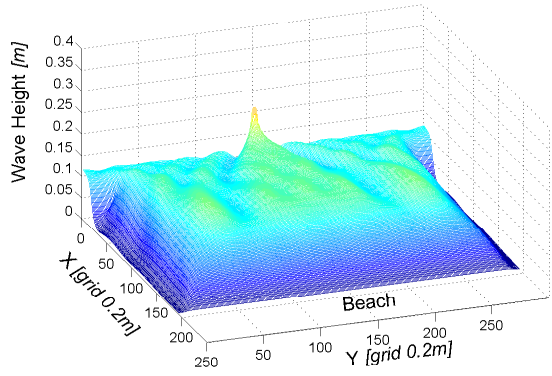

$G = 1\ m$

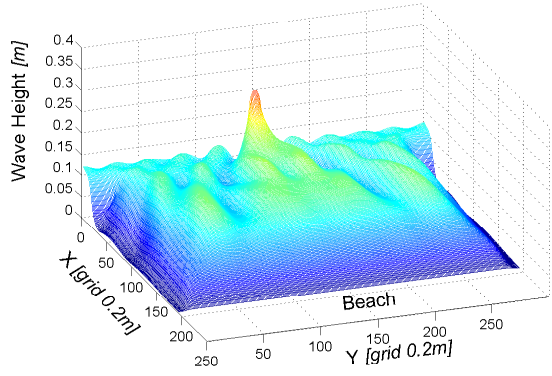

$G = 2\ m$

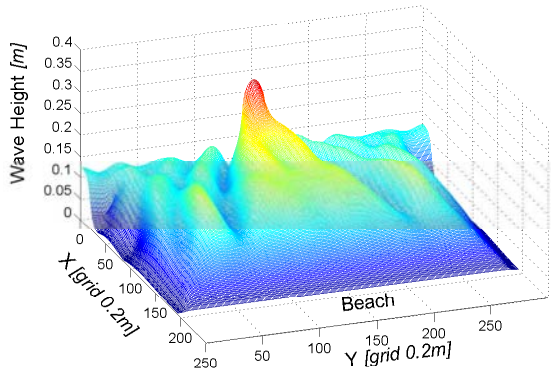
Wave Height [m]
0.4
0.35
0.3
0.25
0.2
0.15
0.1
0.05
0
X [grid 0.2m]
0
50
100
150
200
250
Beach
Y [grid 0.2m]
50
100
150
200
250

$G = 4\ m$

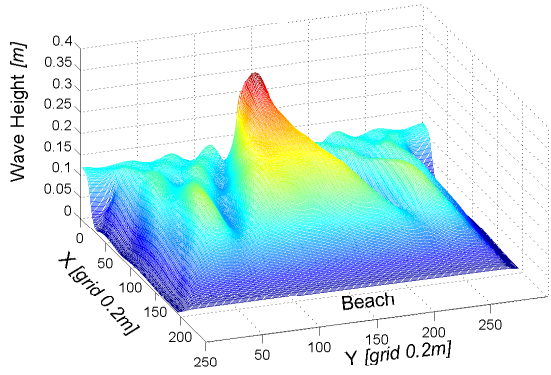
Wave Height [m]
0.4
0.35
0.3
0.25
0.2
0.15
0.1
0.05
0
X [grid 0.2m]
0
50
100
150
200
250
Beach
Y [grid 0.2m]
50
100
150
200
250

$G = 6\ m$

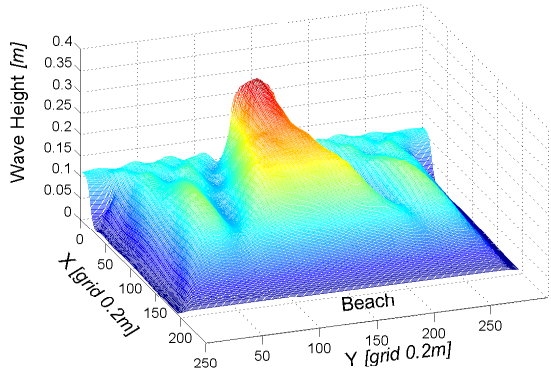
Wave Height [m]
0.4
0.35
0.3
0.25
0.2
0.15
0.1
0.05
0
X [grid 0.2m]
0
50
100
150
200
250
Beach
Y [grid 0.2m]
50
100
150
200
250

$G = 8\ m$

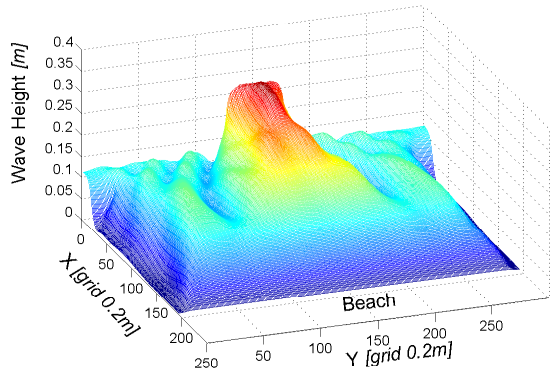

$G = 10\ m$

G.2. Combined diffraction and refraction coefficients in the vicinity of a single gap configuration

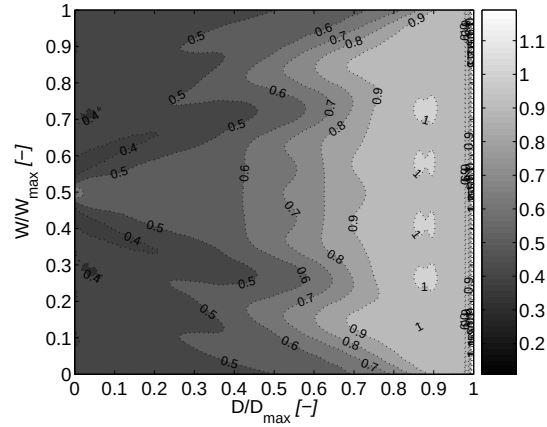

$G = 1\ m$

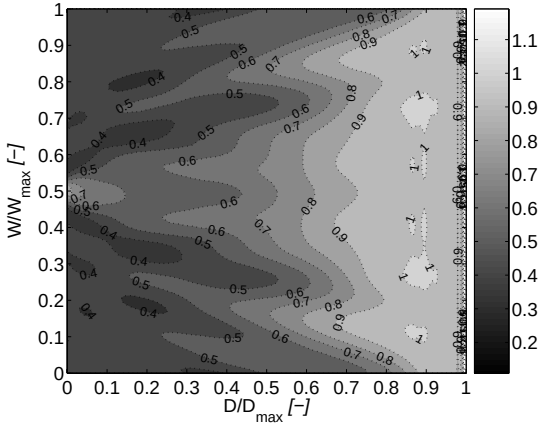

$G = 2\ m$

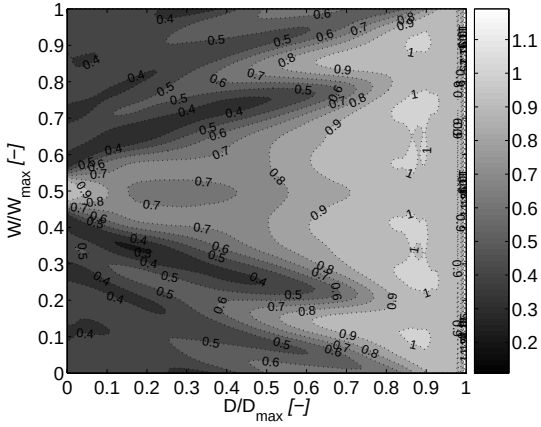

$G = 4\ m$

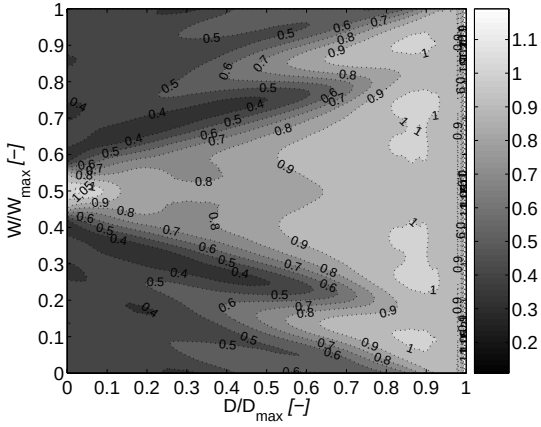

$G = 6\ m$

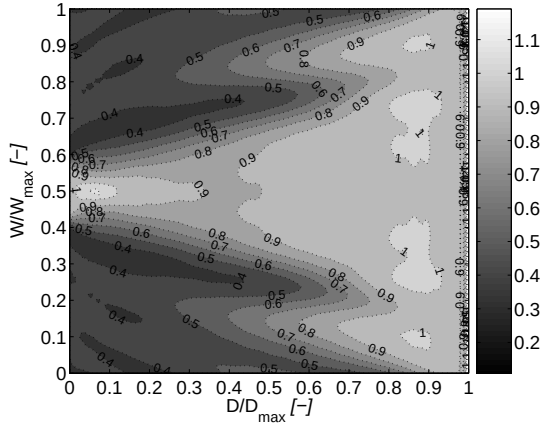

$G = 8\ m$

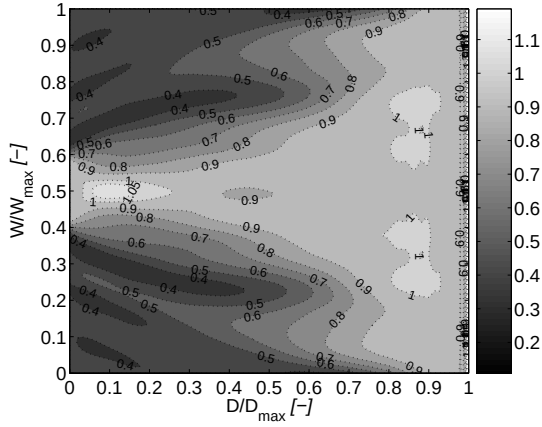

$G = 10\ m$

G.3. Wave field in the vicinity of two gaps configuration

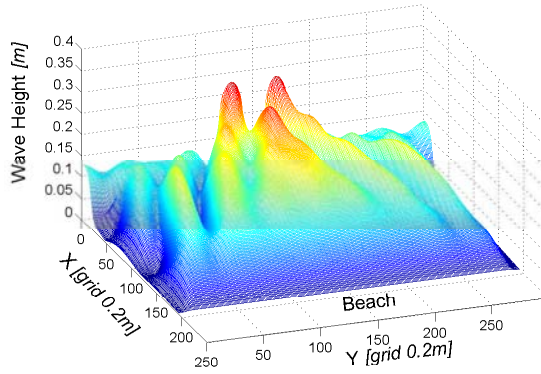

$Es = 4\ m$

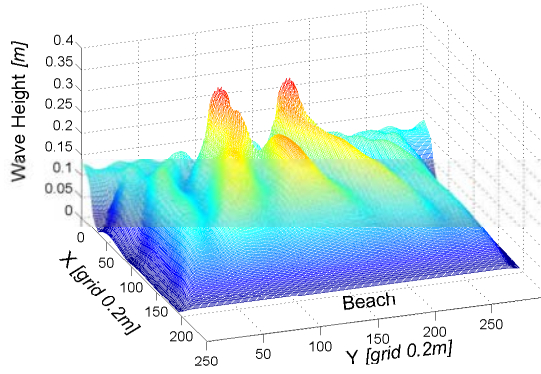

$Es = 8\ m$

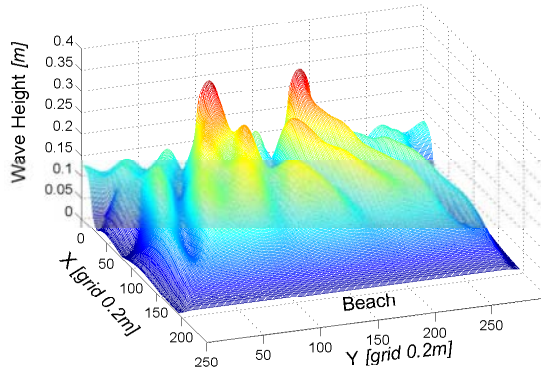

$Es = 12\ m$

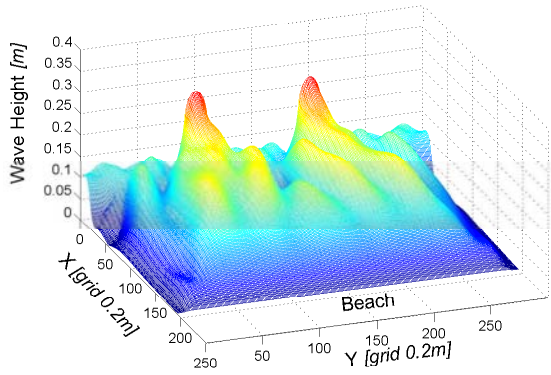

$Es = 16\ m$

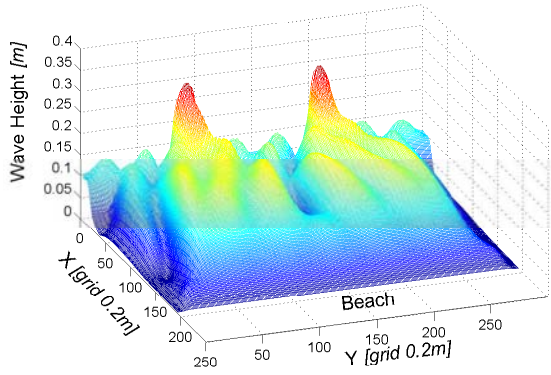

$Es = 20\ m$

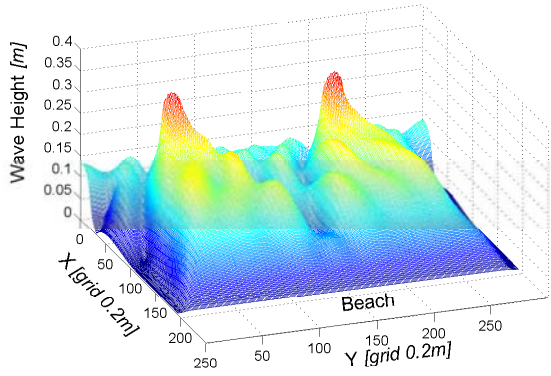

$Es = 24\ m$

G.4. Combined diffraction and refraction coefficients in the vicinity of two gaps configuration

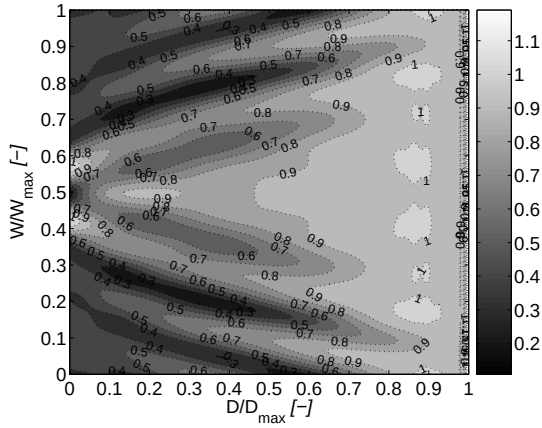

$Es = 4\ m$

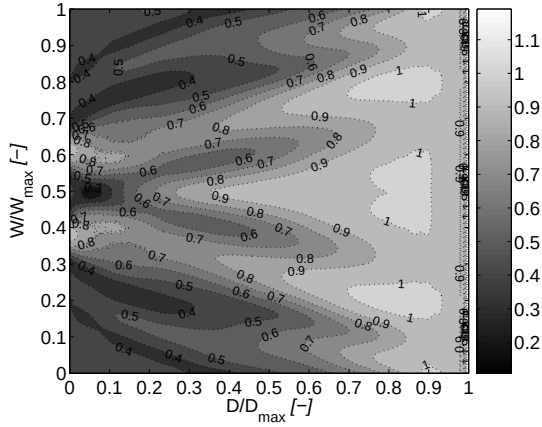

$Es = 8\ m$

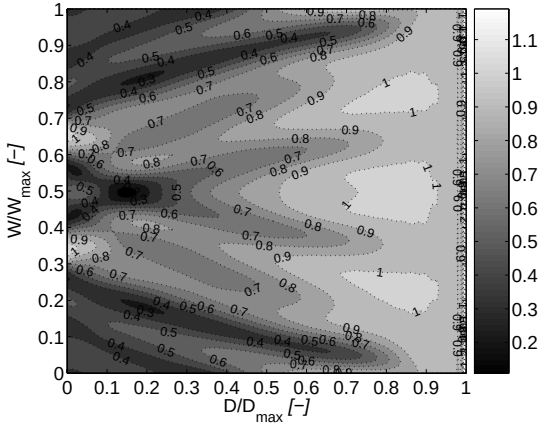

$Es = 12\ m$

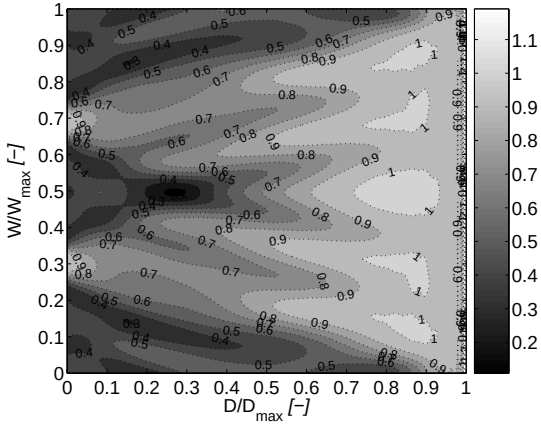

$Es = 16\ m$

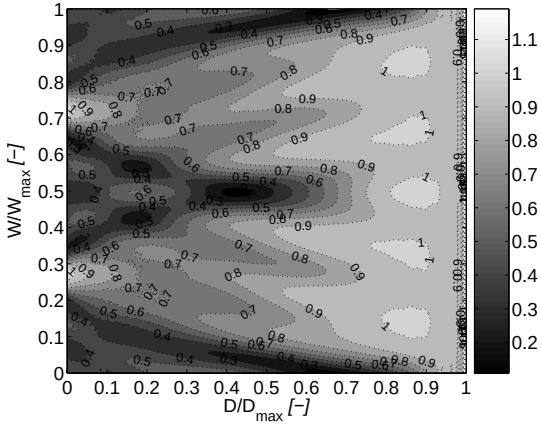

$Es = 20\ m$

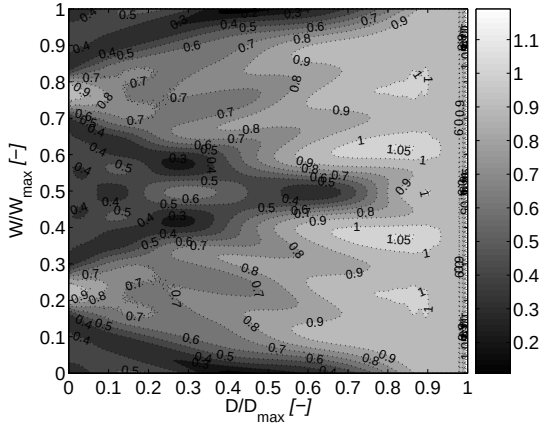

$Es = 24\ m$

H. Results related to the case study

Water level [m]	Return period [$year$]	Duration for F.L. [min]	Wind speed [m/s]	H_s [m]	T_m [s]	Direction [$^\circ$]	Directional spreading [$^\circ$]
429.80	1	120	8.77	0.26	1.86	233.95	18.68
	2	120	9.44	0.29	1.94	233.92	18.56
	5	90	10.87	0.34	2.06	234.98	18.76
	10	90	11.59	0.36	2.10	235.89	19.01
	20	90	12.30	0.38	2.16	236.41	19.17
	50	90	13.25	0.42	2.27	236.40	19.21
429.60	1	120	8.77	0.26	1.85	233.99	18.66
	2	120	9.44	0.29	1.93	234.07	18.58
	5	90	10.87	0.33	2.05	235.21	18.79
	10	90	11.59	0.35	2.10	236.10	19.02
	20	90	12.30	0.37	2.16	236.68	19.15
	50	90	13.25	0.41	2.27	236.91	19.16
429.40	1	120	8.77	0.26	1.85	234.13	18.67
	2	120	9.44	0.29	1.93	234.30	18.62
	5	90	10.87	0.33	2.05	235.45	18.84
	10	90	11.59	0.35	2.09	236.28	19.06
	20	90	12.30	0.37	2.16	236.93	19.17
	50	90	13.25	0.41	2.26	237.47	19.10
429.20	1	120	8.77	0.26	1.84	234.40	18.68
	2	120	9.44	0.28	1.92	234.69	18.64
	5	90	10.87	0.33	2.04	235.79	18.89
	10	90	11.59	0.35	2.09	236.49	19.12
	20	90	12.30	0.37	2.15	237.17	19.21
	50	90	13.25	0.41	2.26	238.00	19.07
429.00	1	120	8.77	0.26	1.84	234.78	18.72
	2	120	9.44	0.28	1.92	235.20	18.67
	5	90	10.87	0.33	2.04	236.20	18.94
	10	90	11.59	0.35	2.09	236.74	19.19
	20	90	12.30	0.37	2.15	237.40	19.28
	50	90	13.25	0.40	2.26	238.50	19.08
428.80	1	120	8.77	0.26	1.84	235.24	18.68
	2	120	9.44	0.28	1.91	235.76	18.65
	5	90	10.87	0.33	2.04	236.68	18.94
	10	90	11.59	0.35	2.09	237.09	19.20
	20	90	12.30	0.37	2.15	237.73	19.28
	50	90	13.25	0.40	2.26	238.99	19.08

Table H.1.: Wind waves calculation at Mörigen during the "Le Vent" wind regime for the sector [210 $^\circ$-240 $^\circ$] based on long term analysis of wind data at Neuchatel station

Water level [m]	Return period [$year$]	Duration for F.L. [min]	Wind speed [m/s]	H_s [m]	T_m [s]	Direction [$^\circ$]	Directional spreading [$^\circ$]
429.80	1	90	8.35	0.24	1.81	233.96	18.76
	2	90	9.09	0.27	1.90	233.93	18.62
	5	90	10.07	0.31	2.00	233.97	18.47
	10	90	10.80	0.33	2.05	234.90	18.74
	20	90	11.54	0.36	2.10	235.83	19.00
	50	90	12.51	0.39	2.19	236.41	19.18
429.60	1	90	8.35	0.24	1.80	233.95	18.72
	2	90	9.09	0.27	1.89	234.03	18.62
	5	90	10.07	0.31	1.99	234.21	18.53
	10	90	10.80	0.33	2.05	235.13	18.77
	20	90	11.54	0.35	2.10	236.04	19.00
	50	90	12.51	0.38	2.19	236.73	19.15
429.40	1	90	8.35	0.24	1.80	234.03	18.70
	2	90	9.09	0.27	1.89	234.21	18.65
	5	90	10.07	0.31	1.99	234.52	18.60
	10	90	10.80	0.33	2.04	235.37	18.83
	20	90	11.54	0.35	2.09	236.23	19.05
	50	90	12.51	0.38	2.18	237.05	19.15
429.20	1	90	8.35	0.24	1.80	234.21	18.71
	2	90	9.09	0.27	1.88	234.54	18.66
	5	90	10.07	0.30	1.98	235.01	18.63
	10	90	10.80	0.32	2.04	235.73	18.87
	20	90	11.54	0.35	2.09	236.45	19.10
	50	90	12.51	0.38	2.18	237.35	19.18
429.00	1	90	8.35	0.24	1.80	234.52	18.75
	2	90	9.09	0.27	1.88	234.98	18.70
	5	90	10.07	0.30	1.98	235.60	18.65
	10	90	10.80	0.32	2.04	236.15	18.92
	20	90	11.54	0.35	2.09	236.71	19.18
	50	90	12.51	0.38	2.18	237.65	19.23
428.80	1	90	8.35	0.24	1.80	234.92	18.70
	2	90	9.09	0.27	1.87	235.49	18.67
	5	90	10.07	0.30	1.98	236.23	18.64
	10	90	10.80	0.32	2.03	236.64	18.91
	20	90	11.54	0.35	2.09	237.06	19.18
	50	90	12.51	0.38	2.18	238.00	19.24

Table H.2.: Wind waves calculation at Mörigen during the "La Bise" wind regime for the sector [30°-60°] based on long term analysis of wind data at Neuchatel station

Water level [m]	Return period [$year$]	Duration for F.L. [min]	Wind speed [m/s]	H_s [m]	T_m [s]	Direction [$^\circ$]	Directional spreading [$^\circ$]
429.80	1	60	9.64	0.30	1.96	233.91	18.52
	2	60	10.39	0.32	2.03	234.38	18.59
	5	60	11.37	0.35	2.09	235.62	18.94
	10	60	12.11	0.37	2.14	236.41	19.16
	20	60	12.84	0.40	2.22	236.41	19.19
	50	60	13.82	0.44	2.33	236.40	19.23
429.60	1	60	9.64	0.30	1.95	234.09	18.56
	2	60	10.39	0.32	2.02	234.61	18.63
	5	60	11.37	0.34	2.09	235.83	18.95
	10	60	12.11	0.36	2.14	236.64	19.15
	20	60	12.84	0.39	2.22	236.81	19.15
	50	60	13.82	0.43	2.33	237.05	19.16
429.40	1	60	9.64	0.30	1.95	234.35	18.61
	2	60	10.39	0.32	2.02	234.89	18.70
	5	60	11.37	0.34	2.08	236.03	19.00
	10	60	12.11	0.36	2.13	236.82	19.18
	20	60	12.84	0.39	2.22	237.24	19.13
	50	60	13.82	0.43	2.33	237.79	19.06
429.20	1	60	9.64	0.29	1.94	234.78	18.63
	2	60	10.39	0.31	2.01	235.32	18.73
	5	60	11.37	0.34	2.08	236.28	19.05
	10	60	12.11	0.36	2.13	236.99	19.23
	20	60	12.84	0.39	2.21	237.64	19.13
	50	60	13.82	0.43	2.32	238.49	19.00
429.00	1	60	9.64	0.29	1.94	235.32	18.66
	2	60	10.39	0.31	2.01	235.84	18.77
	5	60	11.37	0.34	2.08	236.58	19.12
	10	60	12.11	0.36	2.13	237.18	19.32
	20	60	12.84	0.39	2.21	238.03	19.16
	50	60	13.82	0.42	2.32	239.16	18.96
428.80	1	60	9.64	0.29	1.93	235.91	18.64
	2	60	10.39	0.31	2.00	236.41	18.76
	5	60	11.37	0.34	2.07	236.96	19.12
	10	60	12.11	0.36	2.13	237.46	19.33
	20	60	12.84	0.39	2.21	238.44	19.17
	50	60	13.82	0.42	2.32	239.73	18.96

Table H.3.: Wind waves calculation at Mörigen during the "Le Joran" wind regime for the sector [300 $^\circ$-330 $^\circ$] based on long term analysis of wind data at Neuchatel station

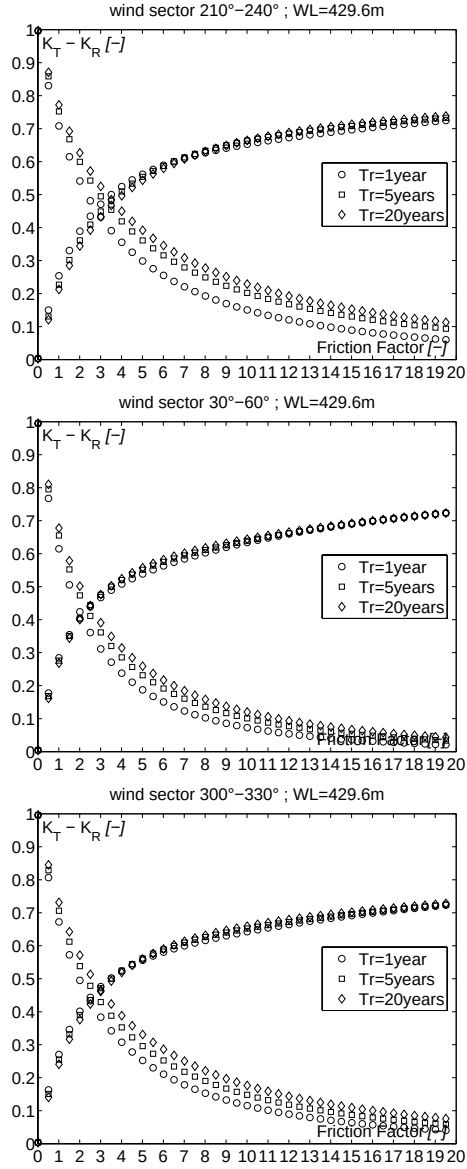

Figure H.1.: Friction factors for $MHWL = 429.60\ m$ of the brushwood fences based in the local hydrodynamic conditions

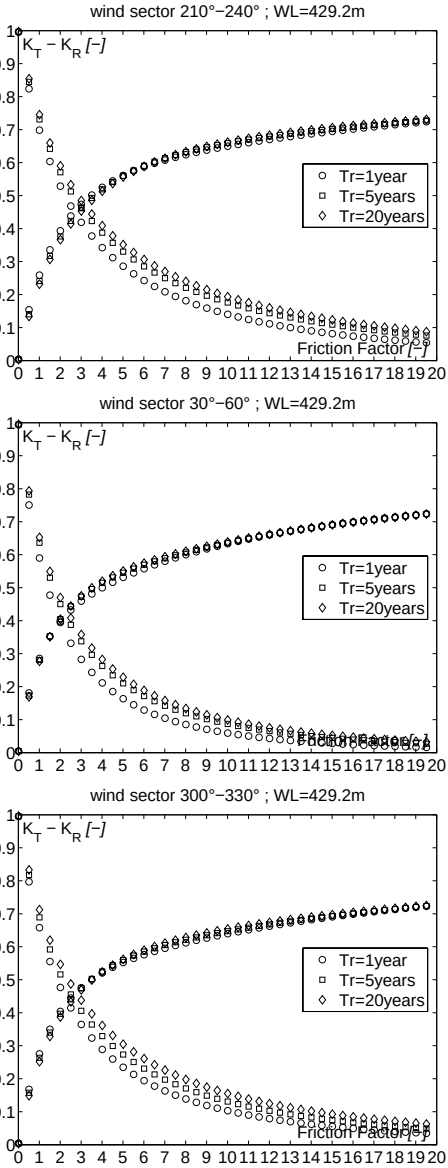

Figure H.2.: Friction factors for $MWL = 429.20\ m$ of the brushwood fences based in the local hydrodynamic conditions

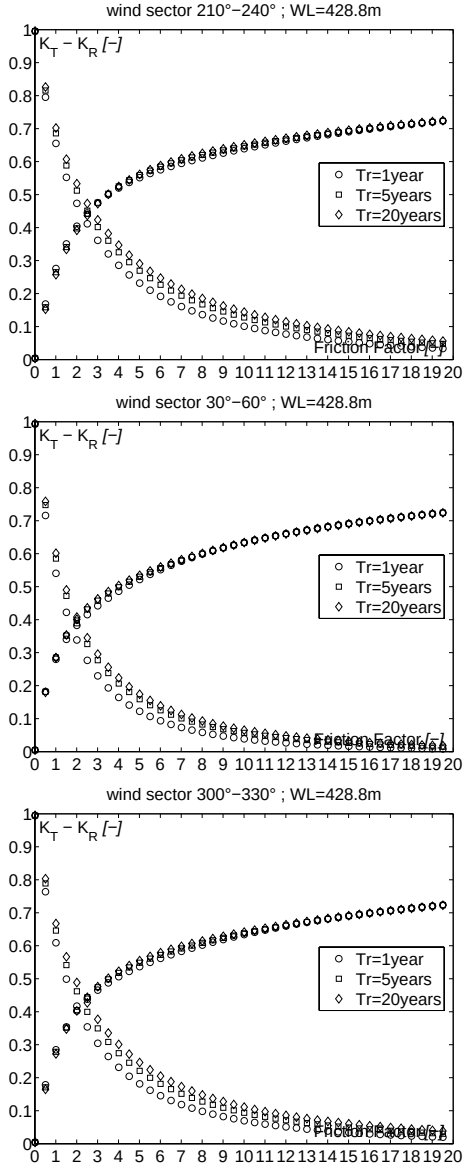

Figure H.3.: Friction factors for $MWL = 428.80\ m$ of the brushwood fences based in the local hydrodynamic conditions

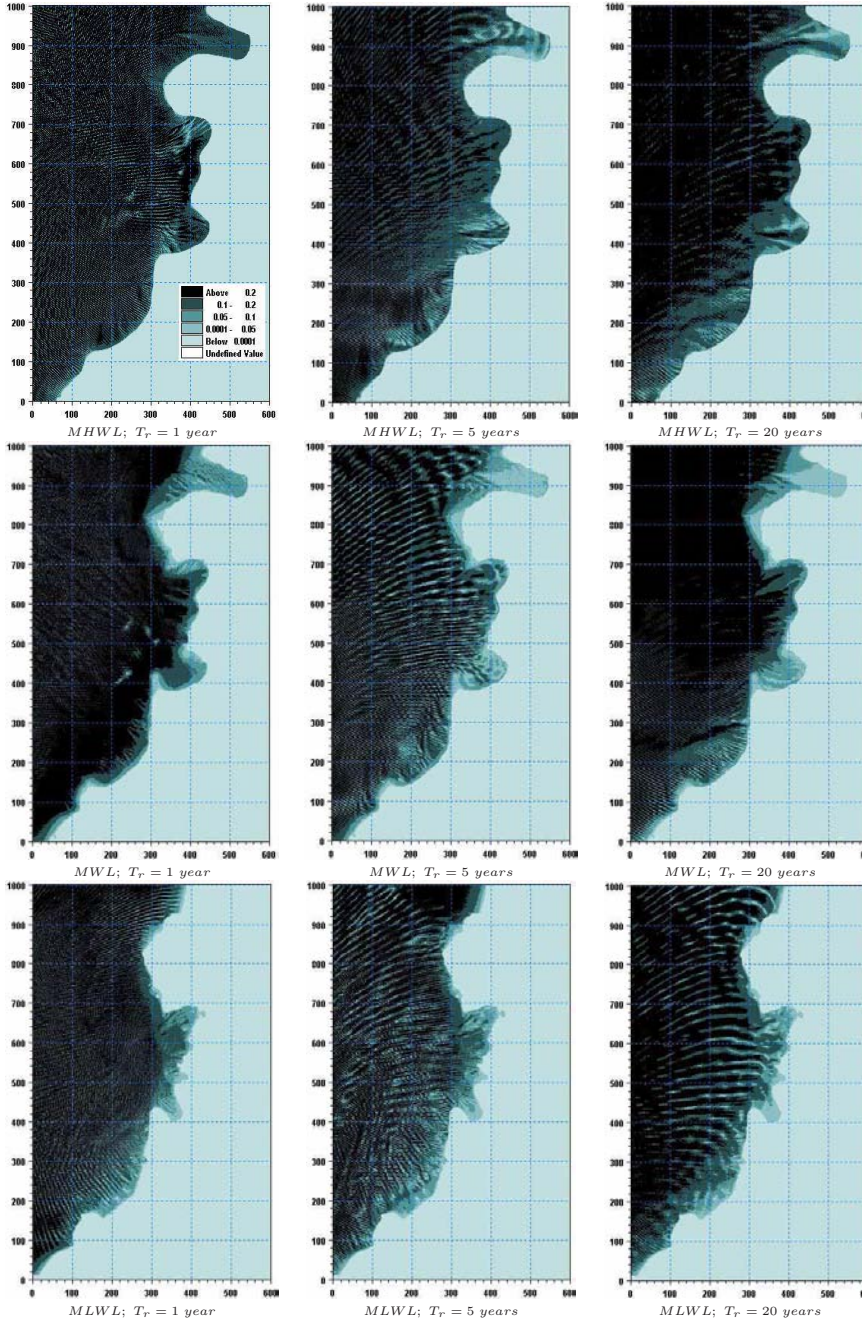

$MHWL;\ T_r = 1\ year$ $MHWL;\ T_r = 5\ years$ $MHWL;\ T_r = 20\ years$

$MWL;\ T_r = 1\ year$ $MWL;\ T_r = 5\ years$ $MWL;\ T_r = 20\ years$

$MLWL;\ T_r = 1\ year$ $MLWL;\ T_r = 5\ years$ $MLWL;\ T_r = 20\ years$

Figure H.4.: Wave field (H_{rms}) at Mörigen during a South-Western wind regime without the presence of the protection structures

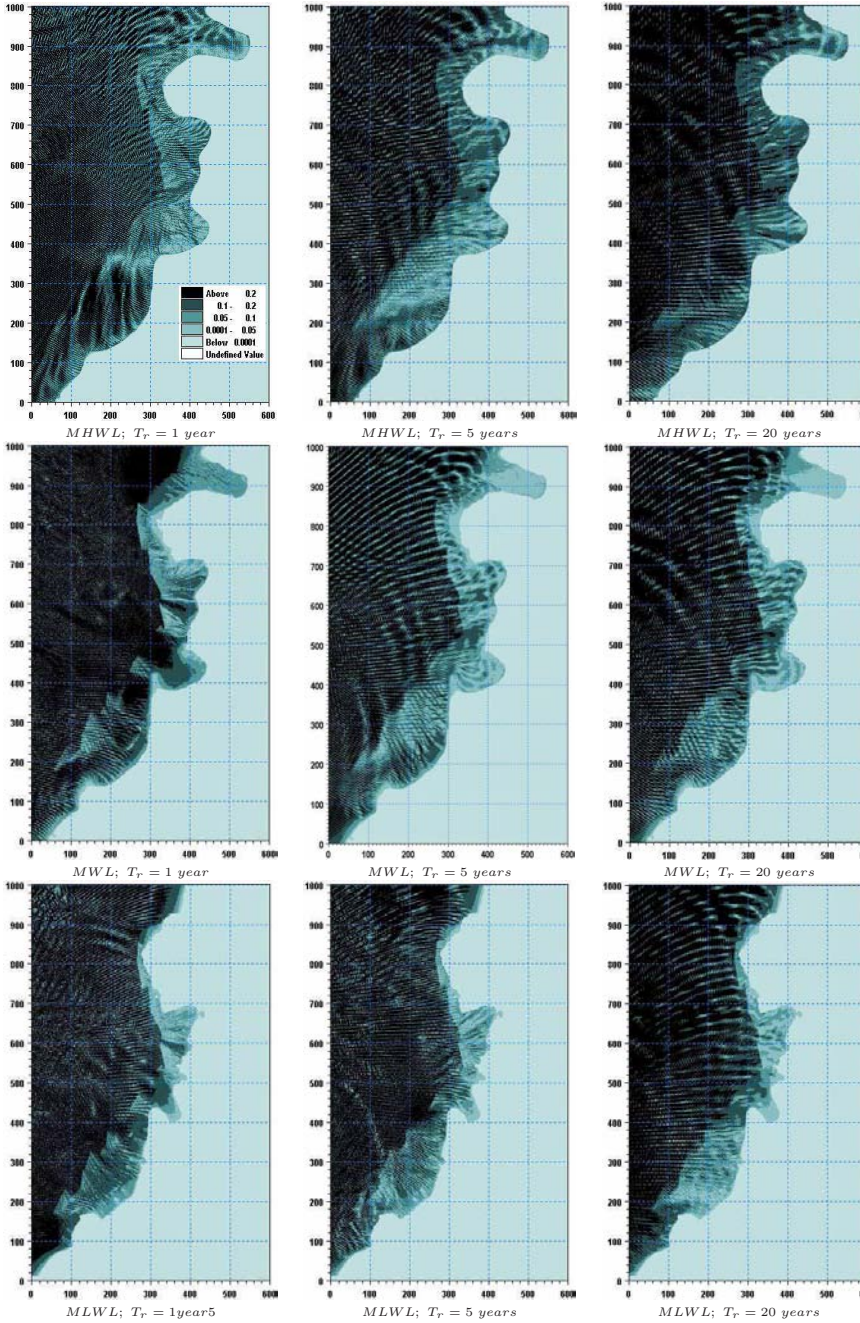

$MHWL;\ T_r = 1\ year$ $MHWL;\ T_r = 5\ years$ $MHWL;\ T_r = 20\ years$

$MWL;\ T_r = 1\ year$ $MWL;\ T_r = 5\ years$ $MWL;\ T_r = 20\ years$

$MLWL;\ T_r = 1year5$ $MLWL;\ T_r = 5\ years$ $MLWL;\ T_r = 20\ years$

Figure H.5.: Wave field (H_{rms}) at Mörigen during a South-Western wind regime with the presence of the protection structures

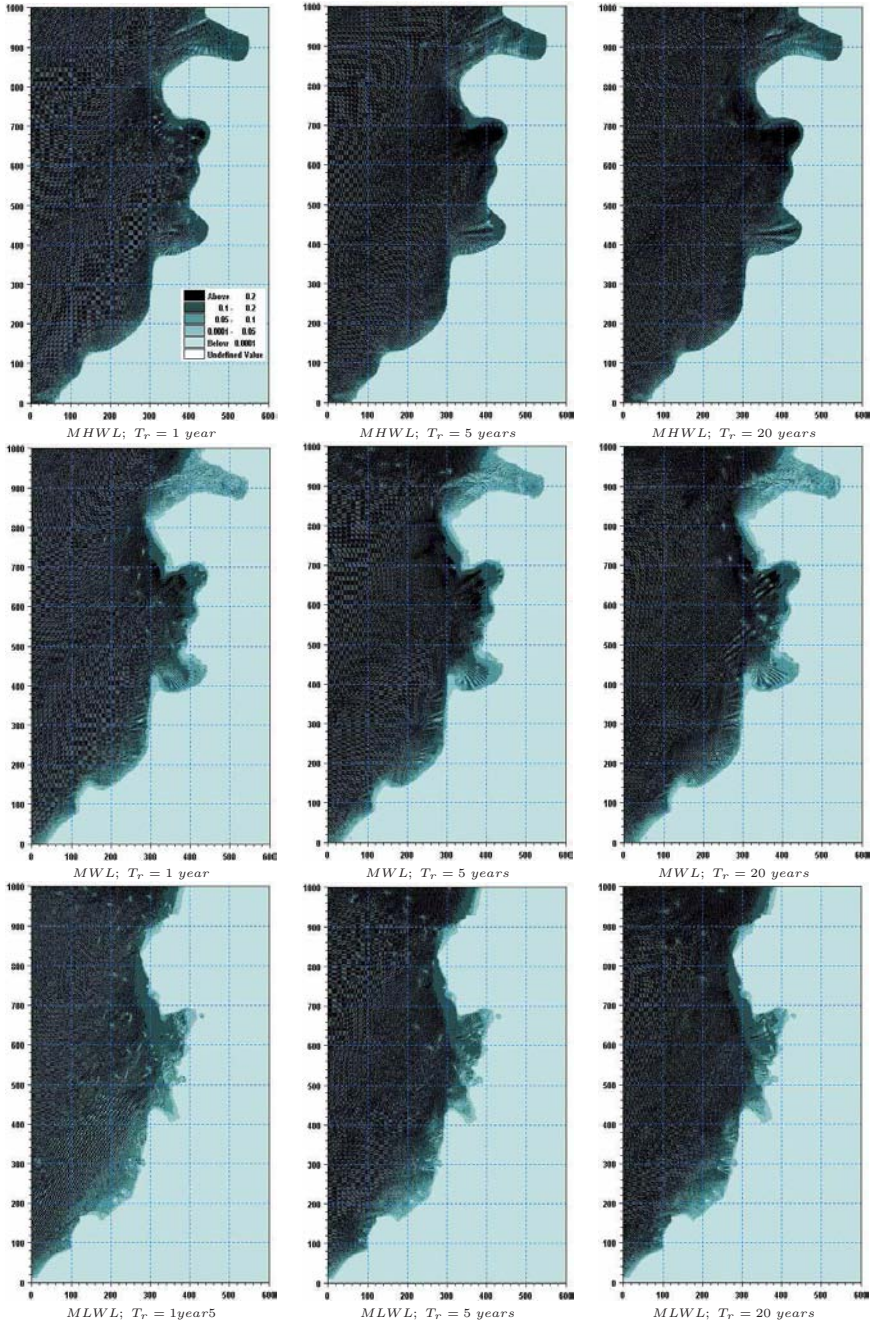

$MHWL;\ T_r = 1\ year$ $MHWL;\ T_r = 5\ years$ $MHWL;\ T_r = 20\ years$

$MWL;\ T_r = 1\ year$ $MWL;\ T_r = 5\ years$ $MWL;\ T_r = 20\ years$

$MLWL;\ T_r = 1year5$ $MLWL;\ T_r = 5\ years$ $MLWL;\ T_r = 20\ years$

Figure H.6.: Wave field (H_{rms}) at Mörigen during a North-Eastern wind regime without the presence of the protection structures

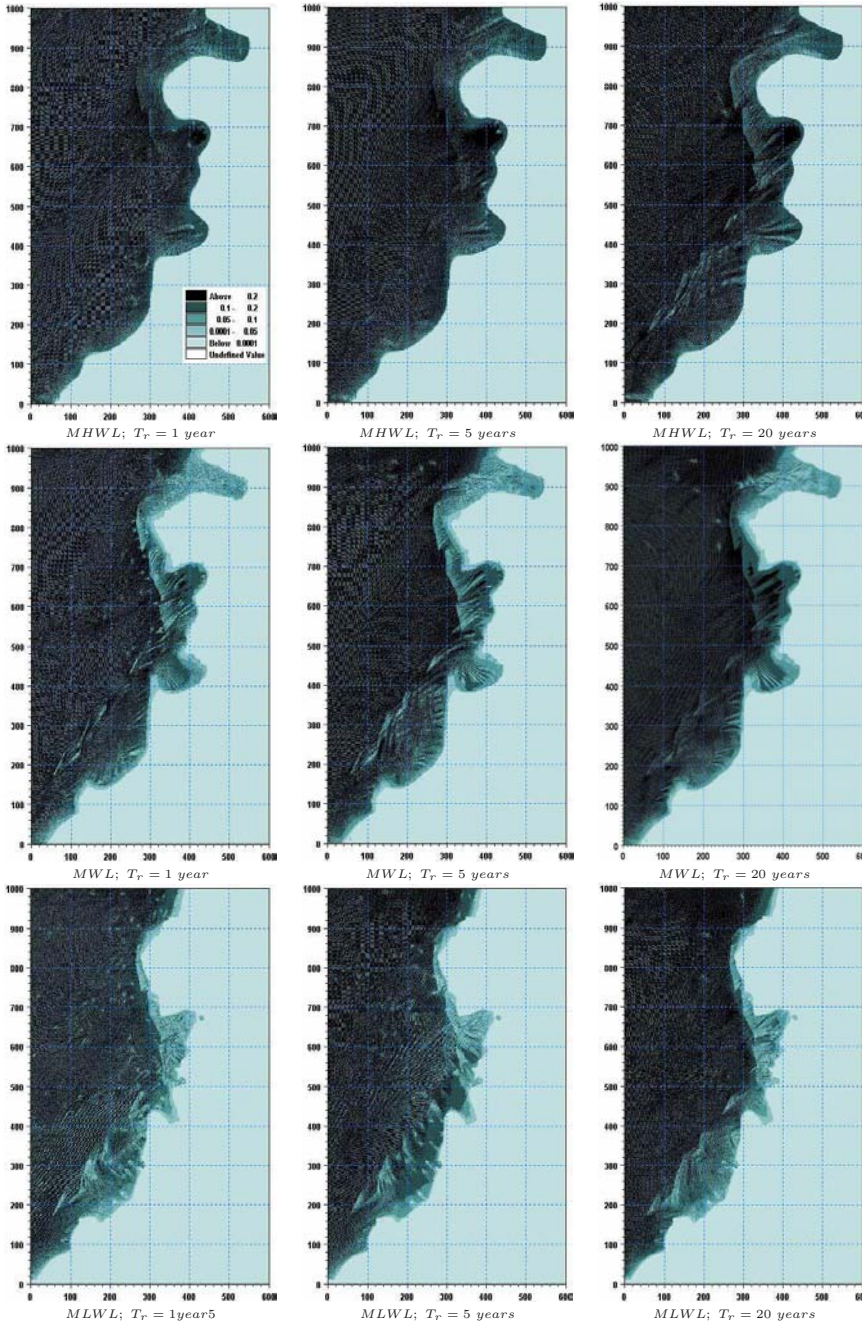

$MHWL;\ T_r = 1\ year$ $MHWL;\ T_r = 5\ years$ $MHWL;\ T_r = 20\ years$

$MWL;\ T_r = 1\ year$ $MWL;\ T_r = 5\ years$ $MWL;\ T_r = 20\ years$

$MLWL;\ T_r = 1 year5$ $MLWL;\ T_r = 5\ years$ $MLWL;\ T_r = 20\ years$

Figure H.7.: Wave field (H_{rms}) at Mörigen during a North-Eastern wind regime with the presence of the protection structures

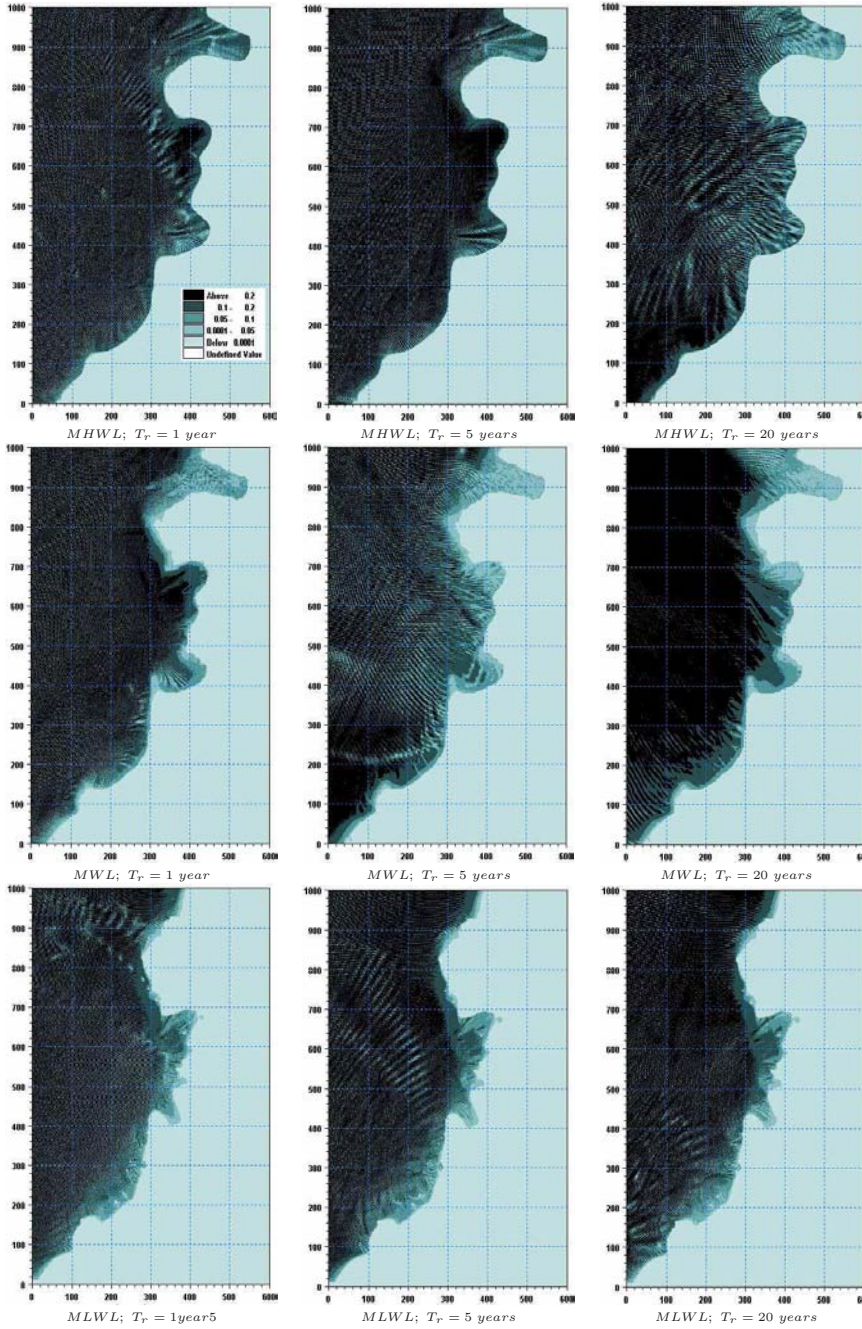

$MHWL;\ T_r = 1\ year$ $MHWL;\ T_r = 5\ years$ $MHWL;\ T_r = 20\ years$

$MWL;\ T_r = 1\ year$ $MWL;\ T_r = 5\ years$ $MWL;\ T_r = 20\ years$

$MLWL;\ T_r = 1year5$ $MLWL;\ T_r = 5\ years$ $MLWL;\ T_r = 20\ years$

Figure H.8.: Wave field (H_{rms}) at Mörigen during a Western wind regime without the presence of the protection structures

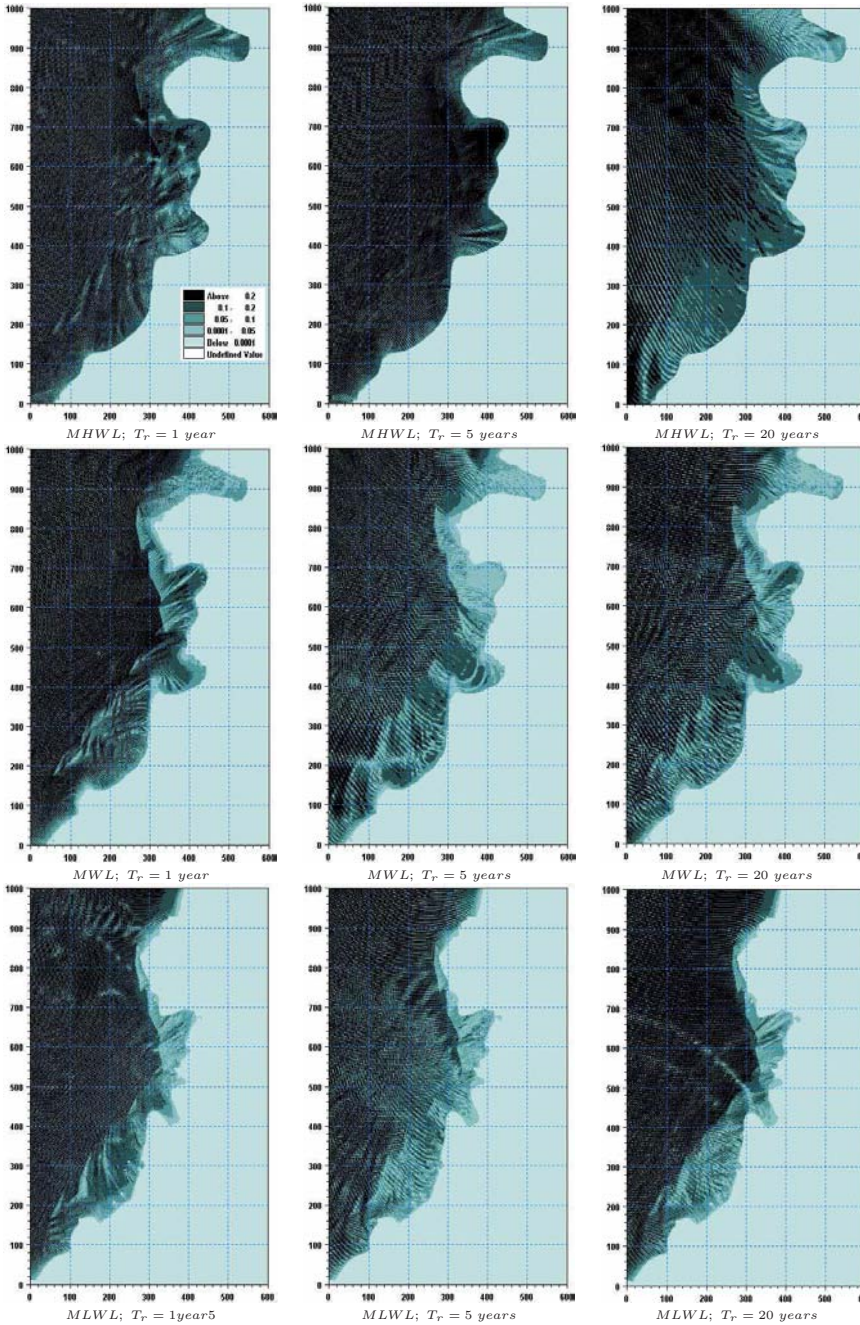

$MHWL;\ T_r = 1\ year$ $MHWL;\ T_r = 5\ years$ $MHWL;\ T_r = 20\ years$

$MWL;\ T_r = 1\ year$ $MWL;\ T_r = 5\ years$ $MWL;\ T_r = 20\ years$

$MLWL;\ T_r = 1year5$ $MLWL;\ T_r = 5\ years$ $MLWL;\ T_r = 20\ years$

Figure H.9.: Wave field (H_{rms}) at Mörigen during a Western wind regime with the presence of the protection structures

Communications du Laboratoire de constructions hydrauliques ISSN 1661-1179
Ecole Polytechnique Fédérale de Lausanne
Editeur: Prof. R. Sinniger

N° 1 1986 W. H. Hager
Discharge measurement structures

N° 2 1988 N. V. Bretz
Ressaut hydraulique forcé par seuil

N° 3 1990 R. Bremen
Expanding stilling basin

N° 4 1996 Dr R. Bremen
Ressaut hydraulique et bassins amortisseurs, aspects hydrauliques particuliers

N° 5 1997 Compte-rendu du séminaire à l'EPFL
Recherche dans le domaine des barrages, crues extrêmes

Communications du Laboratoire de constructions hydrauliques
Ecole Polytechnique Fédérale de Lausanne
Editeur: Prof. Dr A. Schleiss

N° 6 1998 N. Beyer Portner
Erosion des bassins versants alpins suisse par ruissellement de surface

N° 7 1998 G. De Cesare
Alluvionnement des retenues par courants de turbidité

N° 8 1998 J. Dubois
Comportement hydraulique et modélisation des écoulements de surface

N° 9 2000 J. Dubois, J.-L. Boillat
Routing System - Modélisation du routage de crues dans des systèmes hydrauliques à surface libre

N° 10 2002 J. Dubois, M. Pirotton
Génération et transfert des crues extrêmes - Le logiciel Faitou

N° 11 2002 A. Lavelli, G. De Cesare, J.-L. Boillat
Modélisation des courants de turbidité dans le bassin Nord du Lac de Lugano

N° 12 2002 P. de Almeida Manso
Stability of linings by concrete elements for surface protection of overflow earthfill dams

N° 13 2002 E. Bollaert
Transient water pressures in joints and formation of rock scour due to high-velocity jet impact

ISSN 1661-1179

Prof. Dr A. Schleiss
Laboratoire de constructions hydrauliques - LCH
EPFL, Bât. GC, Station 18, CH-1015 Lausanne
http://lchwww.epfl.ch
e-mail: secretariat.lch@epfl.ch